Wave Dynamics of the Middle Atmosphere

Davis, Robin

Award date:
2014

Awarding institution:
University of Bath

Wave Dynamics of the Middle Atmosphere

submitted by

Robin Davis

for the degree of Doctor of Philosophy

of the

University of Bath

Department of Electronic
and Electrical Engineering

April 2014

Abstract

This thesis presents the results from investigations into various features of the dynamics of the middle atmosphere.

Wind measurements from the meteor radar on Ascension Island and temperatures measured by the Aura MLS instrument are used to characterise Ultra-Fast Kelvin Waves (UFKW) in the MLT-region. Rainfall rates from TRMM are used as a proxy for latent heat release in an investigation of the excitation of UFKW, and results are compared with predictions of the Kyushu-GCM. Amplitudes and vertical wavelengths are determined, as are the accelerations resulting from wave dissipation. Intra-seasonal oscillations (ISOs) are observed in the wave amplitudes and accelerations, and oscillations with the same periods are observed in the rainfall and MLT-region winds, suggesting that UFKW play a role in carrying the tropospheric ISOs to higher regions.

The seasonal and interannual variability of the tidal field over Ascension Island is investigated. Amplitudes, phases and vertical wavelengths of the diurnal and semidiurnal tides are reported on. Our observations of tidal parameters are compared with the predictions of the extended Canadian Middle Atmosphere Model (eCMAM) and the Whole Atmosphere Community Climate Model (WACCM). Correlations between tidal amplitudes, the stratospheric Quasi-Biennial Oscillation (QBO) and the El Niño Southern Oscillation (ENSO) are discussed.

The Hocking (2005) method is adapted to recover monthly-mean gravity-wave momentum fluxes and wind variances either side of the Drake passage gravity-wave hotspot. The ability of the method to recover momentum fluxes over each radar are tested by sampling a series of specified (known) wave fields of increasing complexity with the actual meteor distributions, and comparing the recovered momentum fluxes with the specified values. The analysis is then applied to the real data to obtain climatologies of the MLT-region variances and momentum fluxes for a composite year of the 2008 to 2012 data.

Acknowledgements

I would like to thank all of the CSAOS staff and postgraduate students who I have had the pleasure of knowing and working with over the course of my Ph.D., but particularly my supervisor Nick Mitchell for his unerring guidance over the last three and a half years.

I would also like to thank my collaborators Anne Smith, Ying-Wen Chen, Saburo Miyahara, Jian Du and William Ward for their advice and for sending me the eCMAM, WACCM and Kyushu-GCM data that appears in various places throughout this work, Rosmarie de Wit for discussions on the gravity-wave momentum flux method, and the Natural Environment Research Council for funding my studies.

Finally I would like to thank my parents, twin and siblings for all their support during my time here, and Emily for her inexhaustible patience and cheerfulness.

Contents

List of Figures

List of Tables

Chapter 1

Introduction to the MLT Region

1.1 Introduction

The dynamics of the middle atmosphere are dominated by various types of waves, particularly tides, gravity waves and planetary waves. These waves can have a variety of sources but those that propagate upwards can have very large amplitudes by the time they reach the Mesosphere/Lower Thermosphere (MLT) region, at heights of between approximately 50 and 100 km.

The study of these waves in the MLT region can be very difficult as only rockets (which tend to be expensive) can reach these heights for *in situ* measurements. The advent of remote-sensing instruments in recent decades, such as LiDARs, radars and satellites, has opened up the MLT region to investigation. However, the MLT remains perhaps the least well understood region of the atmosphere.

The MLT is a very interesting region that hosts fascinating phenomena such as meteors, noctilucent clouds, airglow, the auroras, and sprite lightning. It also contains the mesopause, the coldest naturally-occurring region on Earth with temperatures that can go below $\sim$ 130 K, unique for having temperatures far lower in summer than in winter. The waves that propagate to the MLT region can deposit energy and momentum, driving the global circulation.

However, the MLT is not only an interesting region to study but also an important one. For example, a doubling of CO_2 has been predicted to result in a cooling of 10 - 15 K in the MLT region (e.g., Berger and Demeris, 1993; Akmaev and Fomichev, 1998). Thomas (1996) found that a doubling of CO_2 and CH_4 could extend the visibility area of Polar Mesospheric Clouds to mid-latitudes. It is also interesting to note that PMCs had not been observed prior to the industrial revolution. It has been proposed that the MLT region will be far more sensitive to climate change than the troposphere, and thus might be a useful indicator of how the atmosphere is changing.

This chapter will outline the structure of the atmosphere, compare the predictions of radiative equilibrium with the observed atmospheric temperature and wind fields, and discuss the reasons for the

differences.

1.1.1 The Structure of the Atmosphere

The atmosphere can be divided into broad layers separated by changes in the atmosphere's temperature gradient (see Figure 1.1).

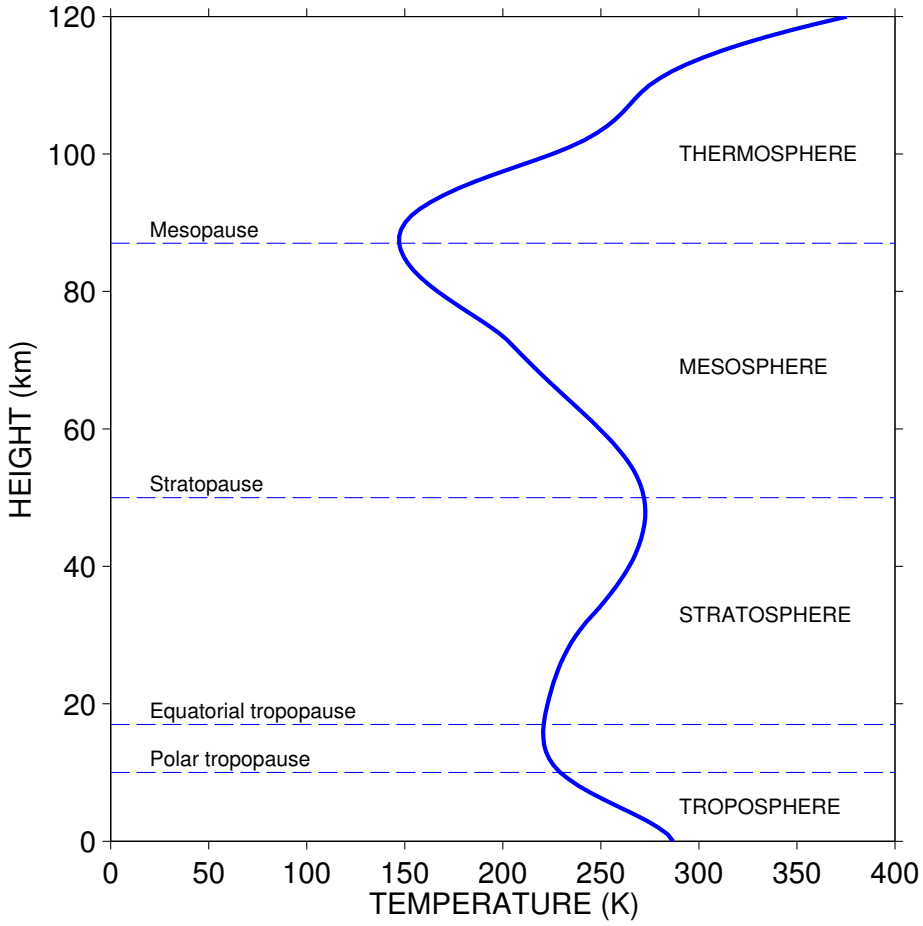

Figure 1.1: Temperature as a function of height from 0 to 120 km, with atmospheric layers labelled. The data plotted is from the MSIS-E-90 model for the month of June 2010 at 55^{o} latitude and 0^{o} longitude.

The temperature profile can be explained in part by the heights at which various chemical constituents are concentrated, and the effect that they have on the radiative balance of the atmosphere. The heating/cooling contribution from each constituent is shown in Figure 1.2.

From the ground up to heights of around 15 km, the temperature decreases with increasing height at a lapse rate of $\sim$ 7 K km^{-1} as solar radiation heats the ground much more strongly than it heats the air. This is the region called the troposphere ("turning" sphere) which contains most of the atmosphere's mass, nearly all of the water, and it is where 'weather' occurs. The troposphere is bound by the tropopause, where most water vapour condenses out due to the temperature minimum; only a tiny fraction exists in the stratosphere and MLT region above. The tallest cumulonimbus clouds of large

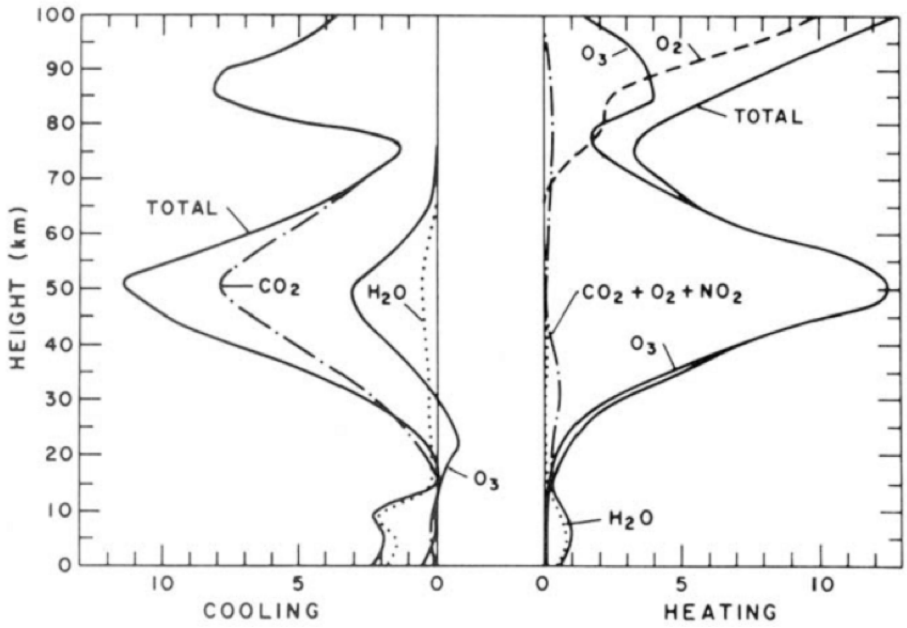

Figure 1.2: Heating/cooling rate (K day^{-1}) as a function of height for important chemical constituents, from London (1980).

thunderstorms are limited in height to the tropopause, where they flatten out such that they can resemble anvils. Commercial airliners usually cruise just above this level.

In the stratosphere, extending from the tropopause up to heights of approximately 50 km, temperature increases with increasing height. As can be seen in Figure 1.2, this is because at these heights solar ultra-violet radiation is absorbed by ozone to a greater extent than energy is radiated away to space by carbon dioxide, resulting in a net heating. The negative lapse rate means that the stratosphere is very stable and inhibits vertical motion, such that most motion is horizontal. The stratosphere is very dry due to the tropopause 'cold trap', with a water content of just 2 - 6 ppm, compared to the 1000 - 40000 ppm of the lower troposphere. Two particularly interesting features of stratospheric dynamics are the Quasi-Biennial Oscillation (QBO), an oscillation of the stratospheric equatorial zonal winds, which reverse from eastwards to westwards and back with a period of approximately 28 months, and Sudden Stratospheric Warmings (SSWs), characterised by a reduction (or reversal) of the polar winter eastwards winds and an accompanying sudden rise in temperature of the polar cap.

At the stratopause (a local temperature maximum), the rate of change of temperature again changes direction, with the mesosphere decreasing in temperature with increasing height. At heights of between approximately 50 - 85 km, CO_2 cooling is reduced but nevertheless dominates ozone heating as ozone is less concentrated than in the stratosphere. The MLT is host to a number of interesting phenomena as mentioned in the introduction to this chapter, with wave-like motions the most important contributor to mesospheric dynamics.

Above the mesopause, solar radiation is absorbed by atomic oxygen and nitrogen leading to a rapid temperature increase with increasing height. There is a strong diurnal cycle in heating, and ionisation

becomes important. This region is the thermosphere.

1.2 The Atmosphere Under Radiative Equilibrium

1.2.1 Temperature Structure

An initial and basic model of the atmosphere's temperature and wind fields can be obtained by considering the atmosphere to be in radiative equlibrium, i.e., with radiative heating and cooling in equilibrium, with no net change. Using the total heating and cooling rates that were seen in Figure 1.2, the resulting zonal-mean temperature field of the atmosphere can be calculated. This is presented as a function of height and latitude for solstitial conditions in Figure 1.3.

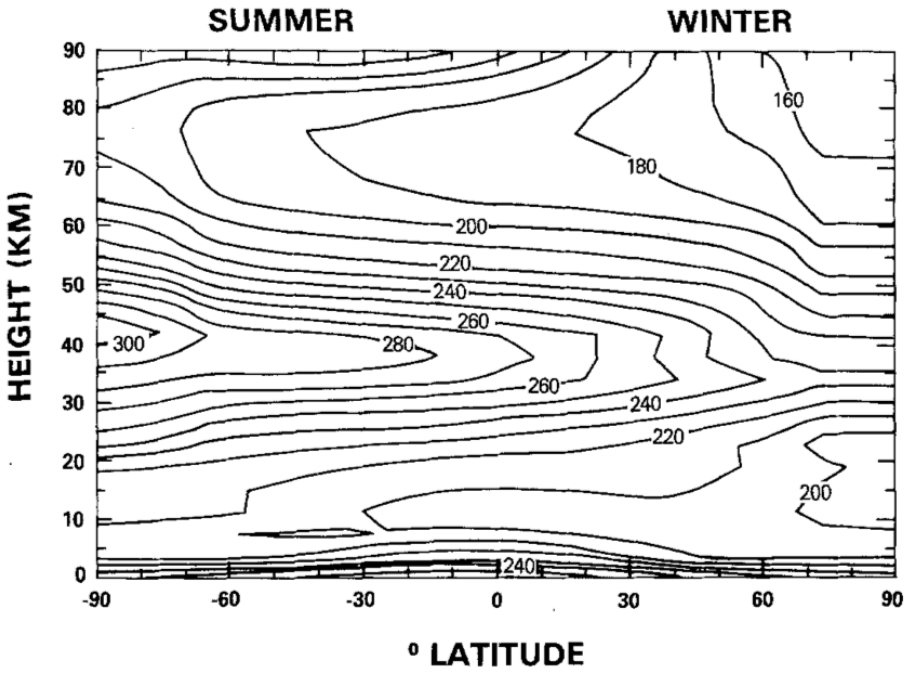

Figure 1.3: Prediction of solstitial atmospheric zonal-mean temperature as a function of height and latitude for an atmosphere , from Geller (1983).

The main feature of the results presented in the figure is the temperature gradient from a warm summer pole to a cool winter pole. This is as one might expect as the summer pole will be subject to constant solar heating during the solstice, while the winter pole will be in continual darkness. Stratospheric temperatures in excess of 300 K are predicted over the summer pole at heights near 40 km, while at similar heights the temperature falls to around 220 K over the winter pole.

The lowest temperatures are at a height of approximately 85 km, the mesopause, with temperatures falling below 160 K over the winter pole. Radiative equilibrium predicts a warmer mesospheric summer pole than winter pole.

1.2.2 General Circulation

The zonal-mean winds that arise from the radiative equilibrium temperature field can be deduced from the thermal wind equation and by considering the forces acting on an air parcel of unit mass.

The pressure gradient force, P, acts to push the air parcel down any pressure gradient from a region of higher pressure towards a region of lower pressure. In the radiative equilibrium model this means motion from the warmer summer hemisphere to the cooler winter hemisphere.

The Coriolis force, C, arises from the rotation of the Earth. It acts to the right of an air parcel's motion in the northern hemisphere, and to the left of motion in the southern hemisphere, with a strength related to the parcel's velocity and to its latitude. When the pressure gradient force is balanced by the Coriolis force with no other forces acting, the air parcel moves parallel to isobars, eastward in the winter hemisphere and westward in the summer hemisphere. This is demonstrated in the diagram of Figure 1.4.

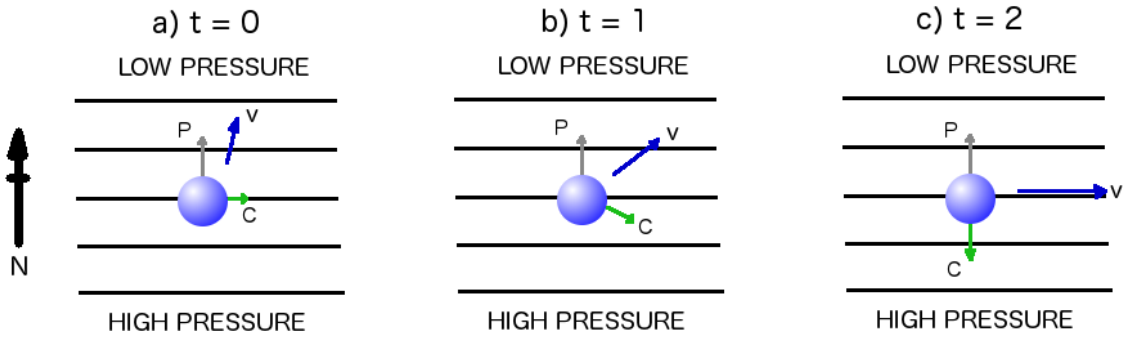

Figure 1.4: Schematic diagrams showing how the pressure gradient and Coriolis forces balance in the northern hemisphere winter with a resulting geostrophic flow that is parallel to the isobars. An air parcel moving with northward motion under the pressure gradient force in the northern hemisphere experiences the Coriolis force, which acts perpendicularly to motion. This adds a zonal component to the parcel's velocity, increasing the total velocity, and so the Coriolis force increases, whilst rotating to remain perpendicular to the motion. The result is balance of Coriolis and pressure gradient forces, with purely zonal air parcel motion.

In Figure 1.4a, the pressure gradient force P (grey arrow) acts on the parcel causing motion from high pressure to low. The Coriolis force (green arrow) acts perpendicularly to the motion, which gives the air parcel a resultant velocity in the direction of the blue arrow, labelled v. At t = 1, the Coriolis force continues to act perpendicularly to the motion, pulling the direction of motion around to the right. As the magnitude of the velocity is now slightly larger with a component from the Coriolis force as well as from the original and unchanged P component, the Coriolis force increases proportionately. At time t = 2, the Coriolis force has increased in magnitude and changed direction to the extent that it now balances the pressure gradient force, resulting in a velocity vector parallel to the isobars. This wind from the balance of P and C is known as geostrophic flow. Critically, in the general circulation as predicted by consideration of radiative equilibrium, there is no vertical or meridional component to the flow.

The zonal-mean winds arising from radiative equilibrium are shown in Figure 1.5. Note that winds are not calculated over the tropics, as the Coriolis force becomes too small near the equator for the thermal wind equation to apply.

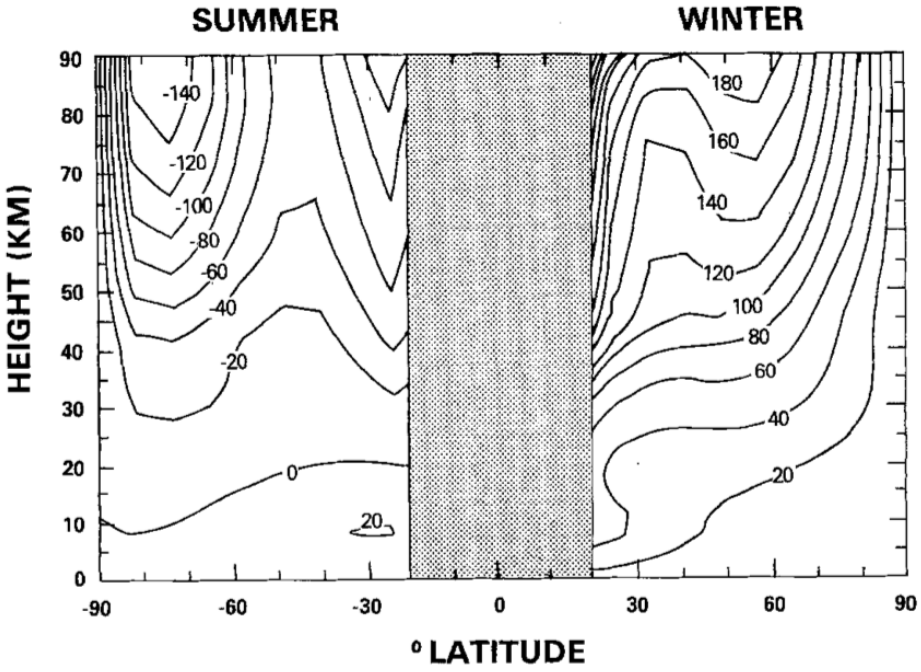

Figure 1.5: Prediction of solstitial atmospheric zonal-mean wind as a function of height and latitude in an atmosphere of radiative equilibrium, from Geller (1983).

From the figure it can be seen that the winds in the middle atmosphere are eastward in the winter hemisphere, westward in the summer, and that the winds increase in magnitude with height. Two open jets are formed with wind speeds that increase with increasing height. These open jets are centred on mid-latitudes in the winter hemisphere, and high latitudes in the summer.

1.3 The Observed Circulation

The COSPAR International Reference Atmosphere (CIRA-86) provides global climatologies of zonal-mean zonal wind and temperatures derived from a combination of ground-based and satellite measurements (global models have been updated since, but the key features of atmospheric structure are unchanged). The temperature field during the northern hemisphere winter solstice is presented in Figure 1.6.

While the radiative equilibrium model reproduces temperatures in the stratosphere reasonably well, there are two major differences between the model and the observed climatologies at other heights. Firstly, the model predicted a general increase in temperature at the tropopause from the winter to the summer pole. However, Figure 1.6 shows a distinct minimum in the observations at the tropopause level over the equator. Secondly, as briefly mentioned in the introduction to this chapter, the observations show that

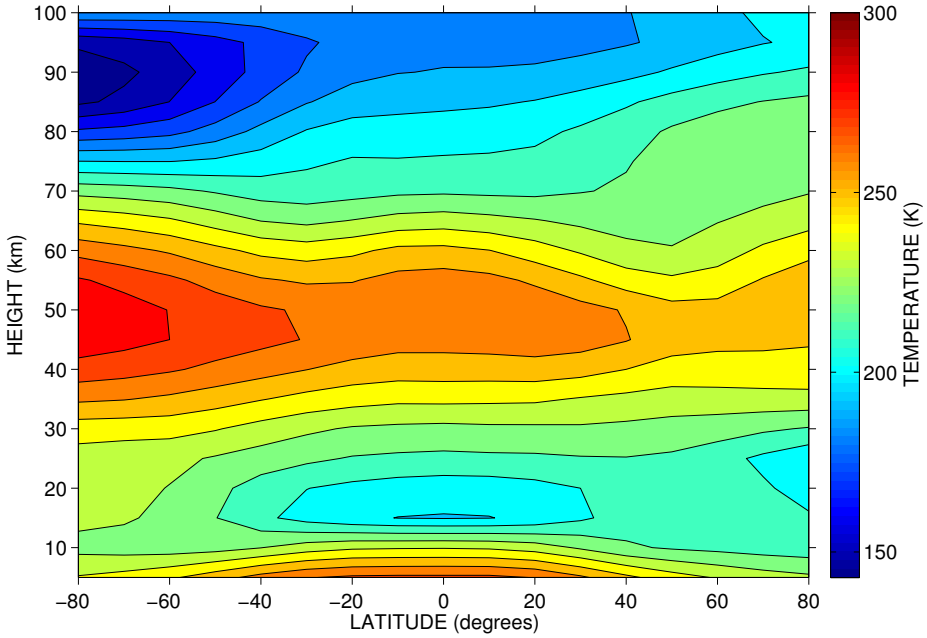

Figure 1.6: CIRA-86 zonal-mean temperatures as a function of latitude and height during the northern hemisphere winter solstice. Note that the mesopause is much colder near the summer pole than the winter.

the summer mesopause is in fact much colder than the winter mesopause, in direct contradiction to the predictions of radiative equilibrium.

The observed winds also show some interesting differences to the model prediction. The CIRA-86 winds during the northern hemisphere winter solstice are presented in Figure 1.7.

It can be seen that the observations reveal a pair of jets in the troposphere/lower stratosphere that are eastward in both hemispheres. These were not present in the radiative equilibrium model. Another difference is that while zonal wind magnitudes continued to grow with height above 90 km in the model, the observations reveal that the jets are actually closed off, with the winds reversing direction at heights near 90 km, above the mesopause.

To account for the differences between the predictions of radiative equilibrium and the observations, in addition to the pressure gradient and Coriolis forces we must consider the effects of a third, additional force. The model predictions were reasonably good at stratospheric heights as the stratosphere has little friction. In the troposphere however, topography can be a major source of friction. In the mesosphere, wave-breaking can add a force that can oppose motion. The addition of a third force, D, means that the pressure gradient force is now balanced by both the Coriolis force and the third force, such that P = C + D. This allows a meridional component of the wind to develop such that the flow is no longer purely parallel to the isobars, as demonstrated in the schematic of Figure 1.8. The meridional winds that were not predicted under radiative equilibrium can reach large amplitudes in the middle atmosphere. Note that the third force is often called wave drag, but note that it is not always strictly a drag force as it does not always oppose motion.

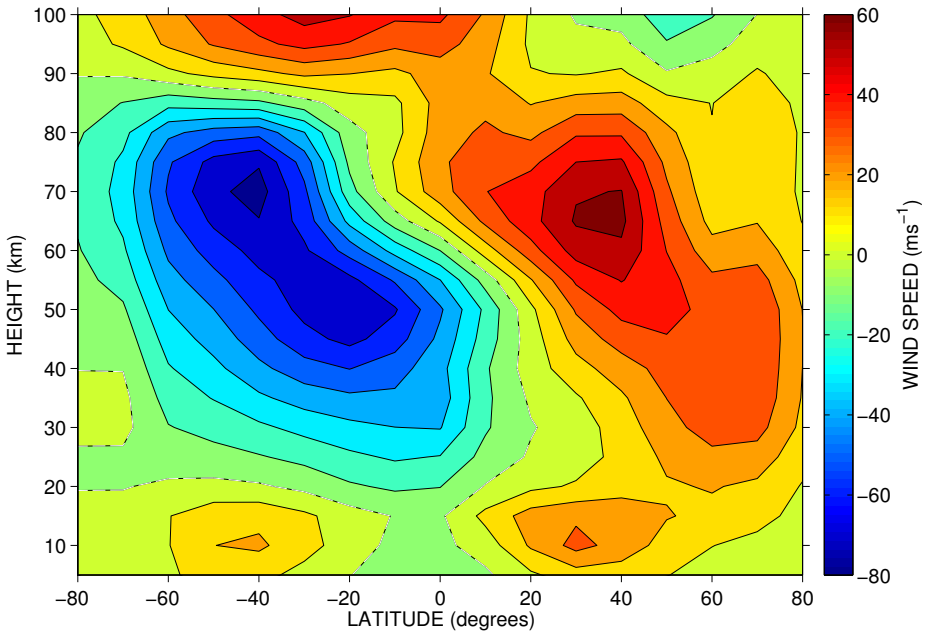

Figure 1.7: CIRA-86 zonal-mean winds as a function of latitude and height during the northern hemisphere winter solstice. The dashed line represents the zero-wind line. Note that the jets are closed, with winds reducing at heights near 70 km and reversing at heights near 90 km.

The figure shows that meridional wind tends to flow from high pressure to low, i.e., summer hemisphere to winter hemisphere. This results in a convergence of air over the winter pole, and a divergence over the summer pole. For continuity to hold, a flow is required to replace the air lost from the summer pole and similarly to remove the air converging over the winter pole. Vertical motion results, with an upwelling over the summer pole that draws up air from lower down, and a downwelling over the winter pole, forming the Dobson-Brewer circulation as presented in Figure 1.9.

The Dobson-Brewer circulation explains the cold summer mesopause as the rising air over the summer pole cools adiabatically, while the sinking air over the winter pole heats adiabatically. The change in direction of temperature gradient has an impact on the thermal wind equation, resulting in the closing of the jets near the mesopause.

1.4 Summary

In this chapter it was seen that the atmosphere can be divided into layers according to the change in temperature as a function of height. Using the heating and cooling rates of atmospheric chemical species, and by considering the balance of the pressure gradient and Coriolis forces, model wind and temperature fields can be predicted for an atmosphere assumed to be in radiative equilibrium.

The major differences between these predictions and the observed wind and temperature fields were noted, such as the cold summer mesopause and the structure of the jets. These differences can be explained by the inclusion of a third force to balance the Coriolis and pressure gradient forces, which

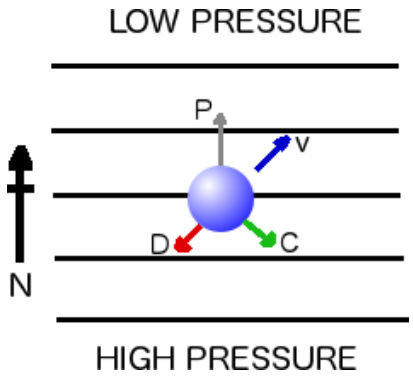

Figure 1.8: The addition of a third force (from topography in the troposphere and breaking waves in the mesosphere) results in a new balance of forces that allows meridional flow.

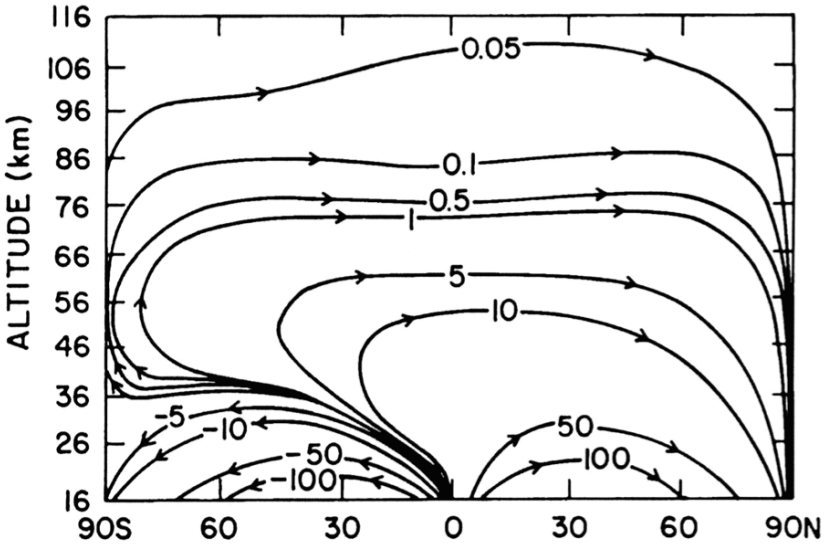

Figure 1.9: Mass meridional stream function for the northern hemisphere winter solstice, demonstrating the Dobson-Brewer circulation. The upwelling over the summer pole results in an adiabatic cooling, causing the cold summer mesopause. Units are $\mathrm{kgm^{-1}s^{-1}}$. From Garcia and Solomon (1983).

creates meridional flow. This third force in the MLT region results from a momentum transfer by waves, which will be the subject of the next chapter.

Chapter 2

Atmospheric Waves and Tides

2.1 Introduction

In the previous chapter it was mentioned that wave activity can impart a force on the middle atmosphere that balances the Coriolis and pressure gradient forces. In fact, waves have a crucial impact on the dynamics of the middle atmosphere, the most important oscillations being gravity waves, tides, and planetary waves. Figure 2.1 presents as an example a Lomb-Scargle periodogram of four months of zonal winds at a height of $\sim$ 91 km recorded by the SAAMER meteor radar at Riogrande, Tierro del Fuego.

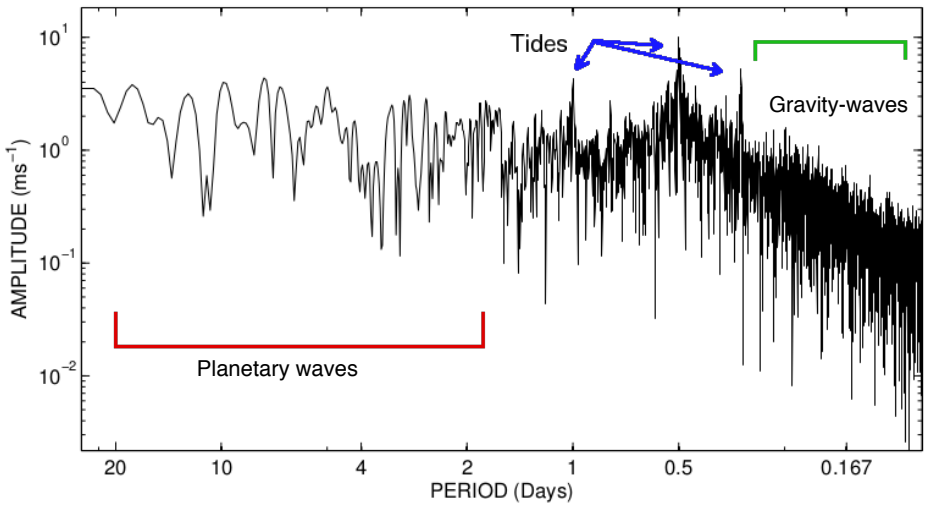

Figure 2.1: Lomb-Scargle periodogram of the zonal wind hourly time series as measured by the SAAMER meteor radar, for the interval January to April, 2009. The periods of the main atmospheric oscillations have been marked.

The spectrum shows distinct peaks at periods of 24, 12 and 8 hours, corresponding to the diurnal, semidiurnal and terdiurnal tides. At higher frequencies of the spectrum are gravity waves, while at longer periods there are signals corresponding to planetary wave activity.

Atmospheric waves can reach very large amplitudes in the MLT region. The density, ρ, of the atmosphere decreases exponentially with height,

$$\rho(z) = \rho_0 e^{-z/H} \tag{2.1}$$

where z is the height, ρ_0 is the density at sea level and H is the scale height. The scale height is the distance over which pressure decreases by a factor of e (typically $\sim$ 7 km in the MLT), and is given by H = kT / mg where k is Boltzmann's constant, T is the temperature, m is the mean molecular mass and g is gravitational acceleration. As these atmospheric waves propagate upwards, the conservation of kinetic energy per unit volume,

$$KE \ = \ \frac{1}{2}\rho A^2 \tag{2.2}$$

(where A is the wave amplitude) implies that the waves would grow exponentially with height at the rate

$$A(z) \ = \ A_0 e^{\frac{z}{2H}} \tag{2.3}$$

While this exponential growth is not always realised in the atmosphere, waves can nevertheless reach large amplitudes in the MLT region and dominate the region's dynamics.

2.2 Internal Atmospheric Gravity Waves

Gravity waves are mesoscale waves, occurring on a relatively small horizontal scale with sizes of the order of tens of kilometres. They have a number of sources including flow over mountainous topography, wind shear, convection and wave-wave interactions. Periods range between the Brunt-Väisälä limit of approximately 5 minutes, up to the inertial period.

2.2.1 The Dispersion Relation of Gravity Waves

The gravity wave dispersion relation can provide an insight into some of the properties of the waves, and so the derivation is outlined here, following Hines (1960), for an idealised isothermal atmosphere with uniform composition, and in which waves are the only perturbations.

Atmospheric wave behaviour is then determined by three equations:

$$\rho_0 \frac{\partial \mathbf{u}}{\partial t} = \rho \mathbf{g} - \nabla p \tag{2.4}$$

$$\frac{\partial p}{\partial t} + \mathbf{u} \cdot \nabla p_0 = C^2 \left[\frac{\partial \rho}{\partial t} + \mathbf{u} \cdot \nabla \rho_0 \right] \tag{2.5}$$

$$\frac{\partial \rho}{\partial t} + \mathbf{u} \cdot \nabla \rho_0 + \rho_0 \nabla \cdot \mathbf{u} = 0 \tag{2.6}$$

These are, respectively, the equations of hydrostatic equilibrium (i.e., vertical accelerations are small in comparison with gravitational acceleration), of adiabatic state, and of mass conservation. ρ_0 and p_0 are the unperturbed density and pressure, ρ and p the perturbed density and pressure, $\mathbf{u}$ is the velocity perturbation, $\mathbf{g}$ the gravitational acceleration, ∇ the grad operator $\nabla = \left(\frac{\partial}{\partial x}, \frac{\partial}{\partial y}, \frac{\partial}{\partial z}\right)$, and C the speed of sound, given by $C^2 = \gamma \frac{p_0}{\rho_0}$ where γ is the ratio of specific heats (a constant, along with C and $\mathbf{g}$ under our idealised atmospheric conditions).

The solutions to the three equations have complex wavenumbers K_x and K_z (where x is any direction perpendicular to z) that are related to the circular frequencies, ω, of the solutions by the dispersion relation:

$$\omega^4 - \omega^2 C^2 \left({K_x}^2 + {K_z}^2\right) + (\gamma - 1) g^2 {K_x}^2 + i\gamma g \omega^2 K_z = 0 \tag{2.7}$$

Further conditions are given by the polarization equations governing pressure variation, density variation, horizontal and vertical motion which are, respectively,

$$P = \gamma \omega^2 K_z - i\gamma g \frac{\omega^2}{C^2} \tag{2.8}$$

$$R = \omega^2 K_z + i(\gamma - 1) g K_x^2 - i\gamma g \frac{\omega^2}{C^2} \tag{2.9}$$

$$X = \omega K_x K_z C^2 - ig\omega K_x \tag{2.10}$$

$$Z = \omega^3 - \omega K_x^2 C^2 \tag{2.11}$$

If gravity is neglected, equation 2.7 reduces to the equation governing sound propagation:

$$\omega^2 = C^2 \left({K_x}^2 + {K_z}^2\right) \tag{2.12}$$

With gravity however, inspection of equation 2.7 reveals that solutions may not have real and non-zero values for both K_x and K_z. For zonal propagation K_x must be real, notated $K_x = k_x$, as a complex or imaginary horizontal wavenumber would cause amplitude to decay exponentially with horizontal distance.

With a real k_x, equation 2.7 allows two possibilities for K_z. K_z may be purely imaginary, which prevents vertical propagation. These 'evanescent' waves (with no change in phase with height) are 'external', and may propagate horizontally along the boundary between two fluids, similar to ocean surface waves.

The second possibility is the complex $K_z = k_z + i\psi$. Equating imaginary coefficients in equation 2.7 then gives

$$-\omega^2 C^2 2k_z\psi + \gamma g\omega^2 k_z = 0$$

Thus the vertical wavenumber for the 'internal' waves is given by:

$$\begin{aligned} K_z &= k_z + i\frac{\gamma g}{2C^2} \\ &= k_z + \frac{i}{2H} \end{aligned} \tag{2.13}$$

These internal waves can propagate vertically. Substituting the complex value for K_z (and the real value for K_x) into equation 2.7 gives the dispersion relation for internal waves:

$$\omega^4 - \omega^2 C^2(k_x^2 + k_z^2) + (\gamma - 1)g^2 k_x^2 - \omega^2 \frac{\gamma^2 g^2}{4C^2} = 0 \tag{2.14}$$

Solving this as a quadratic equation in ω^2 and taking the two positive roots for ω reveals that internal waves may exist at frequencies higher than the acoustic frequency,

$$\omega_a \equiv \frac{\gamma g}{2C} \tag{2.15}$$

or at frequencies below the Brunt-Väisälä frequency,

$$N \equiv (\gamma - 1)\frac{g}{C} \tag{2.16}$$

As $1 < \gamma < 2$ for all gases, $N < \omega_a$. This results in two separate regimes for allowed frequencies, with a 'forbidden zone' in the spectrum such that no internal waves propagate with frequencies $N < \omega < \omega_a$. At frequencies greater than the acoustic frequency, waves propagate longitudinally. At frequencies less than N, waves are transverse; these internal waves are gravity waves. The Brunt-Väisälä frequency is equivalent to a period of approximately 5 minutes in the middle atmosphere.

Physically, a gravity wave at the Brunt-Väisälä frequency corresponds to an air parcel displaced vertically and released, setting up an oscillation with buoyancy as the restoring force. An air parcel displaced with a horizontal component oscillates at a lower frequency dependent on the angle. As the angle of motion approaches the horizontal, the horizontal wavelength increases and the Coriolis force begins to become more and more important as the air parcels are transported long horizontal distances. The Coriolis force imposes a lower limit on the gravity-wave frequency spectrum. Waves near this limit, $\omega_I = 2\Omega\sin(\phi)$ where ϕ is the latitude and Ω the Earth's rotational velocity, are called inertial waves. ω_I corresponds to a period of approximately 12 hours at the poles, and to a period that approaches infinity at the equator.

2.2.2 Energy and Momentum Deposition by the Dissipation of Breaking Waves

In the absence of dissipation, the waves that propagate upwards grow in amplitude according to equation 2.3. However, when the waves reach large amplitudes instabilities can occur which act to limit or decrease the amplitude such that wave energy is no longer conserved. This deposits energy and momentum into the layer in which the waves break (above the 'breaking level'), and waves can thus couple their source regions (often the troposphere) to atmospheric layers higher up. The breaking level is demonstrated for a simplified wave, shown as a function of height in the diagram of Figure 2.2.

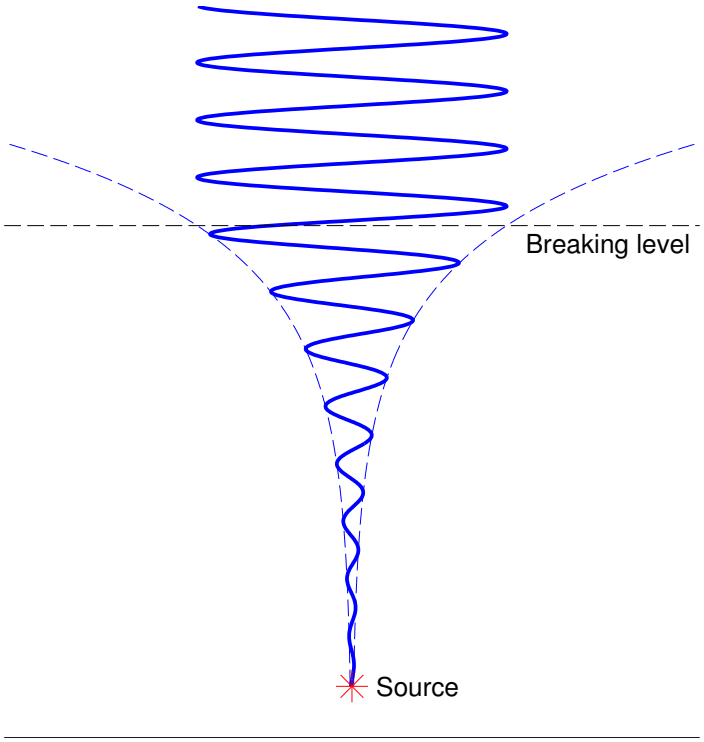

Figure 2.2: Diagram of wave amplitudes increasing due to the conservation of energy in an atmosphere of decreasing density with increasing height. The growth is exponential in the absence of dissipation mechanisms (dashed blue envelope). Above the breaking level, the wave has grown to the extent that instability results in wave-breaking, such that energy is no longer conserved but deposited and wave amplitude growth is inhibited.

There are two main types of instability that can cause waves to break when their amplitude grows too large. The first occurs when the wave produces temperature gradients that are superadiabatic, resulting in local instabilities. This is convective instability (e.g., Fritts and Rastogi, 1985). Shear instabilities occur when the vertical shear of horizontal winds results in a Richardson number of less than 0.25, generating turbulence. The Richardson number is defined

$$R_i = \frac{N^2}{(\partial u/\partial z)^2} \tag{2.17}$$

Flow is dynamically stable (i.e., an air parcel displaced vertically and released will return to its original position or oscillate under simple harmonic motion) when $R_i > 0.25$, dynamic instabilities occur when

R_i is between 0 and 0.25, and convective instabilities occur at $R_i < 0$.

Convective and shear instabilities tend to occur at similar wave amplitudes. However, convective instability begins more rapidly and so is the dominant instability for high frequency gravity waves. For low frequency waves, the transverse velocities induced by the Coriolis force add to the shear, such that nearer the inertial period, shear instability becomes more important (Fritts and Rastogi, 1985).

2.2.3 Critical Levels

Critical levels are an essential filtering mechanism in the atmosphere. The gravity wave spectrum in the lower atmosphere is dependent on the source, however not all of the generated waves can always propagate to the MLT region. Critical levels occur where wave horizontal phase speeds become comparable to the background wind, which leads to wave/mean-flow coupling. At critical levels the wave is either absorbed or reflected, resulting in the transference of energy and momentum into the mean flow, and preventing the propagation to higher altitudes. The intrinsic horizontal phase speed of gravity waves,

$$\hat{c}_h = c_h - \bar{u}_h \tag{2.18}$$

can be related to the vertical wavenumber, m, and Brunt-Väisälä frequency, N, as

$$N = m\hat{c}_h \tag{2.19}$$

If there is a level at which $\bar{u}_h(z) = c_h$, the intrinsic phase speed becomes zero, resulting in an infinite vertical wavenumber and thus a zero vertical wavelength. The wave has become evanescent and is unable to propagate to higher regions, although in the real atmosphere instability and dissipation mechanisms become more probable as $\bar{u}_h(z) \rightarrow c_h$ and act to prevent waves from actually reaching the critical level (Fritts and Alexander, 2003). Waves of differing phase speeds will encounter critical levels at different heights, according to the vertical profile of the background horizontal winds.

The background winds at stratospheric heights have a very large effect on the seasonal cycles of MLT dynamics. For example, the strong westward winds in the stratosphere and lower mesosphere over the summer solstice act to filter out gravity waves with westwards phase speeds, preventing them from reaching higher altitudes. Thus the spectrum of gravity waves reaching the MLT consists mostly of waves with eastwards phase speeds, where they break and deposit eastwards momentum, driving the wind reversal and accounting for the eastwards winds in the MLT (Smith, 2012).

Similarly, the Semi-Annual Oscillation (SAO) over the equatorial MLT region is out of phase with the stratospheric SAO (e.g., Lieberman, 1993; Garcia et al., 1997). This has been explained by the mesospheric SAO being driven by a gravity-wave spectrum that has been filtered by the stratospheric SAO (e.g., Dunkerton, 1982). The QBO is also strongly driven by gravity waves, and alters the spectrum of waves that propagate higher.

2.3 Planetary Waves

Planetary waves are large-scale oscillations that can be observed in the wind, temperature, pressure and density fields. They are coherent around a circle of latitude, and generally occur at low wavenumbers such that their horizontal wavelengths are comparable to the Earth's circumference. They are thus capable of transporting chemical species long horizontal distances.

Planetary waves can be traveling waves with eastwards or westwards propagation, or stationary (i.e., no horizontal propagation). Stationary planetary waves are forced modes, excited and maintained in the troposphere by topographic features such as mountain ranges and the differences in land/ocean heating. Other planetary waves are free modes. Traveling waves generally have periods close to those of the normal modes, which are natural resonances of the atmosphere. These include the quasi-2-day, 5, 10 and 16 day waves (e.g., Geisler and Dickinson, 1976; Prata, 1989; Wu et al., 1994; Day and Mitchell, 2010; Wu et al., 1993; Harris and Vincent, 1993; Tunbridge et al., 2011; Espy et al., 1997; Miyoshi, 1999).

Like tides and gravity waves, planetary waves can reach large amplitudes (tens of ms^{-1}) if they propagate upwards to the MLT region. Vertical propagation is determined by wave/mean flow interactions. Most traveling waves are westward propagating, and so they can propagate through the eastward winds of the winter stratosphere, but not the westward winds of the summer stratosphere (Charney and Drazin, 1961).

The continental configuration and topography of the northern hemisphere produces more planetary wave activity than in the southern hemisphere. This planetary wave activity acts to cause sudden stratospheric warmings and break down the polar vortex at the end of winter in the northern hemisphere. In contrast, the southern polar vortex is more stable and there has only been one major sudden stratospheric warming in the southern hemisphere, which occurred in 2002. Planetary waves can also modulate tidal amplitudes with planetary-wave periodicities (Pancheva et al., 2000).

The generation of the simplest type of planetary wave, the Rossby wave, is demonstrated in the diagram of Figure 2.3. They are caused by the change in the Coriolis force with latitude, and are restored by the conservation of absolute vorticity, such that

$$\frac{d\eta}{dt} = \frac{d}{dt}(\zeta + f) = 0 \tag{2.20}$$

where ζ is the relative vorticity (a measure of the localised rotation with respect to the Earth's surface), f is the planetary vorticity given for a latitude ϕ by the Coriolis parameter $f = 2\Omega\sin(\phi)$, and η is the total vorticity, i.e., the combination of the Earth's rotation and local rotation.

Consider a fluid parcel initially traveling with an eastwards mean flow in the northern hemisphere along a parallel, so that it has a constant planetary vorticity $f_0 = 2\Omega\sin(\phi_0)$. If it is displaced northwards, the increasing latitude results in an increase in the planetary vorticity f. By conservation of total vorticity

(equation 2.20) there must be a corresponding decrease in the relative vorticity, ζ. This results in clockwise rotation of the fluid parcel about its vertical axis. This clockwise rotation of the air parcel (which still has an eastward component to its motion) creates a southern flow ahead of the parcel, and so the particle moves back towards its initial latitude. With its southward momentum the air parcel overshoots, resulting in decreasing planetary vorticity, increasing relative vorticity, anti-clockwise rotation and thus it starts to move northwards again, setting up oscillation.

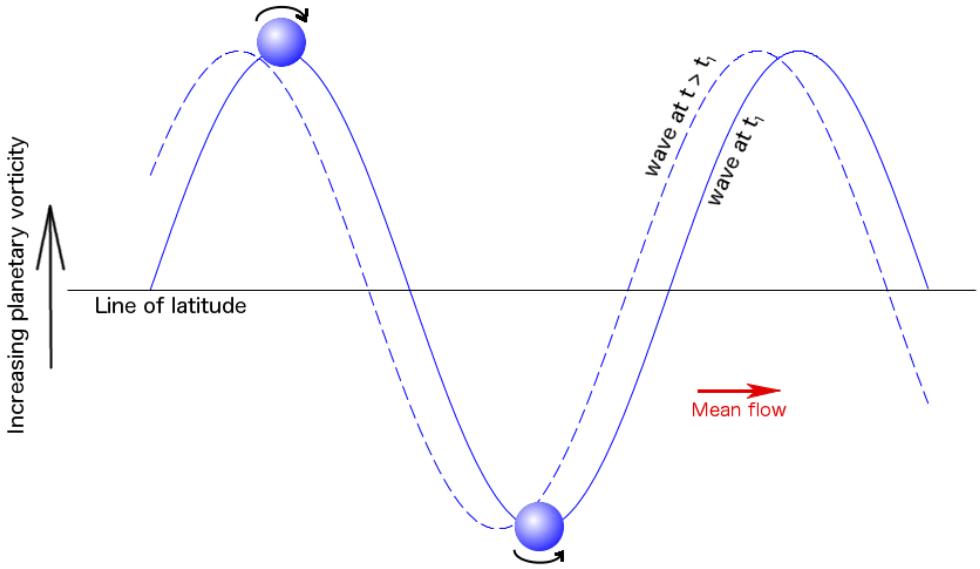

Figure 2.3: Diagram of air parcel motion in Rossby planetary waves. As the air parcels (travelling eastwards with the mean flow) are displaced latitudinally, the latitude-dependent planetary vorticity changes. Absolute vorticity is conserved, resulting in a change in the air parcel's relative vorticity, causing rotation. This rotation creates a meridional flow just ahead of the parcel, returning the parcel to its equilibrium latitude. It overshoots, setting up oscillation.

Note that for Rossby waves the phase fronts propagate westwards with respect to the mean flow.

2.3.1 Kelvin Waves

Kelvin waves are a special case of planetary wave which are equatorially-trapped. They require a boundary to propagate, and in the atmosphere this is provided by the reversal of the Coriolis force at the equator (in the ocean, Kelvin waves can propagate along coast lines). They reach their largest amplitudes over the equator, amplitudes then decay with increasing latitude. As well as requiring a boundary, the Kelvin Wave also differs from Rossby waves in that it consists purely of zonal motion and only travels eastward along the equator.

For the special case of waves in the equatorial region where the Coriolis force shrinks to zero, the β-plane approximation can be used in which the Coriolis parameter, f, is taken to vary linearly with distance from the equator, y:

$$f = \frac{2\Omega}{R_E} y = \beta y \tag{2.21}$$

where Ω is the Earth's rotation rate and R_E is the Earth's radius. Working in log-pressure coordinates, and using prime notation to represent perturbations (e.g., the zonal wind is written $u = \bar{u} + u'$) the following equations can then be obtained from linear wave theory (see Andrews et al. (1987)):

$$-i\omega u' - \beta y v' + ik\Phi' = 0 \tag{2.22}$$

$$-i\omega v' + \beta y u' + \frac{\delta \Phi'}{\delta y} = 0 \tag{2.23}$$

$$iku' + \frac{\delta v'}{\delta y} - i\omega \frac{m^2}{N^2}\Phi' = 0 \tag{2.24}$$

where ω is the frequency, u',v' and Φ' are the wave-induced perturbations to the zonal wind, meridional wind and geopotential height respectively, k and m are the zonal and vertical wavenumbers and N is the Brunt-Väisälä frequency. For the special case of Kelvin waves, these equatorial wave equations are simplified by taking the $v' = 0$ solution (i.e., no meridional component to the perturbations):

$$-\omega u' + k\Phi' = 0 \tag{2.25}$$

$$\beta y u' + \frac{\delta \Phi'}{\delta y} = 0 \tag{2.26}$$

$$ku' - \omega \frac{m^2}{N^2}\Phi' = 0 \tag{2.27}$$

Equations 2.25 and 2.27 can then be combined to obtain $\omega = \pm N\frac{k}{m}$. The corresponding group velocity is then given by $c_g = \frac{\delta\omega}{\delta m} = \mp N\frac{k}{m^2}$. Kelvin waves are excited in the troposphere and propagate upwards so have positive group velocity, giving us the Kelvin wave dispersion relation:

$$\omega = -N\frac{k}{m} \tag{2.28}$$

By re-arranging Equation 2.25 and substituting into Equation 2.26 to eliminate u', we obtain

$$\frac{\delta \Phi'}{\delta y} + \beta k \frac{y}{\omega}\Phi' = 0 \tag{2.29}$$

a first order differential equation with a solution that gives the meridional structure of Kelvin waves:

$$\Phi' = \Phi'_0 e^{-\frac{\beta k}{2\omega}y^2} \tag{2.30}$$

For Kelvin waves to remain bounded at large $|y|$, the exponent of Equation 2.30 must remain negative, $c = \frac{\omega}{k}$ must be positive and thus from the dispersion relation m must be negative, such that phase surfaces (given by $(kx + mz - \omega t)$) move downwards in time and tilt eastwards with increasing height (Andrews et al., 1987).

A diagram showing the structure of Kelvin wave perturbations is shown in Figure 2.4. For the case of a non-zero zonal wind $\bar{u}$, the analysis is similar but for an intrinsic (Doppler-shifted) frequency $\omega' \equiv \omega - k\bar{u}$. Following similar arguments to the above, $\frac{\omega'}{k} > 0$, and so $(c =) \frac{\omega}{k} > \bar{u}$. This agrees with observations of equatorial Kelvin waves traveling eastwards with respect to the mean zonal flow.

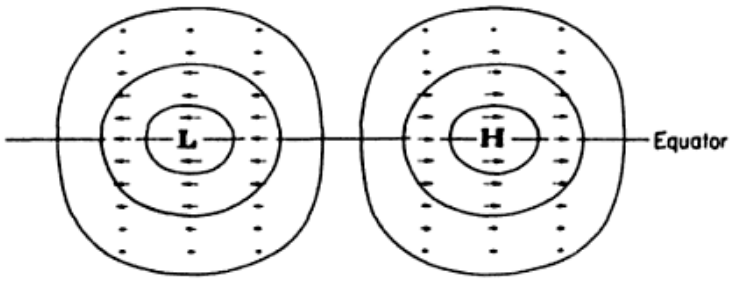

Figure 2.4: Diagram showing the structure of a Kelvin wave perturbation. The wave is symmetrical about the equator, with amplitudes of the zonal wind perturbation decreasing with distance away from the equator. There is no meridional component to the motion. Figure from Andrews et al. (1987).

2.4 Atmospheric Tides

Tides are global-scale oscillations in the wind, temperature and density fields with periods of the solar day and its harmonics, of which the largest in amplitude are the diurnal (24 hour) and semidiurnal (12 hour), though the terdiurnal (8 hour) and quaterdiurnal (6 hour) can also have significant amplitudes. As they are restored by buoyancy, they can be considered a type of gravity-wave. They are predominantly forced by solar heating of ozone near the stratopause and H_2O in the troposphere, as can be seen in the solar heating vs height profile in Figure 2.5a. Negligible *in situ* heating in the MLT region implies that the large amplitude tides observed there must have originated lower down in the atmosphere and propagated upwards (e.g., Andrews et al., 1987). Often reaching tens of ms^{-1} and with global amplitudes less intermittent than planetary or gravity waves, tides are often the dominant component of MLT dynamics. They can have an impact on the critical levels that propagating gravity-waves encounter, producing periodic variations in gravity-wave momentum flux deposition (Fritts and Vincent, 1987).

Gravitational tides also occur (e.g., Sandford et al., 2007), however they have much smaller amplitudes and slightly different periods to the dominant solar-heating forced tides due to the lunar day (24.8 hours) being slightly longer than the solar day.

Figures 2.5b and c show the heating as a function of latitude and local time respectively. The heating as a function of local time can be seen to approximate a square-wave, with heating increasing rapidly at sunrise (SR), remaining constant through the local noon (N), and then dropping rapidly at sunset (SS). The Fourier decomposition of the square wave results in a constant mean component, a diurnal component, a semidiurnal component, and smaller harmonics of the solar day. The tides observed are the response of the atmosphere to these heating components.

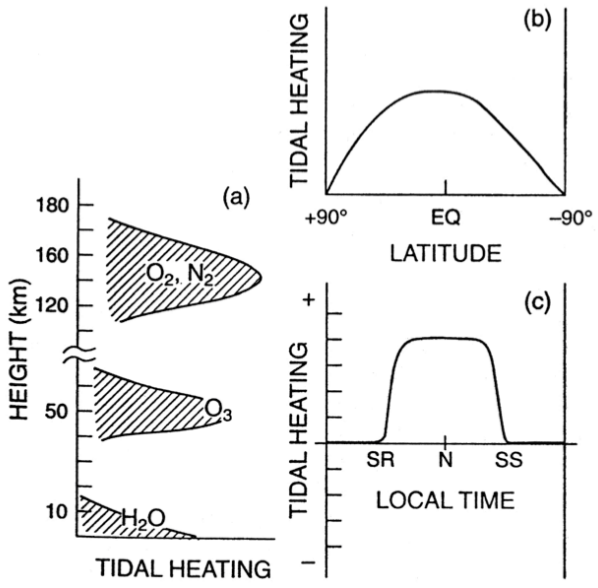

Figure 2.5: (a) Tidal heating as a function of height. It can be seen that the main contributors to excitation of solar tides in the middle atmosphere are from tropospheric water vapour and stratospheric/lower mesospheric ozone. (b) Tidal heating as a function of latitude. Heating is strongest over the equator, and drops off towards the poles. (c) Tidal heating as a function of local time. The heating profile approximates a square wave, with heating rising very quickly after sunrise (SR), staying approximately constant through noon (N), and then dropping rapidly at sunset (SS). Figure from Forbes (1995).

Atmospheric tides can be split into two types: migrating (sun-following) and non-migrating (non-sun-following). Migrating tides can be explained by classical tidal theory and always propagate westwards, such as the diurnal wavenumber 1 mode and the semidiurnal wave number 2 (DW1 and SW2). A relatively recent discovery is that the non-migrating tides can have amplitudes that are not only significant, but sometimes dominate the migrating amplitudes (Smith, 2012). Non-migrating tides can be stationary or propagate eastwards or westwards. As single-site instruments such as radars and LiDARs can not distinguish between the contributions to tidal amplitude from migrating and non-migrating components, either precessing satellites (which can not resolve day-to-day variations and may suffer from aliasing) or longitudinal chains of ground-based instruments must be used.

The non-migrating tides can be excited by longitudinal variations in heating, such as variations in tropical latent heat release (e.g., Hagan et al., 2009) and the equatorial alternation of continents and oceans (Akmaev, 2008). Tidal/planetary-wave interaction can also excite non-migrating tides

2.4.1 Classical Tidal Theory

Classical tidal theory assumes an isothermal atmosphere at rest and with no damping, and is detailed thoroughly in Lindzen and Chapman (1969). It requires Laplace's tidal equation (Equation 2.31), from which the latitudinal structure of the solar tides can determined.

$$L\Theta_n + \epsilon_n \Theta_n = 0 \tag{2.31}$$

L is the Laplace operator, given by

$$L = \frac{d}{d\mu}\left(\frac{1-\mu^2}{f^2-\mu^2}\frac{d}{d\mu}\right) - \frac{1}{f^2-\mu^2}\left[\frac{s}{f}\left(\frac{f^2+\mu^2}{f^2-\mu^2}\right) + \frac{k^2}{1-\mu^2}\right] \tag{2.32}$$

and ϵ_n are the eigenvalues of the equation,

$$\epsilon_n = \frac{4a^2\Omega^2}{gh_n} \tag{2.33}$$

The normalised frequency f is defined $f \equiv \sigma/2\Omega$, where σ is the frequency and Ω is the rotational velocity of the Earth ($\sim 7.3 \times 10^{-5}$ ms^{-1}). μ is the cosine of the colatitude (or the sine of the latitude), h_n is the equivalent depth, and k is the zonal wavenumber, positive for westward propagation and negative for eastward. Θ_n are the eigenfunctions, called Hough functions.

The frequency and wavenumber for each migrating tide are fixed by the forcing (such that $\sigma = k$), but each tide is composed from several Hough functions, or 'modes' which are orthogonal global solutions to the Laplace equation. Modes can be symmetric or antisymmetric about the equator. Each Hough function has an associated meridional index, n, such that the mode has $|n| - k$ nodes between the poles (a negative n indicates an evanescent mode). As an example, Figure 2.6 presents the first three symmetric modes as a function of latitude for the migrating semidiurnal tide (k = 2, σ = 2).

The superposition of the relevant Hough functions gives the classical prediction of tidal structure as a function of latitude.

2.5 Summary

This chapter looked at the some of the main types of waves that the atmosphere supports, and the mechanisms that cause their amplitudes to grow with increasing height until they become unstable and break, depositing energy and momentum into the MLT region. The importance of waves in the dynamics of the middle atmosphere was discussed. Dispersion relations for gravity waves and kelvin waves were examined, which gave an insight into the conditions under which they can propagate. Classical tidal theory was discussed, and it was seen how the superposition of relevant Hough modes gives the classical latitudinal structure of the tides. Non-migrating tides were also mentioned, along with their sources of excitation.

The next chapter will discuss the difficulties of obtaining measurements of geophysical parameters in the middle atmosphere, with a focus on the instruments used in the results chapters of this thesis.

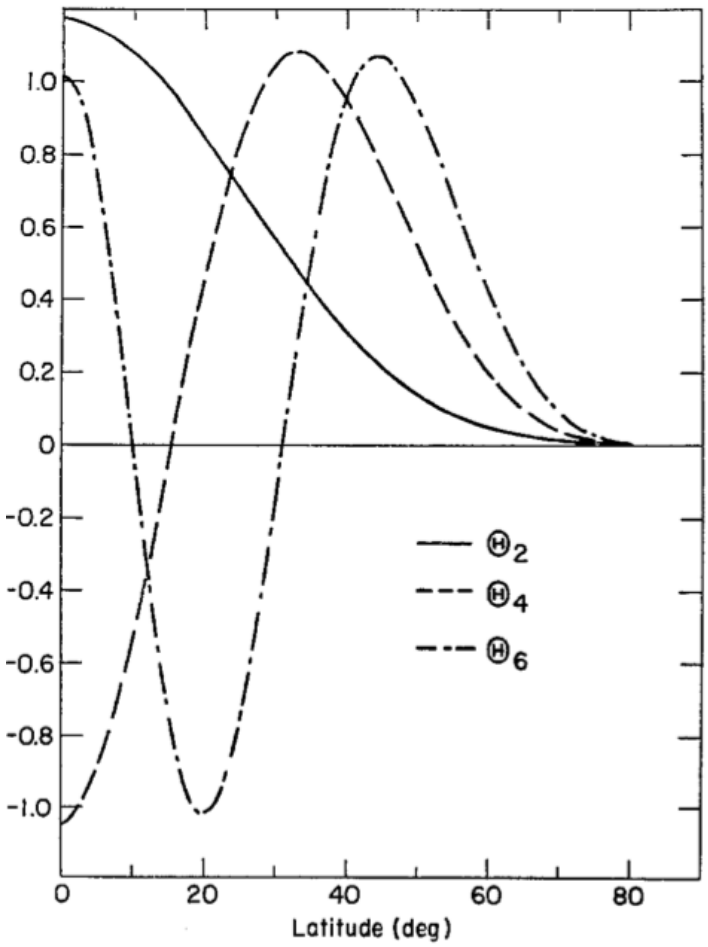

Figure 2.6: The first three symmetric Hough functions for the semidiurnal tide, as functions of latitude. Figure from Lindzen and Chapman (1969).

Chapter 3

Instruments and Techniques

3.1 Introduction

Studies of the middle atmosphere are relatively recent due to the difficulty of obtaining observations at heights of 50 - 100 km. The air density is too low for aircraft and balloons to reach these altitudes, yet the air density is too high for satellites to orbit. Rockets are the only method that can be used for taking measurements *in situ*, but they only provide data for a single flight through the middle atmosphere and for a single location, and long campaigns of rocket launches are expensive. The advent of remote sensing instruments in recent decades has opened up the middle atmosphere to scientific study.

Remote sensing instruments include LiDARs, radars and imagers, and are generally ground-based or borne by satellites and aircraft. This chapter will focus on SKiYMET meteor radars as data collected from these are key to many of the results presented in later chapters of this thesis. The Aura and TRMM satellite missions will also be discussed.

3.2 VHF Meteor Radars

Meteor radars are ground-based instruments that have limited horizontal coverage when compared to satellites, but very good height and time resolution over their locations and are considerably less expensive to build and deploy. Commercially produced meteor radars are available and as well as being relatively cheap to run, they have the added benefit being able to run for long intervals unattended on either a campaign or continuous basis. They are able to record meteors regardless of weather or time of day, and are thus more suited to studying phenomena that require diurnal or continuous coverage than those instruments that are affected by light conditions or cloud cover.

The University of Bath owns (or part-owns) 5 radars. The radar at Bear Lake Observatory (42^{o}N, 111^{o}W), Utah was installed in March 2008 and has the benefit of being co-located with other atmo-

spheric instruments such as LiDARs and imagers. The radar on Ascension Island (8°S, 14°W) was deployed on a small volcanic island near the equator in the South Atlantic Ocean in May, 2001. Its site is particularly useful as there are very few radars near the equator or in oceanic locations, however the radar has been subject to a relatively large amount of downtime due to the difficult operating conditions. The radar at Esrange space centre (68°N, 21°E) near Kiruna in arctic Sweden was installed in August 1999. It is situated at the conjugate latitude of the Rothera radar (68°S, 68°W) that was deployed on the Antarctic peninsula in 2005. It is to the south of the Drake passage gravity-wave hotspot, while to the north (on approximately the same line of longitude) is the SAAMER radar (54°S, 68°W) which was installed in May, 2008. The SAAMER radar utilises a different antenna configuration and higher power than the others, having been specifically designed with gravity-wave measuring capabilities. The sites of these 5 radars are highlighted on Figure 3.1.

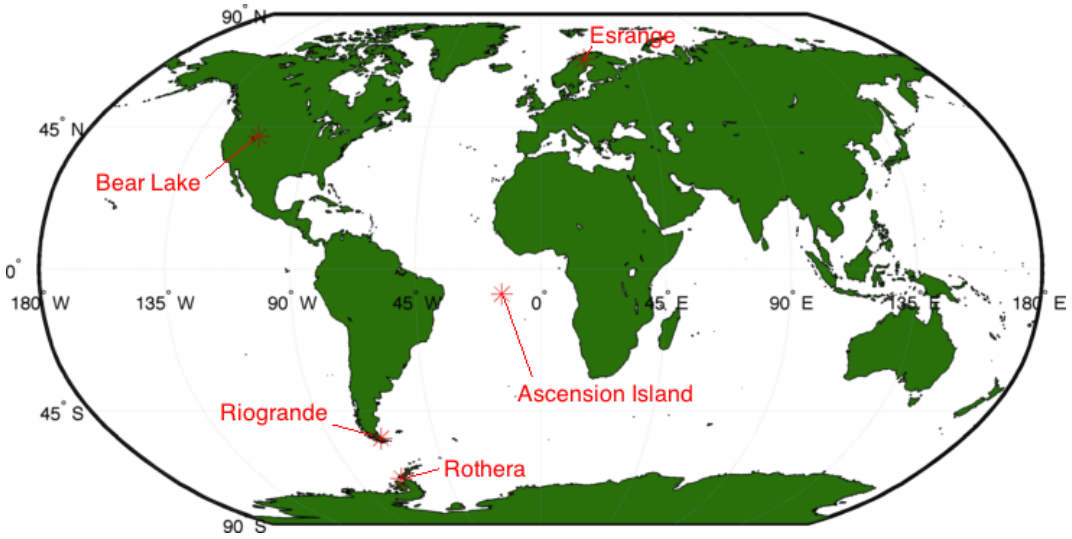

Figure 3.1: Map showing the locations of the University of Bath's meteor radars.

3.2.1 Meteors

Meteors are small pieces of interplanetary debris (commonly asteroid or comet fragments, typically 5 x 10^{-5} m to 0.2 m in diameter) that normally burn up when entering the Earth's atmosphere. Their interaction with the Earth is mostly a collision rather than due to the Earth's gravitational attraction. Meteors from our solar system have entry speeds varying between a minimum of 11 km s^{-1} (the Earth's escape velocity) up to a maximum of 73 km s^{-1}, a combination of the particle's velocity at 1 A.U. from the sun in its heliocentric orbit (43 km s^{-1}) and the Earth's orbital velocity of 30 km s^{-1} (Ceplecha et al., 1998).

As the meteor enters the atmosphere it collides with air molecules causing frictional heating proportional to the air density and the meteor size. Between altitudes of 300 to 100 km the surface layer is heated, but due to the meteor's speed it traverses this altitude range in tens of seconds which only allows negligible heating of the meteor's interior. In the MLT region however, increasing atmospheric density results

in sub-millimetre meteors being heated throughout, while the surface temperatures of larger meteors continue to rise quickly. Once the surface temperatures reach around 2500 K the outer layer sublimates, causing the meteor to lose mass in a process called ablation. This continues until either there is no mass left, or for larger meteors repeated collisions can slow the meteor to terminal velocity, allowing it to cool and reach the Earth's surface (meteorites). The de-excitation of sublimated meteor atoms releases photons at the discrete characteristic frequencies of hot metals (primarily Iron) which are responsible for most of the light emitted.

Meteor ablation in the MLT region leaves behind a plasma trail of charged particles and free electrons which specularly reflect radio waves. As the trail of charged particles is blown by the electrically-neutral wind, a radar can calculate the radial velocity of the trail with respect to the radar by the Doppler shift of a very-high frequency (VHF) radio pulse. Use of multiple receiver antennas allow interferometric determination of meteor locations in time, height and horizontal position, and help in the calculation of the radial velocity.

If the electron line density of the trail is less than approximately 10^{14} m^{-1}, the radio signal penetrates the trail and some of the signal is reflected back. The return signal amplitude is very high initially, but then drops off exponentially over an interval of less than a second. This is not due to recombination of the free electrons, but rather ambipolar diffusion. The trail expands in width until the signal reflecting from different layers of the trail causes destructive interference, reducing the amplitude. The resulting amplitude profile (a sharp rise followed by exponential decay) is known as an underdense echo and is very characteristic.

For trails with electron line densities greater than 10^{14} m^{-1}, the radio signal reflects from the 'surface' of the trail as if it were a solid metal. These overdense echoes have much longer duration than the underdense echoes and so significant distortion can occur over the echo's lifetime, resulting in multiple specular reflection points and a less characteristic shape than underdense echoes. As they are less distinctive they are harder to tell apart from unwanted signals (e.g., aircraft). Also, it is impossible to tell for overdense echoes whether a measured radial velocity is due to the neutral wind or due to movement of the specular point. Thus most radars reject echoes that do not have the underdense profile.

The specular reflection requires the ionised trail to be orthogonal to the propagation direction of the radio pulse in order for some of the power to be reflected back to the receiver antennas (most meteor radars are backscatter systems, i.e., the transmitter and receiver antennas are on the same site). This means that only a small subset of the meteors within the radar's collecting volume are detected.

Meteor trails can be tens of kilometres long, and are conical in shape. As atmospheric density decreases with increasing height, so the mean free path between collisions increases. This causes the trail to be wider at higher altitudes. If the specular point on the underdense trail is above the height at which the trail is wide enough for significant destructive interference to occur, then no signal will be returned and the meteor will not be detected. The height at which this 'underdense echo ceiling' occurs is dependent on the wavelength used by the radar. There is also a minimum height at which meteors are detected; below approximately 75 km meteors of the size that create underdense echoes ($\sim$ 1 mm and smaller)

have fully ablated.

The determination of radial velocity is demonstrated in Figure 3.2. If at time $t_0 + \Delta t$ the total ray path (out and back) is longer by length 2Δd, the radio signal will have a corresponding phase difference of $\Delta\phi$. For a pulse of wavelength λ, $\Delta\phi$ will be equal to 2Δ d $\times 2\pi/\lambda$. The radial component of velocity is then given by

$$V_{rad} = \frac{\Delta d}{\Delta t} = \frac{\lambda \Delta \phi}{4\pi \Delta t} \tag{3.1}$$

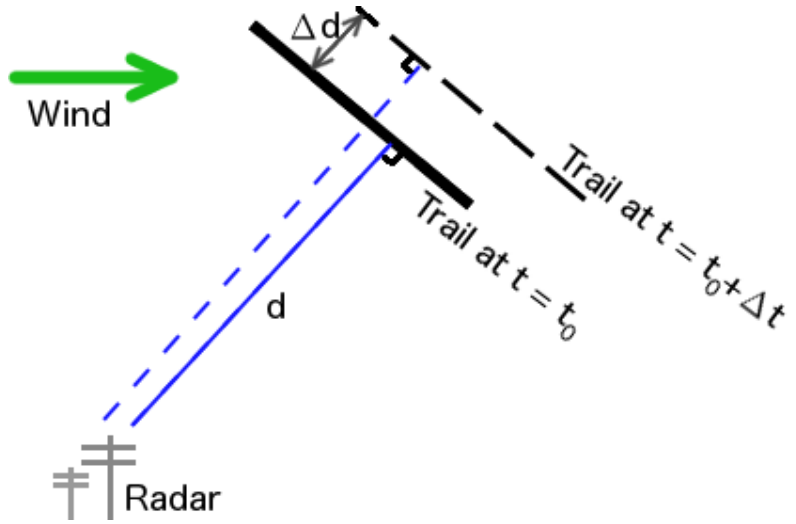

Figure 3.2: Schematic demonstrating how the radial component of the wind velocity is derived from the specular backscatter of a radar pulse from an ionised trail, formed by an ablating meteor. The meteor trail (solid black line) is blown by the neutral wind, of which the component in the radial direction is calculated by the change in phase of the signal between times t and t + Δ t.

3.2.2 SKiYMET Radars

All-sky meteor radars have the advantage over dual-beam radars that as they detect meteors over the whole sky, zonal and meridional winds can be calculated, rather than just the component aligned with the beams.

The All-Sky Interferometric Meteor Radars are commercially produced radars built by Genesis Software and Mardoc Inc. Being all-sky, the radiated power is normally fairly uniform as a function of azimuth. SKiYMET radars typically use a fairly high Pulse Repetition Frequency (PRF) of over 2 kHz. This high time resolution allows meteor entrance speeds to be recovered, but at the expense of a smaller aliasing range of approximately 70 km. As the radars do not use pulse encoding it is not possible to tell which pulse is being reflected. Thus it is not known whether a meteor detected at 80 km is actually at 80 km or 150 km, 220 km, etc. However in practice this is not usually a problem as *a priori* knowledge of the underdense echo ceiling generally allows an unambiguous range to be determined (Hocking, 2001). Transmission frequencies are generally between 20 MHz and 50 MHz, and can be chosen according to user preferences and where gaps appear in a local frequency survey.

A typical antenna layout is shown in the diagram of Figure 3.3. Note that the location of the transmitter antenna is not fixed, as long as it is not too close to the receiver antennas. The meteor events are recorded for each meteor in daily Meteor Position Data (MPD) files. These include some radar operation parameters such as the PRF and transmission frequency in the preamble, and then each meteor is recorded with the parameters given in Table 3.1.

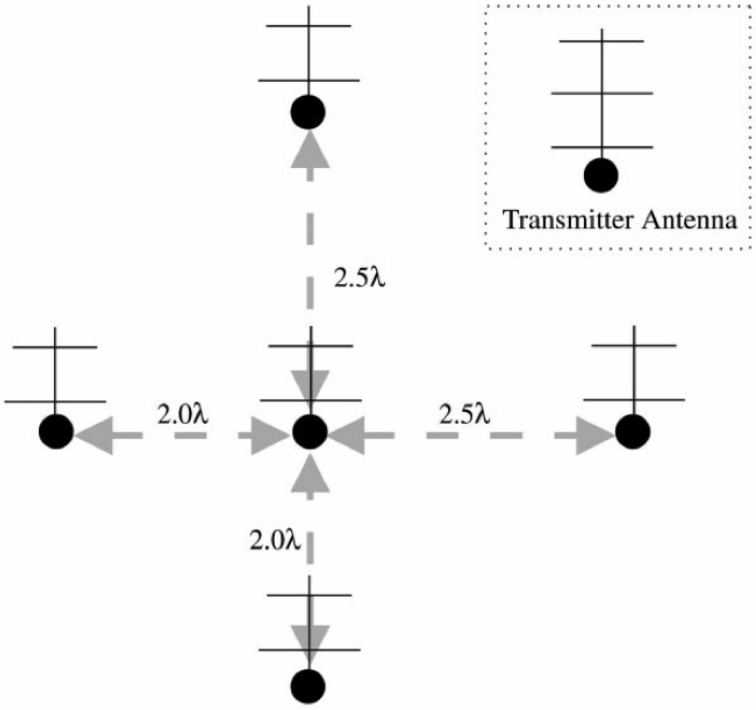

Figure 3.3: Schematic demonstrating the receiver antenna layout for a SKiYMET radar, allowing interferometric determination of meteor positions. Note that the location of the transmitter is not fixed by the design, but can be located anywhere convenient and suitably distanced from the receiver antennas. Figure taken from Hocking (2001).

The ambiguity field identifies which meteors were not unambiguously detected; those meteors that do not have an ambiguity of 1 (i.e., those that were not unambiguously detected) are rejected before further analysis. Meteors with values of DelVr exceeding 5.5 ms^{-1} are also rejected, as are those with values of τ less than 0.015 s to remove noise spikes.

3.2.3 Estimation of Zonal and Meridional Winds from Meteor Drifts

For many scientific purposes the mean winds are required. To obtain these, meteors are binned into six (user-defined) height gates with limits 78 to 83, 83 to 86, 86 to 89, 89 to 92, 92 to 95 and 95 to 100 km. The highest and lowest gates are wider than the middle gates due to the lower meteor counts at these extremes. For hourly winds, meteors are then further sorted into bins of length two hours (to increase the number of meteors included and thus reduce the error), spaced one hour apart. The observed radial velocities from one of these bins from the SAAMER radar is presented in Figure 3.4 as a function of azimuth.

Table 3.1: Table listing some of the parameters recorded in each daily Meteor Position Data file.

Date and time	In Coordinated Universal Time (UTC).
Range	Given to an accuracy of 100 m.
Height	Height above ground to an accuracy of 100 m, corrected for the Earth's curvature.
Radial velocity	The component of the trail's drift velocity along the radar's line of sight.
DelVr	The standard deviation of the radial velocity measurements according to each of the antenna pairs.
Zenith	The angle of the meteor measured from the vertical, accurate to approximately 1.5 degrees.
Azimuth	The angle measured anticlockwise from due East, accurate to approximately 1.5 degrees.
Ambiguity	When there is more than one possible configuration of range, zenith and azimuth due to a poor signal-to-noise ratio (and thus errors in the phase measurements), each possible position is recorded on a separate line and flagged in the ambiguity field.
Delphase	The biggest discrepancy in phase between two antennas.
τ	Decay time (half-life) of the signal reflected from the trail.
Amax	Amplitude of the meteor in digital units.
snrdb	Signal-to-noise ratio.

When there are at least 8 meteors in the bin, a least squares fit is applied to the radial velocities that minimises the sum of the differences between the meteors observed radial velocities and a fitted sine wave. The amplitude of the resulting sine wave gives the magnitude of the fitted wind, while the phase gives the direction (such that the peak of the wave is located at the azimuthal angle in which the wind at that height and time is blowing). This is then split into zonal and meridional components for further analysis. For example, the line of best fit given in Figure 3.4 corresponds to a wind of approximately 60 ms^{-1} blowing from near due South.

3.2.4 Meteor Distributions in Time and Space

Figure 3.5 presents meteor distributions as recorded by the radar on Ascension Island. These are presented as being typical of a SKiYMET radar. Figure 3.5a presents the meteor count per hour for a composite day of the entire year 2005. There is a clear diurnal cycle in the meteor count rate, with a maximum at 0600LT and a minimum at 1800LT. This is caused by the rotation of the Earth and its solar orbit. The longitude experiencing dawn is always at the leading edge of the planet's orbit around the sun, and so it encounters more meteors as they are 'swept up' by the Earth's motion. By contrast, at dusk only the fastest meteors can catch up with the Earth. As a certain number of meteors are required in each time/height bin for the wind speed to be reliably determined (see section 3.2.3), care has to be taken when interpreting gaps in the fitted wind time series.

Figure 3.5b presents the meteor count per kilometre as a function of height for the composite day of

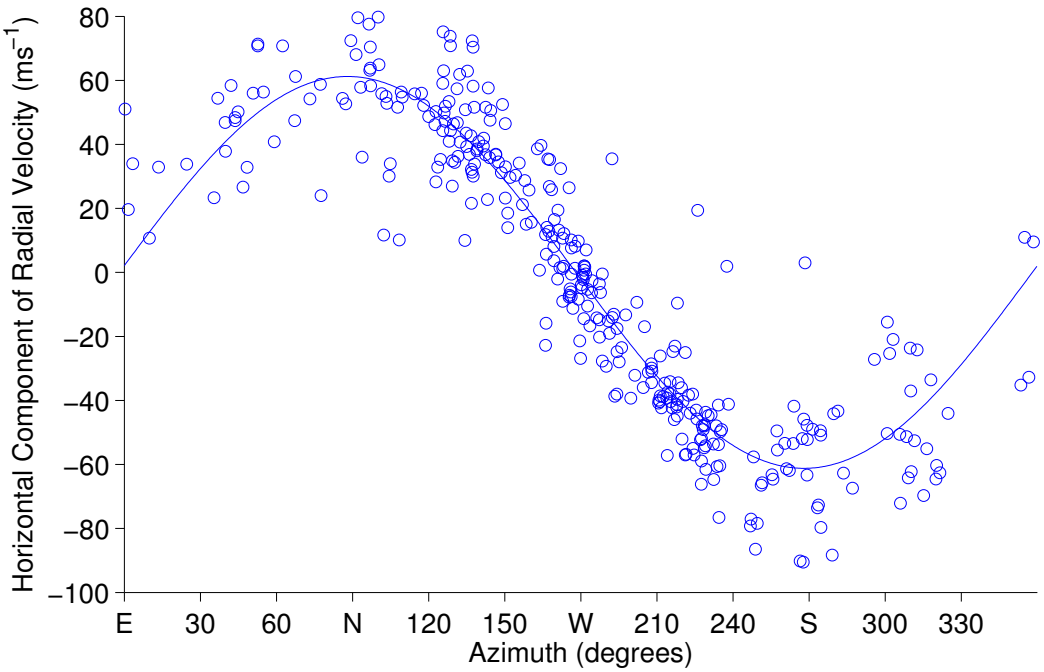

Figure 3.4: Horizontal components of radial velocities plotted as a function of azimuthal angles for all meteors recorded between 0200 and 0400 on 4th November, 2009 at heights between 89 and 92 km. Also plotted is the best fit sine wave, which gives a corresponding fitted velocity of ~ 60 ms^{-1} in the northward direction.

2005. The distribution is approximately Gaussian with a peak at approximately 90 km. The decrease in count rates above and below are due to the factors considered in Section 3.2.1, i.e., the underdense echo ceiling at approximately 110 km, and at the other extreme, the height at which nearly all underdense-echo-forming meteors have fully ablated (approximately 75 km).

Figure 3.5c presents the meteor positions projected onto a horizontal plane for a single typical day of 2005, and for a single height gate (89 - 92 km). It can be seen that the distribution is approximately uniform as a function of azimuth, but two features are particularly interesting.

The first is the lack of any meteors detected directly over the radar itself, i.e., near the zenith. This is due to the geometry of how meteors enter the atmosphere. For a specular reflection to be backscattered at very small zenith angles, the meteor must be traveling near-horizontally through the atmosphere. A horizontal path would include a long distance of atmospheric travel, and meteors traveling horizontally through the atmosphere tend to fully ablate before reaching the tangent point of the radar's zenith.

The second interesting feature are the concentric rings in which meteors are not detected. Meteor trails do occur within these rings, but they are not detected as the receivers are switched off for the duration of the outgoing direct wave during the transmission of pulses, which would otherwise saturate and potentially damage the sensitive equipment. Returning meteor signals are thus not detected at the ranges corresponding to these times, which depend on the radar's aliasing range.

Finally Figure 3.5d presents the distribution of meteors as a function of range for the composite day of 2005. The ranges at which meteors can not be detected are again evident, at ranges of approximately

(70,) 140, 210 and 280 km. Very few meteors are detected at ranges less than $\sim$ 90 km, due to the combination of minimum height and minimum zenith angles. Beyond the range of maximum count rate (approximately 120 km), echo strength decreases quickly as a function of distance and so the distribution tails off with increasing range.

The distributions of meteors presented in Figure 3.5 are similar to those that would be observed at middle and high latitudes except for the larger ratio in the tropics of maximum to minimum meteor counts over the diurnal cycle.

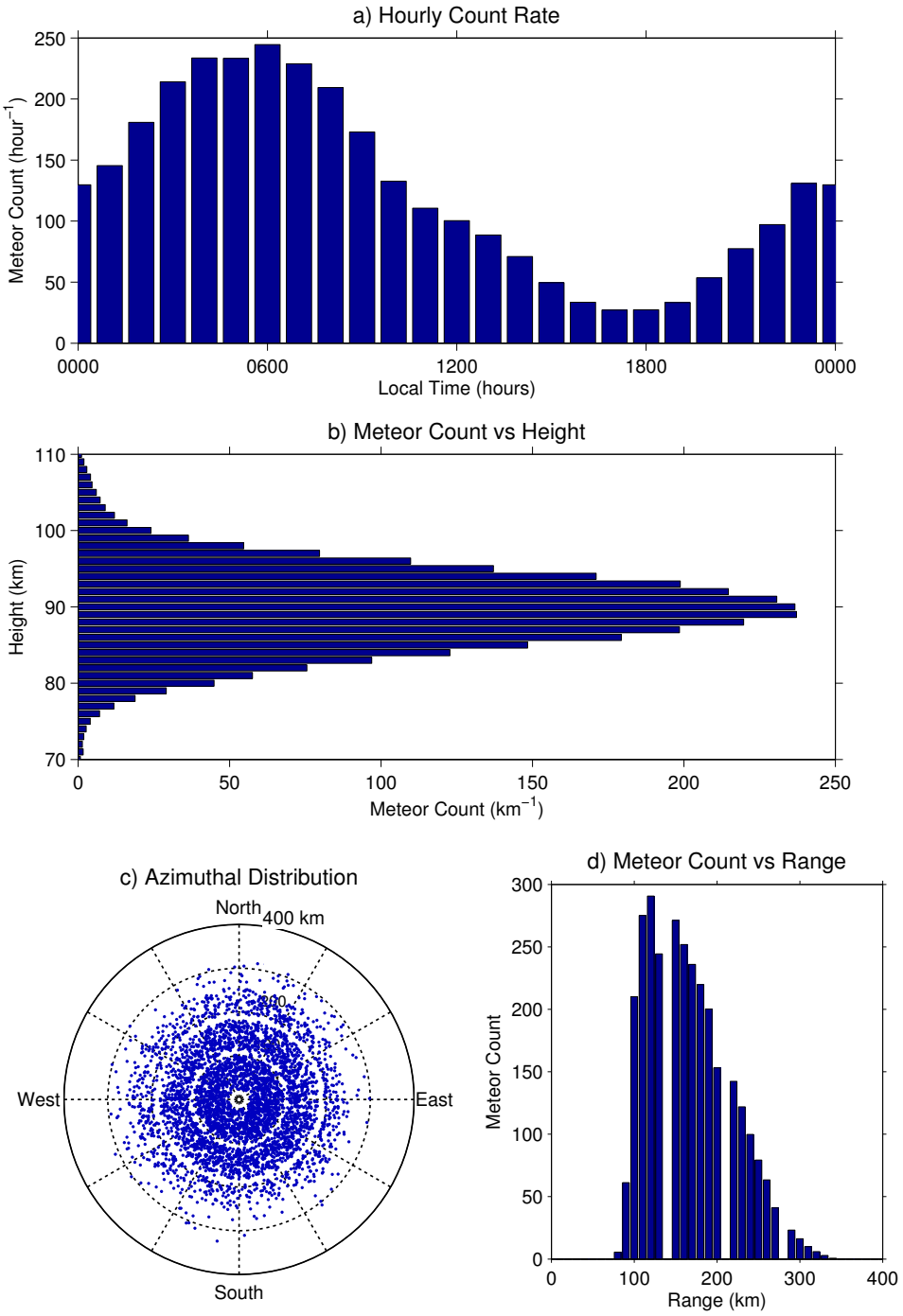

Figure 3.5: Meteor count rates from the Ascension Island radar. (a) Hourly count rate for a composite day of the year 2005, showing a diurnal cycle with most meteors detected at 0600LT and fewest at 1800LT. (b) Count rate as a function of height for a composite day of the year 2005, showing a Gaussian distribution with a peak at heights near 90 km, and fewest at heights above 100 km and below 80 km. (c) Azimuthal distribution for a single day in 2005, showing approximately uniform meteor count as a function of azimuth. (d) Meteor count as a function of range for a composite day of 2005, showing no meteors detected closer than 80 km, a large maximum at 120 km and a rapid decrease in meteor counts with increasing range. Gaps appear due to the temporary switching off of receivers during the radar pulse transmission to avoid saturation.

3.3 Satellite Instruments

3.3.1 Aura Microwave Limb Sounder

NASA's Aura satellite was launched on a Delta II rocket on July 15th, 2004 to fly as part of the 'A-train', a formation of Earth observation satellites that also includes Aqua, CloudSat and CALIPSO. Aura flies in a near-polar orbit at an altitude of 705 km. Its orbit is sun-synchronous and so in each orbit it crosses the equator at the same local time, approximately 1345LT for the ascending node. Each orbit takes 98.8 minutes.

The Aura mission was launched with the aim of helping to answer three key questions (Schoeberl et al., 2006) about the atmosphere:

(i) How is the stratospheric Ozone layer changing and will it fully recover following the international agreements on use of chlorofluorocarbons?

(ii) What processes affect pollutants in the upper troposphere around the globe?

(iii) What roles do water vapour, aerosols and ozone in the upper troposphere play in climate change?

To answer these questions Aura carries four instruments: the Tropospheric Emission Spectrometer (TES), the HIgh Resolution Dynamics Limb Sounder (HIRDLS), the Ozone Monitoring Instrument (OMI) and the Microwave Limb Sounder (MLS). The temperature data used in Chapter 4 are obtained by the MLS instrument.

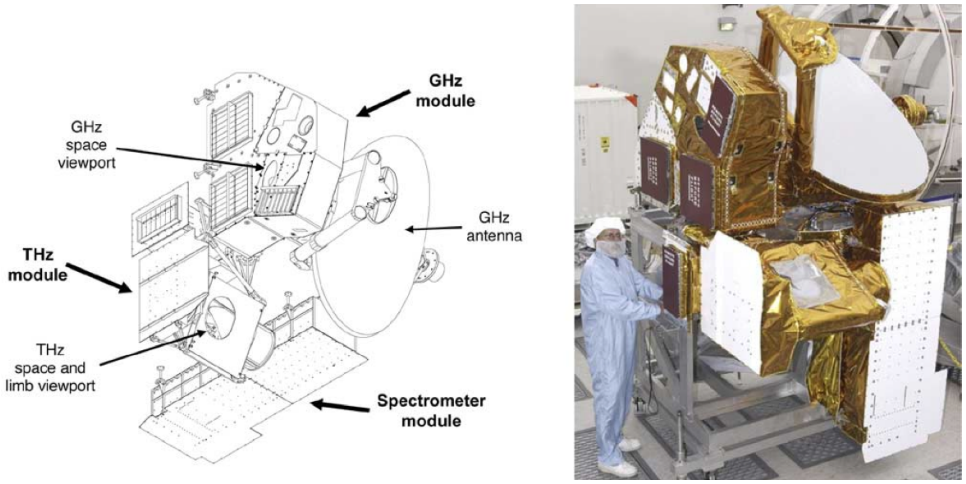

Figure 3.6: Line diagram showing the three main modules and photograph of the Aura MLS instrument. The total mass of the MLS instrument is 453 kg. Figure and photo from Waters et al (2006).

The MLS is a passive instrument that observes the natural microwave emission (radiances) from molecules in the atmosphere in five spectral ranges between 118GHz and 2.5 THz. It is an improvement on the first MLS instrument which was part of the Upper Atmosphere Research Satellite (UARS), deployed from the space shuttle Discovery as part of the STS-48 mission in September 1991. UARS MLS mea-

surements ended in 2001. The Aura MLS is an improvement on the original UARS MLS due to its more advanced microwave technology providing better resolution and precision, and also the fact that the Aura orbit is more suitable for global observations.

The MLS instrument is comprised of three main modules (Waters et al, 2006): a GHz module that includes four radiometers at 118, 190, 240 and 640 GHz, a THz module containing 2.5 THz radiometers, and a Spectrometer module (see Figure 3.6). The temperature profiles are obtained from Oxygen lines at 239 GHz in the upper troposphere, and 118 GHz in the stratosphere and mesosphere.

The MLS is the only Aura instrument to face forwards along the direction of spaceflight; the TES, OMI and HIRDLS all face backwards. Aura MLS scans vertically upwards every 24.7 seconds, of which approximately 20 seconds is scanning time, and the remaining used for calibration and retracing. This allows for 240 scans per 98.8 minute orbit, spaced 1.5 degrees of great circle apart. Aura MLS therefore obtains approximately 3500 temperature profiles per day. This is demonstrated in Figure 3.7a, in which the location of each scan is marked with a cross, and the track of the Aura satellite with a solid line for a 24 hour interval. The scans are set such that the same latitudes are scanned each day. It can be seen that the scans are slightly displaced from the orbital track (and to a greater extent over equatorial latitudes than near the poles), this is due to the rotation of the Earth in the time it takes the satellite to reach the scan latitude.

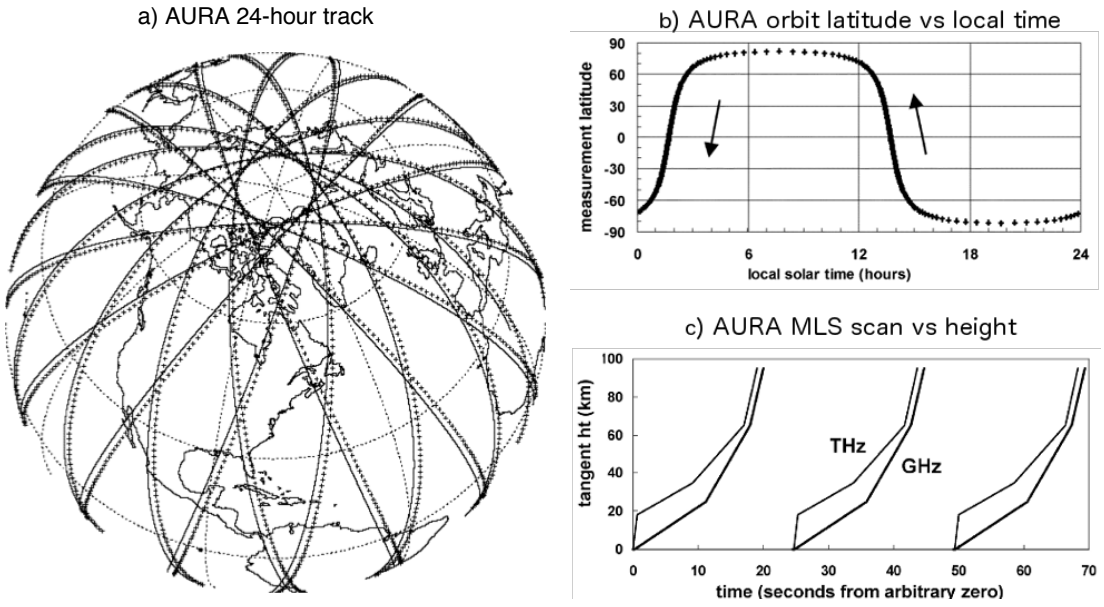

Figure 3.7: a) The track of the Aura satellite (solid black line) in a 24 hour interval and the locations of the limb scans (small crosses). Note that the scans are offset from the track, due to the rotation of the Earth beneath Aura's orbit. b) Aura scans as a function of time and latitude for a single orbit. The arrows mark the direction of orbit. c) Scan rates of the MLS instrument for both the THz and GHz modules. The gap of $\sim$ 4.7 seconds between scans is used for calibration and retracing. Figures after Waters et al. (2004).

Figure 3.7b presents the scan latitudes as a function of local time, with the orbit direction marked by the arrows. The equatorial crossing time of 1345LT for the ascending node can be seen.

The 24.7 second length of each 'major frame' (scan - calibrate - retrace cycle) can be seen in Figure 3.7c, which shows the scanned altitude as a function of time for the GHz and THz antennas. There are two important features of the vertical scanning rates that can be observed from the figure. The first is that the vertical scanning rate is not constant, but changes as a function of height. MLS spends longer scanning lower altitudes, allowing increased integration time and therefore better resolution in the troposphere and lower stratosphere, the rest of the stratosphere is then scanned faster and the MLT region faster still. The second feature is that the THz equipment scans at a different rate to the GHz equipment. This is because the THz module is the only one capable of measuring the $\sim$ 2.5 THz OH lines and so it scans the upper stratosphere for longer than the GHz antenna. The $\sim$ 1 second gap between the THz and GHz scans is to avoid large power transients during the fast movements of the retrace process (Waters et al, 2006).

Output profiles are on 47 pressure levels from 316 to 0.001 hPa, which, for the purposes of comparison with ground-based radar in Chapter 4, are converted into approximate heights using $z = -7\ln(P/1000)$. Averaging kernels are used to estimate the vertical resolution (see Livesey et al. (2006); Rodgers (2000)). Figure 3.8 shows the vertical averaging kernels for the temperature field. For each retrieval level (coloured cross), the corresponding coloured line shows the contribution of temperature from nearby heights. The area under the lines is given by the integrated kernel line (solid black). Values of integrated kernel close to one represent a retrieval that is primarily from MLS atmospheric measurement. Values less than one represent greater reliance on *a priori* information from the GEOS-5 analysis and CIRA86, and should be discarded for scientific analysis. This gives the effective lower altitude limit of 316 hPa or $\sim$ 8 km for MLS data. The Full-Widths at Half-Maximum (FWHM) of the coloured lines are given by the dashed black line, and represent the vertical resolution of the MLS temperature retrievals, from 5.3 km at 316 hPa, down to a minimum of 3.5 km at 32 hPa, and up to a maximum of 15 km at 0.001 hPa (Schwartz et al., 2008).

3.3.2 TRMM

Launched on November 27th, 1997, the Tropical Rainfall Measurement Mission (TRMM) satellite is a joint mission between NASA and JAXA, the Japanese space agency, with the aim of improving understanding of tropical rainfall, storms and convective systems and their relation to the planet's energy and water cycles. It was launched into a precessing, low-inclination (35^{o}) orbit with a period of approximately 92 minutes. Initially at an altitude of 350 km, it was boosted to an altitude of 400 km in 2001 to reduce the fuel needed to maintain orbit against the upper atmosphere and thus extend the mission lifetime.

In Chapter 4 precipitation data from the TRMM "Multi-satellite Precipitation Analysis" 3B42 dataset is used as a proxy for the latent heat release associated with tropospheric convection. This dataset provides three-hourly averages of the precipitation rate (mm/hr) for the latitude range 50^{o}N - 50^{o}S, longitudes 180^{o}W - 180^{o}E, on a grid with a resolution of 0.25^{o} $\times$ 0.25^{o}. The data product is derived by calibrating the observations from various geostationary satellites, such as the GOES and Meteosat

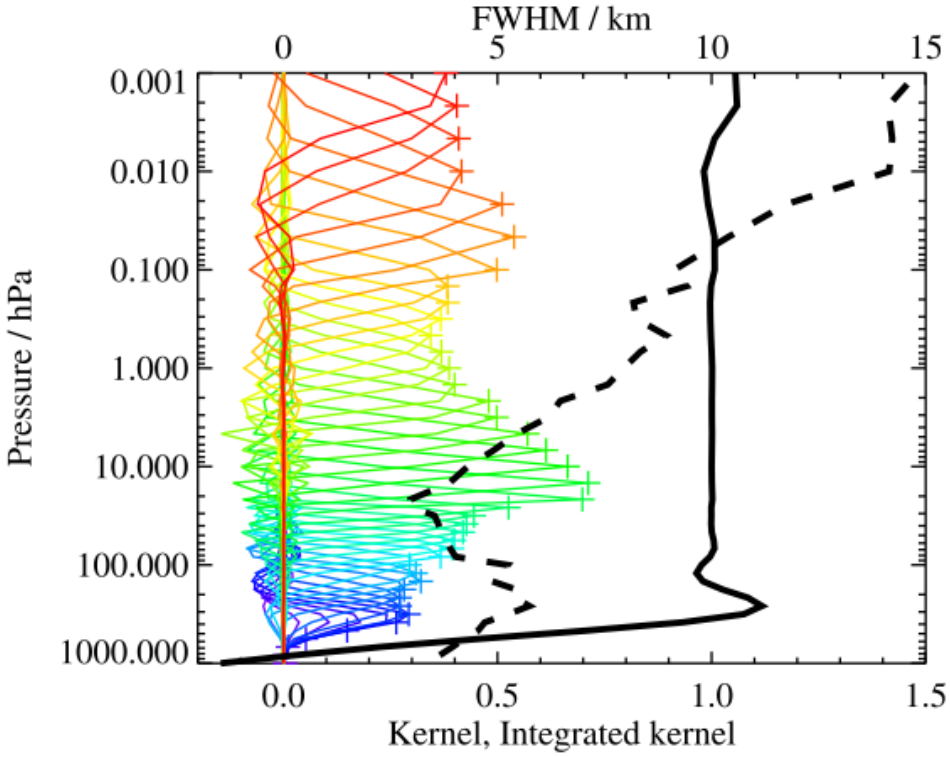

Figure 3.8: Aura MLS temperature vertical-averaging kernels for a September climatology at 35° N as a function of pressure level. Coloured plus signs mark the retrieval levels, with the contributions to the temperature at the retrieval level given by the associated coloured lines. The solid black line gives the area under the coloured lines, representing how much of the retrieved temperature is from atmospheric measurement, and how much from *a priori* information. The dashed black line gives the full-widths at half-maximums of the coloured lines, or the resolution, according to the top axis in units of km. Figure from Schwartz et al. (2008).

satellites, with data from TRMM's Microwave Imager (TMI, a passive microwave sensor) and Visible and Infra-Red Scanner (VIRS) instruments. An example of the data contained in a single 3B42 file is shown in Figure 3.9, which shows the derived precipitation rate at 0600 on January 1st, 2011.

3.4 Summary

In this chapter the problems with obtaining *in situ* measurements of the MLT region were outlined. The advent of remote sensing techniques has led to recent developments in atmospheric studies. Three particular types of instrument were focused on as the data recorded by them is used in later chapters.

SKiYMET radars use the trail of charged particles produced by ablating meteors as a tracer for winds in the MLT region. They have very good time resolution, capable of producing time series of hourly zonal and meridional winds, and are therefore suitable for investigating atmospheric oscillations such as planetary waves and tides. They are also relatively inexpensive and capable of running for extended intervals unattended. A drawback of meteor radars is that as single-site instruments, they are not capable (individually) of global observations or distinguishing migrating from nonmigrating tides.

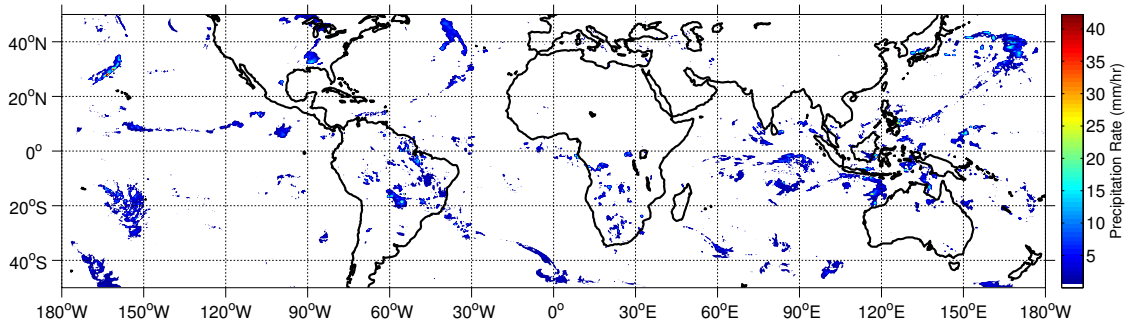

Figure 3.9: Precipitation rate as a function of latitude and longitude, averaged over a three-hour period as an example of the TRMM 3B42 dataset.

The MLS instrument aboard NASA's Aura satellite records thermal microwave emission to produce height profiles of temperature, geopotential height and many chemical species from heights of approximately 8 to 96 km. Aura orbits the Earth with a period of 98.8 minutes in a sun-synchronous orbit, recording approximately 3500 profiles a day at the same latitudes for each orbit and for each hemisphere. With excellent global coverage it is very useful for climatological purposes and for studying planetary waves, but lacks the time resolution required for studies such as short-term tidal variability.

Finally, NASA and JAXA's TRMM 3B42 dataset provides the mean rainfall rate every three hours on a global grid at latitudes equatorward of 50 degrees. Though TRMM is a single satellite, the dataset is possible by the TRMM calibration of various geosynchronous satellites' measurements. The rainfall rate can be used as a proxy for latent heat release.

Chapter 4

The Climatology, Propagation and Excitation of Ultra-Fast Kelvin Waves as observed by Meteor Radar, Aura MLS, TRMM and in the Kyushu-GCM

4.1 Abstract

Wind measurements from the SKiYMET meteor radar on Ascension Island (8^{o}S, 14^{o}W) and simultaneous temperature measurements from the Aura MLS instrument are used to characterise ultra-fast Kelvin waves (UFKW) of zonal wavenumber 1 (E1) in the mesosphere and lower thermosphere (MLT) in the years 2005 to 2010. These observations are compared with some predictions of the Kyushu-general circulation model. Good agreement is found between observations of the UFKW in the winds and temperatures, and also with the properties of the waves in the Kyushu-GCM. UFKW are found at periods between 2.5-4.5 days with amplitudes of up to 40 ms^{-1} in the zonal winds and 6 K in the temperatures. The average vertical wavelength is found to be 44 km. Amplitudes vary with latitude in a Gaussian manner with the maxima centred over the equator. Dissipation of the waves results in monthly-mean eastward accelerations of 0.2-0.9 ms^{-1}day^{-1} at heights around 95 km, with 5-day mean peak values of 4 ms^{-1}day^{-1}. Largest wave amplitudes and variances are observed over Indonesia and central Africa and may be a result of very strong moist convective heating over those regions. Rainfall data from TRMM are used as a proxy for latent-heat release in an investigation of the excitation of these waves. No strong correlation is found between the occurrence of large-amplitude mesospheric UFKW events and either the magnitude of the equatorial rainfall or the amplitudes of E1 signatures in the rainfall time series, indicating that either other sources or the propagation environment are more important in determining the amplitude of UFKW in the MLT. A strong semiannual variation in wave amplitudes is observed. Intraseasonal oscillations (ISOs) with periods 25-60 days are evident in the zonal background winds,

zonal-mean temperature, UFKW amplitudes, UFKW accelerations and the rainfall rate. This suggests that UFKW play a role in carrying the signature of tropospheric ISOs to the MLT region.

The work in this chapter has been published in the journal Atmospheric Chemistry and Physics as Davis, R.N., Chen, Y.-W., Miyahara, S., and Mitchell, N.J.: The Climatology, Propagation and Excitation of Ultra-Fast Kelvin Waves as observed by Meteor Radar, Aura MLS, TRMM and in the Kyushu-GCM, Atmos. Chem. Phys., 12, 1865-1879, 2012.

4.2 Introduction

Kelvin Waves are equatorially-trapped planetary waves that travel eastwards with respect to the background winds. They propagate upwards away from their sources in the troposphere where they are thought to be excited by the latent heat release associated with tropospheric convection (Holton, 1973; Salby and Garcia, 1987). A classical Kelvin wave has no meridional velocity component and has a latitudinal profile of amplitude that is Gaussian in shape and which maximises over the equator. Amplitudes thus decay with increasing latitude away from the equator (Holton, 1979). The waves can be detected as perturbations in atmospheric wind, temperature and pressure.

Kelvin waves occupy three distinct period ranges. The "slow" Kelvin waves have periods in the range 15-20 days and vertical wavelengths of around 10 km. They were first observed in the lower stratosphere in tropical radiosonde measurements by Wallace and Kousky (1968). They are unable to propagate to greater heights due to selective absorption. The "fast" Kelvin waves were first observed by Hirota (1978) in rocketsonde data. They have periods in the range 6-10 days and vertical wavelengths of around 20 km. The "Ultra-Fast Kelvin Waves", hereafter referred to as UFKW, were first observed by Salby et al. (1984) in Nimbus-7 LIMS data. They are usually reported as having periods of around 3.5 days, vertical wavelengths of approximately 40 km and being an eastward-propagating oscillation of zonal wavenumber 1 (i.e. an E1 wave).

Early work suggested that Kelvin waves might provide the major source of eastward momentum required to drive the Quasi-Biannual Oscillation (QBO) (e.g. Wallace and Kousky, 1968; Holton and Lindzen, 1972) and the Stratospheric Semiannual Oscillation (SSAO) (Dunkerton, 1979). However, later satellite studies (e.g. Hitchman and Leovy, 1988) demonstrated that mesoscale gravity waves provide a necessary additional contribution to the eastward accelerations of the SSAO and model studies came to a similar conclusion for the QBO (e.g. Takahashi and Boville, 1992; Dunkerton, 1997). Nevertheless, studies suggest that Kelvin waves make a significant contribution to the driving of the stratospheric QBO (Kawatani et al., 2010) and UFKW contribute to the eastward momentum of winds in the equatorial lower thermosphere (e.g. Lieberman and Riggin, 1997; Forbes, 2000).

UFKW can reach large amplitudes in the mesosphere and lower thermosphere (MLT) where they can be a significant part of the motion field. UFKW in the MLT have been investigated in a limited number of studies using meteor and MF radars (e.g. Riggin et al., 1997; Kovalam et al., 1999; Sridharan et al.,

2002; Pancheva et al., 2004; Younger and Mitchell, 2006; Lima et al., 2008), satellites (e.g. Canziani et al., 1994; Lieberman and Riggin, 1997; Forbes et al., 2009), and models (e.g. Forbes, 2000; Miyoshi and Fujiwara, 2006).

UFKW have been suggested to play a key role in driving the Intraseasonal Oscillations (ISOs) that are observed in the MLT zonal mean temperatures and winds at low latitudes. ISOs with peaks at periods of $\sim$60 days, 35-40 days and 22-25 days were first observed in the MLT region by Eckermann and Vincent (1994) in winds obtained from an MF radar on Christmas Island. Eckermann et al. (1997) found similar periodicities in MLT gravity-wave variances and diurnal-tidal amplitudes. They suggested that the 30-60 day Madden-Julian oscillation manifested in the tropical tropospheric convection (Madden and Julian, 1971, 1994) and a separate 20-25 day oscillation over the western Pacific (Hartmann et al., 1992) modulate the gravity-wave and diurnal-tidal intensities. These modulated waves and tides then propagate upwards to the MLT and create similar periodicities in the wave-induced driving of the zonal mean flow in the MLT region. The suggestion that the ISO in the MLT zonal winds is wave-driven was supported by Lieberman (1998) using observations of winds from HRDI. Rao et al. (2009) considered radar observations of the MLT made at different longitudes and found that ISO amplitudes vary with longitude, suggesting a close connection to the vigour of convective activity in the underlying troposphere. Intraseasonal variability of UFKW temperature amplitudes with periodicities between 20-60 days was observed in SABER data by Forbes et al. (2009). Modelling results from the extended Kyushu-GCM suggested that Eliassen-Palm Flux Divergences from dissipating UFKW are also important in the wave-mean flow interaction driving the ISO in the MLT region (Miyoshi and Fujiwara, 2006).

The high phase speeds of UFKW, approximately 150 ms^{-1}, allow them to propagate into the ionospheric E-region. It has been suggested that UFKW at these heights may be important in the dynamo generation of electric fields and metallic-ion layering of the E-region, with subsequent modulation effects in the F-region (Forbes, 2000). Large UFKW amplitudes have been observed at heights of 100-120 km in TIMED/SABER temperature data (Forbes et al., 2009) and at similar heights in the Global-Scale Wave Model (Forbes, 2000). Takahashi et al. (2007) observed a 3-4 day modulation of the day-to-day variability of the ionospheric minimum virtual height ($h'F$) and of the $F2$ maximum critical frequency ($foF2$) that may have been associated with simultaneous UFKW activity in the mesosphere. Chang et al. (2010a) found in the TIME-GCM that UFKW with realistic MLT amplitudes could cause perturbations in the neutral density at heights of 350 km and in the total electron content around the equatorial ionisation anomalies via modulation of the dynamo electric field. These observations suggest that UFKW can play an important role in the coupling of different layers of the atmosphere.

Here we use mesospheric winds measured by an equatorial meteor radar and temperatures measured by the Aura microwave limb sounder to investigate UFKW. In particular, we define a representative climatology of the waves, consider their interactions with the mean flow, consider the role of tropospheric latent heat release in their excitation and compare our observations with the predictions of the Kyushu-GCM.

4.3 Data and Analysis

The temperature data used in this investigation come from the level 2 version 2.2 temperature product of the Microwave Limb Sounder instrument onboard NASA's Aura satellite. Aura is in a near-polar, sun-synchronous orbit. Temperature values are measured every 25 s for 34 pressure surfaces between 316 and 10^{-3} hPa, corresponding to 34 different height gates. For this study we used the highest gates, centred at heights of approximately 96.7, 91.3, 86.0, 80.6, 75.2, 69.8, 64.4, 61.8, 59.1, 56.4, 53.7 and 51.0 km. There are some small but not significant gaps in the data. The vertical resolution in the mesosphere is approximately 12 km, with temperature precisions of ∼2.5 K (Schwartz et al., 2008). The pressure levels have been converted into geometric heights to allow direct comparison with the radar observations. The data considered here covered the interval 1 January 2005 to 31 December 2010.

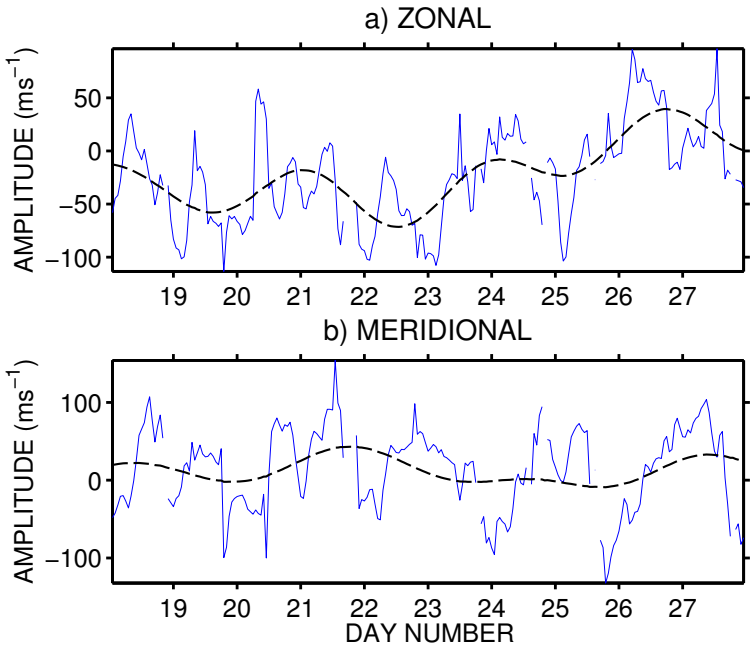

Figure 4.1: Raw hourly (a) zonal and (b) meridional winds at a height of 96 km from the Ascension Island radar with low-pass filtered winds overlaid (dashed line) for the period 18-28 January 2005. The cutoff of the filter is 2.5 days. Note the oscillations in the zonal winds with period near 3 days.

The wind data are from the Ascension Island SKiYMET meteor radar, located at 8°S, 14°W. Winds are obtained as hourly averages within six height gates centred at 80.5, 84.5, 87.5, 90.5, 93.5 and 97.0 km. The radar began operating in May 2001, but for this study we have considered only the data overlapping the complete years available from Aura MLS, i.e., from 1 January 2005 to 31 December 2010. There are some significant gaps in the radar dataset amounting to 22 % of 2005, 17 % of 2006, 71 % of 2007, 100 % of 2008, 58 % of 2009 and 27 % of 2010.

Tropospheric convective heating may play a role in UFKW excitation. Here we have used precipitation data from the TRMM "Multi-satellite Precipitation Analysis" dataset as a proxy for the latent heat

release associated with tropospheric convection.

Finally, our observations are compared to the predictions of the Kyushu-GCM T42L250 version. This model uses triangular-truncation at wavenumber 42 in the horizontal and 250 layers in the vertical. The model covers heights from the ground up to approximately 150 km. In the MLT region the vertical resolution is $\sim$500 m. The GCM includes short- and long-wave radiation processes, moist and dry convective adjustments, a local Richardson number dependent vertical eddy diffusion process and various other physical processes. Monthly-mean sea surface temperatures are used as a lower boundary condition. The ground temperature is calculated in the model by using its heat balance. No gravity-wave parameterization is used, but a Rayleigh friction is imposed on the zonal-mean zonal winds to weaken the zonal winds around the mesopause. More details can be found in Chen and Miyahara (2011).

4.4 Results

4.4.1 Ascension Island Meteor Radar Observations

Zonal winds measured over Ascension Island frequently show wave-like oscillations with periods near 3-4 days. As an example, Fig. 4.1 presents hourly-mean zonal and meridional winds for a height of 96 km for the interval 18-28 January 2005.

The figure shows a motion field dominated by a large-amplitude oscillation of period 24 h, which is the diurnal tide. Also present are lower-frequency oscillations. The dashed lines on the figure show the hourly winds low-pass filtered to reveal oscillations with periods longer than 2.5 days. The filtered winds reveal oscillations of period 3-4 days with amplitudes reaching up to 30 m s^{-1} in the zonal component and 20 m s^{-1} in the meridional component. The fact that the period of oscillation is about 3-4 days, combined with the larger amplitudes in the zonal component, is a strong indication that these winds are the signature of ultra-fast Kelvin waves (note that there is also an indication of the 2-day wave in the meridional unfiltered winds).

To further investigate the possible presence of UFKW, a dynamic spectrum of zonal and meridional winds was calculated for all six radar height gates and for all years of the meteor-radar data. Figure 4.2 presents an example of these results for January-June 2005 for a height of 96 km. The spectra were calculated using a Lomb-Scargle periodogram applied to a data window of ten days, incremented through the dataset in steps of 1 day.

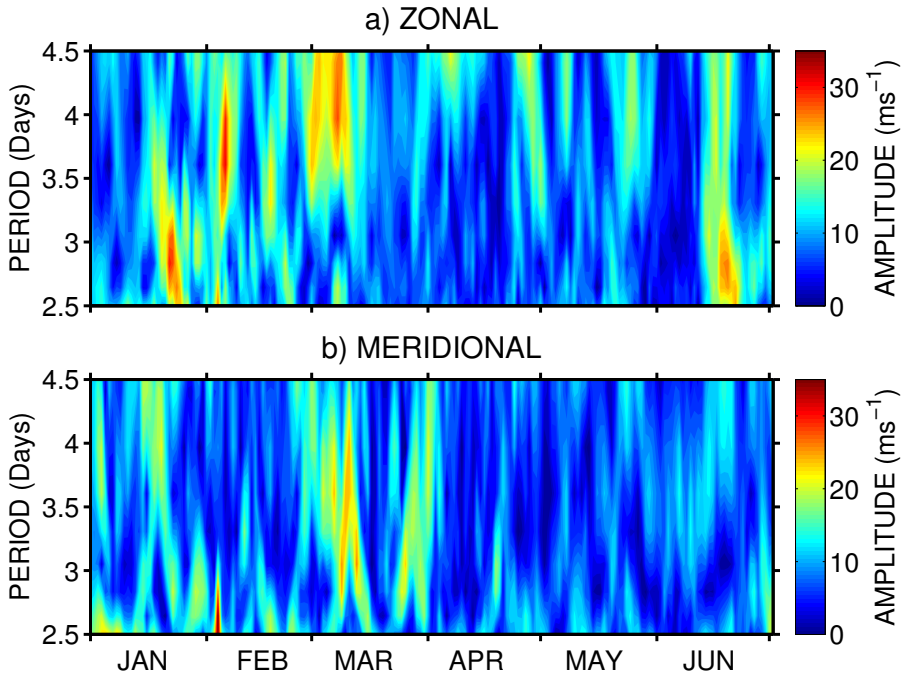

Figure 4.2: Running Lomb-Scargle periodogram of (a) zonal and (b) meridional winds over Ascension Island for January-June 2005 at a height of 96 km.

Considering the figure in detail it can be seen that events with period 3-4 days occur in an episodic manner and are particularly noticeable in January-March 2005. Zonal wind amplitudes regularly exceed $15\,\mathrm{m\,s^{-1}}$ and sometimes exceed $30\,\mathrm{m\,s^{-1}}$ in the wave-period band 2.5-4.5 days associated with UFKW. When we consider the full dataset, we find peak amplitudes of up to $40\,\mathrm{m\,s^{-1}}$. Wave amplitudes and periods vary greatly on timescales of a few days, demonstrating strong intermittency. However, there is also a suggestion of longer-term variability because wave amplitudes in January, February and March appear significantly larger than in April. These features of intermittency and stronger January-March activity (and weaker April-June activity) are typical of all years, however we will consider seasonal variability later. Meridional amplitudes can be large but are generally smaller than the zonal amplitudes. For example, the largest zonal amplitudes in January and February are $>30\,\mathrm{m\,s^{-1}}$ while the largest meridional amplitudes are about $15\,\mathrm{m\,s^{-1}}$. This observation, combined with the observed wave periods, provides a strong indication that these spectral signatures result from UFKW. Further, note that the theoretical suggestion that UFKW have zero meridional velocities is actually based on a simplified set of assumptions and so UFKW observed away from the equator may have non-zero meridional components.

The period range of UFKW in the MLT region can also be investigated in the Kyushu-GCM. The composite-year period-height distribution of E1 wave amplitudes in the model is presented in Fig. 4.3. The figure shows that at heights around 95 km Kelvin waves have a period range of approximately 2-6 days with largest amplitudes between 2.5-4.5 days. The GCM amplitudes seem low when compared to observations but this is because they represent an annual-average, which due to the intermittency of the waves will include intervals of little to no UFKW activity, which supresses the average amplitudes.

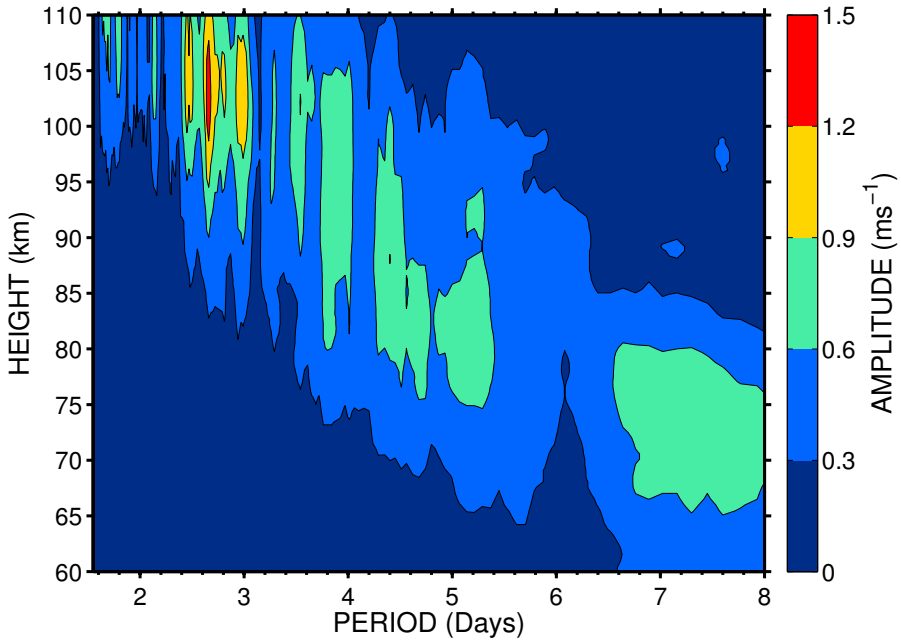

Figure 4.3: Annually-averaged amplitude as a function of wave period vs. height of E1 waves in the zonal wind at 2.1°N in the Kyushu-GCM.

We will hereafter interpret the 2.5-4.5 day oscillations seen in the zonal spectra of Fig. 4.2 as being due to UFKW (further justification for this assumption is provided by the simultaneous observation of eastward-propagating oscillations of zonal wavenumber 1 in the Aura analysis of Section 4.4.2). However, note that the inertial period at Ascension island is 86 h and so low-frequency inertia-gravity waves may also make some contribution to the motion field.

We observe that the UFKW amplitudes vary strongly with height and show a marked tendency to have greater amplitudes at greater heights. As an example, Fig. 4.4 presents the band-passed (2.5-4.5 days) zonal winds for 9-18 January 2006. Wave amplitudes can be seen to increase from about 5 m s^{-1} at 80.5 km to 40 m s^{-1} at 97 km.

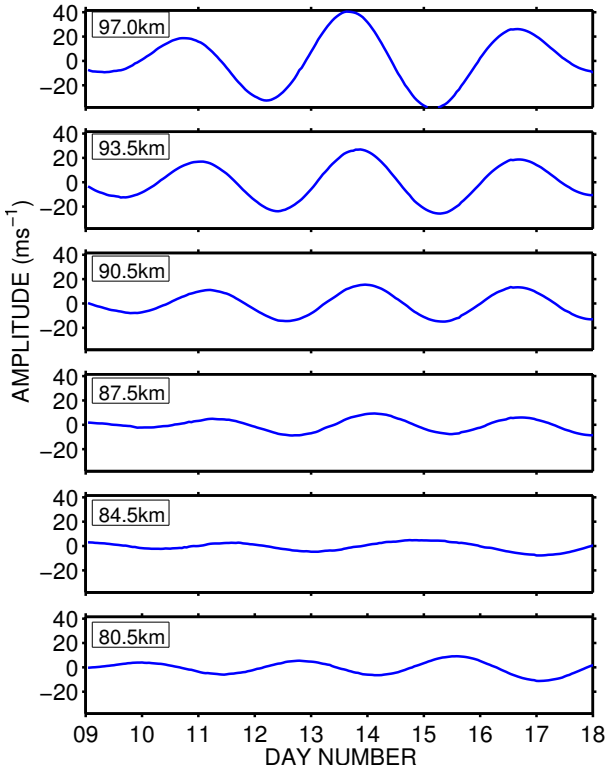

Figure 4.4: Zonal winds over Ascension Island for the period 9-18 January 2006 bandpassed between 2.5-4.5 days for six heights (height labels represent the centre of each gate).

To investigate the seasonal variability of the UFKW observed by the radar we calculated monthly variances of zonal winds in each height gate for each year for the period range 2.5-4.5 days representative of UFKW. A climatology was constructed using a composite-year analysis of all of the monthly variances from all the available data between 2005 and 2010. The results of this analysis are presented in Fig. 4.5a, which shows that the variances reach the largest values in July-August and have minima near the equinoxes in March-May and October. Secondary maxima are evident in January-February and November.

In all months wave variance increases with height. This is particularly striking in August where the variance increases from about 70 m^2 s^{-2} near heights of 80 km to more than 170 m^2 s^{-2} near heights of

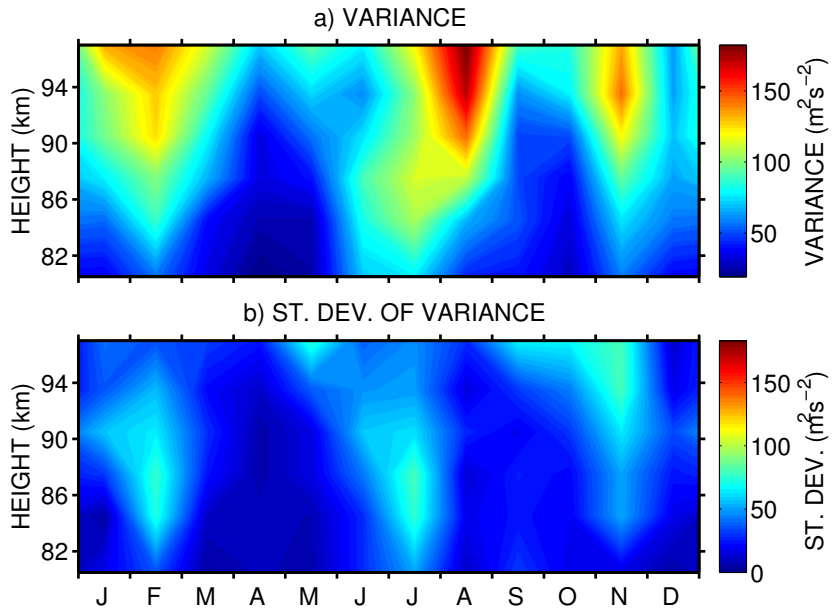

Figure 4.5: (a) Monthly variance as a function of height for a composite year of all available data between 2005 and 2010 of zonal winds over Ascension Island. The winds are bandpassed between periods of 2.5-4.5 days. (b) The standard deviation of the monthly variance values for each height gate and each month.

97 km. The seasonal pattern of variances is generally similar for all years observed. Some year-to-year variability is, however, evident. Figure 4.5b presents contours of the standard deviation of the variance values for each height gate and each month as a measure of this variability. The mean standard deviation averaged over all heights and months was 35 $m^2\,s^{-2}$.

4.4.2 Aura MLS Observations

The UFKW also cause fluctuations in atmospheric temperature which can be measured with Aura MLS.

UFKW can be seen in the unfiltered MLS data when the temperatures are plotted against longitude and time in a Hovmöller diagram. This representation has the advantage of showing any longitudinal variations of the UFKW, rather than the zonal-mean structure. As an example, Fig. 4.6 presents a Hovmöller diagram of wave-induced temperature perturbations as a function of time and longitude for the period 17 July-15 August 2005 for a height of 97 km. The temperature fluctuations are measured within a 10^o latitudinal band centred over the equator, divided into 12 longitudinal sectors, each of 30^o longitudinal extent. A time window of one day is used, stepped through the dataset in increments of 12 h and the daily longitudinal average is subtracted from each segment. No filtering in time is used.

A quasi-monochromatic wave-like pattern is clearly evident, dominating the figure. This corresponds to an eastward propagating wavenumber 1 wave of period $\sim$3.6 days. These properties are characteristic of UFKW and suggest that such waves might be easily identified in the MLS data. Peak amplitudes

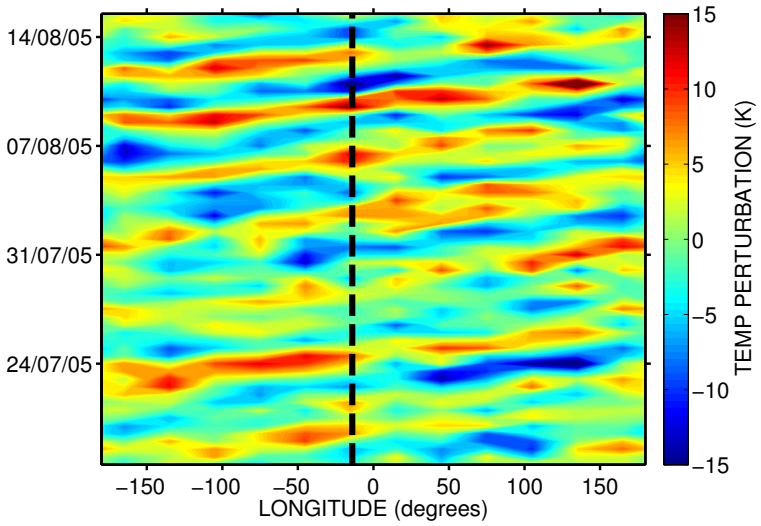

Figure 4.6: Hovmöller diagram of Aura MLS temperatures with daily longitudinal means subtracted for 17 July to 15 August 2005 at a height of 97 km. The dashed line represents the longitude of Ascension Island.

reach up to ∼15 K and are ∼6 K over much of the figure. It can also be seen that the amplitude of the wave shows some longitudinal variability.

To investigate the presence of UFKW at different wavenumbers in the Aura MLS dataset, a 2D-FFT was taken of temperature perturbations as a function of longitude and time for the whole of the 2005-2010 interval (an example of these temperature perturbations were presented in Fig. 4.6). The 2D-FFT identifies the dominant frequencies (from the time domain) and wavenumbers (from the longitudinal domain). The result is presented in Fig. 4.7, which has been limited to showing the E1, E2 and E3 wavenumbers for reasons of clarity.

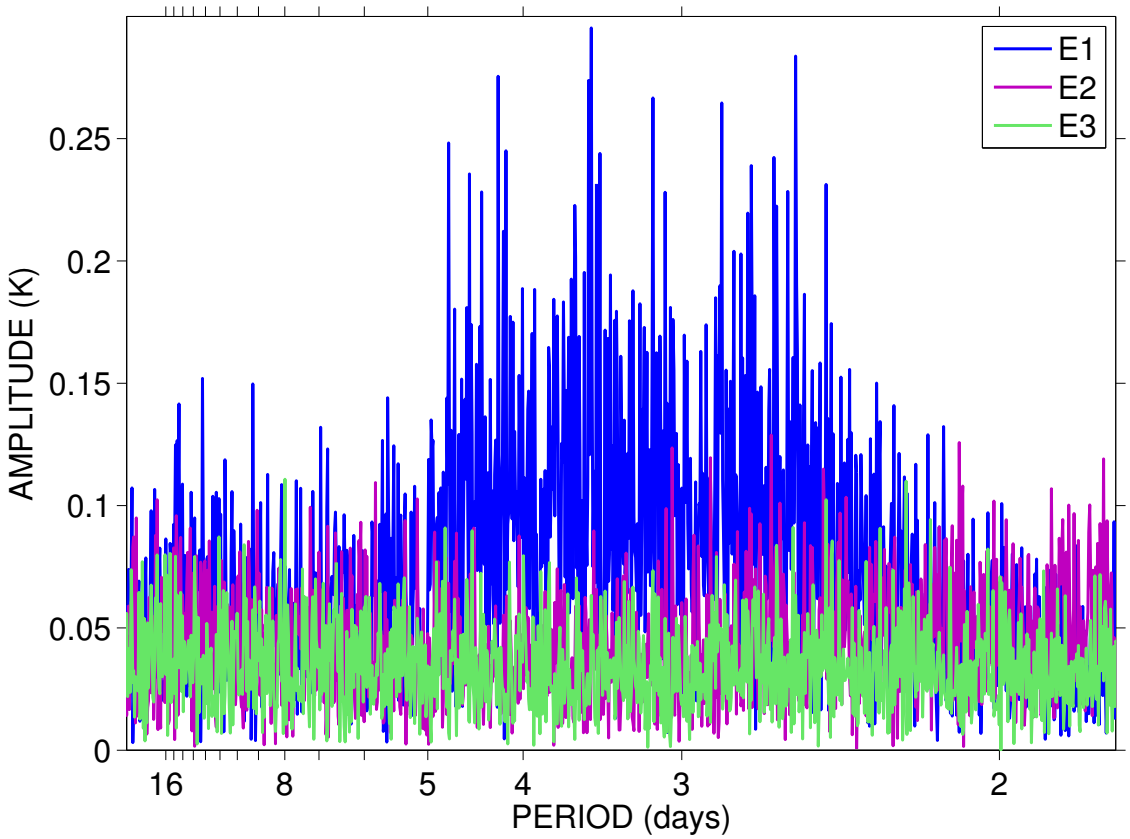

Figure 4.7: Spectra showing amplitudes for E1, E2 and E3 wavenumbers resulting from a 2D-FFT of the temperature perturbations as a function of time and longitude. For the 2D-FFT the entire 2005-2010 interval was used. The data are for a height of 97 km and within a 10^o latitudinal band centred over the equator.

It can be seen in the figure that there are peaks of large amplitude occurring between wave periods of 2.5 and 4.5 days in the E1 component, i.e. periods associated with UFKW. Within this period band only small amplitudes are evident in the E2 and E3 components. We thus restrict the scope of this study to the E1 components of the waves.

The zonal-mean structure of the UFKW in the Aura data was investigated using the least-squares planetary-wave analysis method of Wu et al. (1995), which determines a zonal-mean amplitude for a specified wave period and zonal wavenumber. The spectral composition of the E1 wave field was determined using a dynamic spectrum of the temperature data, in which the amplitude of E1 oscillations was calculated for wave periods stepped through the period range 2.5-4.5 days in increments of 1 h. Fitting windows of length 10 days were used as a compromise between spectral and temporal resolution. This analysis was repeated for the different heights and latitudes of the Aura dataset.

An example of this analysis is presented in Fig. 4.8a, which shows E1 wave amplitudes as a function of wave period and time at a height of 97 km at the latitude of Ascension island for the same interval of time as shown in the radar results of Fig. 4.2 (i.e. January-June 2005). The figure shows short-lived peaks in wave amplitude that often appear to correspond to the UFKW spectral peaks evident in the wind data

from Ascension Island shown in Fig. 4.2. For example, the seven peaks indicated by arrows on the time axis all appear to have corresponding features in the wind spectra of Fig. 4.2. This provides evidence that the radar and Aura MLS are observing the same UFKW since the Wu et al. analysis reveals only E1 planetary waves.

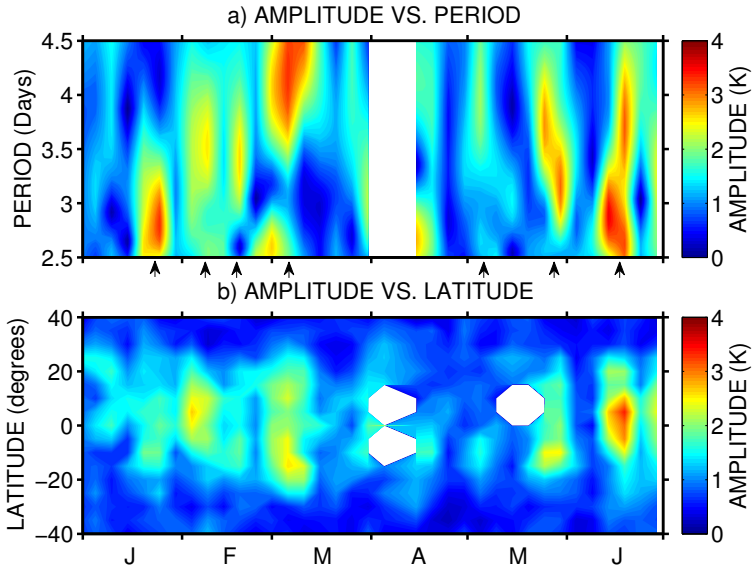

Figure 4.8: Amplitude of E1 waves derived from Aura MLS temperature measurements at a height of 97 km as a function of (a) wave period at the latitude of Ascension Island (8°S) and (b) latitude. In (b), the amplitudes are averaged over wave periods of 2.5-4.5 days. The data cover the interval January-June 2005. The arrows on (a) indicate the times at which large amplitude UFKW events were observed over Ascension Island in Fig. 4.2.

The majority of the spectral peaks in Fig. 4.8a have amplitudes maximising at about 3 K (although note that when the entire 6-year dataset was examined a small number of peaks were found with amplitudes reaching up to 6 K). The largest mean error on the wave amplitudes at equatorial latitudes was found to be about 0.5 K, and so here we will only consider oscillations with amplitudes larger than 0.5 K. The similarity of the peaks in Fig. 4.8 to those in the radar spectra (Fig. 4.2) leads us to conclude that they are the manifestations in MLT temperature of the same UFKW observed by the radar.

To further investigate the agreement between the meteor radar and satellite results, time series of amplitudes were produced for each year 2005 to 2010 for waves with period 3.5 days from both the meteor radar running Lomb-Scargle analysis and from the Aura MLS zonal mean amplitude analysis. Considering only those years with more than eight months of radar data, we calculated correlations between the two time series of amplitudes. This system has 43 degrees of freedom and a correlation of $r = 0.44$, significant at the 99 % level, indicating that the meteor radar and MLS are effectively observing the same UFKW wave field.

Figure 4.8b presents E1 wave amplitudes as a function of latitude and time for a height of 97 km and averaged over the wave-period range 2.5-4.5 days. The figure shows that wave amplitudes maximise at low latitudes near or on the equator.

To investigate the latitudinal structure in more detail the variation of amplitude with latitude was determined for well-defined, large-amplitude events. To do this, an amplitude threshold of 3.5 K at the equator was set for the highest height gate and 16 events exceeding this threshold were identified in the data, the central date of each is given in Table 1. The mean amplitude as a function of latitude for these 16 events is shown in Fig. 4.9 for heights from approximately 65 to 97 km. Also plotted on the figure is the amplitude profile for a 3.75 day UFKW at 97 km height from the Kyushu-GCM, normalised to the largest amplitude in the MLS data.

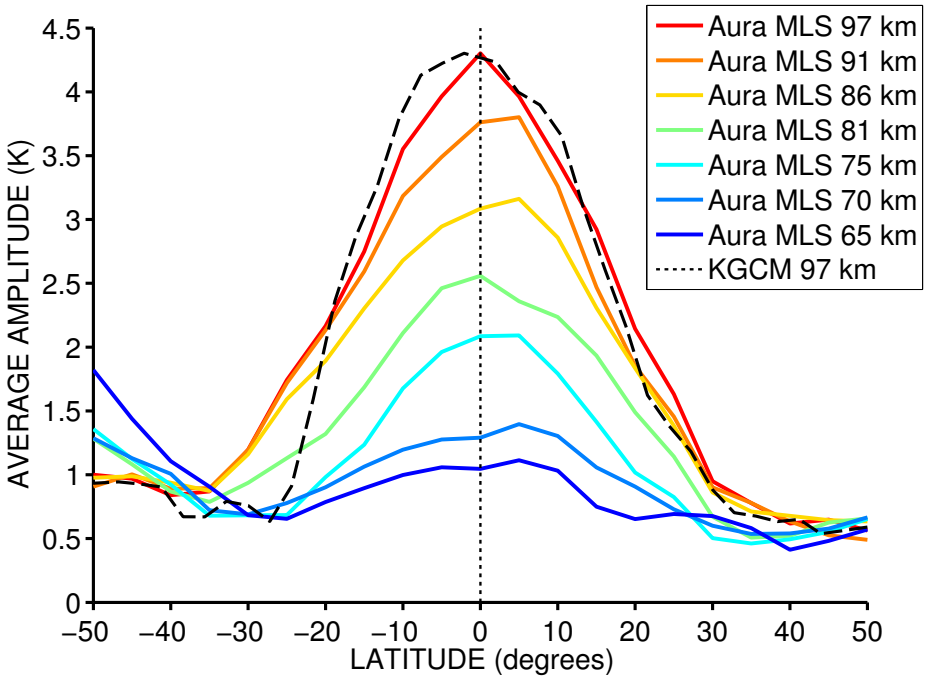

Figure 4.9: Average amplitude as a function of latitude for 16 E1 waves identified in Aura MLS data for seven different heights between 65 and 97 km. Only events with a maximum amplitude exceeding 3.5 K were included. Also plotted is the amplitdue profile for 3.75 day waves at 97 km height from the Kyushu-GCM (black dashed line), normalised to the largest amplitude in the MLS data.

The figure shows that the UFKW amplitudes have an approximately Gaussian shape centred over the equator with an e-folding half-width (at a height of 97 km) of 27^{o} of latitude. Wave amplitudes for all heights reach a minimum value between 25^{o} and 40^{o} latitude in both hemispheres. The shape of the latitudinal profile of amplitude observed in the Aura MLS data is very similar to that of the UFKW produced in the Kyushu-GCM. It is slightly steeper, however this is as expected as the 3.75 day period used to produce the Kyushu line is towards the longer end of the 2.5-4.5 day range that the Aura MLS data were averaged over and longer periods correspond to slower waves and narrower profiles (see Discussion).

The period at which UFKW amplitudes peak as a function of height was investigated in the Aura MLS data by taking the average over all six years of wave amplitudes (derived by the least-squares fit method) for each period and for each satellite height gate. As the amplitude growth with increasing height otherwise dominates the figure, the mean amplitudes were normalised for each height gate to better

show how the amplitudes varied with period at lower heights. The result of this analysis is presented in Fig. 4.10.

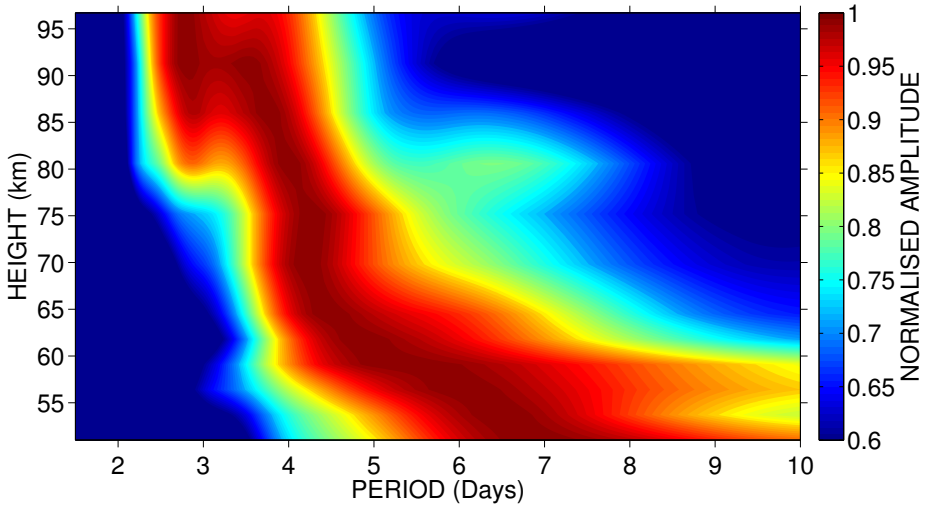

Figure 4.10: Normalised wave amplitudes as a function of height for E1 waves in the MLS temperature data averaged over the interval 2005-2010.

The figure shows that at the heights observed by the meteor radar the dominant wave periods are 2.5-4.5 days. The figure also shows a tendency for wave periods to increase at lower heights. This is in good qualitative agreement with the model results of Fig. 4.3.

The longitudinal variability that can be observed in Fig. 4.6 was explored by producing a Hovmöller diagram for the entire interval of 2005-2010, with 18 sectors of 20^{o} longitudinal width and 10^{o} latitudinal width centred over the equator. Within each sector the time series of temperature perturbations were then bandpassed within period limits of 2.5-4.5 days. This was done to reject the contributions from planetary waves at other periods (e.g. the 6-day wave which can reach large amplitudes at low latitudes). The variance was then calculated for each sector. This was repeated for longitudinal belts centred over other latitudes. The results of this analysis are presented in Fig. 4.11.

The figure shows a longitudinal band of large variance in the 2.5-4.5 day period range that is centred over the equator and diminishes with increasing latitude out to approximately 25^{o} N/S. Peaks in variance are evident over Indonesia (longitudes $\sim$120-160^{o}E) and central Africa (longitudes $\sim$15-35^{o}E). These two regions of the equator are known to be areas of strong convective activity in the troposphere. However, large variances are also apparent over the Indian ocean (longitudes $\sim$60-90^{o}E) and central Pacific (longitudes $\sim$180-150^{o}W). Interestingly, the smallest variances are observed near longitudes of 60^{o}W over South America, despite the fact that this would also be expected to be a region of strong convective activity. A peak in the wave activity was also observed over Indonesia by Kovalam et al. (1999) and Riggin et al. (1997), and is discussed further in Sect. 4. The longitudinal variability is less striking away from the equator, with variances more uniform around the longitudinal circle. Finally, we should note that the relatively short sampling time of the satellite within each latitude-longitude box may result in a contribution to the temperature variance from unresolved inertia-gravity waves.

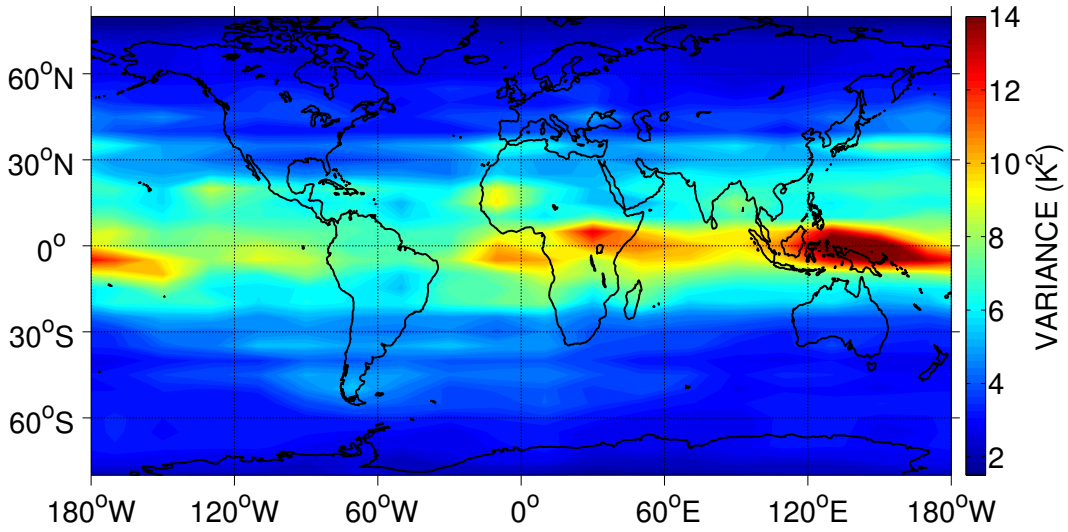

Figure 4.11: Variance of temperature perturbations derived from bandpassed temperature time series between periods of 2.5-4.5 days as a function of latitude and longitude from Aura MLS temperatures for 2005-2010 at a height of 97 km. The sectors are of 20° longitudinal width and 10° latitudinal width.

Table 4.1: Vertical wavelengths, λ_z, for 16 large amplitude UFKW events in the Aura MLS data centred on the dates given. The mean vertical wavelength is 44 ± 2 km.

Date	λ_z (km)	Date	λ_z (km)
3 Aug 2005	41 ± 1	24 Feb 2008	48 ± 3
1 Nov 2005	39 ± 1	3 Jul 2008	42 ± 2
12 Sep 2006	52 ± 2	24 Jan 2009	43 ± 2
22 Oct 2006	41 ± 3	3 Jun 2009	36 ± 1
30 Jan 2007	49 ± 1	27 Aug 2009	43 ± 2
24 Jun 2007	37 ± 1	6 Aug 2009	48 ± 3
4 Jul 2007	43 ± 3	26 Oct 2009	46 ± 2
3 Aug 2007	50 ± 5	23 Jul 2010	41 ± 1

As the UFKW propagate upwards, the phase of the waves change with height and so the vertical wavelength can be estimated. The wavelengths were calculated for the 16 large-amplitude wave events described above. The phase as a function of height is plotted for a typical UFKW event as an example in Fig. 4.12, shifted so that its phase starts at 0 radians in the top height gate. Also plotted is the best fit straight line. In each individual case the wave period was fixed at the period value for which the wave amplitude maximised. The variation of phase against height was then determined for that period. For example, the period of the event shown in Fig. 4.12 was found to be 92 hours. It can be seen from the figure that the phase changes with height in a very smooth and well-defined manner.

The corresponding vertical wavelengths for the 16 events, obtained from the lines of best fit, are given in Table 1. The vertical wavelengths are all rather similar, ranging from 36-52 km, with an average of $\lambda_z = 44 \pm 2$ km.

The seasonal variability of the E1 UFKW amplitudes in the temperature field was investigated by taking

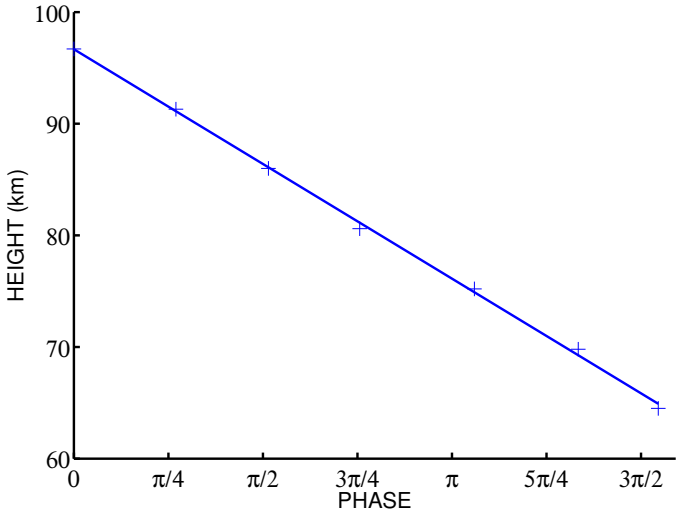

Figure 4.12: Phase as a function of height for the single large-amplitude E1 UFKW event observed over a ten-day interval centred on 3 August 2005, obtained from Aura MLS observations. Phase has been arbitrarily set to zero in the top height gate. The best-fit straight line is indicated and corresponds to a vertical wavelength of 41 ± 1 km.

an average of the least-squares fitted amplitudes over the period range 2.5-4.5 days, for each of the four height gates in the 80-100 km height range and for each month. The results of this analysis are presented as monthly means in a composite year 2005-2010 in Fig. 4.13, which shows a very similar seasonal variability to the corresponding radar result presented in Fig. 4.5.

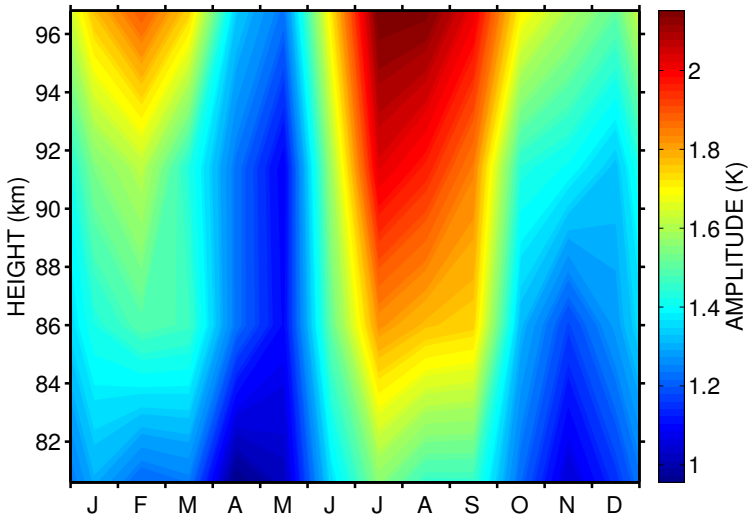

Figure 4.13: Aura MLS E1 UFKW monthly-mean amplitudes averaged over the 2.5-4.5 day period band as a function of height for a composite year of the 2005-2010 data.

Average UFKW amplitude is seen to increase with height from between 1.0-1.5 K at heights near 81 km to peaks of ∼2.2 K at 97 km. The greatest amplitudes are in the months February and August, as observed in the radar data. The peak of 2.2 K is smaller than the amplitudes presented in Fig. 4.9, but this is just a result of averaging many individual events of greater amplitude along with quieter episodes. Individual waves may thus have larger amplitudes than indicated by Fig. 4.13.

4.4.3 Momentum Fluxes

The vertical flux of horizontal momentum, P, carried by the UFKW was determined using the method described in Kovalam et al. (1999) and Riggin et al. (1997). The momentum flux is given by $\rho\overline{u'w'}$. The meteor radar can measure horizontal winds but cannot easily measure vertical winds. However, using the dispersion relation for UFKW allows an estimate of P to be made in terms of atmospheric density, ρ, horizontal perturbation winds from the UFKW, u', the scale height, H, and the horizontal and vertical wavenumbers of the UFKW, k and m, respectively. Following Kovalam et al. (1999), P is given by

$$P = \frac{1}{2}\rho\overline{u'^2}\Re\left[-\frac{k}{(m^2+\frac{1}{4H^2})}(m-\frac{i}{2H})\right]$$

The mesospheric densities for the different height gates and months were obtained from the MSIS-E-90 atmospheric model. The average of the UFKW vertical wavelengths obtained from the Aura MLS analysis was used to determine m ($-0.00014\,\mathrm{rad\,m^{-1}}$). The value for k was obtained by assuming a zonal wavenumber 1. The results of this analysis are shown in Fig. 4.14 in terms of monthly momentum fluxes in a composite year calculated using all available radar data between 2005 and 2010.

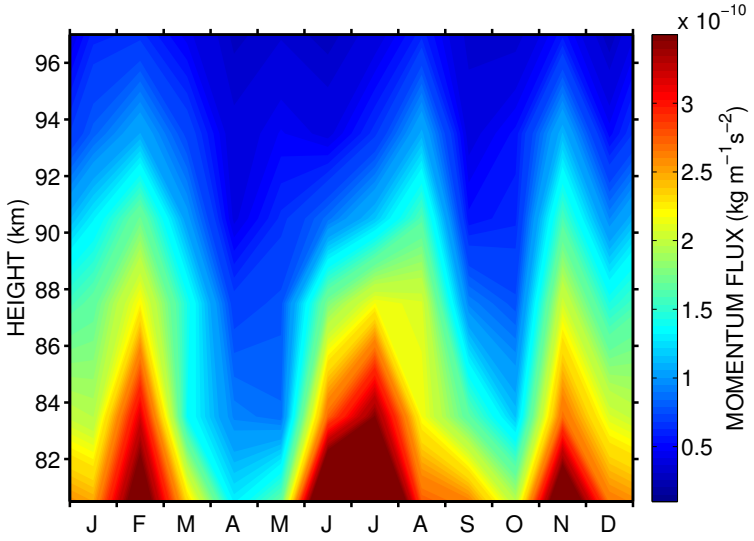

Figure 4.14: UFKW Momentum Fluxes for a composite year of data available between 2005-2010 obtained using Ascension Island meteor-radar. Bandpassed winds were used between period limits of 2.5-4.5 days.

From the figure it can be seen that momentum fluxes maximise in February, July and November, with distinct minima between these months. This seasonal variation is very similar to the variation in UFKW variance shown in Fig. 4.5. However, as height increases, the gas density decreases at a greater rate than the variance increases, resulting in a decrease of momentum flux with height in all months and also explaining the apparent shift of an August variance peak to a July momentum flux peak (at heights near 80 km where the density is much greater than at 97 km, the variance peaks in July). The momentum fluxes decrease strongly with increasing height from peak values at the lowest heights observed. For instance, momentum fluxes in July have peak values of more than $3.5 \times 10^{-10}\,\mathrm{kg\,m^{-1}\,s^{-2}}$ at heights around 80 km, but decrease to around $6 \times 10^{-11}\,\mathrm{kg\,m^{-1}\,s^{-2}}$ at heights around 97 km.

The momentum lost from the UFKW is deposited into the mean flow, where it causes an eastward acceleration of the zonal winds. This acceleration can be calculated from the vertical gradient of P (i.e. $\frac{\mathrm{d}P}{\mathrm{d}z}$) and knowledge of ρ. Using the MSIS-E-90 values of ρ described above, the zonal acceleration in the mean flow resulting from the UFKW was calculated for each year. The results for the acceleration between the two highest height gates for the year 2006 are shown as an example in Fig. 4.15.

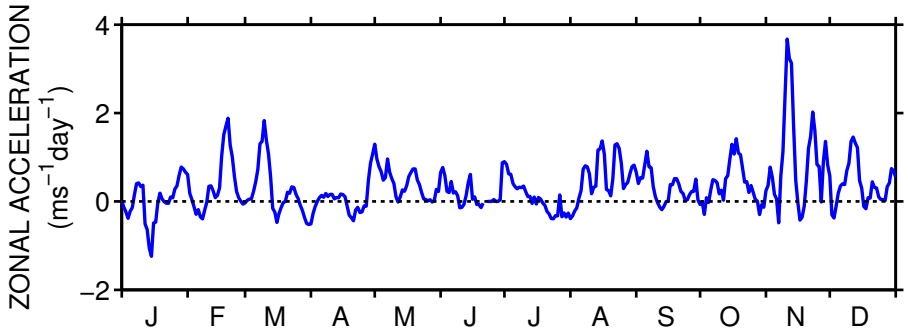

Figure 4.15: Zonal acceleration (or body force per unit mass) obtained from UFKW measured by the Ascension Island meteor-radar at heights between 93.5 and 97.0 km for the year 2006.

Considerable variability in the zonal acceleration is evident on the intraseasonal timescales of 25-60 days. Accelerations vary from $-1\,\mathrm{m\,s^{-1}\,day^{-1}}$ to nearly $4\,\mathrm{m\,s^{-1}\,day^{-1}}$. The acceleration is generally positive (eastward), and this is true for all years considered. However, we note that there are occasional episodes of modest westwards acceleration. These may be the result of inertia-gravity waves or mixed Rossby-gravity waves present in the range of wave periods considered (note that the gravity wave spectrum will extend up to the inertial period of $\sim$86 h at the latitude of Ascension Island). To investigate the seasonal variability of the zonal acceleration, a composite-year figure was produced by averaging all available monthly-mean acceleration values between each height gate. This composite year analysis is presented in Fig. 4.16.

Zonal accelerations are seen to have maximum values in February, August and November, and the zonal acceleration generally increases with increasing height, from values of around $0.1\,\mathrm{m\,s^{-1}\,day^{-1}}$ at lower heights up to peaks of nearly $0.9\,\mathrm{m\,s^{-1}\,day^{-1}}$ higher up. This range of accelerations is similar to that observed by Kovalam et al. (1999) and Riggin et al. (1997). These contours of zonal acceleration look quite similar to those of zonal variance (Fig. 4.5) indicating that zonal acceleration approximately

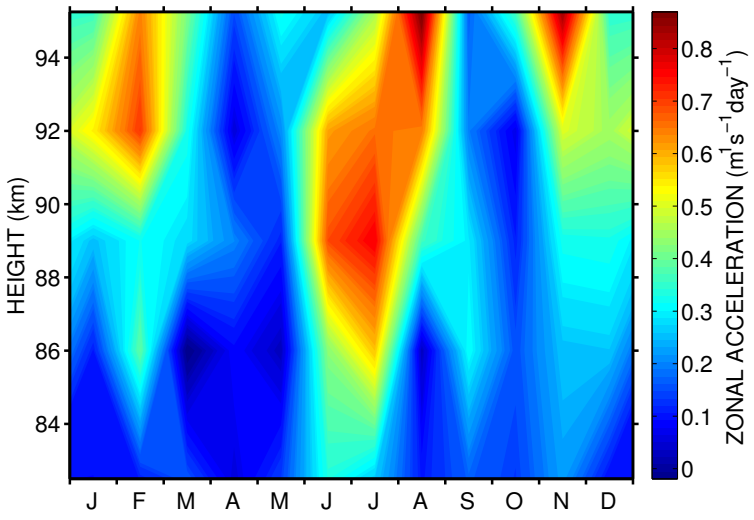

Figure 4.16: Zonal Acceleration (or body force per unit mass) resulting from UFKW with periods between 2.5-4.5 days, measured by the Ascension Island radar for the composite year of data available between 2005 - 2010.

follows UFKW variance.

4.4.4 TRMM Observations and the Kyushu-GCM

A proposed source of UFKW in the MLT is moist convective heating in the equatorial troposphere. To investigate this proposal further, we explored this mechanism in the Kyushu-GCM and used TRMM rainfall data as a proxy for convective heating to enable comparisons with our observations.

An analysis of Kyushu-GCM data was carried out to investigate the correlation and lag between UFKW amplitudes in the MLT and E1 amplitudes of similar period in tropospheric convective heating. In the latter case, E1 amplitudes with periods in the range 2.5-4.0 days were considered. The results of this analysis are presented in Fig. 4.17.

The figure shows correlation as a function of lag for five integrated years of model output. Also indicated on each figure is the 95 % confidence limit. Two of the five years show correlations of about 0.3 which exceeds the 95 % confidence limits. These occur at lags of $\sim$7-8 days, indicating that UFKW amplitudes maximise $\sim$7-8 days after large amplitude E1 signals of similar period in tropospheric convective heating. However, we should note that in three of the years there was no significant correlation evident, suggesting that the connection between convective heating events and UFKW in the MLT of the Kyushu-GCM is not a simple one-to-one relationship.

We also investigated the connection between tropospheric heating and UFKW observed in the MLT using TRMM precipitation data. The precipitation data, used as a proxy for convective heating, was obtained from the TRMM "Multi-Satellite Precipitation Analysis" 3B42 dataset. This provides three-hourly averages of the precipitation rate (mm h^{-1}) for the latitude range 50^{o}N-50^{o}S, longitudes 180^{o}W-180^{o}E, on a grid with a resolution of 0.25×0.25 The data product is derived by calibrating the datasets

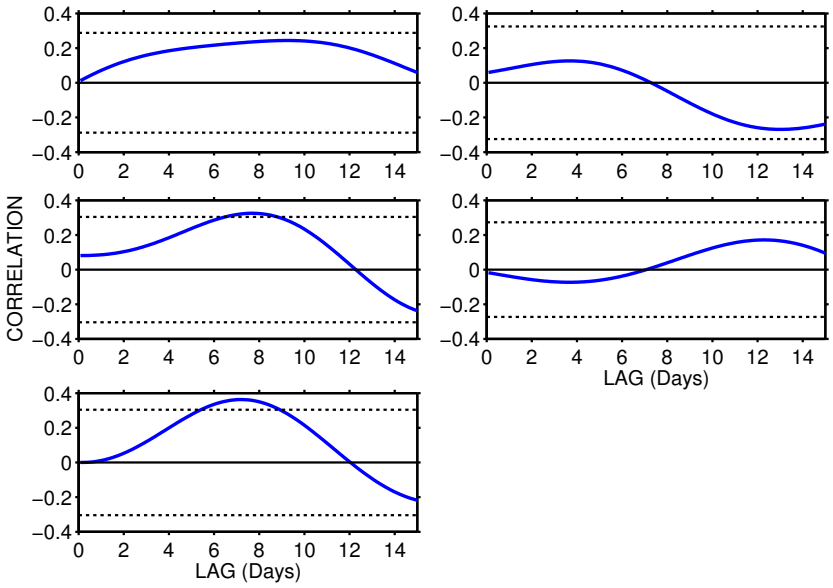

Figure 4.17: Correlations (with lags applied to the UFKW zonal wind amplitude) between E1 amplitudes of oscillations with period 2.5-4.0 days in the tropospheric convective heating and in the amplitude of UFKW in the MLT, for five integrated years of the Kyushu-GCM. The dashed lines on the figures indicate the 95 % confidence limits.

of GMS, GOES-E, GOES-W, Meteosat-7, Meteosat-5 and NOAA-12 with data from TRMM's (Tropical Rainfall Measurement Mission) microwave imager (TMI) and visible and infra-red scanner (VIRS) instruments. TRMM-3B42 is available for all years considered here.

The least squares fit method of Wu et al. (1995) was applied in a similar manner to that of the Aura MLS analysis to measure the amplitudes of E1 oscillations of period 2.5-4.5 days in the TRMM data that might be expected to excite E1 UFKW. Time series were produced of both the Aura E1 UFKW amplitudes in the MLT region and the TRMM E1 spectral component.

Correlations were calculated between the two time series for each year using lags of between −30 and +30 days (such that a negative lag of, for example, −30 days represents the TRMM precipitations being correlated with the Aura results of 30 days earlier, a lag of 0 days represents the two time series being correlated at equal times, and a lag of +20 days represents the TRMM precipitations being correlated with the Aura results of 20 days later). The results of this analysis are presented for years 2005-2010 in Fig. 4.18.

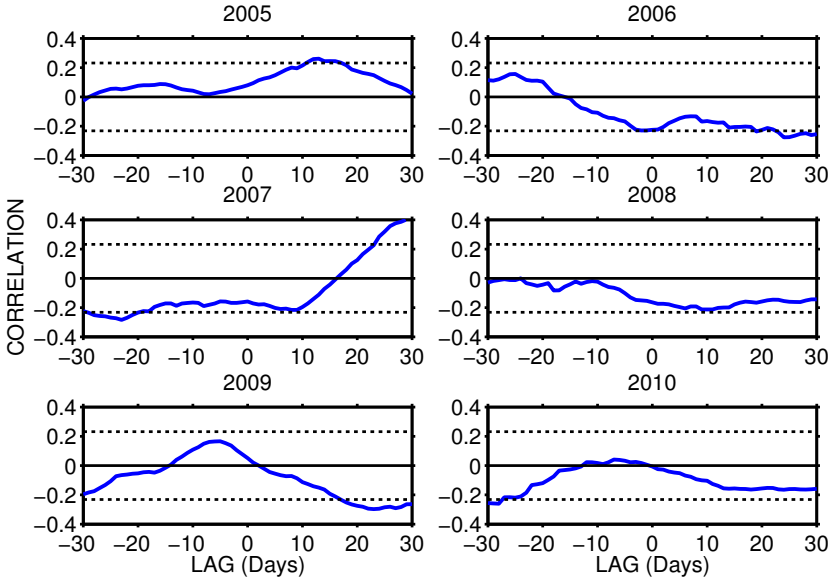

Figure 4.18: Correlations (with time lags applied to the UFKW in the MLT) between E1 waves of period 2.5-4.5 days in the Aura analysis at a height of 97 km and similar oscillations in the TRMM analysis, from 2005 (top left) to 2010 (bottom right). The dashed lines on the figures indicate the 95 % confidence limits.

From Fig. 4.18 it can be seen that the correlations vary greatly from year to year. Considering the results for 2005, the correlation maximises at a lag of approximately 10-15 days suggesting that UFKW manifest in the MLT region 10-15 days after E1 signatures of period 2.5-4.5 days occur in the tropospheric convective heating. This is in reasonable agreement with theoretical predictions that a UFKW with 4 day period should take about 10 days to reach a height of 100 km. However, in the other years considered, this behaviour is not repeated, and significant correlations maximising at lags ranging from less than −20 to more than +20 occur and the correlations can be either positive or negative. Further, we examined the correlations at much greater lags than those shown in the figure, and found that significant correlations, either positive or negative, could also occur at these larger lags. A correlation analysis for the whole period 2005-2010 gave correlations in the range −0.01 to −0.07 for each of the lags but these values were not significant.

These results suggest that there is no significant tendency for mesospheric UFKW bursts to occur fol-

lowing peaks in the E1 signal in the tropospheric convective heating. However, due to the intermittent nature of UFKW, these correlations will include extended intervals when the spectra of the two datasets at the frequencies of interest contain only noise. This may explain the relatively low correlations between the Aura and TRMM datasets.

To try and address this problem, an analysis was applied which considered only the times of the 16 largest-amplitude UFKW events. The amplitudes of the E1 signatures in the TRMM precipitation data at the times and periods of these events were averaged. This was repeated with each of the lags applied. The convention of positive lag signifying that the mesospheric UFKW take place after the precipitation activity was retained. If mesospheric UFKW amplitudes peaked ten days after a large amplitude TRMM E1 signal, we might then expect to see the TRMM mean E1 amplitudes maximising at a lag of +10 days. These TRMM E1 average amplitudes as a function of lag are presented in Fig. 4.19a. A similar analysis was performed in which the total magnitude of the rainfall (rather than the amplitude of the E1 oscillations) was averaged around the full longitudinal circle for the times of the large-amplitude UFKW events, with lags applied. This analysis would identify a tendency for large-amplitude precipitation events to precede large-amplitude UFKW events in the MLT, as might be expected if the magnitude of precipitation was exciting UFKW. This result is presented in Fig. 4.19b. Note that positive lags correspond to a situation in which a high-magnitude precipitation event precedes UFKW in the MLT.

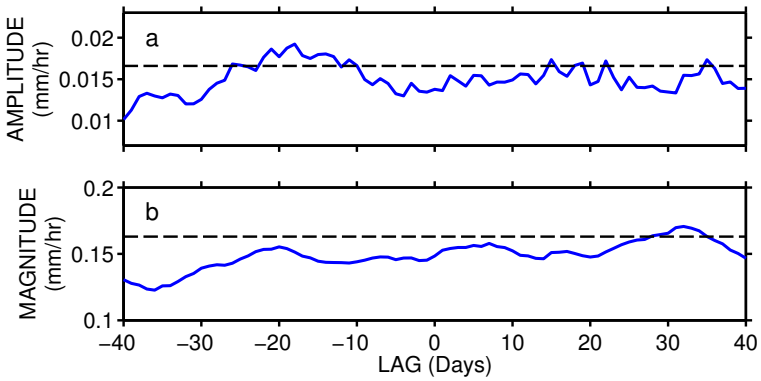

Figure 4.19: (a) The average amplitude of E1 oscillations in the TRMM precipitation data at the same periods and times (with various lags added) at which UFKW are present in the Aura MLS data. (b) The average zonal-mean magnitude of precipitation rate in the TRMM data before (positive lag), during (zero lag) and after (negative lag) the times at which UFKW are present in the Aura MLS data. The dotted lines represent the average over all times, not just the times either side of the large-amplitude mesospheric UFKW events.

Figure 4.19a shows a small peak in the TRMM precipitation E1 amplitudes occurring approximately 10-20 days prior to the large amplitude UFKW events in the MLT region (i.e. the broad peak on the right-hand side of the figure). This might suggest that the mesospheric UFKW tend to reach largest amplitudes 10-20 days after a large amplitude E1 2.5-4.5 day spectral component of large amplitude in precipitation (i.e. latent heat release). However, we note that there is a larger peak on the left-hand side of the figure occurring at a lag of about -20 days, which would indicate mesospheric UFKW amplitudes maximising *before* the peak in tropospheric latent heat release. We regularly observe peaks occuring at negative lags. We therefore conclude that small peaks at positive lags do not necessarily indicate a

simple connection in which a large-amplitude E1 precipitation event leads to a large-amplitude UFKW signature in the MLT region.

Figure 4.19b shows that the magnitude of precipitation rate is similar before, during and after large-amplitude UFKW events in the MLT region. These results, and the observation that the amplitudes of the E1 signatures and the zonal-mean magnitudes of the rainfall at times either side of large-amplitude UFKW events are not above the long-term average, further suggest that there is not a simple relationship between the occurrence of large-amplitude mesospheric UFKW and the magnitude or E1 component of latent heat release.

4.4.5 Intraseasonal Oscillations

It has been shown that there is a semiannual oscillation in the UFKW amplitudes of the radar winds and satellite temperatures. To investigate the presence of variability on shorter intraseasonal timescales, spectra were calculated for the entire datasets of radar winds, UFKW amplitudes in temperature and wind, zonal wind accelerations and TRMM rainfall rates. Figure 4.20 presents results of this analysis for specific heights. The Aura MLS UFKW spectrum has been cut off at the Nyquist limit of 20 days.

Large peaks are apparent at periods corresponding to the semiannual oscillation in many of the figures. However, in addition to these, peaks exceeding the 99 % confidence limit are evident in all the spectra at periods of 25-60 days, corresponding to ISOs. In particular, many of the spectra show peaks at periods near 27, 37, 45 and 61 days; these periods are indicated on the figures by red, green, yellow and purple circles respectively. This result may indicate that regular episodes of increased UFKW amplitude result in regular episodes of increased zonal-wind acceleration, which in turn impose a periodicity at similar periods on the zonal winds themselves. Note that ISO amplitudes in the mean zonal wind in this period range reach up to about $5\,\mathrm{m\,s^{-1}}$ at the height shown ($\sim$87 km), however they reached nearly $10\,\mathrm{m\,s^{-1}}$ in the lowest height gate ($\sim$81 km).

4.5 Discussion

UFKW are observed to occur intermittently throughout the datasets in bursts lasting a few cycles, after which their amplitudes decrease again. UFKW Amplitudes in the zonal wind are seen to regularly exceed 15 m s^{-1} and occasionally reach 40 m s^{-1}. This is comparable with the 25 m s^{-1} peak amplitudes of UFKW reported by Kovalam et al. (1999) using MF radars at Pontianak (0^{o}N, 109^{o}E) and Christmas Island (2^{o}N, 157^{o}W), and peak amplitudes exceeding 30 m s^{-1} reported by Riggin et al. (1997) using a meteor radar at Jakarta (6^{o}S, 107^{o}E) and an MF radar on Christmas Island. Our observed amplitudes are also very similar to the amplitudes of 5-40 m s^{-1} reported for UFKW in the Kyushu-GCM (Chen and Miyahara, 2011).

In the Aura MLS temperature data, UFKW generally have amplitudes of around 3 K, although some individual events reached amplitudes of 6 K. This is in very good agreement with the values reported in TIMED/SABER data by Forbes et al. (2009).

UFKW are usually evident in the radar winds at the same times as they are observed in the satellite data. There is good agreement between the wave frequencies simultaneously observed by the two datasets.

Wave amplitudes in both the radar and MLS data increase with height. Considering the 16 large-amplitude events used in Fig. 4.9, the amplitude grows approximately linearly with height, and is thus less than the $e^{\frac{z}{2h}}$ rate which would correspond to non-dissipative wave propagation. This indicates that there is some dissipation.

The seasonal variability of UFKW in both the wind and temperature data reveals a semiannual variation with largest amplitudes in February and July/August (a smaller secondary maximum is seen in the radar data in November). For comparison, Vincent (1993) observed an approximately similar semiannual pattern with maximum UFKW amplitudes in January-February and August/September over Christmas Island. Similarly, Yoshida et al. (1999) also observed a semiannual variability in UFKW amplitudes over Jakarta.

Our results suggest that UFKW amplitudes and variances in the MLT vary as a function of longitude and reach largest values over Indonesia. Here we should note that Riggin et al. (1997) found higher amplitudes of UFKW over Jakarta in Indonesia (6.4^{o}S, 106^{o}E) than over Christmas Island in the central Pacific (1.9^{o}N, 157.3^{o}W), despite Jakarta being further from the equator and thus further from the equatorial peak in amplitudes. They suggested that the larger amplitudes over Jakarta may be attributed to the Indonesian region's vigorous convection, making it a site for strong UFKW excitation.

Kovalam et al. (1999) also reported different amplitudes at different longitudes, but in a study using two similar MF radars, with larger amplitudes over Pontianak (0^{o}N, 109^{o}E) than over Christmas Island by a factor of 1.4. They also suggested that the longitudinal variability was due to source effects. This suggests that the longitudinal variability evident in Figs. 4.6 and 4.11 is of geophysical origin.

Our global observations confirm the earlier suggestions that UFKW amplitudes maximise over Indonesia. This evidence provides strong support for the suggestion of Riggin et al. (1997) that the region of high convective activity over Indonesia is a vigorous source of equatorial waves. However, we notice that there is no apparent secondary peak in UFKW variances over the convective region of South America. However, our observation that this longitudinal peak in variance is not evident at latitudes away from the equator (where the inertial period limit falls out of the 2.5-4.5 day range) may still suggest that waves other than UFKW are contributing to this maximum.

The variation of amplitude with latitude evident in Fig. 4.9 is approximately gaussian and maximises over the equator with an e-folding half-width of $\sim$27$^{\rm o}$ of latitude. Following the work of Holton and Lindzen (1968) the e-folding half-width of Kelvin waves can be shown to be

$$L_y \simeq \sqrt{\frac{2\omega}{\beta k}}$$

where for the beta-plane centred over the equator $\beta = \frac{2\Omega}{r_{\rm E}}$, for the Earth's rotation rate Ω (in rad s^{-1}) and Earth's radius $r_{\rm E}$. UFKW of zonal wavenumber 1 and period of 3.5 days (the average period of the 16 large-amplitude events included in Fig. 4.9) have zonal phase speeds of $\frac{\omega}{k} \simeq 130\,{\rm m\,s^{-1}}$. This corresponds to a predicted half-width of $L_y \simeq 3400\,{\rm km}$, or 30.5$^{\rm o}$ of latitude. This is remarkably close to our observed result of $\sim$27$^{\rm o}$ of latitude and further confirms our inference that the analysis is detecting UFKW.

The average vertical wavelength of Table 1, $\lambda_z = 44 \pm 2\,{\rm km}$, is consistent with the average λ_z values of 41 km found by Salby et al. (1984), and 43 km found by both Sridharan et al. (2002) and Lima et al. (2008), but considerably shorter than the values of 87 and 116 km reported by Riggin et al. (1997) and values between 53 and 88 km observed by Kovalam et al. (1999). A wave of wavenumber 1 travelling around the equator would have a horizontal wavelength approximately equal to the circumference of the equator, i.e. $\lambda_x = 40\,700\,{\rm km}$. Using the Kelvin wave dispersion relation,

$$\lambda_z = T_B \left[\frac{\lambda_x}{\tau} - \overline{u} \right],$$

and using values of $T_B \simeq 300\,{\rm s}$ for the MLT region Brunt-Väisälä period and $\overline{u} = 0\,{\rm m\,s^{-1}}$ as an approximation for the mean wind (Forbes et al., 2009) we obtain vertical wavelengths ranging from 31.4 to 56.5 km for UFKW with periods $\tau =$ 2.5-4.5 days. These numbers are in excellent agreement with the observations presented in Table 1.

As UFKW dissipate, they deposit their eastward momentum into the mean flow, creating an eastward acceleration. The accelerations measured here (Figs. 4.15 and 4.16) are seen to be almost always eastward. The range of monthly-mean values at heights near 95 km of $\sim$0.2-0.9 m s^{-1} day^{-1}, is similar to that obtained from radar measurements at Pontianak (Kovalam et al., 1999). The average monthly mean value of 0.44 m s^{-1} day^{-1} is slightly greater than that obtained at Christmas Island of 0.32 m s^{-1} day^{-1}, but less than that obtained at Jakarta of 0.67 m s^{-1} day^{-1} (Riggin et al., 1997). Peak accelerations as-

sociated with large events can reach up to $\sim$4 m s^{-1} day^{-1}. This suggests that UFKW make a small contribution to the equatorial MLT region when compared to, for example, the contribution of gravity waves at midlatitudes (e.g. Norton and Thuburn, 1999).

In Sect. 4.4.4 we considered correlations between tropospheric rainfall parameters and UFKW amplitudes in the MLT. Although in 2005 there was a peak in the correlation at lags of 10-20 days that is significant at the 95 % level, in other years the correlation at these lags was actually weakly negative. These low correlation values might be due to the episodic nature of the UFKW, as the time series being correlated will include long intervals of time during which there is little to no activity, and so noise would reduce the correlations. However, we might still have expected that the magnitude or the average amplitude of E1 signatures in the rainfall would be larger than average before the occurrence of a burst of mesospheric UFKW. However, this was not observed. These observations suggest that there is no simple relationship between these rainfall parameters and the occurrence of large-amplitude UFKW in the MLT. Nevertheless, the results presented in Fig. 4.20 suggest a link between ISOs in the rainfall and ISOs in the mesospheric UFKW amplitudes.

ISOs were found in the two rainfall parameters considered, in the UFKW amplitudes and mean-flow accelerations, background zonal winds and zonal-mean temperatures with clusters of spectral peaks at periods in the 30-60 day range associated with the Madden-Julian oscillation and the 20-25 day range associated with the oscillation reported by Hartmann et al. (1992) (Fig. 4.20). Similar observations of ISOs in UFKW temperature amplitudes and zonal-mean temperature have been reported by Forbes et al. (2009) in TIMED/SABER data. Our results suggest that ISOs in zonal-mean rainfall (a proxy for tropospheric convective heating) result in modulation of UFKW amplitudes in the MLT at similar periods. This in turn modulates the mean-wind accelerations caused by the dissipation of those UFKW. It is interesting to note that the zonal winds also show periodicities that match well with those of the mean-wind accelerations, from which one might infer that these oscillations in the mean wind were being driven by the momentum deposition from UFKW. However, we should note that ISOs are also known to exist in gravity-wave and diurnal-tidal amplitudes (Miyoshi and Fujiwara, 2006; Eckermann et al., 1997) which can also contribute to ISOs in the zonal winds. The relative role of UFKW, gravity waves and tides in exciting mean wind ISOs in the MLT thus remains to be determined.

4.6 Conclusions

Winds from the Ascension Island meteor radar (8° S, 14° W) and temperatures recorded simultaneously by the Aura MLS instrument have been analysed to characterise ultra-fast Kelvin waves of period 2.5-4.5 days at equatorial latitudes and at heights of up to $\sim$100 km. These have been compared with observations made from the Kyushu-GCM and in the TRMM rainfall data. Our conclusions are as follows:

1. Clear but intermittent UFKW are observed with zonal wind amplitudes reaching up to 40 m s^{-1} and temperature amplitudes of up to 6 K. The average vertical wavelength is $\lambda_z = 44 \pm 2$ km.

The variation of UFKW amplitude with latitude is observed to be approximately gaussian with an e-folding half-width of 27^{o} of latitude.

2. There is good agreement of UFKW observations in the radar zonal winds and in the Aura MLS temperatures, with UFKW found simultaneously at the same frequencies in both datasets.

3. Amplitudes do not grow at the exponential free growth rate with height which means that the waves dissipate, depositing eastward momentum into the mean flow. Monthly mean acceleration values are found to be 0.2-0.9 $\mathrm{m\,s^{-1}\,day^{-1}}$ at heights near 95 km.

4. A semiannual variation in wave amplitude is evident in both datasets with largest amplitudes in February and July/August.

5. A longitudinal variability is found in the variance of temperature perturbations associated with these waves with largest values over Indonesia and Africa. This is attributed to the strong tropospheric convection of these regions. The absence of a peak in activity over South America is unexplained.

6. No clear link is found between the occurrence of large-amplitude mesospheric UFKW and E1 signatures in rainfall or zonal-mean magnitude of rainfall.

7. ISOs with periods between $\sim$25-60 days are observed in the long-term spectra for the mean zonal winds, the zonal-mean temperatures, the UFKW amplitudes and associated mean-flow accelerations, and in the rainfall magnitudes. This supports the suggestion that the tropospheric Madden-Julian oscillation and the 20-25 day oscillation of Hartmann et al. (1992) modulate the intensity of UFKW, which then propagate upwards and contribute to similar periodicities in the background winds by wave-mean flow interactions. However, the relative role of UFKW, gravity-waves and tides in driving ISOs in the zonal winds has yet to be determined.

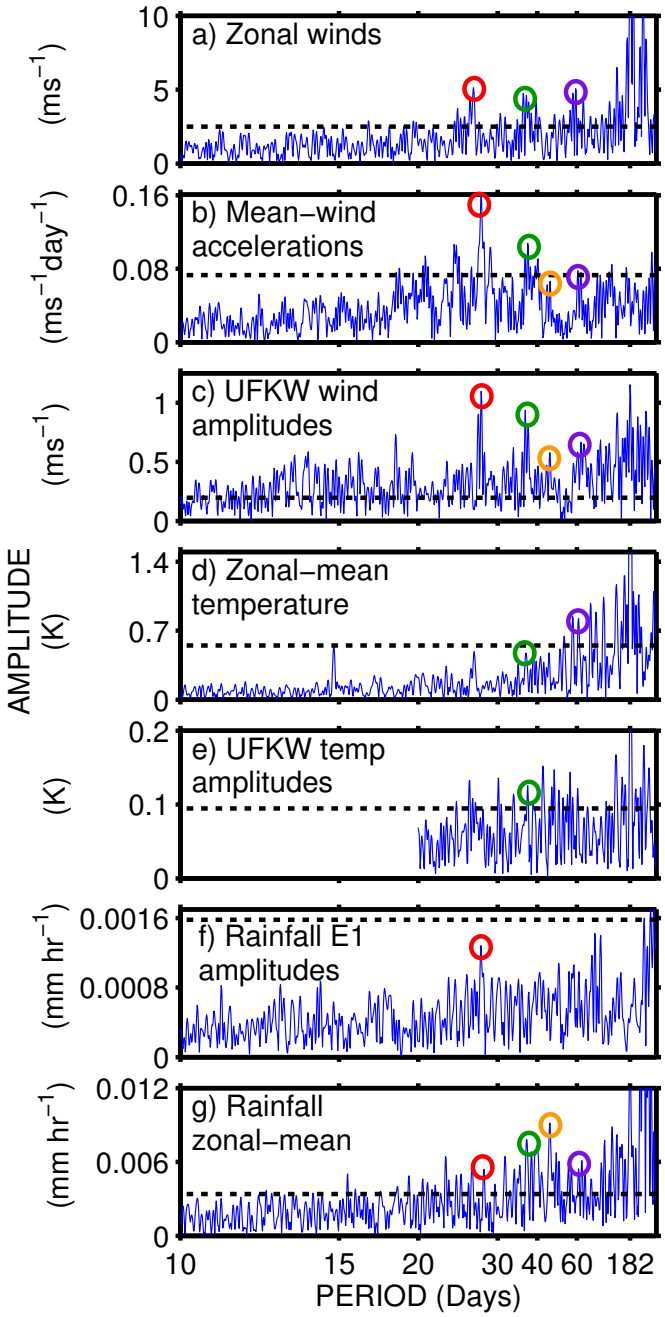

Figure 4.20: Spectra of (a) zonal mean wind at a height of 87 km, (b) mean-flow accelerations from UFKW derived from meteor radar zonal winds bandpassed in the 2.5-4.5 day range at a height of 83 km, (c) UFKW wind amplitudes at a height of 81 km, (d) zonal-mean temperature derived from Aura MLS observations, (e) UFKW temperature amplitudes at a height of 96 km, (f) E1 2.5-4.5 day signatures in the TRMM rainfall rate and (g) zonal-mean rainfall rate magnitudes. A ten day window was used for the UFKW amplitudes in the MLS temperatures so (e) has been cut off at the Nyquist limit. The dashed horizontal lines represent the 95 % confidence limits. Different colour circles are used to identify frequencies of interest in successive plots.

Chapter 5

The Diurnal and Semidiurnal Tides over Ascension Island (8$^{\mathrm{O}}$S, 14$^{\mathrm{O}}$W) and their Interaction with the Stratospheric QBO: Studies with Meteor Radar, eCMAM and WACCM

5.1 Abstract

Horizontal winds in the MLT region have been measured over Ascension Island (8$^{\mathrm{o}}$S, 14$^{\mathrm{o}}$W) in the tropical mid-Atlantic region throughout the years 2002 - 2011. The observations were made by a VHF meteor radar. The observations reveal the presence of atmospheric tides of large amplitude. The observations are analysed to characterise the seasonal and interannual variability of the diurnal and semidiurnal tides. Monthly-mean diurnal tidal amplitudes are found to reach values as large as 48 ms^{-1} in the meridional component and 41 ms^{-1} in the zonal. A semiannual seasonal variation is found in diurnal-tidal amplitudes with amplitude maxima at the equinoxes and amplitude minima at the solstices. Diurnal tidal meridional vertical wavelengths are generally in the range 24 - 30 km. The diurnal zonal vertical wavelengths are similar to the meridional, except for the winter months when the zonal vertical wavelengths are much longer, occasionally exceeding 100 km. Semidiurnal amplitudes are observed to be significantly smaller than diurnal amplitudes. Semidiurnal vertical wavelengths range from 20 to more than 100 km. Our observations of tidal amplitudes and phases are compared with the predictions of the extended Canadian Middle Atmosphere Model (eCMAM) and the Whole Atmosphere Community Climate Model (WACCM). Both eCMAM and WACCM reproduce the trend for greater diurnal amplitudes in the meridional component than the zonal. However, eCMAM tends to overestimate meridional amplitudes, while WACCM underestimates both zonal and meridional amplitudes. Vertical wavelength

predictions are generally good for both models, however eCMAM predicts shorter diurnal zonal vertical wavelengths than are observed in winter, while WACCM predicts longer zonal vertical wavelengths than observed for the semidiurnal tide for most months. Semidiurnal amplitude predictions are generally good for both models. It is found that larger-than-average diurnal and semidiurnal tidal amplitudes occur when the stratospheric QBO at 10 hPa is eastwards, and smaller-than-average amplitudes occur when it is westwards. Correlations between the amplitude perturbations and the El Niño Southern Oscillation are also found. The precise mechanism for these correlations remains unclear.

The work in this chapter has been published in the journal Atmospheric Chemistry and Physics as Davis, R.N., Du, J., Smith, A.K., Ward, W.E., and Mitchell, N.J.: The diurnal and semidiurnal tides over Ascension Island (8^{o}S, 14^{o}W) and their interaction with the stratospheric QBO: studies with meteor radar, eCMAM and WACCM, Atmos. Chem. Phys., 13, 9543-9564, 2013.

5.2 Introduction

The mesosphere and lower thermosphere (MLT) are host to a wide range of oscillations including tides, planetary waves and gravity waves that can manifest in the wind, temperature and pressure fields. However, at most latitudes the dominant oscillations are the tides which can reach amplitudes of many tens of metres per second.

The migrating (sun-synchronous) tides are excited primarily by the diurnal cycle in solar heating of gases in the atmosphere. These gases include water vapour which absorbs infra-red radiation in the troposphere and ozone in the stratosphere/mesosphere which absorbs ultra-violet radiation. The release of latent heat in deep tropospheric convection at tropical latitudes also contributes to the excitation of these tides (e.g., Hagan and Forbes, 2003). There also exist non-migrating (non-sun-synchronous) tides. These non-migrating tides can be excited by a number of mechanisms, including longitudinal differences in tropospheric radiative heating and tropospheric latent heat release (e.g., Williams and Avery, 1996; Hagan and Forbes, 2003; Zhang et al., 2010) and non-linear interaction between migrating tidal modes and planetary waves (e.g., Oberheide et al., 2002).

Observations have revealed the largest amplitude tidal modes to have periods of 24, 12 and 8 hours. These are the diurnal, semidiurnal and terdiurnal tides. At tropical latitudes, the diurnal tide tends to dominate. At middle and high latitudes, the semidiurnal tide tends to dominate. The terdiurnal tide generally reaches smaller amplitudes, but can nevertheless be significant (e.g., Teitelbaum et al., 1989; Younger et al., 2002; Du and Ward, 2010).

Atmospheric tides play an important role in the coupling and dynamics of the atmosphere. In particular, the tides transport momentum and can deposit it at heights above the tidal source region, thus contributing to the wave-driving of the middle atmosphere (e.g., Miyahara et al., 1993; Lieberman and Hays, 1994). The wind and temperature perturbations of tides can act to filter the field of ascending gravity waves and so modulate gravity-wave fluxes of energy and momentum (e.g., Fritts and Vincent, 1987;

Beldon and Mitchell, 2010). Non-linear interactions between tides and planetary waves can generate planetary-scale secondary waves which are thought to play a key role in tidal variability and impose a modulation on tidal amplitudes at planetary-wave periods (e.g., Beard et al., 1999; Chang et al., 2011; Forbes and Moudden, 2012). Additionally, short-term tidal variability may result from the refractive effects of planetary waves (e.g., Riggin et al., 2003). Tides are believed to be an important source of variability of polar mesospheric clouds, where the tidal perturbations of temperature influence the ice crystal population of the clouds (e.g., Chu et al., 2001; Fiedler et al., 2005). Tides are also believed to be important agents in the coupling of the atmosphere and the ionosphere (e.g., Immel et al., 2006; Pedatella et al., 2012).

However, despite the recognised importance of tides, many uncertainties remain about their excitation, interaction with other tides and waves, their variability on timescales from a few days to the interannual and their role in coupling the middle and upper atmosphere. Advances in general circulation models (GCMs) have allowed tides in the MLT to be represented, but significant differences often remain between the predictions of GCMs and observations. A critical task, therefore, is to use observations of tides to constrain their representation in GCMs. Ground-based meteor and MF radars are well suited to observations of tides in the MLT. In particular, the radars offer excellent time resolution of the order of a few hours and so can investigate tidal variability on short timescales. The radars are able to operate for extended intervals and so can also investigate the seasonal and interannual variability of tides. These observations provide a powerful complimentary technique to satellite observations which can investigate zonal wave-numbers etc., but lack the good time resolution offered by the ground-based measurements. In this study we will exploit the capabilities of radars to make extended measurements to investigate the tides of the tropical MLT region.

Tides in the MLT region have been reasonably well characterised at the high and middle latitudes (e.g., Manson et al., 1988; Vincent et al., 1988; Manson et al., 1989; Avery et al., 1989; Portnyagin et al., 1993; Fraser et al., 1995; Mitchell et al., 2002; Manson et al., 2009). At these latitudes the diurnal tidal modes are predominantly trapped and so in the MLT region the semidiurnal tide has larger amplitudes.

However, classical tidal theory predicts that diurnal modes are free to propagate upwards at latitudes equatorwards of $\sim 30^{o}$ (e.g., Lindzen, 1967; Lindzen and Chapman, 1969). We would thus expect the tropical MLT to be dominated by large-amplitude diurnal tides.

In contrast to the situation at middle and high latitudes there have been relatively few radar studies in the tropical regions. Kumar et al. (2008) reported results from one year of meteor radar observations at Trivandrum (8.5^{o}N, 77^{o}E). They focused on short-term variability and used bispectral analysis to find evidence of tidal/planetary-wave interactions. Sridharan et al. (2010) investigated 15 years of MF radar winds and tides at Tirunelveli (9^{o}N, 78^{o}E) and examined correlations with the solar cycle, Quasi-Biennial Oscillation (QBO) and the El Niño Southern Oscillation (ENSO). Chang and Avery (1997) reported the results from five years of meteor radar observations made at Christmas Island (2^{o}N, 158^{o}W). Buriti et al. (2008) reported results from one year of meteor radar observations made at Cariri (7.4^{o}S, 36.5^{o}W). The results from this location are particularly interesting because it is at a similar

latitude to Ascension Island but displaced by approximately 22° westwards.

Tsuda et al. (1999) compared diurnal tide radar results between three equatorial sites and found good agreement between Jakarta (6°S, 107°E) and Pontianak (0°N, 109°W) but significant discrepancies with Christmas Island (2°N, 158°W). Friedman et al. (2009) compared the semidiurnal components at Arecibo (18°N, 67°W) and Maui (21°N, 186°W) as measured by LiDAR with the satellite results from SABER and found that local effects create amplitude perturbations that were missed by SABER's temporal averaging and geographic sampling.

A number of studies have reported strong interannual variability of tidal amplitudes (e.g., Fritts and Isler, 1994; Burrage et al., 1995; Vincent et al., 1998). Some of these studies have suggested that the stratospheric QBO acts to modulate tidal amplitudes in the MLT region. For example, Vincent et al. (1998) compared observations made by radar at Adelaide (35°S, 138°E), Kauai (22°N, 160°W) and Christmas Island (2°N, 158°W) and found strong evidence that higher diurnal tidal amplitudes occur over Adelaide when the QBO is in its eastwards phase. However, the correlation at the other sites was less convincing, possibly as a result of the shorter datasets made at those sites. Gurubaran et al. (2009) similarly found no trace of QBO signatures in tidal amplitudes over Kauai, but found strong QBO signals in tidal amplitudes over Tirunelveli (8.7°N, 77.8°E). Xu et al. (2009a) used SABER observations of the diurnal tide to suggest that its amplitudes are modulated by the QBO. Wu et al. (2011) considered TIDI observations and reported that the semidiurnal response to the QBO was much smaller than the response of the diurnal tide.

Modelling studies of tides have made considerable progress in recent years, and a number of studies have compared observations with model results (e.g., Burrage et al., 1995; Fraser et al., 1995; Chang and Avery, 1997; Mitchell et al., 2002; Andrioli et al., 2009; Manson et al., 1999).

Note that at any one point on the Earth the observed tides will be a superposition of various migrating and non-migrating modes, perhaps resulting in significant longitudinal variability. To obtain realistic predictions of tidal amplitudes and phases for a single site, models must therefore reproduce the major migrating and non-migrating tidal components. Comparisons with single-site observations are thus a demanding but very useful test of the representations of tides in models and essential to guide future model development (e.g., Ward et al., 2010).

This study presents results from a meteor radar deployed on Ascension Island (8°S, 14°W) in the tropical mid-Atlantic sector. Here we report observations of the diurnal and semidiurnal tides in the zonal and meridional winds at heights between 80 - 100 km. These results are compared with the predictions of the eCMAM and WACCM models. The radar began operating in 2001 and so the extended dataset available is particularly suitable for investigating the relationship between tides and the QBO in stratospheric zonal winds.

5.3 Data and Analysis

The wind data used in this study were obtained by a commercially-produced SKiYMET VHF radar located on Ascension Island (7.9^{o}S, 14.4^{o}W). The radar operates in an all-sky configuration. The radio frequency used is 43.5 MHz. Radial velocity measurements inferred from the Doppler-shift of wind-blown meteor-trail echoes are used to derive hourly-mean zonal and meridional winds. The wind measurements are binned into six height gates centred at 80.5, 84.5, 87.5, 90.5, 93.5 and 97.0 km, respectively. The radar began operating in May 2001 and all available data was used in this study.

The hourly horizontal winds recorded by the radar were used to determine tidal parameters. For this investigation, a linear least squares fit was performed which returned the amplitudes and phases of the diurnal, semidiurnal, terdiurnal and quaterdiurnal tides along with the magnitude of the background wind. This was applied to the zonal and meridional winds recorded by the radar. The fits were applied to windows of four-day length, stepped in one-day increments through the time-series of zonal and meridional winds (e.g., Mitchell et al., 2002; Kumar et al., 2008). Each height gate was treated separately and a requirement made that results were only recorded if data was present for more than 70% of the hours within each 4-day window.

The monthly-mean amplitudes and phases of each tidal component within a given month were then calculated by using vector averaging. Note that this method generally produces slightly smaller monthly means than a geometric average because of fluctuations in tidal phase. The results of this analysis are time series of monthly-mean tidal amplitudes and phases in six independent height gates and in zonal and meridional components for the diurnal and semidiurnal tides from October 2001 to June 2011 - albeit with some gaps.

Ascension Island is a demanding environment in which to operate and so the radar has not operated in a continuous manner since deployment. Figure 5.1 presents a schematic diagram illustrating the intervals of time during which the radar was operational from 2001 - 2011. Some height gates may have detected sufficient meteors for winds to be calculated while others recorded too few. There are two large gaps in the data, from October 2003 to May 2004 and May 2007 to March 2009, caused by the radar being off-air for an extended time.

In this study we will make use of two models, eCMAM and WACCM. The extended-CMAM, or eCMAM (Fomichev et al., 2002; Du et al., 2007), extends from the surface to heights of about 210 km. The governing equations are solved in spectral space with triangular truncations at wavenumber 32 (T32), which corresponds to a horizontal grid of approximately 6.0^o x 6.0^o near the equator. The vertical resolution varies from 150 m near the surface to 2 km near the tropopause and 3 km in the regions further above. The geometric heights are calculated from globally-averaged geopotential heights and so are approximations with deviations of up to 5 km possible. Tidal oscillations are self-consistently generated from short- and long-wave radiation absorption, large-scale condensation and convective heating. Non-orographic gravity waves are parameterized using the Doppler-spread parameterization of Hines (1997a,b).

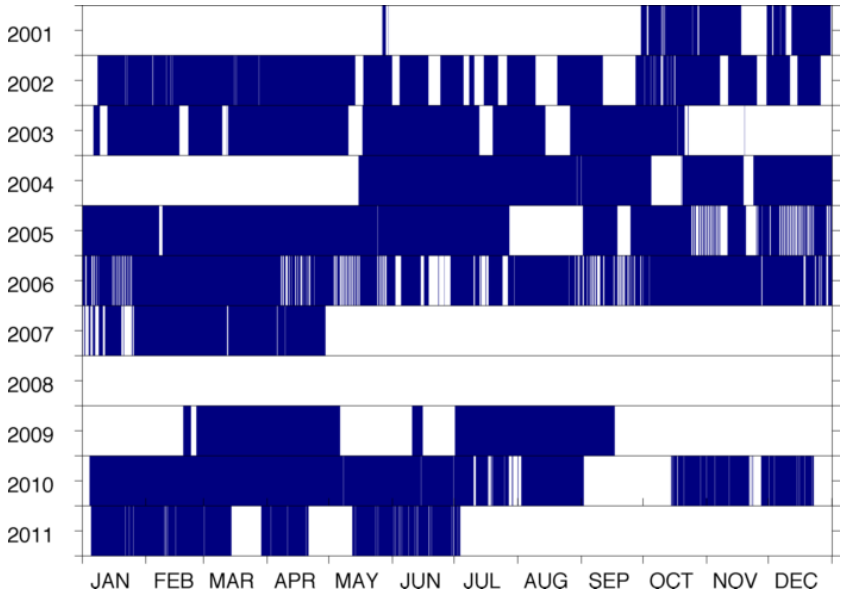

Figure 5.1: Schematic diagram showing when the Ascension Island radar has been operational (blue) and non-operational (white) since deployment in 2001.

The third-year data from a four-year run of the eCMAM is used here. The model sampling time interval was 3 hours. The model output was first converted to time series of complex amplitude for a given wavenumber at each latitude and height by summing over the spherical harmonics associated with wavenumber. These time series were then Fourier analyzed in time to produce the frequencies at a particular wavenumber. The modelled horizontal winds were analyzed to delineate the tides for zonal wavenumber -5 to +5. The tidal results presented here are from the closest grid-point to Ascension Island which is 10^{o}W, 8^{o}S. The data window used was 4-days long, advanced in 2-day increments. The monthly-mean amplitudes and phases of each tide were calculated by using vector averaging in the same manner as the radar analysis. Refer to Du et al. (2007) for more details on this data analysis method.

For the comparisons here, WACCM was run in the specified dynamics mode, referred to as SD-WACCM (Larmarque et al., 2012). Global assimilated meteorological analyses data from 2002 through 2009 were used to constrain WACCM temperature and horizontal winds in the troposphere and stratosphere. The constraint takes the form of nudging by 1% at each time-step over the altitude range from the surface to 50 km and then a decreasing constraint between 50 and 60 km. Above 60 km, WACCM is free running. The data used for the constraints are from MERRA (Modern Era Retrospective Analysis for Research and Applications). Tidal amplitudes and phases in WACCM were calculated daily using model fields with a time step of 0.5 hours. Results from the closest grid-point to Ascension Island (15^{o}W and 8.5^{o}S) were interpolated from pressure to geometric height for comparison with the observations.

5.4 Results

5.4.1 Mean Winds

Figure 5.2 presents zonal and meridional hourly winds from March 2009 as a typical example of the MLT wind field over Ascension Island. The figure reveals a wind field dominated by the diurnal tide. Instantaneous tidal amplitudes can reach values as large as 130 ms^{-1} (e.g. meridional winds at the upper heights on several occasions throughout the month). The amplitudes are usually significantly smaller at the lowest heights. A clear change of phase with height is evident, with phase fronts descending with time corresponding to an upwardly-propagating tide. A high degree of short-term variability is also evident. For instance, meridional tidal amplitudes vary from $\sim$ 130 ms^{-1} at the upper heights on March 14 to only $\sim$ 30 ms^{-1} at the same heights on 28 March.

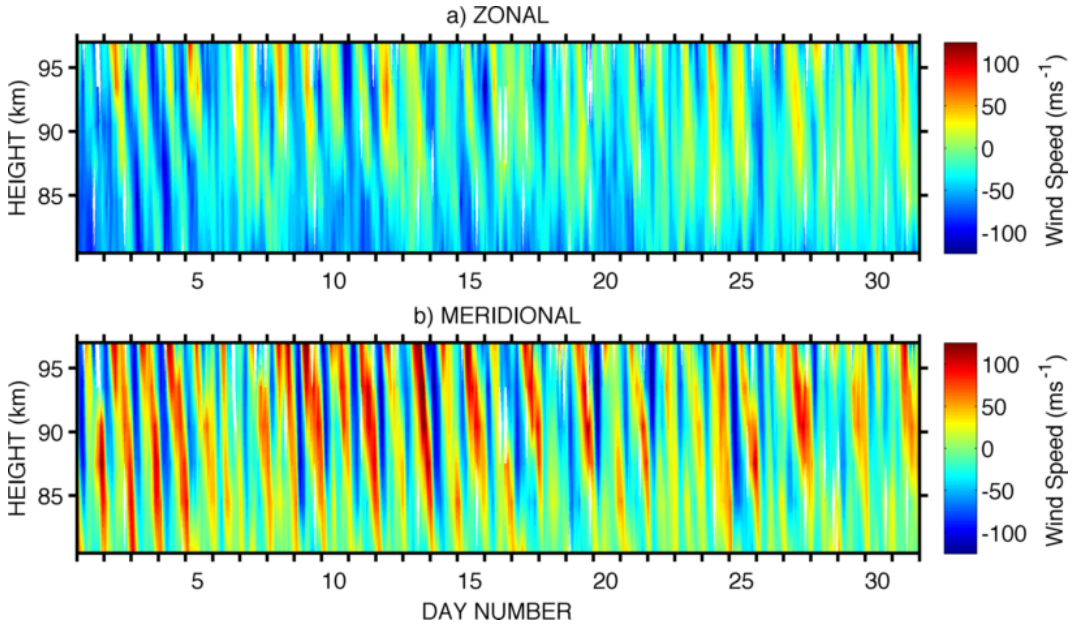

Figure 5.2: Zonal (a) and meridional (b) winds as a function of height and time as recorded by the Ascension Island meteor radar in March 2009. The large-amplitude diurnal tide can clearly be seen in both wind components.

Before we consider the tidal results in detail, we will present the background winds. The composite-year monthly-mean zonal and meridional winds were produced by averaging the mean wind values obtained from the 4-day least square fits, and are presented in Figures 5.3a and 5.3b respectively. In both, the solid line represents the zero-wind line. It can be seen that the zonal winds show the well-known Mesospheric Semiannual Oscillation with the lower four height gates recording predominantly eastward winds at the solstices, and westward winds at the equinoxes. At heights above 93 km however the winds are westward all year. Also of note in the zonal background winds is the strong vertical shear of horizontal wind in the austral winter months. For example, in June and July the wind decreases approximately linearly from around 26 ms^{-1} at heights near 80 km to around -16 ms^{-1} at heights near 97 km.

The meridional windsvary less with height than the zonal winds. An annual oscillation is observed, with

equatorward winds in the austral summer months at all heights, poleward winds in the austral winter months at all heights and minima at the equinoxes. June and July are again the months of strongest vertical wind shear, however the variation is much less pronounced than the zonal case, with the mean wind speed decreasing from approximately -4 ms^{-1} at heights near 80 km to -16 ms^{-1} at heights near 97 km.

Figure 5.4a,b presents Lomb-Scargle periodograms of zonal and meridional winds, respectively, at a height of 94 km calculated using the entire 2001-2011 dataset.

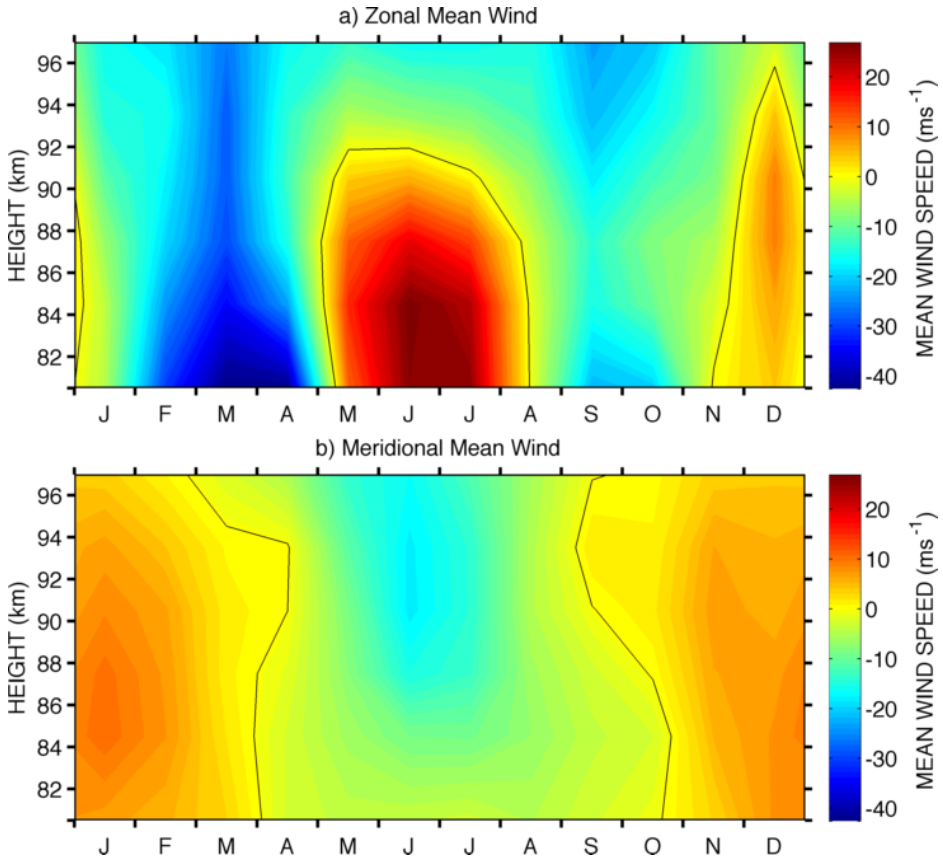

Figure 5.3: Composite-year monthly-mean winds over Ascension Island for the (a) zonal and (b) meridional components for all data recorded from January 2002 to June 2011. The black line represents the zero-wind line.

From the figures it can be seen that there are spectral peaks at frequencies of 1, 2, 3 and 4 cycles per day corresponding to the diurnal, semidiurnal, terdiurnal and quaterdiurnal tides. The figure reveals that the diurnal tide is significantly larger than the other tides. This explains the apparent dominance of the wind field of Figure 5.2 by this tide. In this study we will investigate only the diurnal and semidurnal tides. The terdiurnal tide also reaches significant amplitudes but will be investigated in a follow-on study.

Also clearly evident in the periodograms of Figure 5.4 is a significant oscillation at a frequency of 1.93 cycles per day (corresponding to a period of 12.4 hours). This spectral component is most likely to be the lunar semidiurnal tide. The lunar semidiurnal tide as observed by the Ascension Island radar has

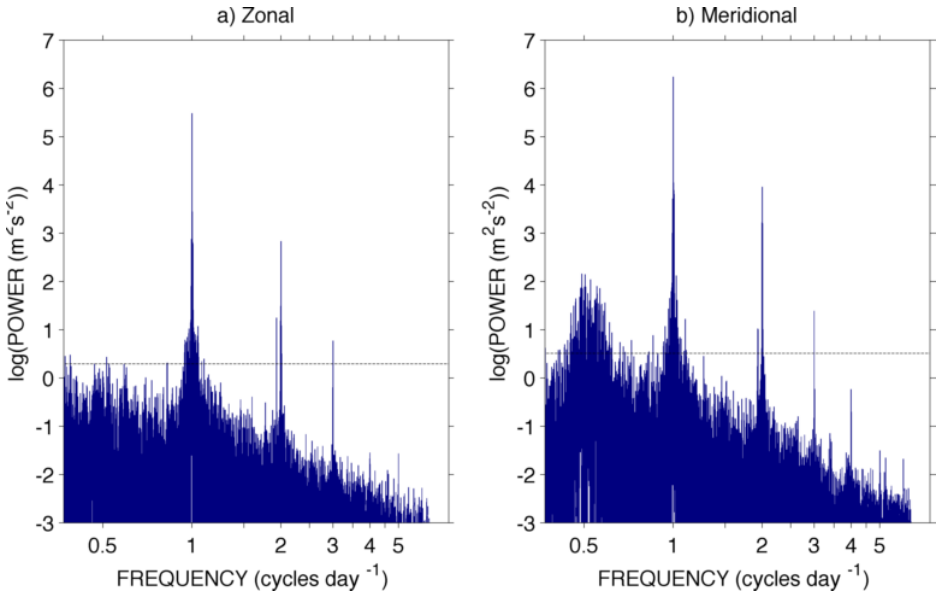

Figure 5.4: Lomb-Scargle periodograms of the (a) zonal and (b) meridional wind components at heights near 94 km for the entire set of Ascension Island data (2002-2011). The horizontal dashed lines show the 95% confidence limit. Note that the strong signal present at 1.93 cycles/day is likely to arise from the lunar semidiurnal tide.

been described by Sandford et al. (2007) and also observed at low latitudes by Paulino et al. (2012). Alternatively, this spectral signature might result from a non-linear interaction between the semidiurnal tide and the 16-day planetary wave where a "difference frequency wave" would occur at a period of 1.938 cycles per day. However, the persistence of this feature in the long-term spectra and its narrow spectral nature strongly supports the interpretation that it is the lunar semidiurnal tide. Also evident in the figure is a broad maxima in power at frequencies around 0.5 cycles per day. This is taken to result from the 2-day planetary wave which produces maximum amplitudes in meridional winds at low latitudes. We will now turn our attention to the diurnal and semidiurnal tides.

5.4.2 Diurnal tide

Amplitudes of the Diurnal Tide

To investigate the seasonal variability of the diurnal and semidiurnal tides, monthly-mean vector averages were calculated from the 4-day least-squares fits as explained in Section 5.3. The monthly vector-mean amplitudes of the diurnal tide in the zonal and meridional wind components are presented as height-time contours in Figure 5.5a,b, respectively. These averages use all available data from January 2002 to June 2011. The diurnal amplitudes in the zonal and meridional components reveal a seasonal cycle. Both components show a semiannual cycle with amplitude maxima at the equinoxes and minima at the solstices. The amplitudes are slightly larger around the austral vernal equinox (September) than the austral autumnal equinox (March). Both zonal and meridional components also show a general increase of amplitude with increasing height. For example, in September amplitudes increase from values

of only a few ms^{-1} to ~ 40 ms^{-1} in the zonal component. However, note that amplitudes do not always increase with height. For example, in the zonal component the amplitudes decrease between the top two height gates in April. In the meridional component during the months of largest diurnal tide (February, March, September and October) the amplitudes often maximised at heights around 90 km.

The meridional diurnal amplitudes are generally slightly larger than the zonal. For example, maximum amplitudes reach 48 ms^{-1} in September's meridional winds compared to 41 ms^{-1} in the zonal.

Note that the monthly-mean vector amplitudes shown in the figure smooth out considerable short-term variability. Instantaneous tidal amplitude values can be significantly greater or smaller than these averages (e.g. see Figure 5.2).

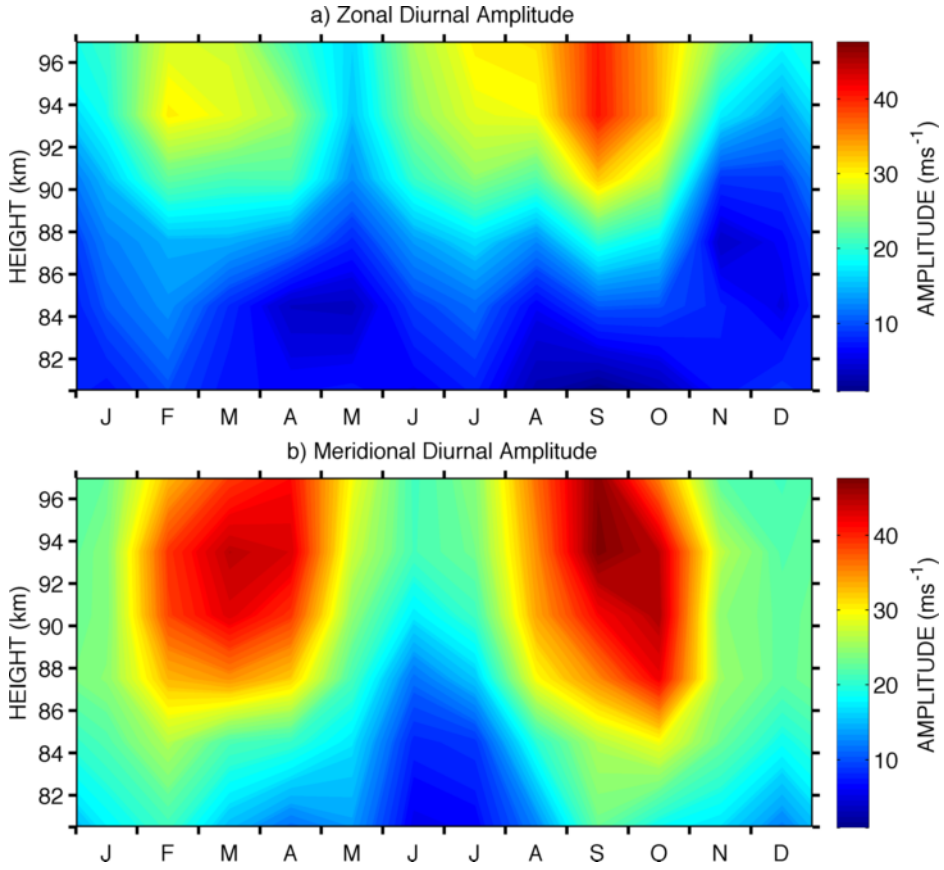

Figure 5.5: Composite-year monthly-mean diurnal tidal amplitudes as a function of month and height over Ascension Island for all data recorded from January 2002 to June 2011.

The data presented in Figure 5.5 are presented in Figure 5.6 in the form of line plots to enable easier comparison with the model results and to allow the variability of the monthly values of each height gate to be represented. The standard errors on the means of the composite-monthly mean amplitudes and phases were calculated by dividing the standard deviation of all the 4-day least-square fit values within a month by the square root of the number of values included. These errors thus include both the systematic error and also the natural inter-monthly variation in tidal parameters. The standard errors on the means are generally small, for example they were 1.1 ms^{-1} (amplitude) and 0.3 hours (phase)

in December 2002, and when averaged over all included months and years the standard-errors on the monthly means were found to be 1.3 ms^{-1} and 0.4 hours. The "error bars" presented on the plot are the standard deviations of monthly averages and so give a measure of the interannual variability.

The meridional and zonal amplitudes from the radar observations are plotted in Figures 5.6a and 5.6b respectively. Also presented are the amplitudes predicted by eCMAM and WACCM. These figures confirm the impression given by the height-time contours of Figure 5.5 and show that the meridional amplitudes are systematically and significantly larger than the zonal amplitudes in most months. Only in winter (June and July) are the zonal and meridional amplitudes approximately similar. Again, largest amplitudes occur around the equinoxes and smallest amplitudes around the solstices.

Considering the monthly-mean amplitudes predicted by eCMAM, it can be seen that the model predicts significantly larger meridional amplitudes than are observed for most months and particularly from November to March. In January to March eCMAM amplitudes reach up to 75 ms^{-1}, compared to observed amplitudes of less than 45 ms^{-1} (note that the x-axis in the figure has been limited to allow comparison between months and to better present the other data sets). Agreement tends to be better for the zonal component, however the model again predicts much greater amplitudes than are observed above heights of $\sim$ 90 km in April, May and October.

Considering the monthly-mean amplitudes predicted by WACCM, it can be seen that the model generally predicts smaller amplitudes than are observed in both zonal and meridional components for most months and heights. This is particularly noticeable in the austral winter/spring months (May - October) when the diurnal amplitudes predicted by WACCM are significantly smaller than observed (sometimes by tens of ms^{-1}) and often do not grow with height as rapidly as the observed amplitudes do. The WACCM predictions do, however, reproduce the observed trend of larger diurnal amplitudes in the meridional component than in the zonal, except for May and June when amplitudes are similar in both components for both the model and the observations.

Phases of the Diurnal Tide

The linear least-squares fit also returns the phases (the hours of peak amplitude) of the fitted tides. The monthly-mean phases of the diurnal tide are presented as line plots in Figure 5.7. As with the corresponding amplitude figure (Figure 5.6), the observed phases and model predictions are all shown on the same set of axes for each month. Again, the "error bars" on the plot are the standard deviations of monthly averages and so give a measure of the interannual variability.

The phases as observed over Ascension Island generally show a smooth decrease with increasing height, corresponding to upwardly-propagating tides. There are, however, some exceptions. Those exceptions that do occur are between the lowest two height gates in the austral winter months (July and August) where the amplitudes are small and phases thus harder to define. Excluding the lowest height gates in these months of small tidal amplitude, the zonal phases were found to lead the meridional phases by an average of $\sim$ 6.5 hours, indicating a quadrature relationship.

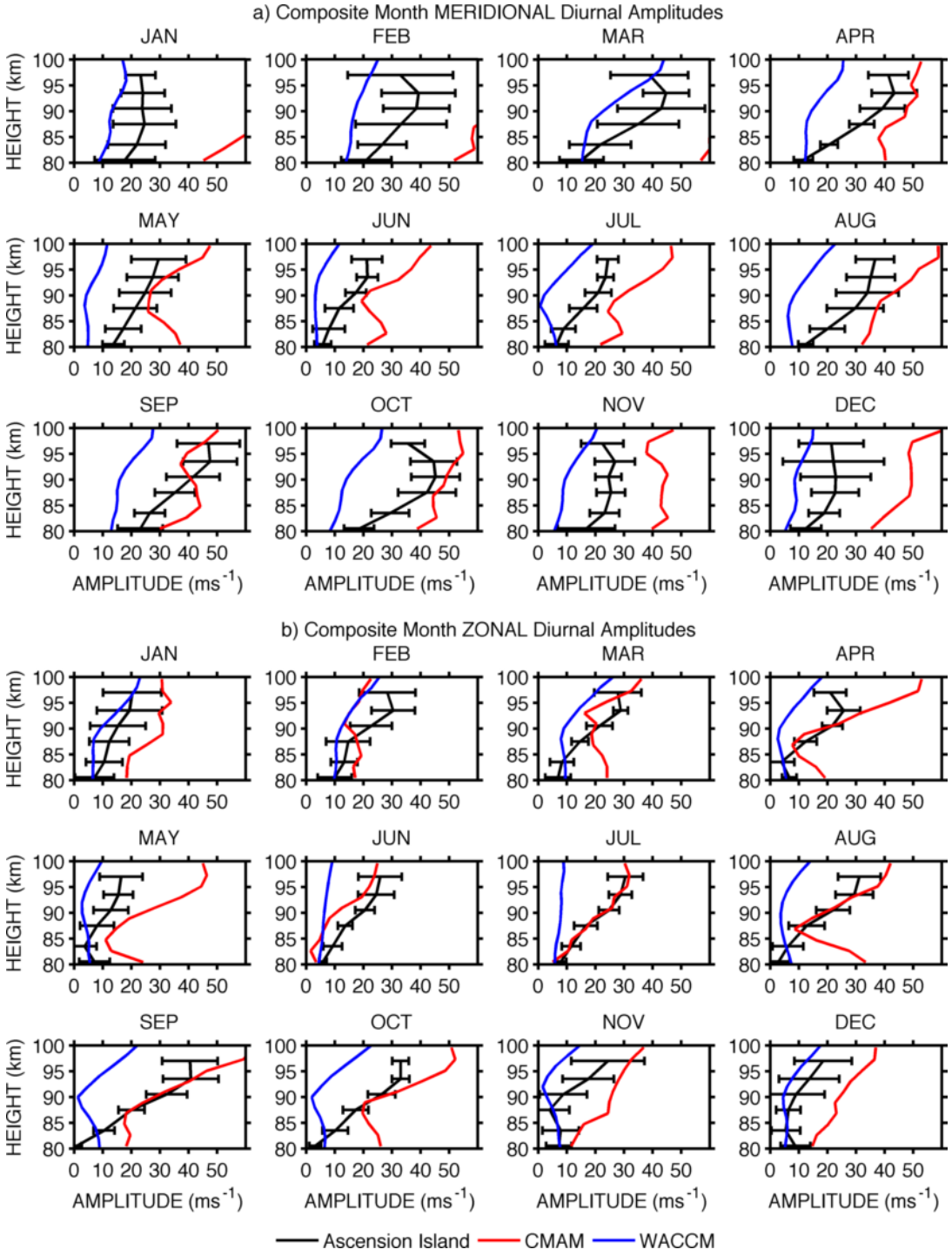

Figure 5.6: Amplitudes of the a) meridional and b) zonal diurnal tide as a function of month and height. The error bars on the radar observations (black lines) indicate the standard deviation of the individual monthly means over the interval 2002 - 2011. Also plotted are the predictions of eCMAM (red lines) and WACCM (blue lines).

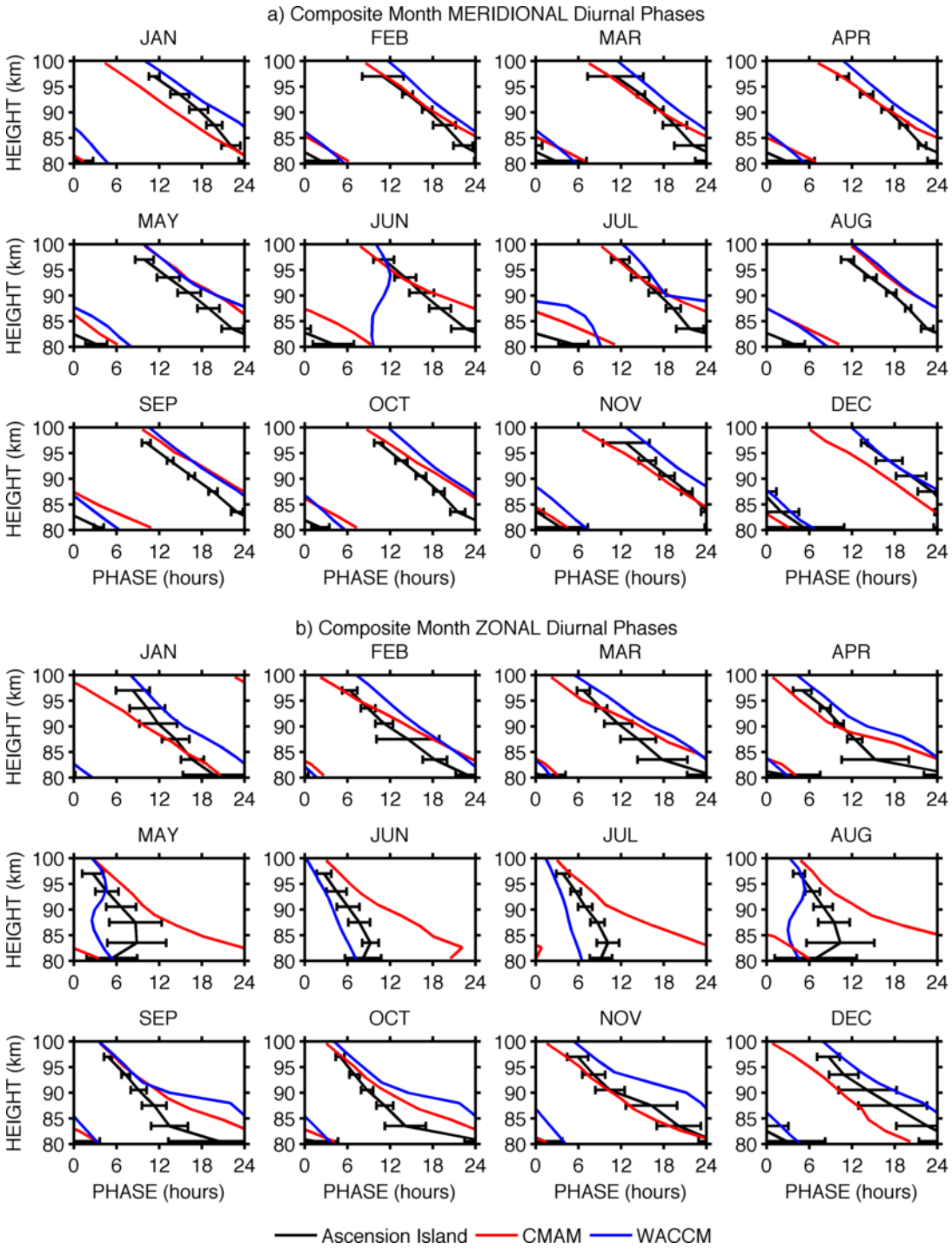

Figure 5.7: Phases of the a) meridional and b) zonal diurnal tide as a function of month and height. The error bars on the radar observations (black lines) indicate the standard deviation of the individual monthly means over the interval 2002 - 2011. Also plotted are the predictions of eCMAM (red lines) and WACCM (blue lines).

The phases of the diurnal tide as predicted by eCMAM are similar to the radar observations for both meridional and zonal components for most months. The phases predicted by WACCM are also similar to the radar observations for both meridional and zonal components for most months.

Straight-line least-squares fits to the observed phases as a function of height were used to calculate the vertical wavelengths of the tides as an average over the 80 - 100 km height interval. These are presented in Table 6.1. Note that the vertical wavelengths are calculated across all six height gates as an average and thus local changes in vertical wavelength arising from different tidal modes dominating at different heights are not distinguished. The average vertical wavelengths do however provide a more useful test of the models' ability to reproduce the different modes over one location than the absolute differences in phase.

The zonal vertical wavelengths have values between 20 and 30 km from September through to April (excepting January). However, the vertical wavelengths increase significantly in the winter months from May to August, where the values increase to be between 64 and 111 km. Note that these larger vertical wavelengths in winter result mostly from a reduction in phase hour in the lowest two height gates. Were the phase to be calculated from the May - August data only above heights of 85 km, the vertical wavelengths would be shorter, though still longer than the rest of the year. For example, in May the vertical wavelength calculated above 85 km has a value of 38 ± 1 km. The meridional vertical wavelengths are very consistent throughout the year with values ranging only from 24 to 30 km. There is no sign of the increase to larger values evident in the zonal results during winter.

Also presented in Table 6.1 are the vertical wavelengths derived from the phases predicted by the models. The eCMAM zonal vertical wavelengths are shorter than the observations for every month except November and December. They do however agree within the uncertainty limits for the months of April, October and November. Differences of more than 40 km are evident in May to August (Austral winter), months during which the measured vertical wavelengths can greatly exceed those predicted by eCMAM. However, we note that the large zonal vertical wavelengths measured by the radar data in May to August result from the tidal phase having smaller values at the lower height gates yielding a more vertical straight-line fit. If we were to consider data from heights above 85 km only, then the vertical wavelengths would in fact be significantly shorter, ranging from 28 to 47 km. It is interesting to note that other ground-based studies have also observed tidal phase which increases with height at heights near 80 km (e.g., Tsuda et al., 1999; Buriti et al., 2008; Vincent et al., 1998). Considering the meridional wavelengths presented in Table 6.1, it can be seen that both observations and eCMAM indicate vertical wavelengths to be between 17 and 30 km for all months. The meridional wavelengths predicted by the model are again shorter than those observed, averaging 20 km c.f. 26 km respectively.

The WACCM vertical wavelengths are generally in good agreement with the observations. They agree to within the bars representing the interannual variability for all months except January, May, June, August and September in the zonal component. In the meridional component, they agree to within the uncertainty limits for all months except January, June, July and August. Excluding the months with vertical wavelengths of magnitude ≥ 100 km, the zonal vertical wavelengths predicted by WACCM are

Table 5.1: Table of the mean diurnal tide vertical wavelengths (km) as observed by the Ascension Island radar (AI) for each month, and the values predicted by eCMAM and WACCM.

	Zonal λ_z (km)			Meridional λ_z (km)		
	AI	eCMAM	WACCM	AI	eCMAM	WACCM
January	35 ± 1	21 ± 1	21 ± 1	30 ± 1	22 ± 1	25 ± 1
February	24 ± 1	18 ± 1	25 ± 1	27 ± 1	21 ± 1	25 ± 1
March	23 ± 3	17 ± 1	25 ± 1	27 ± 1	20 ± 1	26 ± 1
April	21 ± 5	16 ± 2	22 ± 1	26 ± 1	20 ± 1	26 ± 1
May	100 ± 15	19 ± 2	19 ± 1	24 ± 1	23 ± 1	25 ± 1
June	64 ± 4	23 ± 1	>100	25 ± 2	17 ± 1	20 ± 1
July	66 ± 4	19 ± 2	69 ± 1	25 ± 3	17 ± 1	$<$-100
August	>100	17 ± 2	98 ± 1	26 ± 2	21 ± 1	19 ± 2
September	28 ± 3	19 ± 2	$<$-100	24 ± 1	18 ± 1	23 ± 1
October	22 ± 5	18 ± 2	17 ± 2	26 ± 1	20 ± 1	24 ± 1
November	20 ± 2	21 ± 1	18 ± 2	27 ± 1	21 ± 1	26 ± 1
December	21 ± 1	26 ± 1	19 ± 2	26 ± 1	22 ± 1	25 ± 1

slightly shorter on average than those observed, 27 km c.f. 29 km, respectively. This is also true for the meridional component, with the WACCM-predicted vertical wavelengths being slightly shorter on average than those observed, 24 c.f. 26 km, respectively.

The "error bars" on Figure 5.7 are again the standard deviations of monthly means and thus represent the interannual variability. It can be seen that in many months there is actually only a small variation in phase from year to year, indicated by the small error bars. The tidal phases thus appear to repeat from year to year with little variation. The largest standard deviations on the monthly phases tend to be in the zonal component in the lower height gates, possibly due to the corresponding amplitudes being somewhat lower and the phases thus harder to define.

5.4.3 Semidiurnal Tide

Amplitudes of the Semidiurnal Tide

A similar analysis to the above was applied for the semidiurnal tide. The monthly-mean vector-averaged amplitudes of the semidiurnal tide in the zonal and meridional wind components are presented in Figure 5.8a,b, respectively. The semidiurnal amplitudes are significantly smaller than the diurnal amplitudes, typically reaching values of only 25% of the diurnal amplitudes (when averaged across all heights and months). In contrast to the diurnal tide, there is a significant difference between the amplitudes of the zonal and meridional components. The meridional amplitudes are generally larger and reach peak values of around 25 ms^{-1}, compared to zonal amplitudes of up to around 14 ms^{-1}. With the exception of January, the meridional amplitudes are generally about a factor of 3 larger than the zonal amplitudes.

As with the diurnal tide, a strong seasonal variability is apparent. Up to heights of about 90 km, tidal amplitudes exhibit two relatively short-lived maxima, one in April (autumn) and one in October (spring). At heights above 90 km the seasonal variability becomes more complicated with a weaker maximum in amplitude becoming evident in the winter months (June - August). Note also that the zonal amplitudes reach large values around the summer solstice (January) at the upper heights.

A semiannual variability is also evident in the meridional component of the semidiurnal tide amplitudes. Maximum amplitudes occur in March/April and October. A distinct amplitude minimum occurs around the austral summer solstice (December - January) at all heights. A secondary amplitude minimum occurs in the lower height gates around the austral winter solstice (June - July).

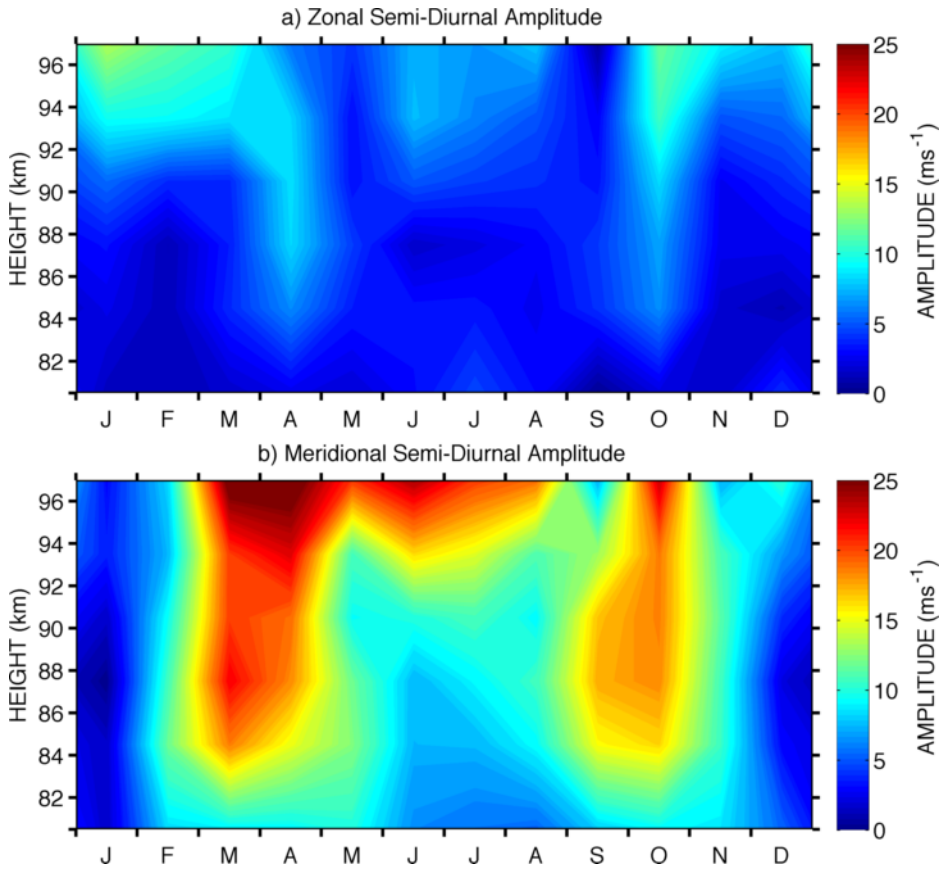

Figure 5.8: Composite-year monthly-mean semidiurnal tidal amplitudes as a function of month and height over Ascension Island for all data recorded from January 2002 to June 2011.

As with the diurnal amplitudes, the data presented in Figure 5.8 are presented in Figure 5.9 as line plots to enable easier comparison with the model results and to show the interannual variability as indicated by the error bars. For each month the amplitude observations are shown on the same set of axes as the predictions of eCMAM and WACCM.

Considering the monthly-mean amplitudes predicted by eCMAM, it can be seen that there is generally excellent agreement between the predicted amplitudes and the radar observations for the zonal components, except for the month of March when predicted amplitudes are up to 15 ms^{-1} greater than observed

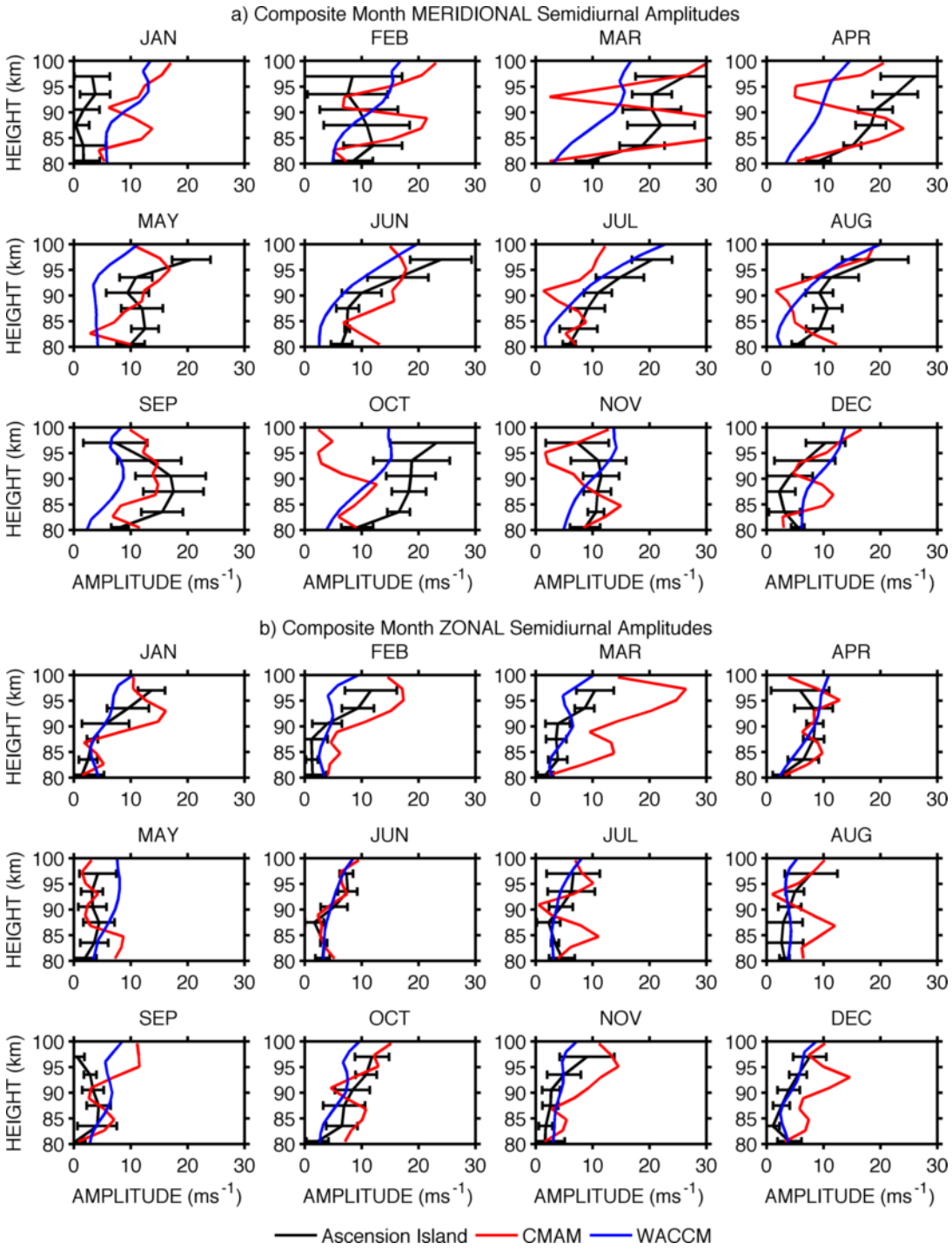

Figure 5.9: Amplitudes of the a) meridional and b) zonal semidiurnal tide as a function of month and height. The error bars on the radar observations (black lines) indicate the standard deviation of the individual monthly means over the interval 2002 - 2011. Also plotted are the predictions of eCMAM (red lines) and WACCM (blue lines).

amplitudes. In many months, the model predictions lie within the error bars of the observations, at least in some height gates. In the meridional component, agreement is good for most heights in May to September, November and December. eCMAM predicts much smaller amplitudes than are observed in October, and amplitudes to vary much more as a function of height than is observed in February, March and April.

Considering the monthly-mean amplitudes predicted by WACCM, it can be seen that there is generally excellent agreement with the observations in the zonal component, for nearly all months and heights. In the meridional component there is often good agreement, but the model tends to underestimate the amplitudes in March, April, May and September.

Phases of the Semidiurnal Tide

The monthly vector-mean phases of the semidiurnal tide are presented as line plots in Figure 5.10. Again, the observations and the model results are all shown on the same set of axes for each month to enable easier comparisons.

It can be seen that there is a clear annual variation in the zonal phases especially in the lower height gates (around 80 - 90 km) with a maximum of approximately 10:00 LT in the summer months and a minimum of $\sim$ 05:00 LT (or 17:00 LT) in the winter. In the meridional component, there is an annual oscillation in the upper height gates (90 - 100 km) with a maximum in the winter months and a minimum in the summer, but in the lower height gates the phase stays constant at $\sim$10:00 LT throughout the year.

Phases in the zonal component generally decrease with increasing height (i.e., downward phase propagation indicating upwards energy flux) in the austral winter months, but are more constant with height in the summer. In contrast, the phases in the meridional component generally decreases with increasing height in the austral summer months, but are more constant with height in the winter.

During the Austral winter months the meridional phases are approximately constant with height, corresponding to very large vertical wavelengths indicating an evanescent semidiurnal tide. The semidiurnal vertical wavelengths calculated from least-squares straight line fits to the phases are presented in Table 5.2. The semidiurnal vertical wavelengths are found in both wind components to be much longer and with greater month-to-month variability than the diurnal vertical wavelengths.

Considering the monthly-mean semidiurnal phases predicted by eCMAM and the vertical wavelengths that are calculated from them, it can be seen that there is less agreement with the observations than was the case for the diurnal tide. The vertical wavelengths predicted by eCMAM only agree within the uncertainty limits with those observed by the radar for two months for the zonal component, and none for the meridional component. Generally, eCMAM tends to predict shorter vertical wavelengths than are observed.

Considering the monthly-mean semidiurnal phases predicted by WACCM and the vertical wavelengths that are calculated from them, it can again be seen that there is less agreement with the observations

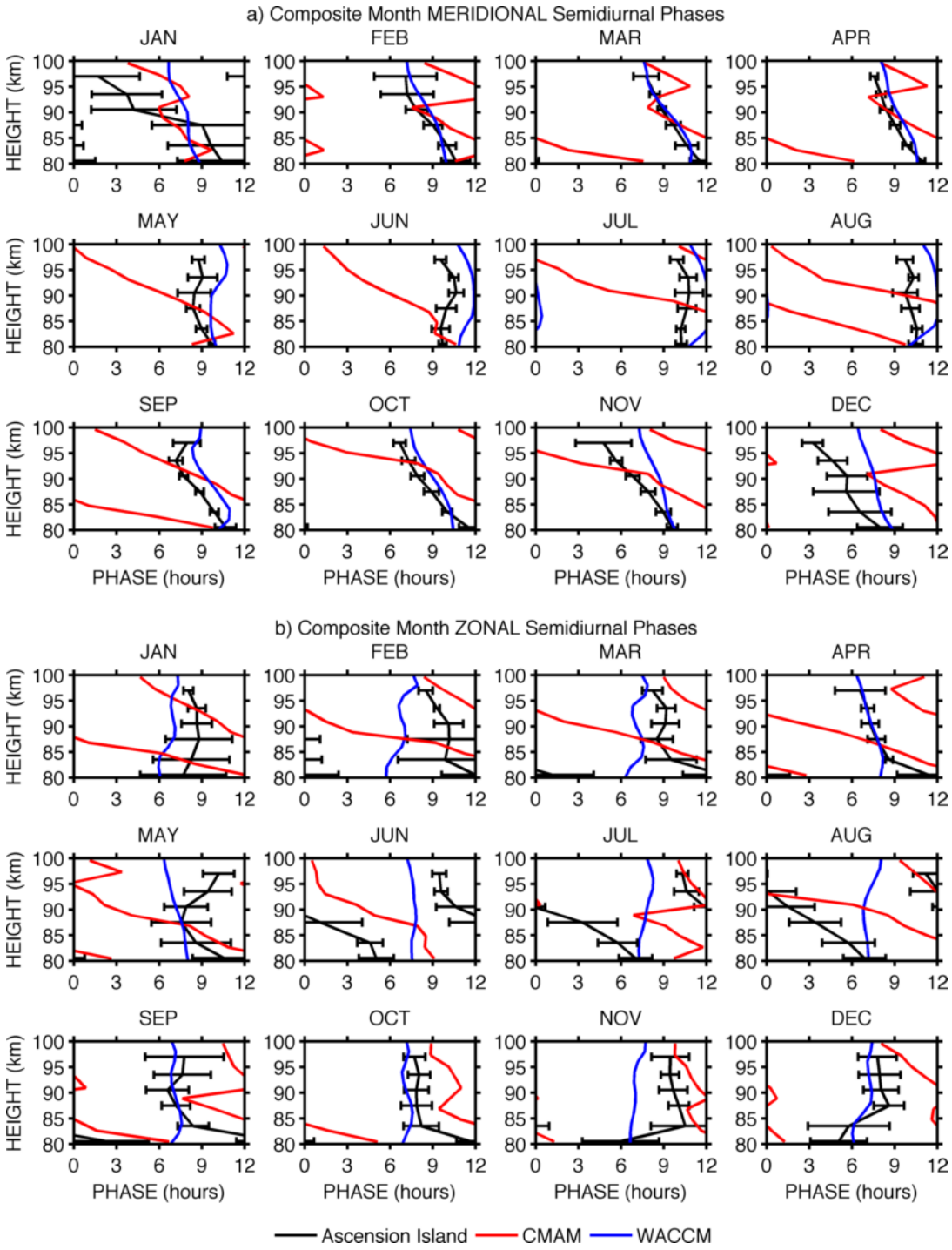

Figure 5.10: Phases of the a) meridional and b) zonal semidiurnal tide as a function of month and height. The error bars on the radar observations (black lines) indicate the standard deviation of the individual monthly means over the interval 2002 - 2011. Also plotted are the predictions of eCMAM (red lines) and WACCM (blue lines).

Table 5.2: Table of the mean semidiurnal tide vertical wavelengths (km) as observed by the Ascension Island radar (AI) for each month, and the values predicted by eCMAM and WACCM.

	Zonal λ_z (km)			Meridional λ_z (km)		
	AI	eCMAM	WACCM	AI	eCMAM	WACCM
January	<-100	12 ± 1	<-100	21 ± 2	66 ± 4	>100
February	73 ± 3	10 ± 1	<-100	51 ± 1	>100	>100
March	54 ± 5	11 ± 1	<-100	52 ± 1	27 ± 3	76 ± 1
April	47 ± 3	13 ± 1	<-100	60 ± 1	30 ± 4	61 ± 1
May	<-100	17 ± 2	>100	>100	20 ± 2	84 ± 1
June	22 ± 2	22 ± 1	>100	<-100	23 ± 1	<-100
July	20 ± 1	<-100	>100	<-100	10 ± 1	<-100
August	24 ± 1	11 ± 1	<-100	>100	10 ± 1	>100
September	39 ± 7	49 ± 7	<-100	61 ± 3	12 ± 1	<-100
October	68 ± 6	38 ± 3	>100	42 ± 1	11 ± 1	97 ± 2
November	<-100	89 ± 3	>100	39 ± 1	12 ± 1	68 ± 1
December	-69 $\pm$ 5	54 ± 2	<-100	99 ± 10	67 ± 2	-92 $\pm$ 1

than there was for the diurnal tide. There is good agreement for some months however. WACCM generally predicts much longer vertical wavelengths than are observed in the zonal component. WACCM also often predicts long vertical wavelengths in the meridional component. However, these WACCM predictions are closer to the observations in April, September, October and December.

5.4.4 Effects of the QBO

To investigate whether or not the phase of the QBO has any affect on diurnal-tidal amplitudes, the monthly-mean zonal winds as measured by radiosonde at Singapore were used to define the phase of the QBO (this data is available from the Institute of Meteorology, Freie Universität Berlin website). The mesospheric tidal amplitude observations were binned into two sets according to the phase (eastward or westward) of the QBO at 10 hPa and composite months then made. The result of this analysis is two composite-years of tidal amplitudes, one for when the QBO was eastward and one for westward. The result for the meridional component of the diurnal tide is shown in Figure 5.11.

The figure shows a pronounced effect in which greater amplitudes occur during the eastwards QBO phases than during the westwards QBO phases. For instance, the months February, March and October show an increase in average meridional amplitudes of over 12 ms^{-1} at all heights when the QBO phase is eastward compared to when it is westward. The largest difference in tidal amplitude between eastward and westward phase of the QBO occurs in the top height gate during February when the difference is around 30 ms^{-1}. The effect of the QBO phase is smaller for the September equinox than the March equinox, for example, at heights near 87 km in March the diurnal amplitudes increase by approximately 50% from Westward to Eastward QBO phase, while in September at the same height the increase is only around 10%. The affect of the QBO is smaller still for the months of smaller mean amplitude (e.g., at the solstices). Note that while December appears to show an increase in amplitude occurring during

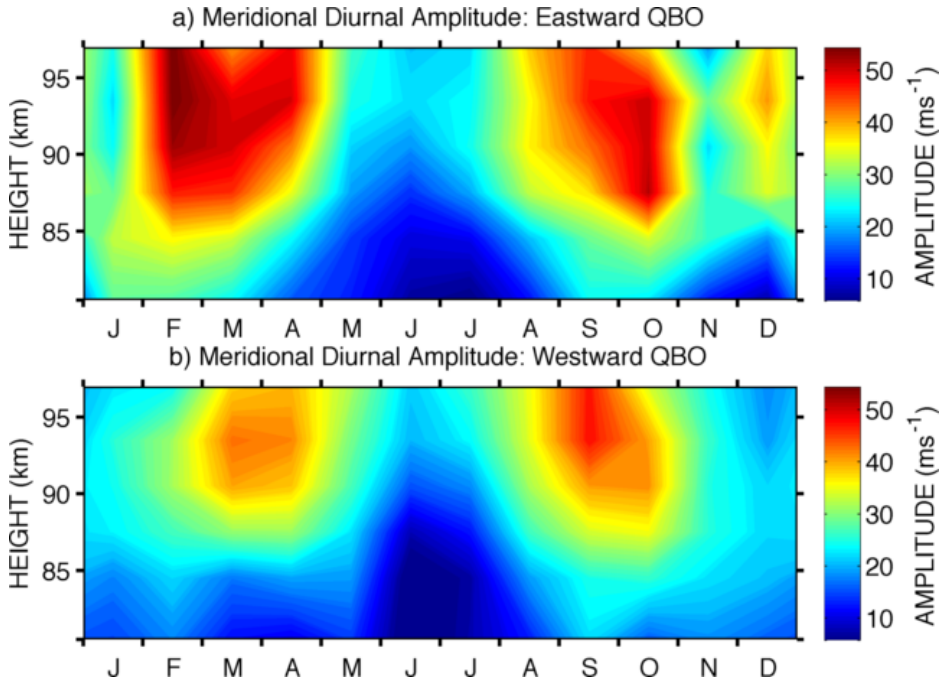

Figure 5.11: Diurnal tidal amplitudes as a function of month and height for eastward (upper) and westward (lower) QBO phase defined at 10 hPa.

eastward QBO phase, there are in fact only two years of observations in December during eastward QBO phases and so this result may not be significant.

To further investigate the effect of the QBO phase on diurnal tidal amplitudes, the composite-year monthly-mean amplitudes were subtracted from each individual monthly amplitude for the entire dataset. This removes the dominant semiannual variation in the tidal amplitudes and yields a dataset of perturbations around the annual-mean amplitude behaviour. The results of this analysis for the meridional component at heights near 84 km for the interval 2002 - 2011 are plotted in Figure 5.12. The QBO wind speed at 15 hPa (from the Singapore radiosonde data) is plotted on the same figure. The tidal-amplitude perturbations and mean winds at 15 hPa in this figure have been smoothed using a seven-month running mean to remove short-term fluctuations. The results were only plotted when at least four months of tidal amplitudes were present within each running-mean window, with the missing months set to the mean of the remaining months. Further, recall that monthly-mean tidal amplitudes were only calculated in cases where winds were available for 40% or more of the hours within a particular month.

Good correlation between the two time series in the figure can be seen by eye, with larger-than-average meridional diurnal amplitudes (positive perturbations) occurring when the QBO winds are eastward, and smaller-than-average meridional diurnal amplitudes when the QBO winds are westward. The correlation coefficient between meridional diurnal tidal-amplitude perturbation and the QBO winds for this height gate is 0.72. Note however that strong correlation does not imply causality.

This analysis was repeated such that correlations between amplitude perturbations and QBO winds were obtained for all six radar height gates and for all available pressure levels of QBO winds (between 10

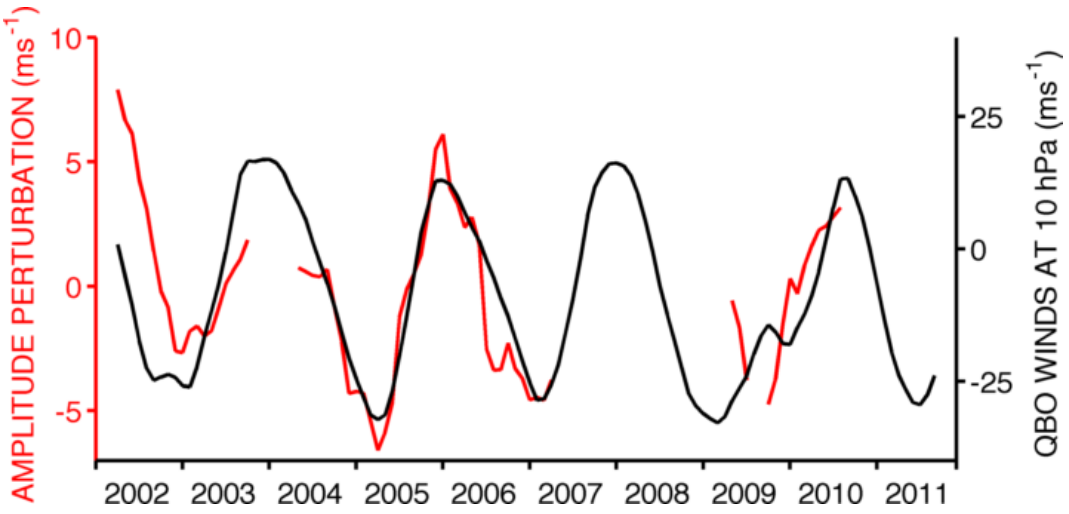

Figure 5.12: Perturbations in meridional diurnal tide amplitudes (calculated by subtracting the composite-year monthly mean from each individual month) at heights near 84 km for 2002 - 2011 over Ascension Island (red line). Also plotted are the QBO background winds at 15 hPa (black line). The diurnal-tidal amplitude perturbations and background winds are smoothed with a seven-month running mean. Note the two different axes, with the red axis on the left corresponding to the diurnal amplitude perturbations and the black axis on the right corresponding to the QBO line.

and 50 hPa in the Singapore radiosonde dataset). These correlations are plotted as a function of height and QBO pressure level in Figure 5.13.

It can be seen that the meridional diurnal amplitude perturbations at all heights are strongly and positively correlated with QBO winds at pressure levels between 10-15 hPa, that there is no correlation with QBO winds defined at around 30 hPa and that there is strong anti-correlation with QBO winds defined at 50hPa.

To identify the pressure level in the QBO which correlates most strongly with the variability of the mesospheric tides, we calculated the average of the correlations across all radar height gates for each QBO pressure level. This yielded a maximum mean correlation coefficient of 0.58 between meridional diurnal tidal amplitude perturbations and the QBO winds at 10 hPa. This is above the 99% confidence level and indicates a strong tendency for larger meridional diurnal tidal amplitudes to occur during the eastward phase of the stratospheric QBO at 10 hPa.

This correlation analysis between tidal amplitudes and QBO winds was repeated for the diurnal zonal amplitudes and semidiurnal meridional and zonal amplitudes. These analyses gave mean correlations of 0.21 (at 10 hPa), 0.37 (at 10 hPa) and 0.40 (at 20 hPa), respectively. The bracketed number indicates the QBO pressure level at which highest correlation was obtained for that particular tidal component.

These results appear to indicate a clear connection between the amplitude of certain components of the tropical tide in the upper mesosphere and the phase of the stratospheric QBO winds at a height of 10 hPa. This is particularly noticeable for the meridional component of the diurnal tide.

We performed a similar analysis using the predictions of SD-WACCM. As an example, Figure 5.14

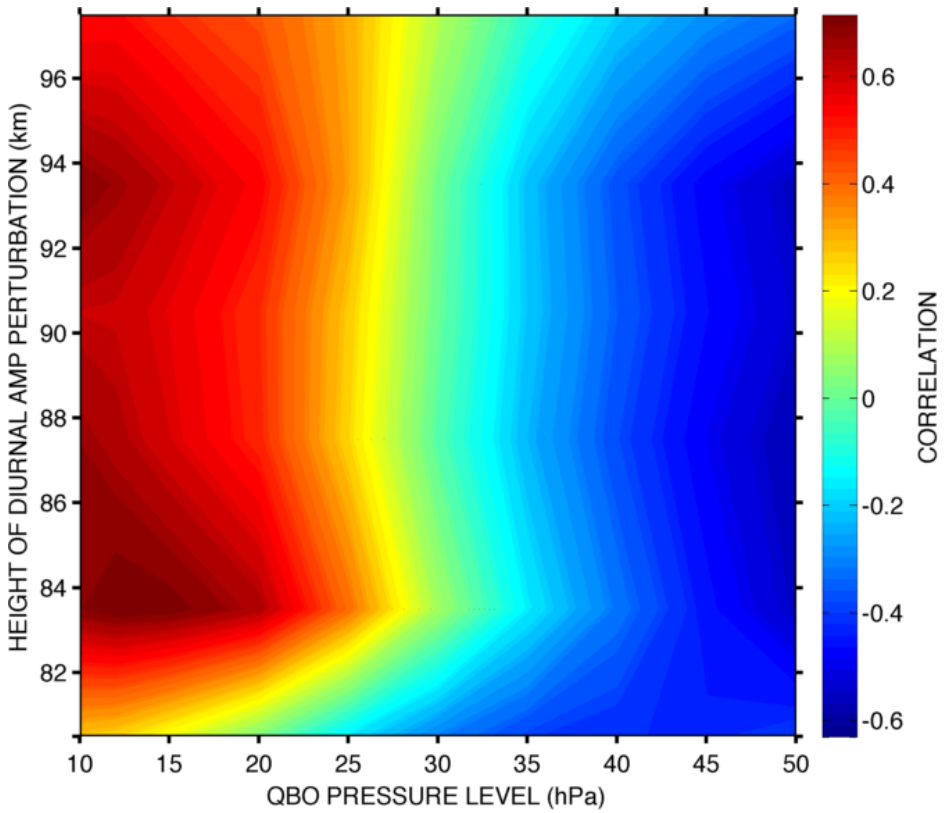

Figure 5.13: Correlation between meridional diurnal amplitude perturbations and stratospheric QBO winds as a function of height and pressure level.

presents the meridional diurnal tidal amplitude perturbations at a height of 96 km from WACCM, along with the mean winds at a pressure level of 15 hPa. The correlation between the two can clearly be seen by eye in the figure and has a value of 0.69.

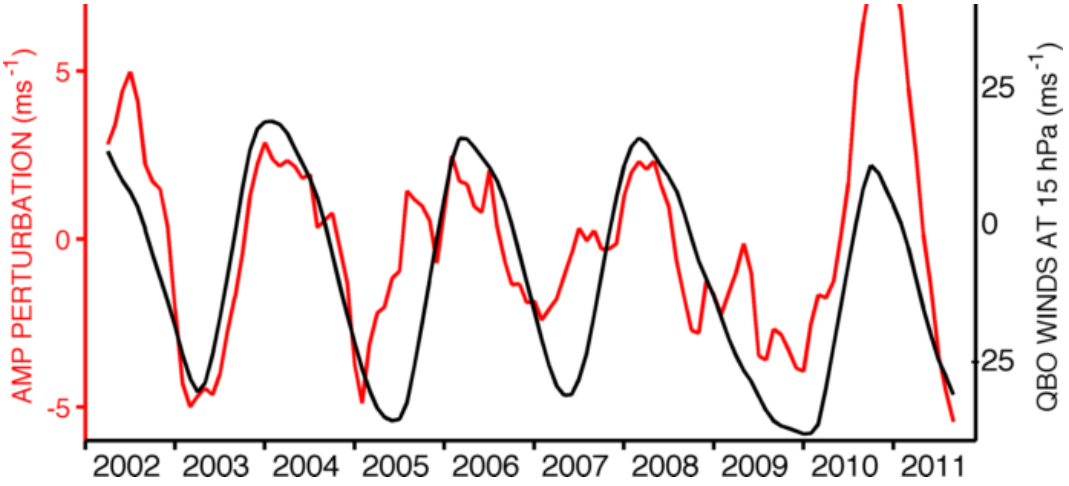

Figure 5.14: Perturbations in WACCM meridional diurnal tidal amplitudes (calculated by subtracting the composite-year monthly mean from each individual month) at heights near 96 km (red line) for 2002 - 2011. Also plotted are the QBO background winds at 15 hPa (black line). The diurnal-tidal amplitude perturbations and background winds are smoothed with a seven-month running mean. Note the two different axes, with the red axis on the left corresponding to the WACCM diurnal tidal amplitude perturbations and the black axis on the right corresponding to the QBO line.

The analysis was repeated for other heights and QBO pressure levels. The resulting correlations are plotted as a function of height and QBO pressure level in Figure 5.15 in a similar manner to the observational data presented in Figure 5.13.

The figure is remarkably similar to the Ascension Island radar result of Figure 5.13, with positive correlation between the meridional diurnal tidal amplitude perturbations and the QBO winds as defined at pressure levels around 10 - 20 hPa and negative correlations with the QBO winds as defined at pressure levels around 40 - 50 hPa. When averaged across the 80 - 100 km height range shown in the figure, the greatest correlation in SD-WACCM is 0.60 with the QBO winds at 18 hPa. This is in excellent agreement with the value of 0.58 at QBO pressure level of 10 hPA observations presented in Figure 5.13.

Finally, we note that the QBO is not the only possible cause of the interannual variability observed in the tidal amplitudes. For example, the El Niño Southern Oscillation (ENSO) is a cycle of warmer and cooler Pacific Ocean surface temperatures which affects atmospheric convection and latent heat release and so may affect the amplitude of atmospheric tides. Over the 2002 - 2011 interval of this study, the ENSO had a similar period to the QBO. The data of the standard Niño 3.4 index is presented in Figure 5.16. Also plotted on the figure are the meridional diurnal tidal amplitude perturbations (as per FIgure 5.12). The figure suggests an out of phase relationship between the two time series. The correlation coefficient between the two series is found to be -0.45. Although smaller in magnitude than the correlation with the QBO, this result nevertheless may indicate a connection between ENSO and tidal amplitudes in the equatorial MLT region.

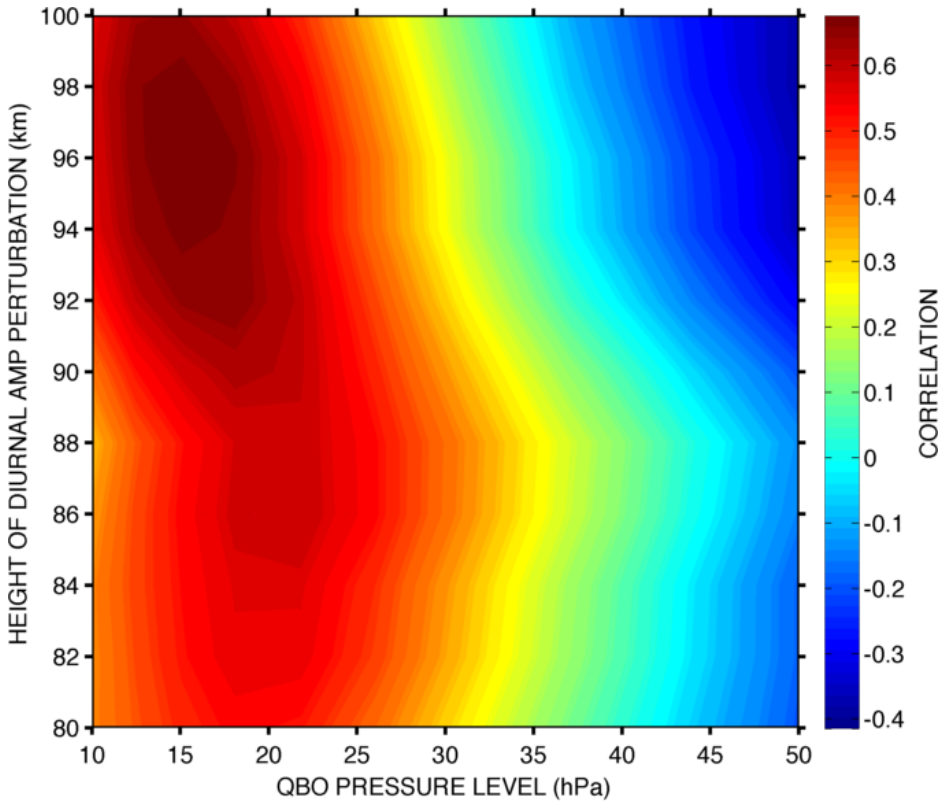

Figure 5.15: Correlation between WACCM meridional diurnal tidal amplitude perturbations and stratospheric QBO winds as a function of height and pressure level.

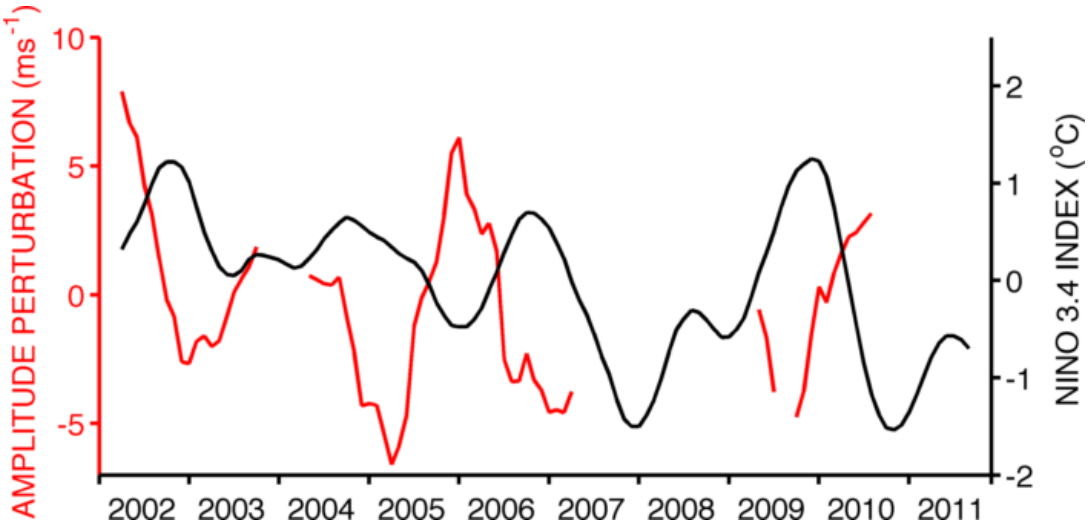

Figure 5.16: Perturbations in meridional diurnal tide amplitudes (calculated by subtracting the composite-year monthly mean from each individual month) at heights near 84 km (red line) for 2002 - 2011 over Ascension Island. Also plotted is the data from the Niño 3.4 index (black line), representing sea surface temperature perturbations in the Niño 3.4 Pacific ocean region. The diurnal-tidal amplitude perturbations and Niño 3.4 index are smoothed with a seven-month running mean. Note the two different axes, with the red axis on the left corresponding to the diurnal amplitude perturbations and the black axis on the right corresponding to the Niño 3.4 line.

5.4.5 Model Wavenumber Contributions

The model predictions shown here are actually a superposition of a number of different migrating and nonmigrating tidal components. As an example to demonstrate the relative magnitudes and phases of these components, we present in Figure 5.17 phasor plots of the contribution from each wavenumber to the total zonal diurnal tide in eCMAM for each month, ranging from wavenumber s = -5 to +5 at a height of 90 km. Note that the length of each line gives the amplitude of the component and the phase is given by the angle measured anti-clockwise from the positive x-axis. Only wavenumbers with amplitudes greater than a threshold of 3 ms^{-1} are shown for each month. Note that we do not show equivalent results for the diurnal meridional and semidiurnal tides for reasons of space.

It is apparent that the W1 migrating tide (blue line) often makes the largest contribution to the eCMAM zonal diurnal tide over Ascension Island. However, for some months (January, February, June, July and September) the amplitude of the E3 component is similar to or even larger than the amplitude of the migrating component. It can also be seen that the phase of the migrating tide does not vary throughout the year as much as the phase of the E3 component.

The results from an equivalent analysis of WACCM output are presented in Figure 5.18, but with a lower amplitude threshold of 1.5 ms^{-1} because of the generally lower amplitudes in WACCM.

Again the migrating W1 component (blue line) is the dominant component for most months, with the E3 component also having large magnitude for many months. The E2 component is also large for many months (purple line). It can be seen that for some months (e.g. August - October) even though the migrating component is relatively large, the vector sum with the other components (that are often out of phase with the migrating) results in near-zero total amplitude.

Our observations thus indicate that the tidal field over Ascension Island is dominated by a diurnal tide of large amplitude which displays a semiannual seasonal cycle. Tidal amplitudes appear to be modulated by the QBO and also possibly by the ENSO. The model results indicate that the dominant tidal components over Ascension Island are the migrating W1 and the nonmigrating E3 (eCMAM) or the W1, E3 and E2 (WACCM).

5.5 Discussion

The long-term spectra presented in Figure 5.4 reveal the dominance of the diurnal and semidiurnal tides in the MLT region over Ascension Island. Planetary and gravity waves over the region can have significant amplitudes, but do not contribute to the long-term spectra as strongly as they are generally either smaller or more intermittent in amplitude than the tides as well as being randomly phased (e.g., Pancheva et al., 2004; Davis et al., 2012).

The results presented in Figure 5.5 reveal a very clear semiannual oscillation in the diurnal-tidal amplitudes. This seasonal cycle has been reported in other studies (e.g., Deepa et al., 2006; Burrage et

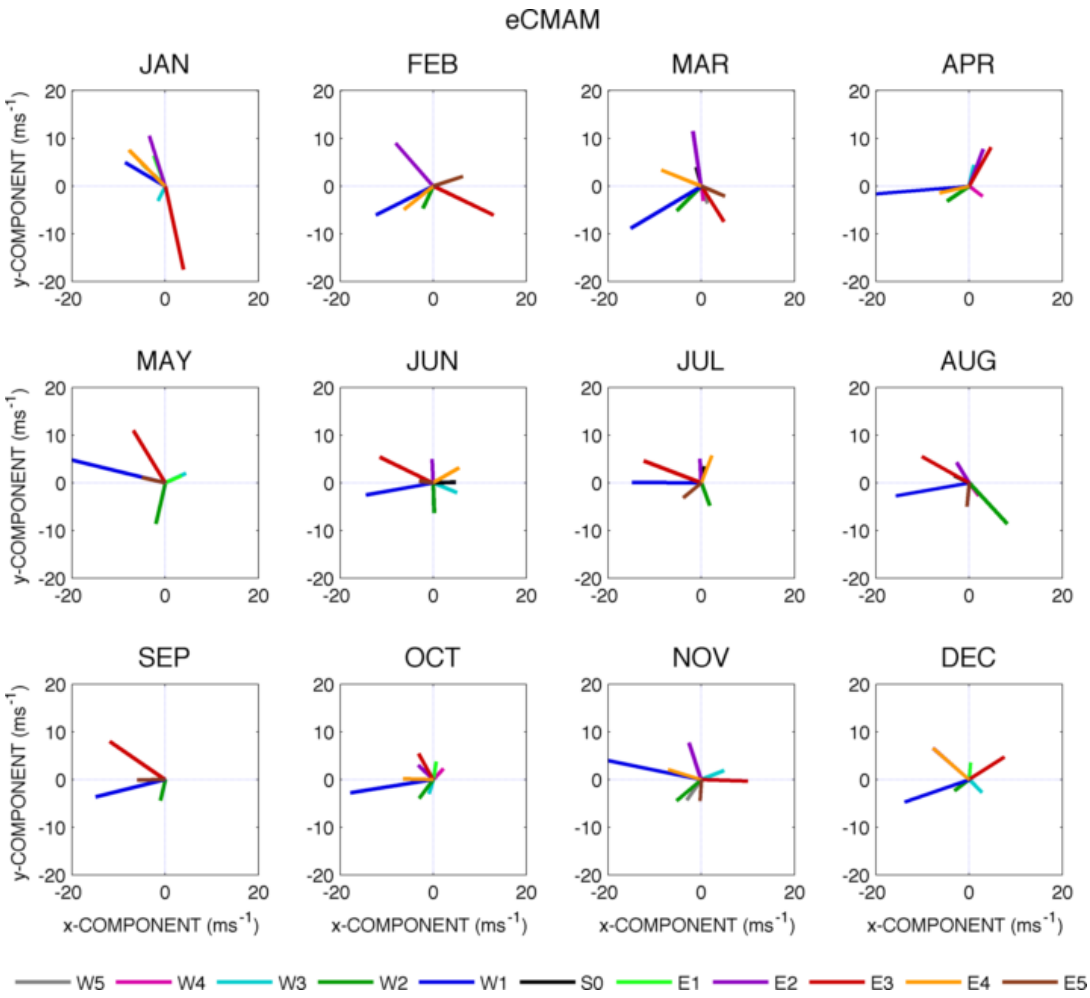

Figure 5.17: Phasor plots of the individual wavenumbers contributing to the eCMAM-predicted zonal diurnal tide at a height of 90 km. The length of each component represents the magnitude of its contribution, and the angle as measured anticlockwise from the positive x-axis gives the phase. Only those components with magnitude greater than 3 ms^{-1} are shown.

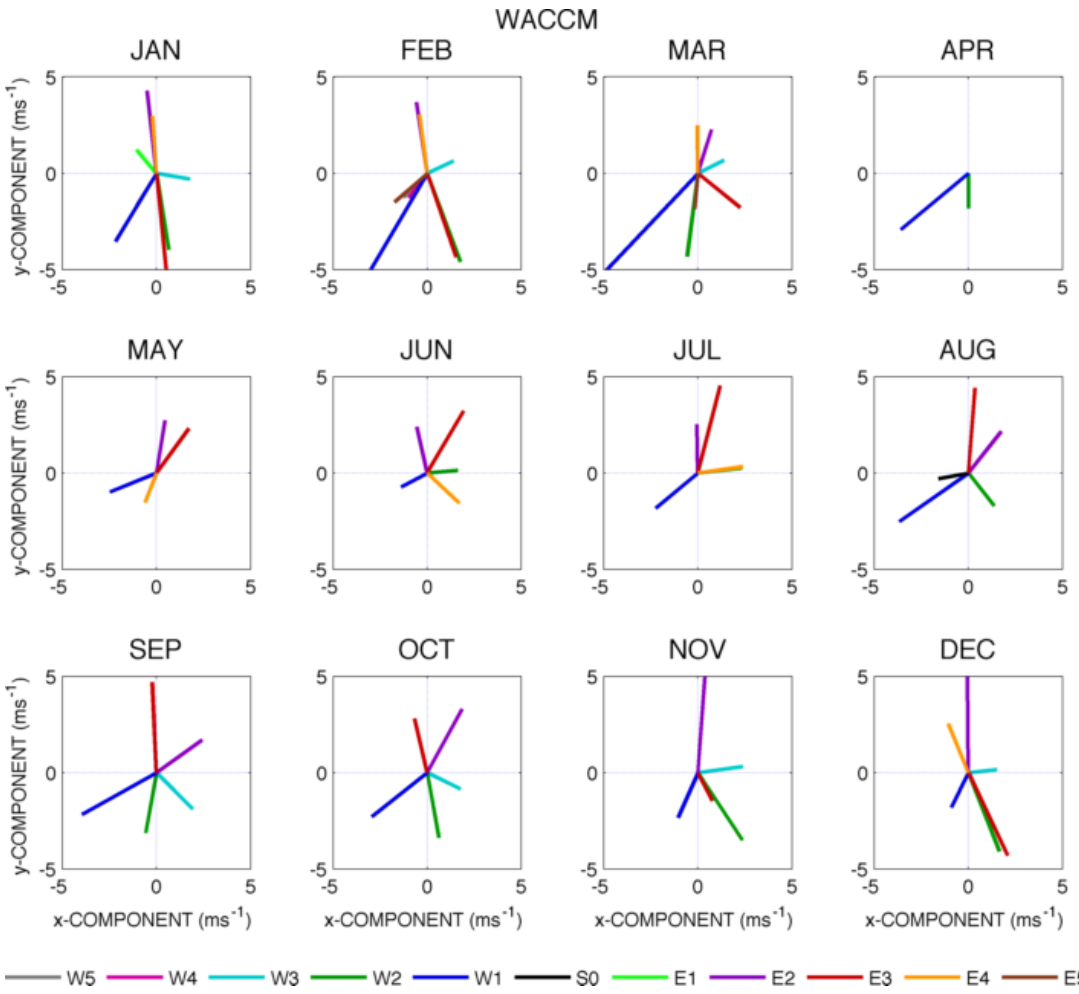

Figure 5.18: Phasor plots of the individual wavenumbers contributing to the WACCM-predicted zonal diurnal tide at a height of 90 km. The length of each component represents the magnitude of its contribution, and the angle as measured anticlockwise from the positive x-axis gives the phase. Only those components with magnitude greater than 1.5 ms^{-1} are shown.

al., 1995; McLandress et al., 1996). This semiannual seasonal cycle in the diurnal-tidal amplitudes has been attributed by Hagan et al. (1999a) to a seasonal variation of gravity-wave drag on the tide and these authors were able to model this variation in diurnal-tidal amplitudes in the Global Scale Wave Model (GSWM-98). Analysis of CMAM simulations by McLandress (2002a,b) showed that the seasonal variations in the heating that forced the tide and in the structure of the background wind in the stratosphere together accounted for the seasonal cycle in the migrating diurnal tide. However, Xu et al. (2009b) found using TIMED observations that the damping was positively correlated with the tidal winds, i.e., the damping was strongest during the equinox periods and so could not explain the observed amplitude variations.

When comparing the Ascension Island results with those from other equatorial sites, the all-sky meteor radar observations from Cariri (7.4^{o}S, 36.5^{o}W) reported by Buriti et al. (2008) are of particular interest due to Cariri's relative proximity to Ascension Island and the similar instrument used. A semiannual cycle in tidal amplitude was observed in the zonal diurnal tides over Cariri between heights of 91 and 98 km, with maxima at the equinoxes. In the meridional component, the diurnal amplitudes over Cariri were also observed to have a semiannual cycle with maximum amplitudes at the equinoxes. This behaviour agrees well with that observed over Ascension Island and the amplitudes are found to be generally similar. There are, however, some differences. For example, the semiannual cycle in amplitudes is observed in the highest height gate of $\sim$ 97 km in the Ascension Island meridional diurnal amplitudes but not at the same heights over Cariri. Also, the ratio of meridional amplitudes to zonal amplitudes averaged over all heights and months is observed to be 2 at Cariri, but just 1.6 over Ascension Island.

The diurnal phases between the two sites also have many aspects in common. The average meridional vertical wavelength over Ascension Island is 26 ± 2 km, agreeing well with the 23.8 ± 2.6 km reported over Cariri. The semidiurnal amplitudes over Cariri generally agree well with those observed over Ascension Island and reported here. The average amplitude over all heights and months at Cariri is 5.8 ms^{-1} in the zonal component and 15.0 ms^{-1} in the meridional component. This compares to Ascension Island's 4.8 $^{-1}$ and 11.9 ms^{-1} respectively. Features such as the general increase of amplitude with height and the sharp increase in amplitude between February and March are also observed over both sites. The semidiurnal tidal phases are also generally in good agreement between the two sites.

It should be noted that Buriti et al. (2008) were reporting results from just one year of observations over Cariri in contrast to the multi-year Ascension Island climatological means reported here. The two sites are separated in latitude by just half a degree, so it would be expected that the *migrating* diurnal tide over Cariri would have similar amplitudes and phases to those over Ascension Island. However, the longitudinal difference of 22.5^{o} between the two sites means that any significant nonmigrating components present may explain the relatively small differences observed between the two sites.

In fact, nonmigrating tides have been proposed to cause large differences in ground-based tidal measurements between two locations at the same latitude. For example, Hagan et al. (1997) found that non-migrating components modelled in the GSWM could subtract from the migrating diurnal tide in

the low-latitude Pacific, accounting for the large observational differences between the radar situated on Kauai and the migrating tidal amplitudes from satellite observations. Chang et al. (2010b) examined diurnal-tidal amplitudes from three sites at approximately equivalent latitudes near 22°S. These were Learmonth (23°S, 114°E), Rarotonga (22°S, 160°W), and Cachoeira Paulista (23°S, 45°W)). They compared these amplitudes with the predictions of four models (WACCM, eCMAM, TIME-GCM and the GSWM-02). They found significant differences in amplitude between the three sites due to differing superpositions of migrating and non-migrating tides. They also found that while the models failed to accurately reproduce the observed longitudinal differences, a common general pattern of zonal variation was observed in three of the models. The importance of the longitudinal structure of the tides was discussed in detail by Ward et al. (2010). However, the superposition of tidal components deduced from TIDI observations presented by these authors reveals that Ascension Island happens to be in a region of comparatively constant tidal amplitude as a function of longitude. This would again help explain the similarities between the Ascension Island and Cariri observations. Our results in comparison with those from Cariri reported by Buriti et al. (2008) thus support the conclusions of Ward et al. (2010).

Other comparisons of particular interest are with the results of Deepa et al. (2006) from the radar at Trivandrum (8.5°N, 77°E), approximately at Ascension Island's conjugate latitude. Again the results were obtained from an all-sky meteor radar and so instrumental differences should be negligible. Deepa et al. (2006) observed the diurnal amplitudes to be larger than the semidiurnal and the meridional components for both tides to be larger than the zonal. They also observed a semiannual cycle in diurnal amplitudes with maxima around the equinoxes in the zonal component. These observations agree well with the observations presented here from Ascension Island. However, in the meridional component, at heights above 90 km Deepa et al. (2006) observed an annual cycle in tidal amplitudes with maxima in the winter months and minima in the summer in contrast to the semiannual cycle with equinoctial maxima observed. The mean amplitudes were slightly larger than those observed over Ascension Island, with peak amplitudes of $\sim$ 60 ms^{-1}, c.f. 48 ms^{-1} over Ascension Island. Vertical wavelengths in both zonal and meridional components were found to be $\sim$ 25 km, similar to the Ascension Island results.

Deepa et al. (2006) also observed slightly larger semidiurnal amplitudes than are observed over Ascension Island. The vertical wavelengths observed were generally similar to the Ascension Island results. They attributed the presence of vertical wavelengths greater than 100 km to the dominance of the (2,2) mode as predicted by Forbes (1982).

We will now consider the results from eCMAM and WACCM. In the case of comparisons of eCMAM with observations, it has been noted in previous studies that the amplitudes of the eastward-propagating tidal components in eCMAM are much larger than the values observed by the TIMED Doppler Interferometer (TIDI), while westward propagating components are of comparable magnitudes (Du et al., 2007; Du, 2008; Chang et al., 2010b). It is therefore possible that eCMAM overestimates the parameterizations of latent heat release and deep convection responsible for generating the eastward-propagating tidal components.

It is known that tidal vertical wavelengths are affected by eddy diffusion and momentum deposition in the MLT from gravity-wave breaking (Ortland and Alexander, 2006). The slightly shorter vertical wavelengths in the eCMAM compared to our observations may thus be a result of in-phase gravity-wave momentum forcing, commonly associated with the Hines parameterization employed in the model (McLandress, 2002a).

Futher, differences could also be caused by differences between the actual tidal sources during the time period of the radar observations compared to the tidal sources in the model. Differences could also be caused by differences in the background atmosphere between that used in the model and the real atmosphere, which would result in differences in the propagation conditions for the component and/or Hough mode. Finally, since only one year of model data are used in these comparisons, year-to-year variations in the model may also play a role. Given these uncertainties, it is striking that the agreement is as good as reported here.

The most consistent of the differences between the WACCM simulations and the observations are the lower amplitudes in WACCM. Since SD-WACCM nudges to observational data in the troposphere and stratosphere, the differences are likely not due to tidal heating or other tidal sources. However, there are several processes that could contribute to these differences. Firstly, the tidal amplitudes may be suppressed in the MERRA analyses used for the nudging because the meteorological data used in the assimilation are ingested at infrequent intervals, thus damping high-frequency variability such as tides. It is also possible that the conditions for tidal propagation in WACCM (background winds and temperatures in the mesosphere) are incorrect, or that tides in WACCM are excessively damped by parameterized gravity-wave processes. Finally, insufficient vertical resolution in the mesosphere could also affect the simulation of the tides. In general, tidal amplitudes in WACCM that are systematically too low are a known problem that is currently under investigation (Smith, 2012).

Our results (Figures 5.17 and 5.18) show that the dominant wavenumbers contributing to the total zonal diurnal tidal field in both eCMAM and WACCM are the migrating W1 and the nonmigrating E3. The figures also highlight one of the difficulties models face in attempting to accurately predict tidal amplitudes and phases. With many wavenumbers contributing to the total tidal field, identifying whether differences between the observed tidal field and the model predictions are due to, for example, the over-estimation of the amplitude of one component, or the under-estimation of another, or the incorrect phase of a third etc., becomes very difficult. A useful step towards solving some of these problems might involve studies made with chains of radars at approximately equal latitudes, or alternatively studies focusing on satellite data, which would be able to distinguish wavenumbers but at the price of poorer time resolution.

Our observations (e.g. Figure 5.13) indicate that the QBO appears to influence the amplitudes of the diurnal tidal in the MLT, with larger amplitudes occurring when the QBO wind at 10 hPa is eastward. This connection has been reported in a limited number of other studies, for example Vincent et al. (1998). However, it should be noted that the positive correlation we report here does not necessarily imply that any mechanism linking the QBO and tidal amplitudes exists at heights around 10 hPa.

The correlations between QBO wind at 10 hPa and tidal-amplitude perturbations reported in Section 5.4.4 show that the correlation (averaged across all radar height gates) is higher for the meridional diurnal-tidal amplitudes (0.58) than the semidiurnal (0.37). This greater affect of the QBO on the meridional diurnal amplitudes compared to the effect on the meridional semidiurnal amplitudes provides support to similar conclusions drawn from the TIDI/TIMED satellite observations reported by Wu et al. (2011).

Hagan et al. (1999b) performed a number of numerical experiments with the GSWM-98 to investigate two possible causes of this QBO modulation of MLT diurnal tidal amplitudes. These causes were i) the QBO in zonal-mean zonal winds and ii) variable forcing arising from the QBO in stratospheric ozone. They suggested that the QBO in zonal-mean zonal winds cause variations in tidal amplitude by approximately 40%, somewhat larger than what we observe over Ascension Island. They also concluded that the QBO in stratospheric ozone has negligible effect on MLT diurnal tidal amplitudes because the major ozone variations occur below the height of the majority of the ozone heating. Mayr and Mengel (2005) were able to produce a QBO with realistic periods in the Numerical Spectral Model and found that it can modulate tidal amplitudes by up to 30%. They found that at heights above 80 km this modulation was driven by gravity-wave momentum deposition.

However, in contrast, Xu et al. (2009a) came to a different conclusion about the role of gravity waves. They found that the tropical zonal wind variations associated with the QBO had little effect on the filtering of gravity waves because the effect was masked by the larger magnitude winds in the upper stratosphere. As of now, there is thus no consensus on the processes that are responsible for the QBO variation in tidal amplitudes.

Our results (Figure 5.16) show that the observed mesospheric tidal amplitudes over Ascension Island have negative correlation with the ENSO index. This is particularly interesting when contrasted with the enhanced diurnal amplitudes in the MLT observed during El Niño events, i.e. positive correlations, at various ground-based stations in the Pacific (Tirunelveli, Jakarta, Kauai, and Christmas Island) as observed by Gurubaran et al. (2005) and Lieberman et al. (2007). This is the opposite of the effect we observe over Ascension Island. However, the regional impact of ENSO can be very complicated and further analysis would require decomposing the observed tides into migrating and non-migrating components. This would allow an examination of how water vapor and latent heat release changes both globally and locally during El Niño and La Niña events and how these affect tides in the mesosphere. The relative impact of the QBO and the ENSO on tidal amplitudes in the mesosphere remains an interesting question.

5.6 Conclusions

Ten years (2002-2011) of wind observations from the Ascension Island meteor radar (8°S, 14°W) have been analysed to characterise the diurnal and semidiurnal tides over the tropical mid-Atlantic region. The length of the dataset enables an investigation into the effect of the stratospheric QBO on the tidal

amplitudes. Comparisons have been made between the observed tidal parameters and those predicted by the eCMAM and WACCM models.

The MLT wind field over Ascension Island has been shown to be dominated by the diurnal tide, which can have instantaneous amplitudes on occasion reaching in excess of 100 ms^{-1}. The semidiurnal tide is also present but smaller in amplitude.

Considering the diurnal tide over the height range observed, monthly-mean diurnal amplitudes generally increase with height. In both zonal and meridional components of the diurnal tide there is a semiannual seasonal variation apparent, with amplitude maxima at the equinoxes and amplitude minima at the solstices. Amplitudes are greater in the meridional component than the zonal for all months except the low-amplitude Austral winter months of June and July. The meridional diurnal tidal vertical wavelengths are generally similar throughout the year, ranging from 24 to 30 km. The zonal vertical wavelengths are generally similar to the meridional, except for during the austral winter months when the zonal vertical wavelengths are much longer.

Semidiurnal tidal amplitudes are observed to be approximately 25% of the diurnal amplitudes (when averaged across all heights and months). There is a greater difference in amplitude between the meridional and zonal components of the semidiurnal tide than was the case with the diurnal tide. The semidiurnal tidal vertical wavelengths vary much more than is the case for the diurnal tide.

Both eCMAM and WACCM reproduce the trend for greater diurnal amplitudes in the meridional component than the zonal. However, eCMAM tends to over-predict meridional amplitudes, while WACCM under-predicts zonal and meridional amplitudes. Semidiurnal amplitude predictions were generally good for both models. Vertical wavelength predictions were also often good for both models, however eCMAM predicts shorter zonal vertical wavelengths than observed for the diurnal tide in Austral winter, while WACCM predicts longer zonal semidiurnal vertical wavelengths than observed for most months.

Component analysis of the eCMAM and WACCM zonal diurnal tide shows that the migrating W1 and the nonmigrating E3 components were the dominant contributors to the total tidal field.

Finally, sorting MLT region tidal amplitudes by QBO phase at 10 hPa revealed that larger-than-average meridional diurnal amplitudes occur when the stratospheric QBO winds are eastwards, and smaller-than-average meridional diurnal amplitudes occur when the QBO winds are westwards. Correlations show that the QBO appears to have most effect on the diurnal tide in the meridional component. Despite the significant magnitude of QBO modulation of tidal amplitudes, there appears to be no consensus as to the underlying physical cause. The similar period of the ENSO during the 2002 - 2011 interval further complicates the issue. This highlights the need for further studies on the coupling between the ENSO, the stratospheric QBO and the tides of the MLT.

Chapter 6

Gravity-Wave Momentum Fluxes in the MLT region over the Southern Andes and Antarctic Peninsula

6.1 Abstract

This chapter presents the results from an investigation into the MLT-region gravity-wave momentum fluxes and variances over the Drake passage hotspot using measurements from two all-sky VHF meteor radars; one at Rothera (68^{o} S, 68^{o} W) on the Antarctic peninsula, and one near Riogrande on the Tierra del Fuego (54^{o} S, 68^{o} W). We use the method described in Hocking (2005) to obtain monthly-mean momentum fluxes and variances by subtracting the homogeneous motion from the radial velocities of each meteor, to leave the contribution from mesoscale gravity waves. Here we apply a slight adaptation of the method to reduce contamination of the recovered momentum fluxes and variances by the strong vertical wind shears and semidiurnal tides in the region.

The method and the suitability of the meteor distributions of each radar are tested by sampling a series of specified (known) wave fields of increasing complexity with the actual meteor distributions, and comparing the recovered momentum fluxes with the specified values. Both instruments are revealed to recover the specified fluxes with good accuracy. The analysis is then applied to the real data to produce monthly-mean variances and momentum fluxes over the height range 80 to 100 km for a composite year of the 2008 to 2012 data. The variances are similar for both zonal and meridional components of both radars, and reveal a semiannual oscillation with maxima near the solstices and minima at the equinoxes. Momentum fluxes are generally less than 25 m^2s^{-2} and the zonal fluxes are observed to decrease with increasing height in the summer, corresponding to a deposition of eastward momentum that may play an important role in the reversal of the mean winds.

The work presented in this chapter is (at the time of writing) being prepared for submission to the Journal

of Geophysical Research - Atmospheres.

6.2 Introduction

The importance of gravity waves in driving the mean circulation is widely recognised (e.g., Fritts and Alexander, 2003), however their short periods and timescales can make them difficult to investigate. The vertical fluxes of horizontal momentum produced by gravity waves as they propagate upwards through the Mesosphere/Lower Thermosphere (MLT) region are a crucial parameter in the understanding of atmospheric dynamics and improving models, however they remain relatively under-studied.

After Hines (1960) pioneered the research of gravity waves, momentum flux studies have been performed at a number of sites, including Adelaide, Australia (Reid and Vincent, 1987; Murphy and Vincent, 1993, 1998; Reid et al., 2004), Jicamarca, Peru (Fritts et al., 1992), Shigaraki, Japan (Gavrilov et al., 2000), and Poker Flat, Alaska (Fritts and Yuan, 1989; Nicolls et al., 2012).

These studies often used a technique developed by Vincent and Reid (1983) that allowed zonal momentum fluxes to be recovered by a dual beam radar with coplanar beams orientated east-west, and meridional momentum fluxes with beams orientated north-south. Fritts et al. (1990) adapted the technique for use with a multi-beam radar.

Hocking (2005) identified the global distribution and seasonal coverage of already-deployed meteor radars as being potentially a very useful tool in the study of momentum fluxes. In principle subsets of the recorded meteors could be used to replicate the beams of previous studies, however in practice meteor count rates are too low. Hocking thus generalized the method to an all-sky summation, of which the two-beam technique was shown to be a special case. This statistical method provides a solution to the problem of the difficulty of obtaining mesospheric measurements of small vertical motions. It produces the covariances $u'w'$ and $v'w'$, which are the zonal and meridional momentum fluxes per unit of density, but will be referred to as momentum fluxes throughout this chapter.

The Hocking technique has been applied to data collected by meteor radars at, e.g., Trivandrum, India (Antonita et al., 2008), Cariri, Cachoeira Paulista and Santa Maria, Brazil (Clemesha et al., 2009), King George Island, Antarctica (Fritts et al., 2012a), Andenes, Norway, Juliusruh and Collm, Germany (Placke et al., 2011a). Here we present results from VHF meteor radars at two sites: Rothera on the Antarctic peninsula and the SAAMER radar at Riogrande, Tierra del Fuego. The locations and azimuthal distributions of the two radars are plotted in Figure 6.1.

The two sites reported on here are of particular interest in part due to their proximity to each other, but also as they are either side of the Drake passage. This region has been identified as a gravity wave hotspot, and the intense gravity-wave activity has been well documented (Figure 6.2, after Alexander et al. (2008) and Ern et al., (2004), and Figure 6.3, after Wright et al. (2014)).

Our motivations in this study are to evaluate the capabilities of a momentum flux method adapted from

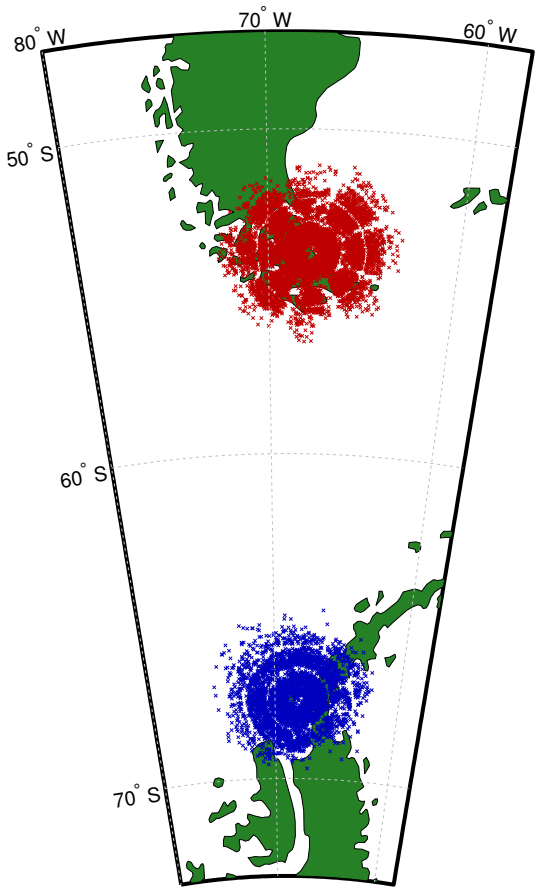

Figure 6.1: Map showing the location of the Rothera (blue) and SAAMER (red) radars. The crosses represent the horizontal projections of the locations of individual meteors recorded by the radars at heights between 89 and 92 km for a single day. The radars are at the centres of the meteor distributions. The SAAMER radar utilises a higher-power transmitter and projects its power into lobes focused at lower zenith angles than the Rothera radar, hence the differences in count rate and azimuthal distributions.

Hocking (2005) and also to evaluate the Rothera radar, which operates at a much lower power than the SAAMER radar. We will then compare fluxes between the two sites. In Section 6.3 we describe the radars in more detail and outline the method used to recover gravity-wave momentum fluxes. In Section 6.4 we present results first from the specified wave field tests, and then from the observations. The results are discussed in Section 6.5, with conclusions made in Section 6.6.

6.3 Method and Analysis

The radars used in this study are the SKiYMET meteor radar located at Rothera, Antarctica (68^o S, 68^o W) and the SKiYMET Southern Andes MEteor Radar (SAAMER) near Riogrande on the Tierra del Fuego, Argentina (54^o S, 68^o W). The Rothera radar has been operational since February 2005, providing near-continuous data since then. SAAMER was installed in May 2008 and was specifically designed with the capabilities of measuring gravity-wave momentum fluxes. Again it has provided

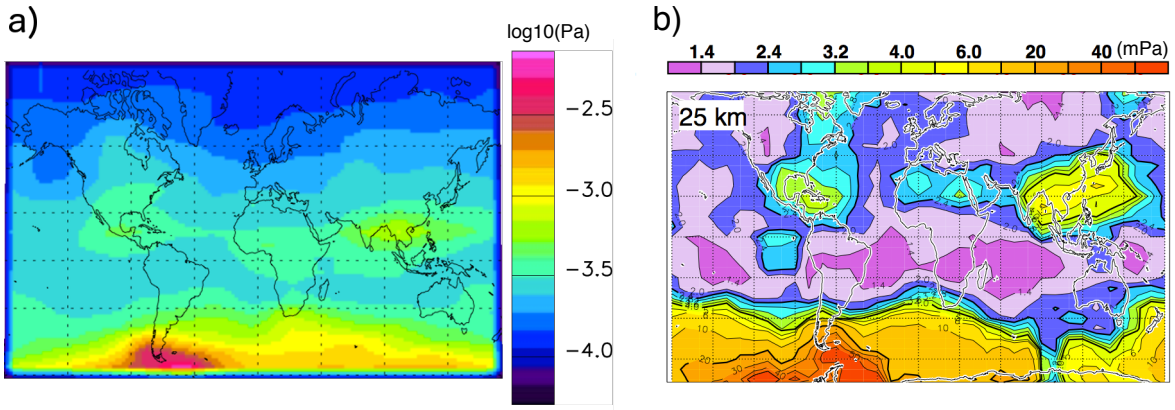

Figure 6.2: Figures from other studies showing global estimates of momentum fluxes at heights near 25 km. a) is derived from measurements taken by the HIRDLS instrument aboard the Aura satellite. b) is derived from measurements from the CRISTA-2 mission. In both figures the large stratospheric gravity-wave momentum fluxes near the Drake passage are evident. a) and b) are after Alexander et al. (2008) and Ern et al., (2004), respectively.

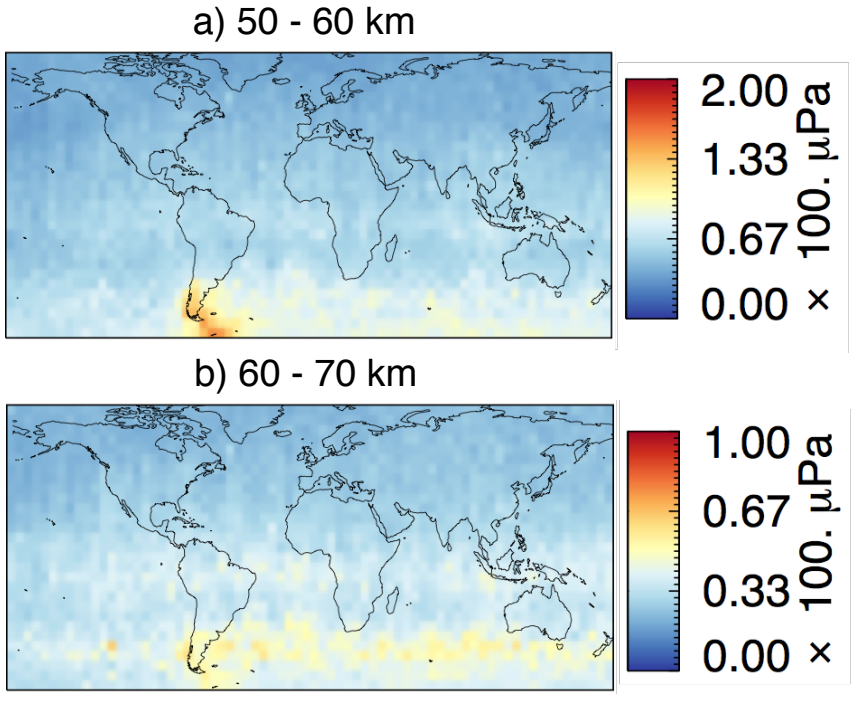

Figure 6.3: Mesospheric momentum fluxes derived from HIRDLS at heights of a) 50 - 60 km, and b) 60 - 70 km, using an overlapping-wave S-Transform method (Wright and Gille, 2013). Fluxes shown are an average of March/April/May 2005 - 2007, after Wright et al. (2014).

near-continuous data since installation. In this study we shall present results from data recorded over the interval 2008 to 2012.

These two meteor radars have slightly different characteristics, which have been described in detail elsewhere (e.g., Fritts et al., 2010a; Younger et al., 2009). Here we will only note the principle characteristics of the radars.

The Rothera radar is a standard all-sky SKiYMET VHF radar, operating at a radio frequency of 32.5 MHz and using a single 6 kW peak-power transmitter. The radar uses a single crossed-element Yagi transmitter antenna and 5 separate crossed-element receiver Yagi antennas which form an interferometer, allowing the determination of meteor echo zenith and azimuth angles. Most meteor echoes are detected at zenith angles of approximately 50^o - 60^o. The distribution of meteors detected as a function of height is approximately Gaussian, with most meteors detected at heights around 90 km, with fewer above and below.

SAAMER also operates at a frequency of 32.5 MHz, but uses a higher transmitted peak power of 60 kW. This increases the number of meteor echoes detected. SAAMER transmits using an array of 8 crossed-element Yagi antennas and receives using an array of five crossed-element YAGI antennas. This antenna configuration is designed so that more of the meteor echoes are detected at zenith angles in the range 15^o to 50^o. This increases the contribution made by vertical velocities to the radial drifts measured by SAAMER. Since gravity-wave momentum-flux determinations require measurement of these vertical velocities, this makes SAAMER particularly well suited to this task. The meteor counts as a function of zenith angle for the two radars are presented as daily means in Figure 6.4.

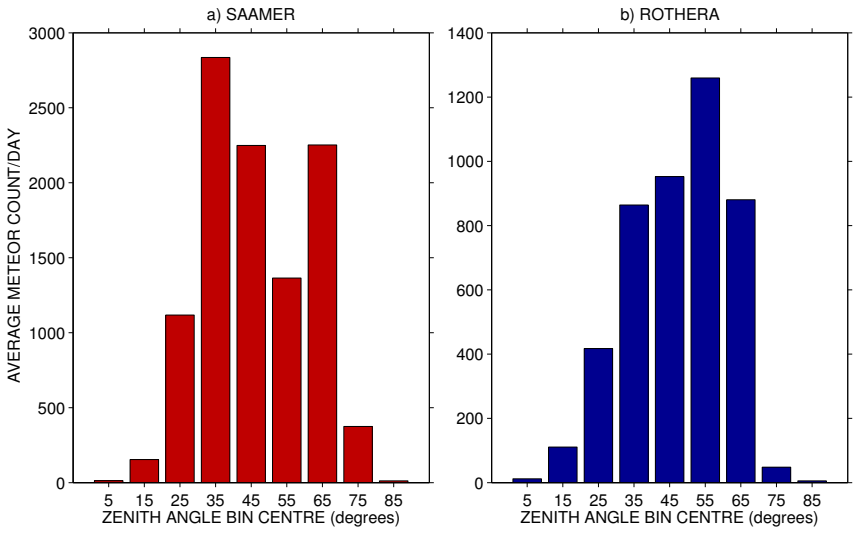

Figure 6.4: Meteor count per day as a function of zenith, averaged over all days in the year 2009 for a) SAAMER and b) Rothera. SAAMER has a distribution skewed towards lower zenith angles than the Rothera radar.

For this study we reject all meteors with zenith angles (θ) less than 15^o and greater than 50^o as is common in meteor radar studies (Fritts et al., 2012b). The reasoning behind these limits is that at higher zenith angles the relative contribution of the vertical wind to the radial velocities decreases. Also for

meteors recorded nearer the horizon, an error on the zenith angle corresponds to a larger error on the height than for meteors nearer the zenith. Meteor count rates are not generally high enough to reduce the 50^{o} limit to angles any closer to the zenith. Meteors recorded at zenith angles less than 15^{o} are not included as there are too few to get reliable wind estimations.

A crucial step in the determination of gravity wave variances and momentum fluxes is the subtraction of the mean flow, tides and planetary waves to leave the gravity wave wind perturbations. The original Hocking (2005) method involved collecting meteors into time/height bins, fitting a sine wave to the radial velocities to obtain a single value of mean wind within the bin, and then subtracting the component of that wind along the radial direction from the radial velocity of each individual meteor to leave the gravity-wave contribution. Hocking (2005) set a minimum limit of 30 meteors per bin for the momentum fluxes to be calculated, as this was the threshold at which the matrix ceased to produce negative values for the recovered vertical variances (a squared quantity). To reliably obtain a minimum of 30 meteors per bin, height and time windows of 3 km and 3 hours were selected.

A problem with this method is that the semidiurnal tide can reach large amplitudes at the latitudes of Rothera and SAAMER. Over the course of three hours the semidiurnal tide will rotate through a quarter of a cycle, so that a single averaged wind value will not represent the changing zonal and meridional semidiurnal tidal amplitudes accurately enough. For example, Andrioli et al. (2013) found that the variances recovered with the original method are often contaminated by the tides. Similarly, the zonal winds over Rothera and SAAMER can exhibit very strong vertical shears. For example, the magnitude of the monthly-mean zonal wind over Rothera in January can differ by more than 10 ms^{-1} across a 3 km vertical interval. The result is that vertical mean-wind shears and tides contribute to the variances and affect the recovered momentum fluxes. Monthly-mean zonal winds over Rothera for a composite year of the 2008 to 2012 interval are presented in Figure 6.5a to demonstrate the wind shears that occur at these heights and latitudes. Figure 6.5b presents the semidiurnal tidal amplitudes for a composite month of May as an example of the large-amplitude semidiurnal tides (calculated from the method of Section 5.3).

Here we adapt the method of Hocking (2005) to remove interpolated wind values rather than bin-means. Meteors are temporarily binned according to zenith angle, and within each bin those with radial velocities exceeding the mean radial velocity by more than 3 standard deviations are removed from the dataset. This outlier-removal step retains 99.7% of all meteors. The difference in antenna configuration and peak power means that the SAAMER radar generally detects two or three times as many meteors in the 15^{o} to 50^{o} range as the Rothera radar. The meteor counts in the 15^{o} to 50^{o} range are presented for each radar and each month of 2009 in Figure 6.6.

Meteors in the 15^{o} - 50^{o} range are binned into 6 height gates: 78 - 83, 83 - 86, 86 - 89, 89 - 92, 92 - 95 and 95 - 100 km with the highest and lowest gates being larger to compensate for the reduced meteor counts at those heights. The background zonal and meridional winds are calculated from a horizontal least-squares fit of the horizontal components of the radial velocities (the vertical mean wind is assumed to be zero) for two-hour windows stepped every hour. A minimum of 8 meteors in each time/height bin

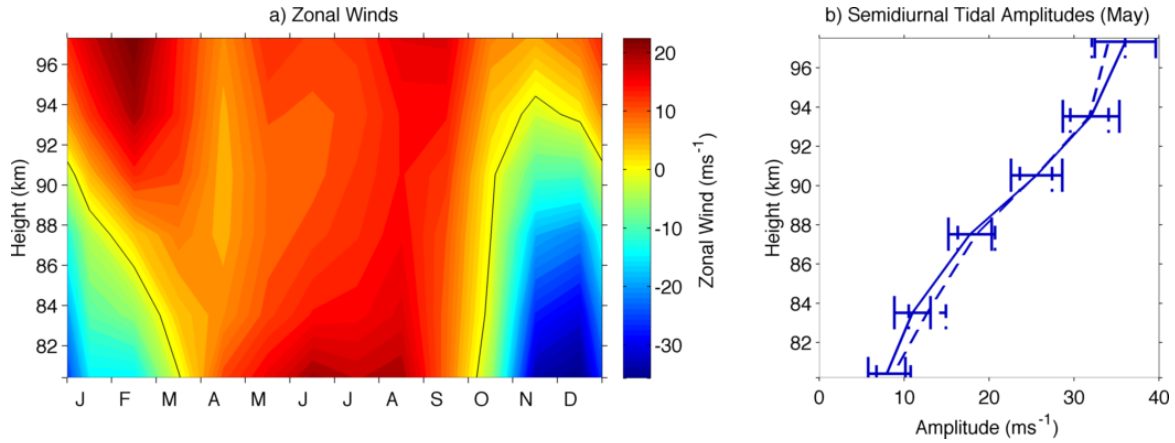

Figure 6.5: a) Monthly-mean zonal winds over Rothera as a function of height for a composite year of the 2008 to 2012 interval, presented as a demonstration of the strong vertical wind shears that can occur in the MLT region at Rothera's latitude. b) Semidiurnal tidal amplitude as a function of height over Rothera for the month of May in a composite year of the 2008 to 2012 interval, presented as an example of the very large semidiurnal tidal amplitudes that can occur at Rothera's latitude. The horizontal bars represent the standard deviations of the individual monthly means.

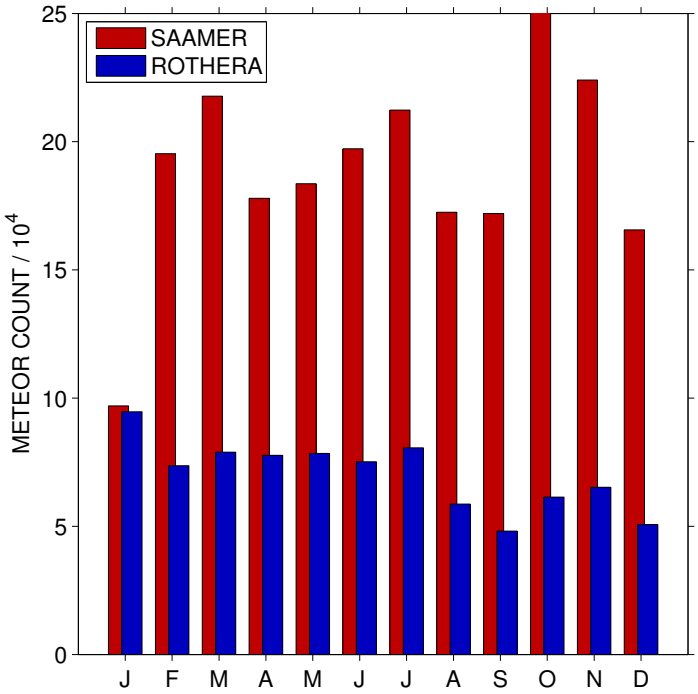

Figure 6.6: Total meteor count per month for the example year of 2009. Note that all meteors with zenith angles outside of the 15° to 50° range have been excluded.

are required for the fit. Individual meteors with radial velocities differing from the fitted value by more than 30 ms^{-1} are deemed to be atypical of the mean conditions and temporarily removed from the bin before the winds are re-fitted (Hocking, 2001).

These background winds are assumed to contain the mean flow and all large-scale oscillations such as the diurnal tides and semidiurnal tides, any planetary waves present, and also any gravity waves with horizontal wavelengths greater than the collecting diameter. For each individual meteor the background winds are linearly interpolated between the nearest two wind-fit heights and nearest two wind-fit times to obtain the expected background wind at each meteor's time and location. This interpolated value will represent the true mean wind at each meteor's position much better than a mean value for a bin that is relatively large in time and space. Meteors beyond the mean meteor heights of the outer two height gates (i.e., those meteors recorded at heights z $<$ 80.8 km and z $>$ 97.8 km) are discarded as interpolated wind values can not be obtained for them. For each meteor, the radial velocity that would produce the interpolated fitted wind at that meteor's position in space and time (known as the model value, v_{radm}) is calculated and subtracted from the measured radial velocity. These model values will differ from the measured radial velocity (v_{rad}) due to true wind variability, the main contributor of which is assumed to be gravity waves which are unresolved by the radar but nevertheless contribute to the variance.

Following Hocking (2005), we wish to minimise Λ, where Λ is given by

$$\Lambda = \Sigma[(v'_{rad})^2 - (v'_{radm})^2]^2 \tag{6.1}$$

where the summation (indices omitted) is over all meteors in the time/height bin. Here, v'_{rad} is the difference between the measured and modeled radial velocities, $v'_{rad} = v_{rad} - v_{radm}$, and v'_{radm} is the component of the modeled radial velocity due to wave motion, i.e.,

$$v'_{radm} = u'\sin(\theta)\cos(\phi) + v'\sin(\theta)\sin(\phi) + w'\cos(\theta) \tag{6.2}$$

Substituting equation 6.2 into equation 6.1, we obtain

$$\begin{aligned}\Lambda = \Sigma[(v'_{rad})^2 - (&u'^2\sin^2(\theta)\cos^2(\phi) + v'^2\sin^2(\theta)\sin^2(\phi) + w'^2\cos^2(\theta) \\ &+ 2u'v'\sin^2(\theta)\sin(\phi)\cos(\phi) + 2u'w'\sin(\theta)\cos(\theta)\cos(\phi) \\ &+ 2v'w'\sin(\theta)\cos(\theta)\sin(\phi))]^2\end{aligned} \tag{6.3}$$

Λ is minimised by taking the partial derivatives of equation 6.3 with respect to u'^2, v^2, w'^2, $u'v'$, $u'w'$ and $v'w'$, and setting each of them equal to zero. This results in six equations with six unknowns which can be put into matrix form:

$$\begin{bmatrix} \Sigma\sin^4(\theta)\cos^4(\phi) & \Sigma\sin^4(\theta)\cos^2(\phi)\sin^2(\phi) & \Sigma\sin^2(\theta)\cos^2(\theta)\cos^2(\phi) & \Sigma 2\sin^4(\theta)\cos^3(\phi)\sin(\phi) & \Sigma 2\sin^3(\theta)\cos(\theta)\cos^3(\phi) & \Sigma 2\sin^3(\theta)\cos(\theta)\cos^2(\phi)\sin(\phi) \\ \Sigma\sin^4(\theta)\cos^2(\phi)\sin^2(\phi) & \Sigma\sin^4(\theta)\sin^4(\phi) & \Sigma\sin^2(\theta)\cos^2(\theta)\sin^2(\phi) & \Sigma 2\sin^4(\theta)\sin^3(\phi)\cos(\phi) & \Sigma 2\sin^3(\theta)\cos(\theta)\sin^2(\phi)\cos(\phi) & \Sigma 2\sin^3(\theta)\cos(\theta)\sin^3(\phi) \\ \Sigma\sin^2(\theta)\cos^2(\theta)\cos^2(\phi) & \Sigma\sin^2(\theta)\cos^2(\theta)\sin^2(\phi) & \Sigma\cos^4(\theta) & \Sigma 2\sin^2(\theta)\cos^2(\phi)\cos(\phi)\sin(\phi) & \Sigma 2\cos^3(\theta)\sin(\theta)\cos(\phi) & \Sigma 2\cos^3(\theta)\sin(\theta)\sin(\phi) \\ \Sigma 2\sin^4(\theta)\cos^3(\phi)\sin(\phi) & \Sigma 2\sin^4(\theta)\sin^3(\phi)\cos(\phi) & \Sigma 2\sin^2(\theta)\cos^2(\theta)\cos(\phi)\sin(\phi) & \Sigma 4\sin^4(\theta)\cos^2(\phi)\sin^2(\phi)\sin(\phi) & \Sigma 4\sin^3(\theta)\cos(\theta)\cos^2(\phi)\sin(\phi) & \Sigma 4\sin^3(\theta)\cos(\theta)\sin^2(\phi)\cos(\phi) \\ \Sigma 2\sin^3(\theta)\cos(\theta)\cos^3(\phi) & \Sigma 2\sin^3(\theta)\cos(\theta)\sin^2(\phi)\cos(\phi) & \Sigma 2\cos^3(\theta)\sin(\theta)\cos(\phi) & \Sigma 4\sin^3(\theta)\cos(\theta)\cos^2(\phi)\sin(\phi) & \Sigma 4\sin^2(\theta)\cos^2(\theta)\cos^2(\phi) & \Sigma 4\sin^2(\theta)\cos^2(\theta)\cos(\phi)\sin(\phi) \\ \Sigma 2\sin^3(\theta)\cos(\theta)\cos^2(\phi)\sin(\phi) & \Sigma 2\sin^3(\theta)\cos(\theta)\sin^3(\phi) & \Sigma 2\cos^3(\theta)\sin(\theta)\sin(\phi) & \Sigma 4\sin^3(\theta)\cos(\theta)\sin^2(\phi)\cos(\phi) & \Sigma 4\sin^2(\theta)\cos^2(\theta)\cos(\phi)\sin(\phi) & \Sigma 4\sin^2(\theta)\cos^2(\theta)\sin^2(\phi) \end{bmatrix} \begin{bmatrix} u'^2 \\ v'^2 \\ w'^2 \\ u'v' \\ u'w' \\ v'w' \end{bmatrix} = \begin{bmatrix} \Sigma {v'_{rad}}^2\sin^2(\theta)\cos^2(\phi) \\ \Sigma {v'_{rad}}^2\sin^2(\theta)\sin^2(\phi) \\ \Sigma {v'_{rad}}^2\cos^2(\theta) \\ \Sigma {v'_{rad}}^2\sin^2(\theta)\cos(\phi)\sin(\phi) \\ \Sigma {v'_{rad}}^2\sin(\theta)\cos(\theta)\cos(\phi) \\ \Sigma {v'_{rad}}^2\sin(\theta)\cos(\theta)\sin(\phi) \end{bmatrix}$$

Again the summations are over every meteor in the time/height bin for the "full-field" analysis. By inverting this matrix, estimates can be obtained of u'^2, v^2, w'^2, $u'v'$, $u'w'$ and $v'w'$, which are respectively the zonal variance, meridional variance, vertical variance, the flux of zonal momentum in the northward direction (or the flux of meridional flux in the eastward direction), the flux of zonal momentum in the vertical direction (or the flux of vertical momentum in the eastward direction), and the flux of meridional momentum in the vertical direction (or the flux of vertical momentum in the northward direction). These are all assumed to be uniform across the collecting volume for each height gate.

The binning in height and time of the meteors for the wind-fitting process determines the portion of the gravity wave spectrum that is observed, as the method relies on the variance of the individual radial velocities around the fitted wind to distinguish the gravity wave perturbations from the mean flow and tides. We thus expect to resolve gravity waves with vertical wavelengths less than $\sim$ 3 km, periods less than $\sim$ 2 hours, or horizontal wavelengths less than $\sim$ 300 km (the diameter of the collecting volume). Note however that a gravity wave need only meet one of these three criteria for detection.

Vincent et al. (2010) found that though horizontal variances can be reliably determined over averaging intervals of the order of days, the difficulty in obtaining reliable estimates of w' means that averaging over timescales of a month is required to obtain reliable momentum fluxes. For the climatological purposes of this study we do not require temporal resolution finer than 1 month and so the "full field" summation of Hocking (2005) was applied to all the meteors of each month, binned into the same height gates as were used in the wind fitting step. As the method used in this study differs slightly from Hocking (2005), we carried out an investigation of the response of the gravity-wave momentum flux analysis to data recorded by the two radars. In particular, we followed Fritts et al. (2010b) and used the recorded meteor distributions from each radar (in space and time) to sample a specified gravity-wave field of known momentum flux. The test fields are described by the following equations:

$$\begin{aligned} U &= U_M + U_D(z,t)\sin(2\pi t/T_D + U_{SD}(z,t)\sin(2\pi t/T_{SD}) \\ &\quad + U_{GW1}(x,y,z,t)\sin(k_1 x + l_1 y + m_1 z - 2\pi t/T_{GW1}) \\ &\quad + U_{GW2}(x,y,z,t)\sin(k_2 x + l_2 y + m_2 z - 2\pi t/T_{GW2}) \\ &\quad + U_{GW3}(x,y,z,t)\sin(k_3 x + l_3 y + m_3 z - 2\pi t/T_{GW3}) \\ &\quad + U_{GW4}(x,y,z,t)\sin(k_4 x + l_4 y + m_4 z - 2\pi t/T_{GW4}) \end{aligned}$$

$$
\begin{aligned}
V &= V_M - V_D(z,t)\cos(2\pi t/T_D - V_{SD}(z,t)\cos(2\pi t/T_{SD}) \\
&\quad + V_{GW1}(x,y,z,t)\sin(k_1 x + l_1 y + m_1 z - 2\pi t/T_{GW1}) \\
&\quad + V_{GW2}(x,y,z,t)\sin(k_2 x + l_2 y + m_2 z - 2\pi t/T_{GW2}) \\
&\quad + V_{GW3}(x,y,z,t)\sin(k_3 x + l_3 y + m_3 z - 2\pi t/T_{GW3}) \\
&\quad + V_{GW4}(x,y,z,t)\sin(k_4 x + l_4 y + m_4 z - 2\pi t/T_{GW4})
\end{aligned}
$$

$$
\begin{aligned}
W &= W_{GW1}(x,y,z,t)\sin(k_1 x + l_1 y + m_1 z - 2\pi t/T_{GW1}) \\
&\quad + W_{GW2}(x,y,z,t)\sin(k_2 x + l_2 y + m_2 z - 2\pi t/T_{GW2}) \\
&\quad + W_{GW3}(x,y,z,t)\sin(k_3 x + l_3 y + m_3 z - 2\pi t/T_{GW3}) \\
&\quad + W_{GW4}(x,y,z,t)\sin(k_4 x + l_4 y + m_4 z - 2\pi t/T_{GW4})
\end{aligned}
$$

The specified wave fields thus contain: zonal and meridional mean winds (U_M and V_M), diurnal and semidiurnal tides (U_D, V_D, U_{SD} and V_{SD}) with periods $T_D = 24$hrs and $T_{SD} = 12$hrs, and gravity waves with amplitudes U_{GW}, V_{GW} and W_{GW}. Fritts et al. (2010b) tested 7 different cases with wave fields of increasingly realistic complexity. The test wave field parameters used in the seven cases are given in Table 6.1.

Table 6.1: Table of specified-wave-field parameters for cases 1 to 7, after Fritts et al. (2010b).

Parameter	Case 1	Case 2	Case 3	Case 4	Case 5	Case 6	Case 7
U_M, V_M (ms^{-1})	20, 10	0, 0	0, 0	20, 10	40, -20	-20, -10	-20, -10
U_D, V_D (ms^{-1})	10, 10	0, 0	0, 0	10, 10	20, 20	10, 10	10, 10
U_{SD}, V_{SD} (ms^{-1})	50, 50	0, 0	0, 0	50, 50	20 + 2(z-80)$^2(\pi t/T_M)$	50, 50	50, 50
U_{GW1} (ms^{-1})	10	20	20	10	$20\|\sin(2\pi t/T_M)\|\sin(2\pi t/T_{SD})$	$40F_6(t)$	$30F_7(t)$
V_{GW1} (ms^{-1})	0	0	0	0	0	0	$30F_7(t)$
W_{GW1} (ms^{-1})	5	5	-10	5	$-10\|\sin(2\pi t/T_M)\sin(2\pi t/T_{SD})\|$	$20F_6(t)$	$10F_7(t)$
k_1 (km^{-1})	2π/50	2π/50	2π/30	2π/50	2π/50	2π/50	2π/40
l_1 (km^{-1})	0	0	0	0	0	0	2π/40
m_1 (km^{-1})	0	2π/15	0	0	0	2π/15	2π/15
T_{GW1} (min)	20	∞	∞	20	20	20	20
U_{GW2} (ms^{-1})	0	-	0	0	0	0	$30G_7(t)$
V_{GW2} (ms^{-1})	20		10	20	$20\|\sin(2\pi t/T_M)\|\cos(2\pi t/T_{SD})$	$-30G_6(t)$	$-30G_7(t)$
W_{GW2} (ms^{-1})	2		2	2	$5\|\sin(2\pi t/T_M)\cos(2\pi t/T_{SD})\|$	$10G_6(t)$	$20G_7(t)$
k_2 (km^{-1})	0		0	0	0	0	2π/50
l_2 (km^{-1})	2π/100		2π/40	2π/100	2π/100	2π/100	2π/50
m_2 (km^{-1})	0		0	0	0	2π/20	2π/20
T_{GW2} (min)	30		∞	30	30	30	15
U_{GW3} (ms^{-1})	-	-	-	20	20	-	-
W_{GW3} (ms^{-1})				-10	-10		
k_3 (km^{-1})				2π/30	2π/30		
m_3 (km^{-1})				0	0		
T_{GW3} (min)				∞	∞		
V_{GW4} (ms^{-1})	-	-	-	10	10	-	-
W_{GW4} (ms^{-1})				2	2		
l_4 (km^{-1})				2π/40	2π/40		
m_4 (km^{-1})				0	0		
T_{GW4} (min)				∞	∞		
$< u'w' >$ (m^2s^{-2})	25	50	-100	-75	-100	50	75
$< v'w' >$ (m^2s^{-2})	20	0	10	30	10	-25	-25

$F_6(t)$, $F_7(t)$, $G_6(t)$ and $G_7(t)$ are functions that introduce intermittency to the gravity wave amplitudes, such that $F_6(t)$ = 1 for t = 0-3 h + 21R_1 h and 0 otherwise, $G_6(t)$ = 1 for t = 0-4 h + 20R_2 h and 0 otherwise, $F_7(t)$ = 1 for t = (0-2, 8-10) h + 14R_3 h and 0 otherwise, $G_7(t)$ = 1 for (0-1, 6-7, 10-11, 19-20) + 4R_4 hr and 0 otherwise, where R_1, R_2, R_3 and R_4 are random numbers between 0 and 1 assigned each day. T_M is 10 days, T_{SD} is 12 hours.

The results of the specified wave field investigations are presented in Section 6.4.1. The analysis was then applied to the real data observed by the Rothera and SAAMER radars for the years 2008 to 2012. The results from the real Rothera and SAAMER data are presented in Section 6.4.2.

6.4 Results

6.4.1 Specified Wave Fields

The first results we present are those from the testing of the momentum-flux method using the actual recorded distributions of meteors from the two radars, but with specified wave fields. As described earlier, these tests are essential if we are to have confidence in the calculated properties of the gravity-wave field, and in particular the momentum fluxes.

The recorded meteors from each radar were first sorted into monthly groups. For each month, the model, or specified, wave fields were sampled using the real meteor positions. For cases 6 and 7, twenty specified test wave fields were generated (each different due to the randomised elements of cases 6 and 7) for each month's meteor distribution and the ability of the gravity-wave analysis to recover the known specified momentum flux of these generated wave fields was measured. For brevity, only a single example month's distribution is presented here for cases 1 to 5, as the fixed, constant waves for these cases present a simpler test of the method than the transient gravity wave packets of cases 6 and 7.

Cases 1 to 5

The key features for the first five cases are as follows. The specified wave field of case 1 contains gravity waves that only vary horizontally, superimposed on background winds that comprise a mean flow and temporally-varying tides that do not vary with height. Case 2 contains no mean flow or tides but only a stationary gravity wave. Like case 2, case 3 also contains no mean flow or tidal activity, but has stationary zonal and meridional waves with no vertical phase variations and different spatial scales. Case 4 is more complicated in that it contains a superposition of all of the motions (wave, mean and tidal) from cases 1 and 3. It thus contains mean winds and tides, and zonal and meridional gravity-wave momentum fluxes, each of which have contributions from stationary and horizontally-propagating gravity waves of varying spatial structure. Case 5 introduces more complexity. It contains larger mean flow and diurnal tidal amplitude values, and a semidiurnal tide that increases in amplitude with increasing height, and is modulated with a period of 10 days. The gravity wave activity includes four waves, two contributing zonal momentum flux and two meridional. For each component there is a stationary gravity wave with fixed amplitude, and also a propagating wave whose momentum flux is modulated in magnitude by a 10-day oscillation and in magnitude and sign by the semidiurnal tide. The horizontal wavelength is different for each of the four waves.

The recovered momentum fluxes for cases 1 to 5 sampled by the meteor distributions recorded by the Rothera and SAAMER radars in May 2009 (as an example month) are given in Figure 6.7. Also shown are the specified momentum fluxes which the analysis is trying to recover. Since the specified wave field has constant momentum flux at all heights (each height gate is treated fully independently in the analysis), these specified fluxes appear as vertical lines on the plots at the chosen specified values.

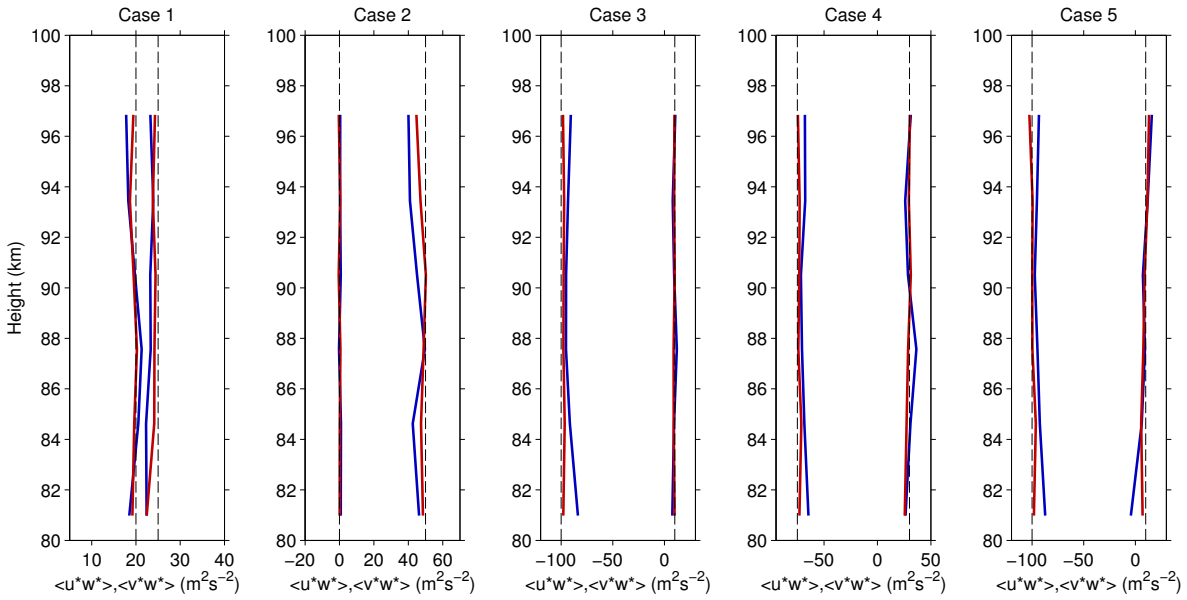

Figure 6.7: Recovered zonal and meridional momentum fluxes for cases 1 to 5, with the specified fluxes plotted as dashed lines. The results from both Rothera (blue) and SAAMER (red) are plotted on the same axes for each case.

The figure shows that the method is able to recover the momentum fluxes very accurately for the meteor distributions of the SAAMER radar, with the largest discrepancy being in the lowest height gate in case 1, where the difference between the specified and the recovered momentum flux is approximately 2.5 m^2s^{-2} ($\sim 10\%$). It is evident that the meteor distribution recorded by the Rothera radar is not able to recover the specified momentum fluxes as accurately as the SAAMER distribution, with the largest differences between specified and recovered momentum fluxes reaching nearly 20%. However, when averaged across all heights and cases, the mean discrepancy is less than 10% for both radars, and thus encourages confidence in the capability of the method.

Case 6

For each height gate, the mean and standard deviation of the recovered momentum fluxes for 20 specified fields (all with the same mean specified momentum flux) were calculated and compared to the specified momentum flux at that height. The results for each month are presented in Figure 6.8 for the sixth case as described in Table 6.1. This specified wave field featured two transient gravity waves that occurred for 3 and 4 hours each day, at random times. They had zonal and meridional propagation, horizontal and vertical phase variations, and periods of 20 and 30 minutes, with underlying mean winds and tides

of typical magnitudes and amplitudes for these latitudes.

In the Figure, the mean zonal and meridional momentum fluxes recovered for each monthly meteor distribution of 2009 in each height gate are shown. The mean momentum fluxes shown are each calculated from the 20 recovered momentum-flux estimates made for each height gate in each month. The error bars indicate the standard deviation of these 20 estimates for each height gate and month.

As can be seen from the figure, at all heights in most months for both radars the recovered momentum fluxes have values very close to those of the specified wave field. This is true for both the zonal and meridional components. The RMS difference between the recovered and specified momentum fluxes when averaged across all heights and months is ~ 6 m^{2}s^{-2} for both zonal and meridional components, for both radars. This RMS error comes most often from a slight overestimation. The largest differences however are for the Rothera radar in the lowest height gate in the summer months of November, December and January, when amplitudes are underestimated by up to 8 m^{2}s^{-2} in the meridional component and by up to 23 m^{2}s^{-2} in the meridional.

The standard deviations of the recovered momentum fluxes averaged across both radars, all months and height gates is of order ~ 6 m^{2}s^{-2}, though standard deviations are usually larger for the highest and lowest height gates, and for the Rothera radar.

The results presented above provide a way of deciding whether or not to use the gravity-wave fluxes recovered from any particular month of data in any particular height gate. In particular, if the attempts to recover the single momentum flux associated with the specified wave fields leads to a large standard deviation in the recovered fluxes, then this is an indication that the distribution of meteors in space and time for this particular month and height gate will not permit reliable recovery of the momentum flux of the real wave field.

Case 7

The results for each month are presented in Figure 6.9 for the seventh case as described in Section 6.3. This specified wave field had similar parameters to case 6 but with more intermittent gravity wave activity. One of the gravity wave packets has duration 1 hr, occurring 4 times a day, and propagates to the northeast, while the other has duration 2 hrs, occurs twice a day, and propagates to the southeast. Their periods are 15 and 20 minutes.

Again the mean zonal and meridional momentum fluxes recovered for each monthly meteor distribution of 2009 in each height gate are shown along with the specified values. From the figure it can be seen that the recovered fluxes show more variation than was seen for case 6.

The RMS differences between the recovered values and those specified, averaged across all months and heights, were $\sim$ 8, 12, 7 and 8 m^{2}s^{-2} for the SAAMER zonal, Rothera zonal, SAAMER meridional and Rothera meridional momentum fluxes respectively. Both radars' meteor distributions tend to produce slight underestimates of the zonal amplitudes for most months except for the winter months of

May to August. The meridional results are more complicated but Rothera often slightly overestimates momentum fluxes while SAAMER underestimates.

The standard deviation bars are often very small, except for the lowest height gate for the summer months of November to January for the Rothera radar, as was seen in case 6. This is accompanied by a large overestimate of the momentum flux in the lowest height gate of the Rothera results in December. The standard deviation averaged across all heights, months and zonal/meridional components was 4 m^2s^{-2} for the SAAMER radar and 6 m^2s^{-2} for Rothera.

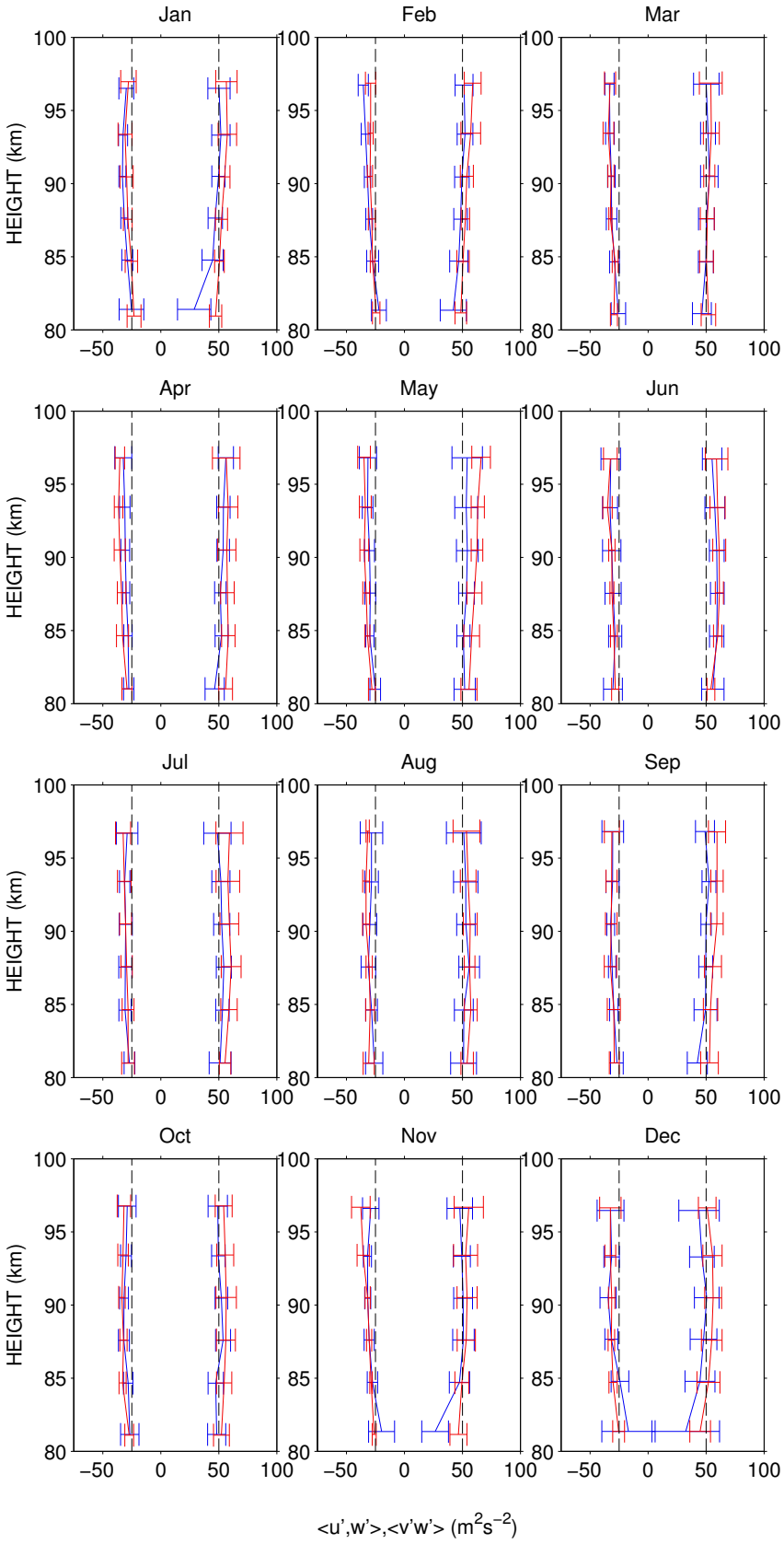

Figure 6.8: Recovered zonal and meridional momentum fluxes for case 6 of the specified wave fields. The results from both Rothera (blue) and SAAMER (red) are plotted on the same axes for each month of 2009. The points plotted represent the means of twenty randomised wave fields that all had the specified momentum fluxes given by the dashed black lines. The horizontal bars represent the standard deviations of the 20 recovered fluxes at each height.

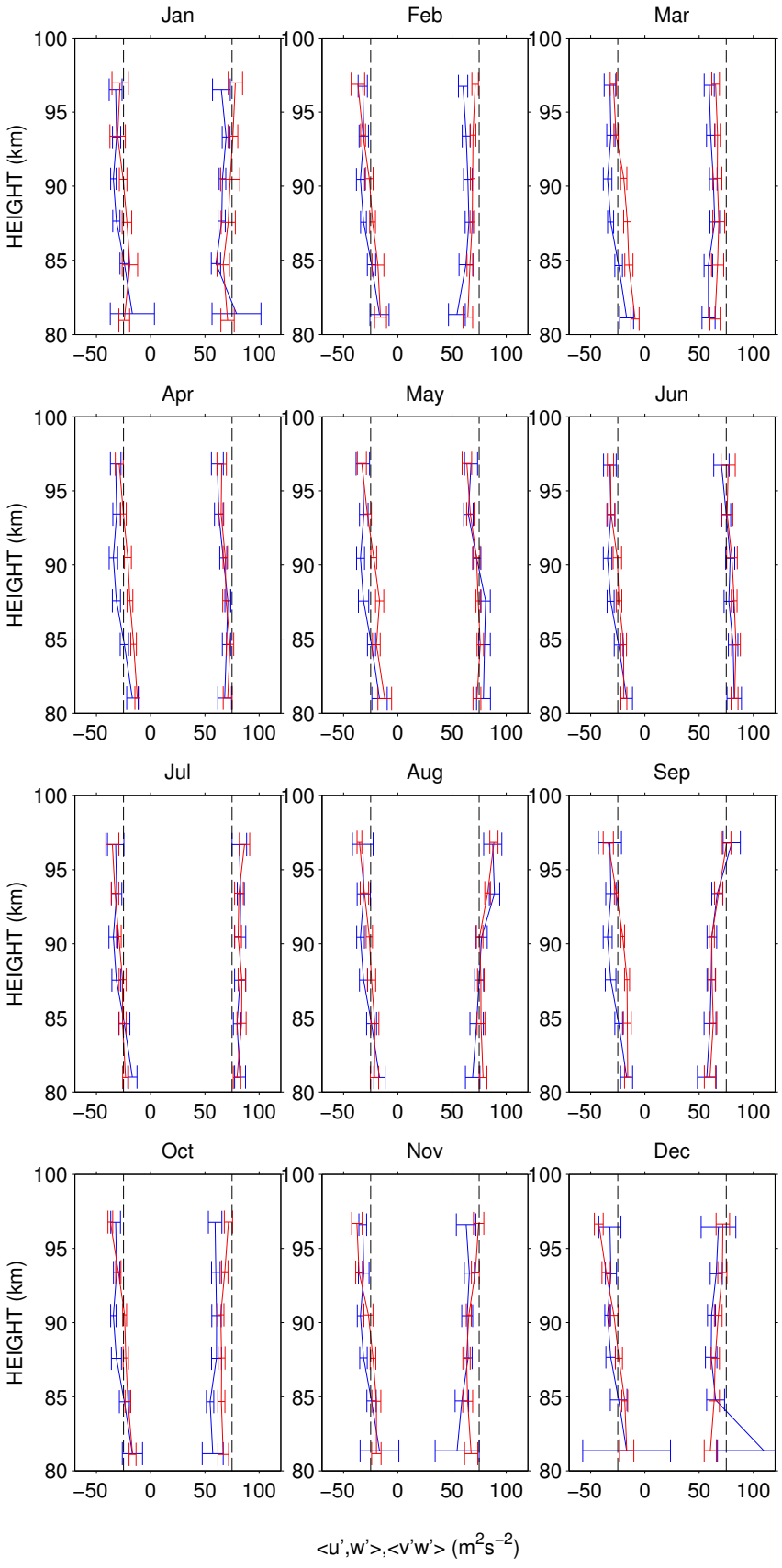

Figure 6.9: Recovered zonal and meridional momentum fluxes for case 7 of the specified wave fields. The results from both Rothera (blue) and SAAMER (red) are plotted on the same axes for each month of 2009. The points plotted represent the means of twenty randomised wave fields that all had the specified momentum fluxes given by the dashed black lines. The horizontal bars represent the standard deviations of the 20 recovered fluxes at each height.

Uncertainty on Meteor Positions

Meteors are recorded by SKiYMET radars with an uncertainty of $\pm$ 1.5^{o} in the azimuthal and zenith angles (Hocking, 2005). The possible error on the zenith angle is of particular concern as this would have an effect on the determined height of the meteor, and thus the background winds that are subtracted from the meteor's radial velocity, which can vary greatly with height.

To investigate the possible impact zenith uncertainty might have on the recovered momentum fluxes, a specified wave field analysis was performed with artificial errors added to each meteor's zenith angle (with each meteor's height adjusted and the Earth curvature correction applied appropriately). The artificial errors were normally distributed with a standard deviation of 1.5^{o}. The momentum flux analysis was performed with the zenith angles as recorded by the radar, and then the analysis was repeated but with the new zenith angles and heights (with the added errors). The specified radial velocities were fixed between analyses. The specified wave field of case 7 was used as it represented the toughest test with the most transient gravity wave field. However, the fixed zonal mean winds of case 7 were replaced with a strong vertical shear ranging from -30 ms^{-1} at 80 km to +30 ms^{-1} at 100 km, to further test the effects that zenith measurement error might have.

Figure 6.10 presents the results for both radars for a typical month (March 2009). The results for the original zenith angles (solid lines) and the zenith angles with errors added (dashed lines) are shown on the same axes.

The largest differences between the recovered momentum fluxes with and without artificial errors are for the Rothera radar in the highest and lowest height gates. However, averaged over all heights, the mean absolute discrepancy is just 5 m^{2}s^{-2} for the Rothera radar and less than 3 m^{2}s^{-2} for the SAAMER radar. This suggests that the measurement error in zenith angle (and thus height) is not a major impediment to the ability of the method to recover gravity-wave momentum fluxes.

6.4.2 Results From Observations Made at Riogrande and Rothera

We now turn our attention to the observed (real) data recorded by the SAAMER and Rothera radars during the years 2008 to 2012. This includes 60 months of observations for the Rothera radar, and 55 for SAAMER, which was deployed in May 2008.

Variances

The zonal and meridional variances, u'^2 and v'^2 respectively, are presented for both radars in Figure 6.11. The figures represent a composite year, obtained by averaging the monthly-mean variances over years 2008 to 2012. It can be seen that for nearly all months, for both radars and both directions, variance tends to increase with height. All four figures also reveal an approximately semiannual pattern, with

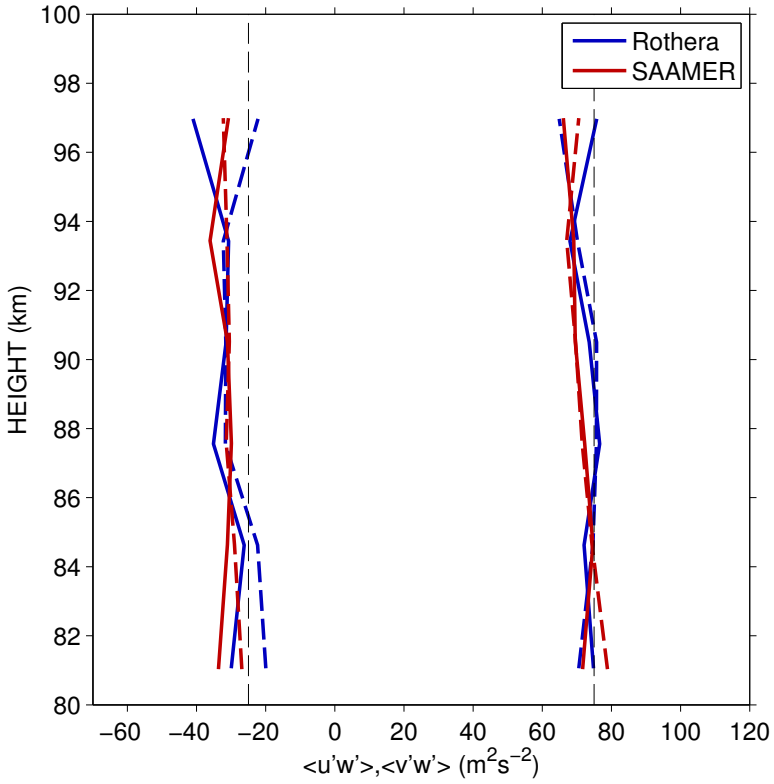

Figure 6.10: Recovered zonal and meridional momentum fluxes for case 7 of the specified fields over Rothera (blue) and SAAMER (red), for the original meteor zenith angles (solid coloured lines) and for the meteors with artificial errors added to the zenith angles (dashed coloured lines). The dashed black lines represent the specified momentum fluxes.

nearly all heights showing greatest variance in January and July, and least in March and October. The meridional variances tend to be slightly greater than the zonal variances.

Momentum Fluxes

The zonal and meridional momentum fluxes ($u'w'$ and $v'w'$ respectively) are presented for both radars in Figure 6.12. The lines represent the mean momentum fluxes as a function of height for the years 2008 to 2012. The "error bars" are the standard error on the means, and thus give an indication of the interannual variability. For each month, the zonal and meridional momentum fluxes are plotted on separate axes, with the SAAMER results in red and the Rothera results in blue.

The data presented in Figure 6.12 are reproduced as contour plots in Figure 6.13 for easier seasonal comparisons. The figure reveals that the momentum fluxes have an annual cycle for most heights in the zonal component over Rothera and SAAMER. The meridional seasonal cycle is less clear but there is a semiannual cycle in momentum fluxes over both sites at heights above 90 km.

It is apparent that for most months and heights, the momentum fluxes recovered are very similar for both radars, as would be expected for two sites so close to each other. Momentum fluxes are generally directed

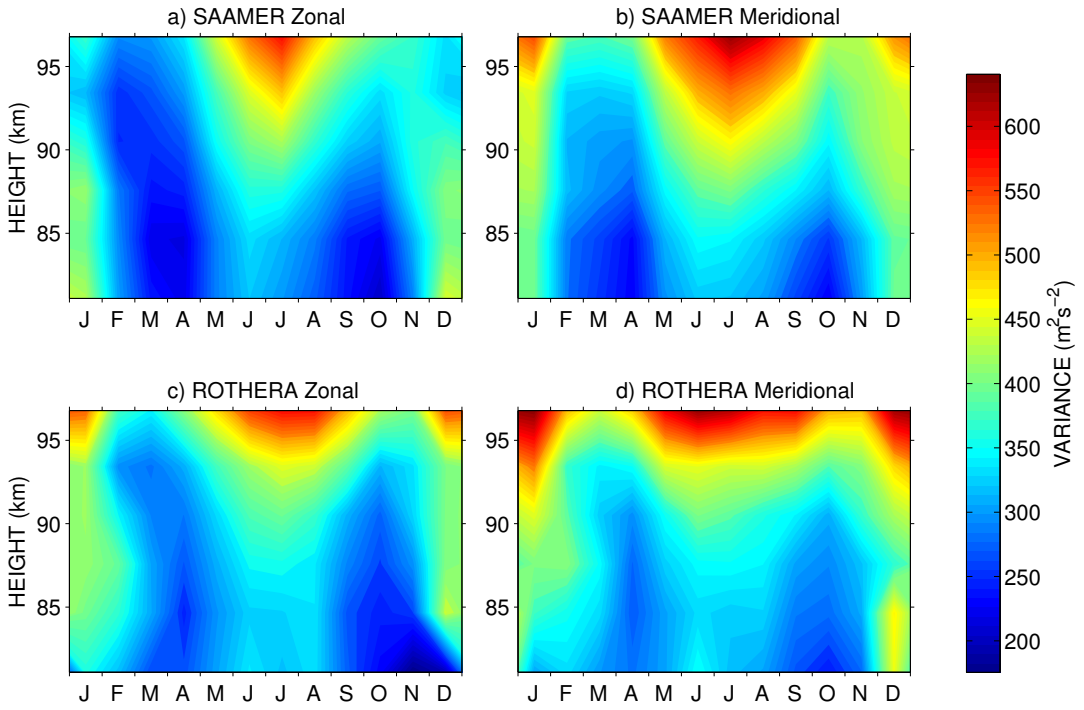

Figure 6.11: Variances as functions of month and height for composite years of the 2008 to 2012 data, for a) SAAMER zonal, b) SAAMER meridional, c) Rothera zonal and d) Rothera meridional.

northwards and eastwards, with some exceptions, and the fluxes over Rothera are more northward and more eastward than over the SAAMER radar for most months and heights.

From October to March, zonal fluxes decrease with increasing height, while in April to August, zonal fluxes are either constant with increasing height, or increase. The largest monthly-mean zonal fluxes are at heights near 80 km in the summer month of January, reaching values of $\sim$40 m^2s^{-2} over the SAAMER radar and approximately 60 m^2s^{-2} over Rothera. However, it should be remembered that the specified wave analysis highlighted the inaccuracy of momentum flux retrievals at 80 km over Rothera.

The meridional fluxes increase with increasing height above 90 km for every month and for both sites. Below 90 km, meridional fluxes tend to remain approximately constant with increasing height, but decrease with increasing height in February and June, and over Rothera in December.

The standard error bars representing the inter-annual variability are nearly always largest in the highest and lowest gates, and are generally larger over Rothera than SAAMER. For most months and heights however, the bars are small, indicating strong similarities from year to year.

Accelerations

The acceleration associated with momentum flux divergence can be calculated (Liu et al., 2013) according to the equation

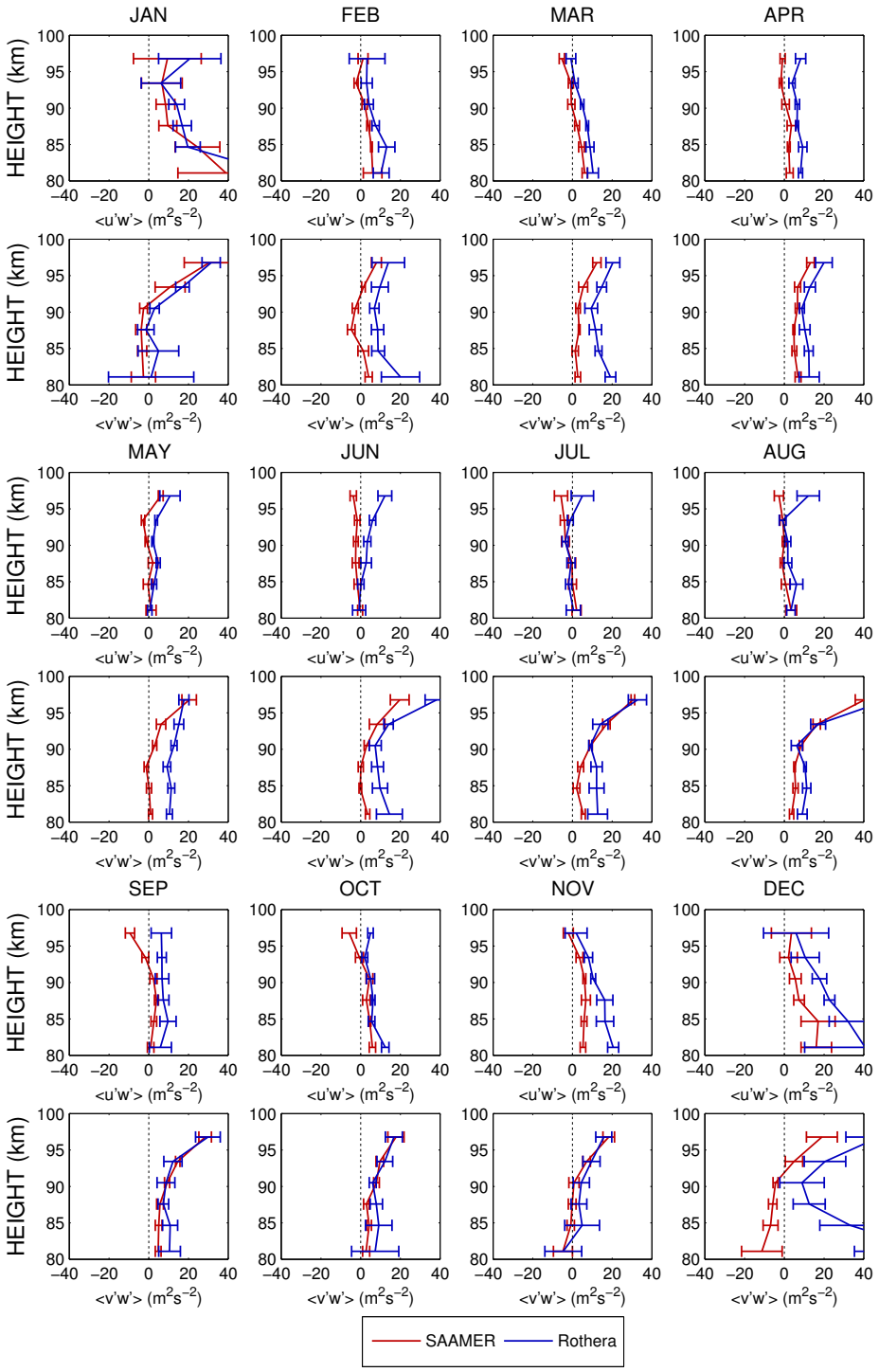

Figure 6.12: Monthly-mean momentum fluxes as a function of height for the Rothera (blue) and SAAMER (red) radars for a composite year of the 2008 to 2012 data. For each month, the zonal momentum fluxes are plotted in the subfigures above the meridional momentum fluxes. The horizontal bars are the standard errors and thus give an indication of the interannual variability.

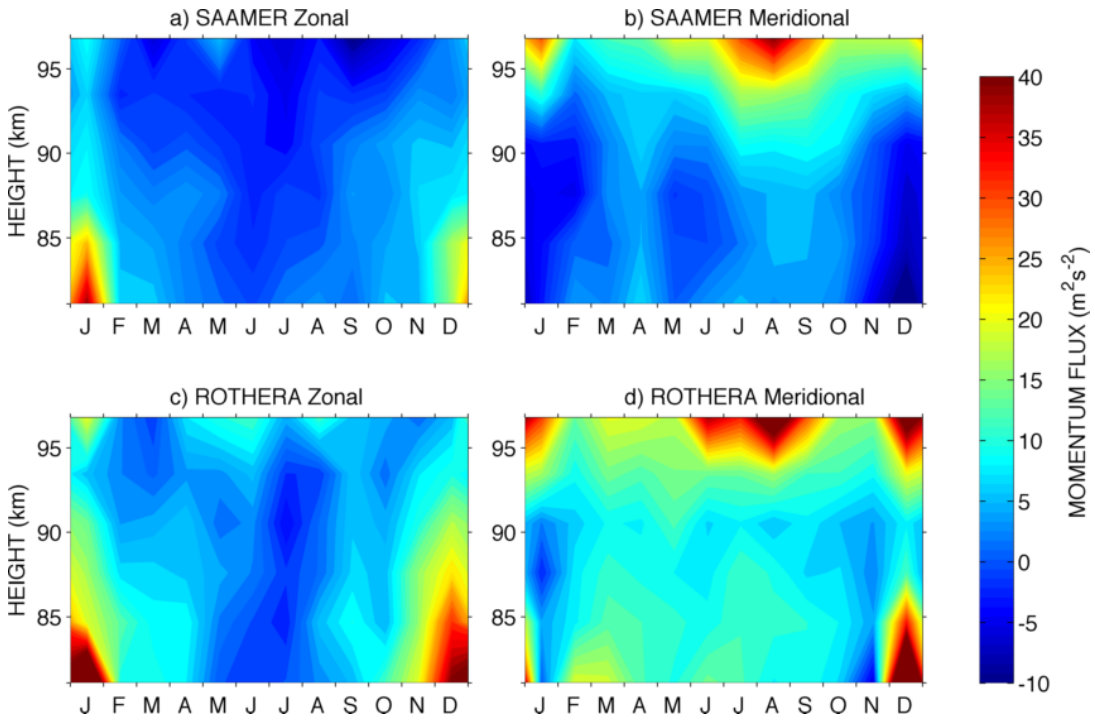

Figure 6.13: Monthly-mean momentum fluxes as a function of height for a composite year of the 2008 to 2012 data for a) SAAMER zonal, b) SAAMER meridional, c) Rothera zonal and d) Rothera meridional.

$$X = -\frac{1}{\rho}\frac{\partial}{\partial z}(\rho < u'w' >) \tag{6.4}$$

where X is the acceleration caused by the deposited momentum, and ρ is the density, taken for each height from the MSIS-E-90 model atmosphere. The monthly-mean accelerations calculated between the middle two height gates (i.e., at approximately 90 km) are presented for SAAMER and Rothera in Figures 6.14a and b respectively, for the entire 2008 to 2012 interval. The middle two heights were chosen as they showed the least variability in the specified wave field analysis due to the peak in meteor count rates at heights near 90 km. Also plotted on the figures are the monthly-mean zonal winds calculated at the same height by the least squares fit method outlined in section 3.2.3.

Considering the SAAMER result first, there is an annual oscillation apparent, with strong eastward accelerations in the summers and weaker westwards accelerations in the winters. The largest eastward accelerations occur when the zonal winds are westwards, just before the winds turn eastward. The correlation coefficient between the two time series is -0.26, showing anti-correlation with a two-tailed p-value of 0.054 (i.e., there is approximately a 1 in 18 chance of obtaining the same correlation between two time series of random noise).

The Rothera result has similar features, but the anti-correlation between zonal acceleration and zonal winds is much more evident. This is because while the mean winds are very similar between the two sites, the annual cycle in accelerations over Rothera is more consistent, with clear peaks of eastward acceleration in the summer of every year. The correlation coefficient between the accelerations and the

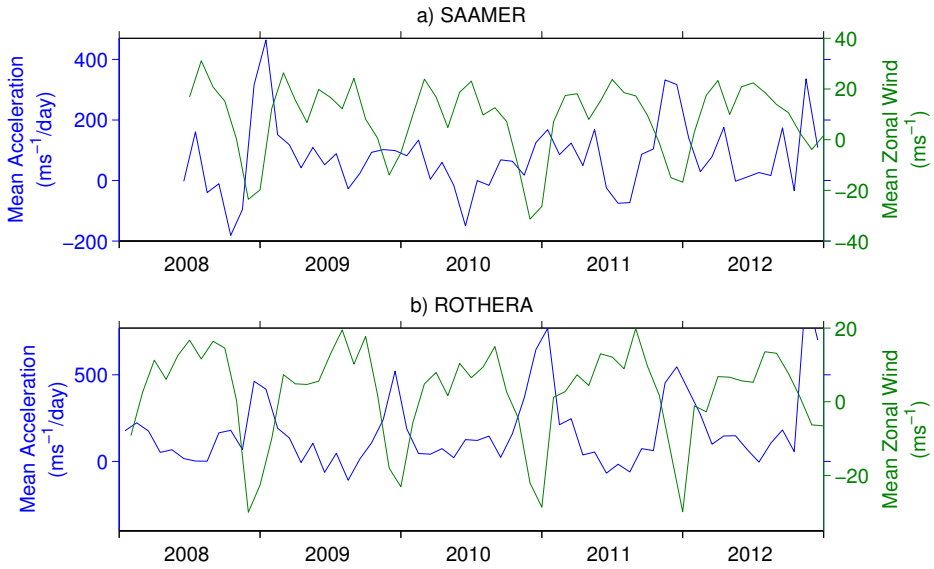

Figure 6.14: Derived monthly-mean accelerations as a function of time for a) SAAMER and b) Rothera at a height of ∼90 km (blue, left y-axis). Also plotted are the monthly-mean zonal winds at the same height (green, right y-axis).

winds over Rothera was -0.63, with a corresponding significance above 99.9%.

6.5 Discussion

It was seen in Figure 6.7 that the momentum flux method outlined in section 6.3 was able to recover the five simplest specified wave field zonal and meridional fluxes very well, with absolute differences between specified and recovered fluxes of less than 10% for both radars, when averaged over all heights. However, the Rothera radar tended to recover fluxes slightly less accurately than the SAAMER instrument. This is most likely due to the lower meteor count rate recorded by the Rothera radar, as the largest discrepancies occur in the highest and lowest height gates, where count rates are naturally low anyway.

The specified wave field analysis of Case 6 (Figure 6.8) showed that the method was able to accurately recover the momentum fluxes of transient waves, appearing for just 3 and 4 hours each day, at different times. The largest differences were in lowest height gate for the summer months of November to January over the Rothera site.

Figure 6.9 revealed that the recovered momentum fluxes for the more intermittent waves of case 7 were again generally very good, however the RMS differences between the specified and recovered fluxes were slightly larger than those seen in case 6. The largest standard deviations were again for the Rothera site in the lowest height gate of the summer months. This can likely be attributed to low meteor counts (or an unsuitable meteor distribution in space and time), and implies that the observed summer momentum fluxes over Rothera may be subject to large errors at this lowest height.

The results do suggest however that the ability of the analysis to recover the momentum flux from measurements made by the Rothera radar is sufficient to allow meaningful investigation of the real gravity-wave momentum fluxes for the great majority of months and heights, at least when using monthly means.

The results essentially confirm the conclusions of Fritts et al. (2010) that SAAMER yields accurate estimates of the specified monthly-mean momentum flux. Further, they indicate that the Rothera radar, despite not being optimised for gravity-wave measurements, can almost as accurately estimate specified monthly-mean gravity-wave momentum fluxes. However, our analysis here for cases 6 and 7 extends the work of the Fritts et al. study to consider data from a whole year of observation rather than from just one example month, and to a larger number of specified wave fields (20 rather than 10). We will therefore make the assumption as per Fritts et al. (2010b, 2012a) that the analysis technique applied to the actual recorded meteors can yield accurate estimates of monthly-mean gravity-wave momentum flux.

The analysis leading to Figure 6.10 investigated the effect of introducing artificial errors to the meteors' zenith angles, as zenith measurement by SKiYMET radars can have errors of $\pm 1.5^{\circ}$ (Hocking, 2005). This test was performed because the standard specified-wave field analysis tests the robustness of the mathematics of the method, but assumes that the measurements are made with perfect accuracy. The momentum flux analysis was thus performed twice with the same set of meteors, but with errors on the zenith angles added for the second run and the heights adjusted accordingly. The error distribution was normal with a standard deviation of $\sigma = 1.5^{o}$. This was thus a pessimistic test, as some meteors would have had errors as large as 5° assigned. The differences between the two analyses (with and without errors) were largest in the highest and lowest gates. This is as would be expected for the meteor counts as a function of height. Note that the specified mean winds in this analysis would not have adversely affected the recovered momentum flux accuracy in the extreme height gates any more than the central heights, as although the winds were strongest at 80 and 100 km, the vertical shear was constant at all heights (realistic for the summer months at these latitudes) and thus a fixed error in the height determination would have affected all height gates equally. However, the analysis nevertheless revealed that the effects of zenith error were small for the Rothera radar (with RMS differences of 5 $\mathrm{m^2 s^{-2}}$), and smaller still for SAAMER (RMS differences less than 3 $\mathrm{m^2 s^{-2}}$).

The variances presented in Figure 6.11 revealed an approximately semiannual oscillation, with maxima near the solstices and minima near the equinoxes, and an increase in zonal and meridional variance with height for nearly all months over both sites. This seasonal pattern and increase of variance with height is in excellent agreement with the MF radar observations of Dowdy et al. (2007) made at the Davis and Syowa Antarctic bases (69°S, 78°E and 69°, 40°E, respectively). The increase of variance with height is less than the exponential growth that would be expected for wave energy conservation in an atmosphere that decreases in density with increasing height. This is likely due to the MLT-region wave field that is observed by the radar (with vertical wavelengths less than ~ 3 km) being comprised of a mixture of unsaturated and saturated waves, i.e., those that do and do not increase in amplitude with height (Mitchell and Beldon, 2009).

It was seen in Figure 6.12 that the standard error bars for the composite month momentum fluxes were often small, and the individual years (not shown) generally showed little interannual variability. The largest standard error bars were for the lowest height gate in the summer months of the Rothera results. However, as was seen in the specified wave field results of Figures 6.8 and 6.9, this is unlikely to be due to true natural variability, and more likely to be a result of low meteor counts and less suitable meteor distributions at these times and heights.

When comparing the momentum fluxes presented in Figure 6.12 with the variances of Figure 6.11, it should be remembered that the momentum fluxes are obtained from monthly-means of vector quantities, and so give an indication of the anisotropy of the wave field. For example, large variances are observed over both sites in the winter months of June and July, however the zonal momentum fluxes in these months are relatively small. This implies that the waves contributing to the large zonal variance are approximately equally distributed between eastward and westward propagating. In contrast, the larger (and positive) meridional momentum fluxes imply that the wave field is skewed towards northward-propagating waves.

With the exception of the summer months of December and January, and in the upper heights of the meridional component in the winter, momentum flux magnitudes are generally less than 25 m^2s^{-2} over both sites. For comparison, Placke et al. (2011b) applied the Hocking method to data from the meteor radar at Andenes (69^{o}N, 16^{o}E) and found that both zonal and meridional momentum fluxes were in the range -12 m^2s^{-2} to +12 m^2s^{-2}. Espy et al. (2006) combined the cross-correlation coefficients between horizontal and vertical wind perturbations from a sodium airglow imager at Rothera and wind variances from the co-located MF radar with a gravity-wave model to obtain predictions of the gravity-wave momentum flux at a height of $\sim$ 90 km, using the spectral analysis technique first published in Gardener et al. (1999). The momentum fluxes were in good agreement with the results reported here for the meridional component, with momentum fluxes increasing in the autumn to weakly positive values in the winter, and then becoming negative again in the spring. In the zonal component, the general trend was again very similar, with the momentum fluxes being approximately 15 m^2s^{-2} more westward in the winter. However, the zonal momentum fluxes at 90 km found by Espy et al. (2006) were more westward than the zonal momentum fluxes at similar heights presented here for all months shown. A possible reason for this difference might be that the method of Espy et al. (2006) gives an upper limit to the momentum fluxes (as it neglects ducting), which has previously been found to give larger fluxes than other techniques (Swenson et al., 1999; Fritts and Alexander, 2003). Secondly, the results presented in Espy et al. (2006) are obtained from 77 nights of observations over a 2 year interval, in contrast to the sustained observations used here.

The zonal momentum fluxes in Figure 6.12 were seen to be positive over both sites at all heights in summer. This can be explained by considering the zonal winds lower in the atmosphere (see for example Figure 1.7). In the summer, the stratospheric winds are strongly westwards, such that the westward-propagating gravity waves encounter critical levels as they ascend and are filtered out. As a result, the spectrum of waves that reaches the MLT are carrying mostly eastwards (positive) momentum. In the winter the reverse occurs, as can be seen by the westwards momentum fluxes over SAAMER in June

and July. The weakly eastward momentum fluxes over Rothera in June are surprising and unexplained, but could be due to tropospheric excitation conditions.

The zonal momentum flux was seen to decrease with increasing height over both sites in the months October through to March, and while SAAMER zonal momentum fluxes were approximately constant with height in June, July and August, the Rothera zonal fluxes increased with increasing height for these months. These observations support the theory of decreasing zonal momentum fluxes (with increasing height) in the summer months (due to deposition of momentum) causing the mean winds to reverse in the MLT region, such that the westward winds of radiative balance become eastward and dynamically balanced (see for example sections 1.2.2 and 1.3).

The possible relationship between the change in the zonal momentum flux with height and the mean wind was investigated further in Figure 6.14. At first glance the accelerations seem large, with summertime values reaching over 400 $ms^{-1}day^{-1}$ over SAAMER and 700 $ms^{-1}day^{-1}$ over Rothera. For example, the Fritts and Alexander (2003) gravity wave review summarised findings of mean flow forcings not reaching more than 70 $ms^{-1}day^{-1}$ over extra-tropical sites. However, when the summer months of November, December and January are excluded, the mean (absolute) accelerations are 96 $ms^{-1}day^{-1}$ and 72 $ms^{-1}day^{-1}$ over Rothera and SAAMER respectively. Hocking (2005) found summertime accelerations reached monthly-mean values of nearly 200 $ms^{-1}day^{-1}$ over Resolute Bay, in arctic Canada. The values found here are thus not unreasonable, especially when it is considered that they are over the most intense gravity-wave hotspot in the world (e.g., Figure 6.2, after Alexander et al. (2008) and Ern et al., (2004)). Further, a very similar analysis applied to data from the Trondheim SKiYMET radar has produced accelerations that are in good agreement with the predictions of the Whole Atmosphere Community Climate Model (Rosmarie de Wit, private communication).

The figure revealed an anti-correlation between the accelerations over SAAMER and the mean winds at the same height, and a stronger anti-correlation between the same parameters over Rothera. This is in agreement with the Fritts and Alexander (2003) summary of gravity-wave accelerations generally opposing the mean winds. A full analysis of forcing and propagation conditions at lower heights would be required to investigate the reasons for the stronger anti-correlation over Rothera than SAAMER. The results of the figure do however provide evidence supporting the idea of the divergence of the vertical flux of zonal momentum accelerating the mean flow, such that the westward winds are turned eastwards, and vice versa in winter. However, it should be noted that the gravity-wave forcings presented here are localised and not necessarily sustained around the longitudinal circle, reducing their impact on the zonal-mean zonal winds.

6.6 Conclusions

In this chapter, we evaluated the capabilities of the Hocking (2005) method to measure gravity-wave momentum fluxes and variances using the Rothera (68^o S, 68^o W) and SAAMER (54^o S, 68^o W) all-sky VHF meteor radars, located either side of the Drake passage gravity-wave hotspot. The method was

adapted to reduce the contamination from the large semidiurnal tides and vertical wind shears that can occur at these latitudes.

The method was tested by sampling various specified wave fields of increasing complexity with the actual meteor positions in time and space as recorded by the two radars. It was seen that the momentum fluxes recovered by the Rothera radar's meteor distributions tended to differ from the specified values by slightly more than the results from the SAAMER radar, due to SAAMER's greater power and antenna configuration providing higher meteor counts (and at lower zenith angles). Nevertheless, the recovered fluxes were in very good agreement with the specified values for most months and heights, providing confidence in the method's ability to obtain meaningful gravity-wave momentum fluxes. Further, an investigation into the effects of measurement error on the zenith angle (and thus the height at which the background winds are interpolated to before subtraction) revealed that this error has only small effects on the recovered fluxes and is not a major impediment to the method.

For climatology purposes, monthly-mean gravity-wave momentum fluxes and variances were reported for a composite year of the 2008 to 2012 data for both radars. The horizontal variances revealed semi-annual oscillations with maxima near the solstices and minima near the equinoxes, and an increase in variance with height, in excellent agreement with other studies at these latitudes.

Momentum flux magnitudes were seen to be less than 25 m^2s^{-2} for most months and heights. Zonal momentum fluxes decreased with increasing height in the Summer months, indicating the deposition of eastwards momentum via wave-breaking mechanisms. This supports the theory of summertime gravity-wave activity acting to decrease and reverse the westward winds in the MLT-region.

Accelerations calculated from the change in momentum flux with height were found to be consistent with previous studies for most months, but were larger than previously reported results in the summer. The accelerations were found to be strongly anti-correlated with the mean zonal winds at the same height, in agreement with other studies.

Chapter 7

Suggestions for Further Work

The previous chapters have highlighted a number of questions that remain unanswered. Possible topics for further investigation include:

Intra-seasonal Oscillations over Ascension Island

Section 4.4.5 revealed the presence of signals in the MLT region wind spectra that were at the same periods as intra-seasonal oscillations in the tropospheric latent heat release and ultra-fast Kelvin wave amplitudes. However, oscillations at these periods have also been noted in tidal and gravity wave amplitudes (e.g., Miyoshi and Fujiwara, 2006; Eckermann et al., 1997). A modeling study might help to quantify the contribution that UFKW make to the MLT region winds in comparison to gravity waves and tides, clarify the mechanisms that create this coupling between atmospheric layers, and in particular those processes that carry ISO periodicities to mesospheric winds.

Migrating and Non-migrating Tidal Modes

It was seen in Chapter 5 that eCMAM and WACCM have difficulties producing the tidal fields over Ascension Island. A large part of the discrepancies are likely due to the longitudinal variability created by non-migrating tidal modes. To improve the accuracy of model predictions, more observational studies are needed. As discussed, single-site instruments can't distinguish between migrating and non-migrating modes, and while various satellite studies have been able to separate them, the satellite orbits generally require averaging on timescales of 2 to 3 months. Murphy et al. (2003) used three MF radars situated at approximately the same latitudes in Antarctica to obtain a common migrating tidal component and subtract it to leave the non-migrating modes over each site. The relatively large number of meteor radars deployed around the world make them a good candidate for investigating non-migrating modes at other latitudes. Separation of migrating from non-migrating components would also help in investigations of how latent heat release changes during El Niño and La Niña events affect MLT-region tides. The relative impact of the QBO and the ENSO on tidal amplitudes in the MLT region remains an interesting question.

Instrumental Biases

The requirement for chains of ground-based instruments at other latitudes could be eased by multi-instrument studies. However, the biases that can cause different instruments to produce different measurements of the same fields would need to be better understood. Three of the University of Bath's SKiYMET radars are particularly well placed to help investigate these biases: the Rothera radar is co-located with an MF radar, there is an MST radar at the Esrange site near Kiruna, and the Bear Lake site also contains a LiDAR.

Gravity-wave Momentum Fluxes

Chapter 6 demonstrated that meteor radars can measure gravity-wave momentum fluxes over Rothera and Riogrande (SAAMER) either side of the Drake passage However, radars operate at other places, regions where wave sources would be very different. For example, over the small and oceanic Ascension Island, unlike the topography-generated gravity-wave field over the Drake passage hotspot, most waves would be generated by deep tropospheric convection and so it would be very interesting to investigate the momentum fluxes there. Alternatively, the radar at Esrange is situated at the conjugate latitude to Rothera, but in a much less mountainous location.

Tides over Esrange

While the Ascension Island site is the only one of the University of Bath's radars to be situated close enough to the equator for Kelvin wave studies, the tidal analysis of section 5.3 could easily be applied to the data recorded by the other radars. For example, data from the Esrange radar (68^{o} N) could be studied to investigate the relationship between sudden stratospheric warmings and short-term tidal variability, and how the tides interact with the planetary wave activity associated with SSWs.

Long-term Variability and the Solar Cycle

The Ascension Island and Esrange radars have been operating for 13 and 15 years respectively. While the Esrange dataset has far fewer gaps than the Ascension Island data, both would be suitable for studies investigating long-term variability of MLT-region winds and waves, particularly that due to the 11-year solar cycle.

Stratospheric Propagation Conditions

The seasonal and interannual variabilities of the gravity-wave momentum fluxes over Rothera and the Tierra del Fuego reported in Chapter 6 might be explained in part by a detailed analysis of the propagation conditions for the years 2008 to 2012. Stratospheric winds can be obtained from the UKMO stratospheric data assimilation system, and are available for the years studied.

References

Akmaev, R.A., Fuller-Rowell, T.J., Wu, F., Forbes, J.M., Zhang, X., Anghel, A.F., Iredell, M.D., Moorthi, S., and Juang, H.M.: Tidal variability in the lower thermosphere: comparison of whole atmosphere model (WAM) simulations with observations from TIMED, Geophys. Res. Lett., 86, L03810, doi:10.1029/2007GL 032584, 2008

Akmaev, R.A., and Fomichev, V.: Cooling of the mesosphere and lower thermosphere due to doubling of CO2, Ann. Geophys., 16, 1501-1512, 1998

Alexander, M.J., Gille, J., Cavanaugh, C., Coffey, M., Craig, C., Eden, T., Francis, G., Halvorson, C., Hannigan, J., Khosravi, R., Kinnison, D., Lee, H., Massie, S., Nardi, B., Barnett, J., Hepplewhite, C., Lambert, A., and Dean, V.: Global estimates of gravity wave momentum flux from High Resolution Dynamics Limb Sounder observations, J. Geophys. Res., 113, D15S18, doi:10.1029/2007JD008807, 2008

Andrews, D.G., Holton, J.R., and Leovy, C.B.: Middle Atmosphere Dynamics, Academic Press, 1987.

Andrioli, V.F., Clemesha, B.R., Batista, P.P, and Schuch, N.J.: Atmospheric tides and mean winds in the meteor region over Santa Maria (29.71S; 53.81W), J. Atmos. Sol. Terr. Phys., 71, 1864-1876, 2009

Andrioli, V.F., Fritts, D.C., Batista, P.P., and Clemesha, B.R.: Improved analysis of all-sky meteor radar measurements of gravity wave variances and momentum fluxes, Ann. Geophys., 31, 889-908, 2013

Antonita, T.M., Ramkumar, G., Kumar, K.K., and Deepa, V.: Meteor wind radar observations of gravity wave momentum fluxes and their forcing toward the Mesospheric Semiannual Oscillation, J. Geophys. Res., 113, D10115, doi:10.1029/2007JD009089, 2008

Avery, S.K., Vincent, R.A., Phillips, A., Manson, A.H., and Fraser, G.J.: High-latitude tidal behaviour in the mesosphere and lower thermosphere, J. Atmos. Terr. Phys., 51, 7-8, 595-608, doi:10.1016/0021-9169(89)90057-3, 1989

Beard, A.G., Mitchell, N.J., Williams, P.J.S., Kunitake, M.:Non-linear interactions between tides and planetary waves resulting in periodic tidal variability, J. Atmos. Sol. Terr. Phys., 61, 5, 363-376, doi: 10.1016/S1364-6826(99)00003-6, 1999

Beldon, C.L. and Mitchell, N.J.: Gravity wave-tidal interactions in the mesosphere and lower thermosphere over Rothera, Antarctica (68 degrees S, 68 degrees W), J. Geophys. Res.-Atmos., 115, D18101, doi: 10.1029/2009JD013617, 2010

Berger, U., and Demeris, M.: Cooling of the upper-atmosphere due to CO2 increases - a model study, Ann. Geophys., 11, 9, 809-819, 1993

Buriti, R.A., Hocking, W.K., Batista, P.P., Medeiros, A.F., and Clemesha, B.R.: Observations of equatorial mesospheric winds over Cariri (7.4S) by a meteor radar and comparison with existing models, Ann. Geophys., 26, 485-497, 2008

Burrage, M.D., Hagan, M.E., Skinner, W.R., Wu, D.L., and Hays, P.B.: Long-term variability in the solar diurnal tide observed by HRDI and simulated by the GSWM, Geophys. Res. Lett., 22, 19, 2641-2644, doi:10.1029/95GL02635, 1995

Canziani, P. O., Holton, J. R., Fishbein, E., Froidevaux, L., and Waters, J. W.: Equatorial Kelvin waves - a UARS MLS view, J. Atmos. Sci., 51, 3053-3076, 1994.

Ceplecha, Z., Borovicka, J., Elford, W.G., ReVelle, D.O., Hawkes, R.L., Prubcan, V., and Simek, M.: Meteor Phenomena and Bodies. Space Science Reviews, 84(3-4), 327-471, doi: 10.1023/A:1005069928850, 1998

Chang, J.L., and Avery, S.K.: Observations of the diurnal tide in the mesosphere and lower thermosphere over Christmas Island, J. Geophys. Res.-Atmos. , 102, D2, 1895-1907, 1997

Chang, L. C., Palo, S. E., Liu, H. L., Fang, T. W., and Lin, C. S.: Response of the thermosphere and ionosphere to an ultra fast Kelvin wave, J. Geophys. Res.-Space, 115, A00G04, 2010.

Chang, L. C., Ward, W.E., Palo, S.E., Du, J., Wang, D.-Y, Liu, H.-L., Hagan, M. E., Portnyagin, Y., Oberheide, J., Goncharenko, L.P., Nakamura, T., Homann, P., Singer, W., Batista, P., Clemesha, B., Manson, A.H., Riggin, D.M., She, C.-Y., Tsuda, T., and Yuan, T.: Comparison of diurnal tide in models and ground-based observations during the 2005 equinox CAWSES tidal campaign, J. Atmos. Sol. Terr. Phys., 78-9, 19-30, doi:10.1016/j.jastp.2010.12.010, 2010

Chang, L.C., Palo, S.E. and Liu, H.L.: Short-term variability in the migrating diurnal tide caused by interactions with the quasi 2 day wave, J. Geophys. Res.-Atmos., 116, D12112, doi: 10.1029/2010JD014996, 2011

Charney, J.G., and Drazin,P.G.: Propagation of planetary-scale disturbances from the lower into the upper atmosphere, J. Geophys. Res.-Atmos, 66(1), 83-109, 1961

Chen, Y.-W. and Miyahara, S.: Analysis of fast and ultra-fast Kelvin waves simulated by the Kyushu-GCM, J. Atmos. Sol.-Terr. Phy., submitted, 2011.

Chu, X.Z., Gardner, C.S. and Papen, G.: Lidar observations of polar mesospheric clouds at South Pole: Diurnal variations, Geophys. Res. Lett., 28, 10, 1937-1940, doi: 10.1029/2000GL012525, 2001

Clemesha, B.R., Batista, P.P., Buriti da Costa, R.A., and Schuch, N.: Seasonal variations in gravity wave activity at three locations in Brazil, Ann. Geophys., 27, 1059-1065, 2009

Davis, R.N., Chen, Y.-W., Miyahara, S., and Mitchell, N.J.: The climatology, propagation and excitation of ultra-fast Kelvin waves as observed by meteor radar, Aura MLS, TRMM and in the Kyushu-GCM, Atmos. Chem. Phys., 12, 4, 1865-1879, doi: 10.5194/acp-12-1865-2012, 2012

Day, K.A., and Mitchell, N.J.: The 5-day wave in the Arctic and Antarctic mesosphere and lower thermosphere, J. Geophys. Res., 115, D01109, doi:10.1029/2009JD012545, 2010

Deepa, V., Ramkumar, G., Antonita, M., Kumar, K.K., and Sasi, M.N.: Vertical propagation characteristics and seasonal variability of tidal wind oscillations in the MLT region over Trivandrum (8.5^{o}N, 77^{o}E): first results from SKiYMET meteor radar, Ann. Geophys., 24, 2877-2889, 2006

Dowdy, A.J., Vincent, R.A., Tsutsumi, M., Igarashi, K., Murayama, Y., Singer, W., and Murphy, D.J.: Polar mesosphere and lower thermosphere dynamics: 1. Mean wind and gravity wave climatologies, J. Geophys. Res., 112, D17104, doi:10.1029/2006JD008126, 2007

Du, J., Ward, W.E., Oberheide, J., Nakamura, T., and Tsuda, T.: Semidiurnal tides from the Extended Canadian Middle Atmosphere Model (CMAM) and comparisons with TIMED Doppler Interferometer (TIDI) and meter radar observations, J. Atmos. Sol. Terr. Phys., 69, 2159-2202, doi:10.1016/j.jastp.2007.07.014, 2007

Du, J.: A mesosphere and lower thermosphere dynamics study using the extended Canadian Middle Atmosphere Model (CMAM), University of New Brunswick (Canada), 2008

Du, J., and Ward, W.E.: Terdiurnal tide in the extended Canadian Middle Atmospheric Model (CMAM), J. Geophys. Res.-Atmos., 115, D24106, doi: 10.1029/2010JD014479, 2010

Dunkerton, T. J.: Role of the Kelvin wave in the westerly phase of the semiannual zonal wind oscillation, J. Atmos. Sci., 36, 32-41, 1979.

Dunkerton, T.J.: Theory of the mesopause semiannual oscillation, J. Atmos. Sci., 39, 2681-2690, 1982

Dunkerton, T. J.: The role of gravity waves in the quasi-biennial oscillation, J. Geophys. Res.-Atmos., 102, 26053-26076, 1997.

Eckermann, S. D. and Vincent, R. A.: 1st observations of intraseasonal oscillations in the equatorial mesosphere and lower thermosphere, Geophys. Res. Lett., 21, 265-268, 1994.

Eckermann, S. D., Rajopadhyaya, D. K., and Vincent, R. A.: Intraseasonal wind variability in the equatorial mesosphere and lower thermosphere: Long-term observations from the central Pacific, J. Atmos. Sol.-Terr. Phy., 59, 603-627, 1997.

Ern, M., Preusse, P., Alexander, M.J., and Warner, C.D., Absolute values of gravity wave momentum flux derived from satellite data, J. Geophys. Res., 109, D20103, doi:10.1029/2004JD004752, 2004

Espy, P.J., Stegman, J., and Witt, G.: Interannual variations of the quasi-16-day oscillation in the polar summer mesospheric temperature, J. Geophys. Res.-Atmos, 102, D2, 1983-1990, 1997

Espy, P.J., Hibbins, R.E., Swenson, G.R., Tang, J., Taylor, M.J., Riggin, D.M., and Fritts, D.C.: Regional variations of mesospheric gravity-wave momentum flux over Antarctica, Ann. Geophys., 24, 81-88, 2006

Fiedler, J., Baumgarten, G. and von Cossart, G.: Mean diurnal variations of noctilucent clouds during 7 years of lidar observations at ALOMAR, Ann. Geophys., 23, 4, 1175-1181, 2005

Fomichev, V. I., Ward, W. E., Beagley, S.R., McLandress, C., McConnell, J.C., McFarlane, N.A., and Shepherd, T.G.: Extended Canadian Middle Atmosphere Model: Zonal-mean climatology and physical parameterizations, J. Geophys. Res., 107(D10), 4087, doi:10.1029/2001JD000479, 2002

Forbes, J. M.: Atmospheric tides. 1: Model description and results for the solar diurnal component, J. Geophys. Res., 87(A7), 5222-5240, doi:10.1029/JA087iA07p05222, 1982

Forbes, J.M.: Tidal and Planetary Waves, in The Upper Mesosphere and Lower Thermosphere: A review of Experiment and Theory, edited by Johnson, R.M., and Killeen, T.L., Geophysical Monograph, 87, 67-87, American Geophysical Union, 1995

Forbes, J. M.: Wave coupling between the lower and upper atmosphere: case study of an ultra-fast Kelvin Wave, J. Atmos. Sol.-Terr. Phy., 62, 1603-1621, 2000.

Forbes, J. M., Zhang, X. L., Palo, S. E., Russell, J., Mertens, C. J., and Mlynczak, M.: Kelvin waves in stratosphere, mesosphere and lower thermosphere temperatures as observed by TIMED/SABER during 2002-2006, Earth Planets Space, 61, 447-453, 2009.

Forbes, J.M. and Moudden, Y.: Quasi-two-day wave-tide interactions as revealed in satellite observations, J. Geophys. Res.-Atmos., 117, D12110 doi: 10.1029/2011JD017114, 2012

Fraser, G.J., Portnyagin, Y.I., Forbes, J.M., Vincent, R.A., Lysenko, I.A., and Makarov, N.A.: Diurnal tide in the Antarctic and Arctic mesosphere/lower thermosphere regions, J. Atmos. Terr. Phys., 57, 4, 383-393, 1995

Friedman, J.S., Zhang, X., Chu, X., and Forbes, J.M.: Longitude variations of the solar semidiurnal tides in the mesosphere and lower thermosphere at low latitudes observed from ground and space, J. Geophys. Res.-Atmos., 114, doi:10.1029/2009JD011763, 2009

Fritts, D.C., and Vincent, R.A.: Mesospheric momentum flux studies at Adelaide, Australia: Observations and a gravity wave/tidal interaction model, J. Atmos. Sci., 44, 605-619, 1987.

Fritts, D.C., and Isler, J.R.: Mean motions and tidal and two-day structure and variability in the mesosphere and lower thermosphere over Hawaii, J. Atmos. Sci., 51, 14, 2145-2164, 1994

Fritts, D.C., and Yuan, L.: Measurement of Momentum Fluxes Near the Summer Mesopause at Poker Flat, Alaska, J. Atmos. Sci., 46, 16, 2569-2579, doi: 10.1175/1520-0469(1989)046¡2569:MOMFNT¿2.0.CO;2, 1989

Fritts, D.C., Tsuda, T., VanZandt, T.E., Smith, S.A., Sato, T., Fukao, S., and Kato, S.: Studies of Velocity Fluctuations in the Lower Atmosphere Using the MU Radar. Part II: Momentum Fluxes and Energy Densities, J. Atmos. Sci., 47, 51-66, 1990

Fritts, D.C., Yuan, L., Hitchman, M.H., Coy, L., Kudeki, E., and Woodman, R.F.: Dynamics of the Equatorial Mesosphere Observed Using the Jicamarca MST Radar during June and August 1987, J. Atmos. Sci., 49, 2353-2371, 1992

Fritts, D.C., and Alexander, M.J.: Gravity wave dynamics and effects in the middle atmosphere, Rev. Geophys., 41, 1, 1003, 2003

Fritts, D.C., and Rastogi, P.K.: Convective and dynamical instabilities due to gravity wave motions in the lower and middle atmosphere: theory and observations, Radio Sci., 20(6), 1247 - 1277, 1985

Fritts, D. C., Janches, D., Iimura, H., Hocking, W.K., Mitchell, N.J., Fuller, B., Vandepeer, B., Hormaechea, J., Brunini, C., and Levato, H.: Southern Argentina Agile Meteor Radar (SAAMER): System design and initial measurements of large-scale winds and tides, J. Geophys. Res., doi:10.1029/2010JD013850, 2010

Fritts, D.C., Janches, D., and Hocking, W.K.: Southern Argentina Agile Meteor Radar: Initial assessment of gravity wave momentum fluxes, J. Geophys. Res., 115, D19123, doi:10.1029/2010JD013891, 2010

Fritts, D.C., Janches, D., Hocking, W.K., Mitchell, N.J., and Taylor, M.J.: Assessment of gravity wave momentum flux measurement capabilities by meteor radars having different transmitter power and antenna configurations, J. Geophys. Res.,117, D10108, doi:10.1029/2011JD017174, 2012

Fritts, D.C., Janches, D., Iimura, H., Hocking, W.K., Bageston, J.V., and Leme, N.M.P.: Drake Antarctic Agile Meteor Radar first results: Configuration and comparison of mean and tidal wind and gravity wave momentum flux measurements with Southern Argentina Agile Meteor Radar, J. Geophys. Res., 117, D02105, doi:10.1029/2011JD016651, 2012

Gardner, C. S., Gulati, K., Zhao, Y., and Swenson, G.: Measuring gravity wave momentum fluxes with airglow imagers, J. Geophys. Res., 104, 11 903-915, 1999

Garcia, R.R., and Solomon, S.: A numerical model of the zonally averages dynamical and chemical structure of the middle atmosphere, J. Geophys. Res.-Oc. Atm., 88, 1379-1400, 1983

Garcia, R.R., Dunkerton, T.J., Lieberman, R.S., Vincent, R.A.: Climatology of the semiannual oscillation of the tropical middle atmosphere, J. Geophys. Res., 102, 26, 19-26, 032, 1997

Gavrilov, N.M., Fukao, S., and Nakamura, T.: Gravity wave intensity and momentum fluxes in the mesosphere over Shigaraki, Japan (35N, 136E) during 1986-1997,Ann. Geophys., 18, 834-843, 2000

Geisler, J.E., and Dickinson, R.E.: The five-day wave on a sphere with realistic zonal winds, J. Atmos. Sci., 33, 632-641, 1976

Geller, M.A., Dynamics of the middle atmosphere. Space Sci. Rev., 34, 359 - 375, 1983

Gurubaran, S., Rajaram, R., Nakamura, T., and Tsuda, T.: Interannual variability of diurnal tide in the tropical mesopause region: A signature of the El Nino-Southern Oscillation (ENSO), Geophys. Res. Lett., 32, 13, L13805, doi: 10.1029/2005GL022928, 2005

Gurubaran, S., Rajaram, R., Nakamura, T., Tsuda, T., Riggin, D., and Vincent, R.A.: Radar observations of the diurnal tide in the tropical mesosphere-lower thermosphere region: Longitudinal variabilities, Earth Planets Space, 61, 513-524, 2009

Hagan, M.E., and Forbes, J.M.: Migrating and nonmigrating ssemidiurnal tides in the upper atmosphere excited by tropospheric latent heat release, J. Geophys. Res.-Atmos., 108, A2, 1062, doi: 10.1029/2002JA009466, 2003

Hagan, M.E., McLandress, C., and Forbes, J.M.: Diurnal tidal variability in the upper mesosphere and lower thermosphere, Ann. Geophys., 15, 1176-1186, 1997

Hagan, M. E., Burrage, M. D., Forbes, J. M., Hackney, J., Randel, W. J., and Zhang, X.: GSWM-98: Results for migrating solar tides, J. Geophys. Res., 104, 6813-6828, 1999.

Hagan, M.E., Burrage, M.D., Forbes, J.M., Hackney, J., Randel, W.J., and Zhang, X.: QBO effects on the diurnal tide in the upper atmosphere, Earth Planets Space, 51, 571-578, 1999

Hagan, M.E., Maute, A., and Roble, R.G.: Tropospheric tidal effects on the middle and upper atmosphere, J. Geophys. Res., 114, A01302, doi:10.1029/2008JA0136376, 2009

Harris, T.J., and Vincent, R.A.: The Quasi-2-day Wave Observed in the Equatorial Middle Atmosphere, J. Geophys. Res.-Atmos, 98, D6, 10481-10490, 1993

Hartmann, D. L., Michelsen, M. L., and Klein, S. A.: Seasonal-variations of tropical intraseasonal oscillations - a 20-25 day oscillation in the western Pacific, J. Atmos. Sci., 49, 1277-1289, 1992.

Hays, P.B., and Wu, D.L.: Observations of the diurnal tide from space, J. Atmos. Sci., 51, 20, 3077-3093, 1994

Hines, C.O.: Internal atmospheric gravity waves at ionospheric heights, Can. J. Phys., 38, 1441-1481, 1960

Hines, C. O.: Doppler spread parameterization of gravity wave momentum deposition in the middle atmosphere. Part 1. Basic formulation, J. Atmos. Sol. Terr. Phys., 59, 371-386, doi:10.1016/S1364-6826 (96)00079-X, 1997

Hines, C. O.: Doppler spread parameterization of gravity wave momentum deposition in the middle atmosphere. Part 2. Broad and quasimonochromatic spectra, and implementation, J. Atmos. Sol. Terr. Phys., 59, 387-400, doi:10.1016/S1364-6826(96)00080-6, 1997

Hirota, I.: Equatorial waves in upper stratosphere and mesosphere in relation to semiannual oscillation of zonal wind, J. Atmos. Sci., 35, 714-722, 1978.

Hitchman, M. H. and Leovy, C. B.: Estimation of the Kelvin wave contribution to the Semiannual Oscillation, J. Atmos. Sci., 45, 1462-1475, 1988.

Hocking, W.K., Fuller, B., and Vandepeer, B.: Real-time determination of meteor-related parameters utilizing modern digital technology, J. Atmos. Solar. Terr. Phys., 63, 155-169, 2001

Hocking, W.K.: A New Approach to Momentum Flux Determinations Using SKiYMET Meteor Radars, Ann. Geophys., 23, 2433-2439, 2005

Holton, J. R.: On the frequency distribution of atmospheric Kelvin waves, J. Atmos. Sci., 30, 499-501, 1973.

Holton, J. R.: An introduction to dynamic meteorology second edition, Academic Press Inc., New York, 1979.

Holton, J. R. and Lindzen, R. S.: A note on Kelvin waves in the atmosphere, Mon. Weather Rev., 96, 385-386, 1968.

Holton, J. R. and Lindzen, R. S.: Updated theory for quasi-biennial cycle of tropical stratosphere, J. Atmos. Sci., 29, 1076-1080, 1972.

Immel, T.J., Sagawa, E., England, S.L., Henderson, S.B., Hagan, M.E., Mende, S.B., Frey, H.U., Swenson, C.M. and Paxton, L.J.: Control of equatorial ionospheric morphology by atmospheric tides, Geophys. Res. Lett., 33, 15, L15108, doi: 10.1029/2006GL026161, 2006

Kawatani, Y., Sato, K., Dunkerton, T. J., Watanabe, S., Miyahara, S., and Takahashi, M.: The roles of equatorial trapped waves and internal inertia-gravity waves in driving the Quasi-Biennial Oscillation. Part I: Zonal mean wave forcing, J. Atmos. Sci., 67, 963-980, 2010.

Kovalam, S., Vincent, R. A., Reid, I. M., Tsuda, T., Nakamura, T., Ohnishi, K., Nuryanto, A., and Wiryosumarto, H.: Longitudinal variations in planetary wave activity in the equatorial mesosphere, Earth Planets Space, 51, 665-674, 1999.

Kumar, K.K., Deepa, V., Antonita, T.M., and Ramkuma, G.: Meteor radar observations of short-term tidal variabilities in the low-latitude mesosphere-lower thermosphere: Evidence for nonlinear wave-wave interactions, J. Geophys. Res., VOL. 113, D16108, doi:10.1029/2007JD009610, 2008

Lamarque, J.-F., Emmons, L.K., Hess, P.G., Kinnison, D.E., Tilmes, S., Vitt, F., Heald, C.L., Holland, E.A., Lauritzen, P.H., Neu, J., Orlando, J.J., Rasch, P.J., and Tyndall, G.K.: CAM-chem: description and evaluation of interactive atmospheric chemistry in the Community Earth System Model, Geosci. Model Dev., 5, 369-411, 2012

Lieberman, R.S.: Long-term variations of zonal mean winds and (1,1) driving in the equatorial lower thermosphere, J. Atmos. Solar. Terr. Phys. 59, 1483-1490, 1993

Lieberman, R. S.: Intraseasonal variability of high-resolution Doppler imager winds in the equatorial mesosphere and lower thermosphere, J. Geophys. Res.-Atmos., 103, 11221-11228, 1998.

Lieberman, R.S., and Hays, P.B.: An estimate of the momentum deposition in the lower thermosphere by the observed diurnal tide, J. Atmos. Sci., 51, 20, 3094-3105, 1994

Lieberman, R. S. and Riggin, D. M.: High resolution Doppler imager observations of Kelvin waves in the equatorial mesosphere and lower thermosphere, J. Geophys. Res.-Atmos., 102, 26117-26130, 1997.

Lieberman, R.S., Oberheide, J., Hagan, M.E., Remsberg, E.E., and Gordley, L.L.: Variability of diurnal tides and planetary waves during November 1978-May 1979. J. Atmos. Solar. Terr. Phys., 65, 517-528, 2004

Lieberman, R.S., Riggin, D.M., Ortland, D.A., Nesbitt, S.W., and Vincent, R.A.: Variability of mesospheric diurnal tides and tropospheric diurnal heating during 1997-1998, J. Geophys. Res.-Atmos., 112, D20, D20110, doi: 10.1029/2007JD008578, 2007

Lima, L. M., Alves, E. D., Medeiros, A. F., Buriti, R. A., Batista, P. P., Clemesha, B. R., and Takahashi, H.: 3-4 day Kelvin waves observed in the MLT region at 7.4 degrees S, Brazil, Geofisica Int., 47, 153-160, 2008.

Lindzen, R. D.: Planetary waves on beta-planes, Mon. Weather Rev., 95, 441-451, 1967.

Lindzen, R.S.: Thermally driven diurnal tide in atmosphere, Q. J. Roy. Meteor. Soc., 93, 395, 18, doi: 10.1002/qj.49709339503, 1967

Lindzen, R.S., and Chapman, S.: Atmospheric Tides, Sp. Sci. Revs., 10, 3-188, 1969

Liu, A.Z., Lu, X., and Franke, S.J.: Diurnal variation of gravity wave momentum flux and its forcing on the diurnal tide, J. Geophys. Res.-Atmos., 118, 1668-1678, doi:10.1029/2012JD018653, 2013

Livesey, N.J.,Van Snyder, W., Read, W.G., and Wagner, P.A.: Retrieval algorithms for the EOS Microwave Limb Sounder (MLS). IEEE Transactions on Geoscience and Remote Sensing, 44(5), 1144-1155, 2006

London, J.: Radiative energy sources and sinks in the stratosphere and mesosphere, Proceedings of the NATO Advanced Study Institute on Atmospheric Ozone: Its Variation and Human Influences, 703 - 721, 1980

Madden, R. A. and Julian, P. R.: Detection of a 40-50 day oscillation in zonal wind in tropical Pacific, J. Atmos. Sci., 28, 702-708, 1971.

Madden, R. A. and Julian, P. R.: Observations of the 40-50 day tropical oscillation - a review, Mon. Weather Rev., 122, 814-837, 1994.

Manson, A.H., Meek, C.E., Avery, S.K., and Tetenbaum, D.: Comparison of mean wind and tidal fields at Saskatoon (52N, 107W) and Poker Flat (65N, 147W) during 1983/1984, Phys. Scripta, 37, 169-177, 1988

Manson, A.H., Meek, C.E., Teitelbaum, H., Vial, F., Schminder, R., Kurschner, D., Smith, M.J., Fraser, G.J., and Clark, R.R.: Climatologies of semi-diurnal and diurnal tides in the middle atmosphere (70-110 km) at middle latitudes (40-55-degrees), J. Atmos. Terr. Phys., 51, 7-8, 579-593, doi: 10.1016/0021-9169(89)90056-1, 1989

Manson, A., Meek, C., Hagan, M., Hall, C., Hocking, W., MacDougall, J., Franke, S., Riggin, D., Fritts, D., Vincent, R., and Burrage, M.: Seasonal variations of the semi-diurnal and diurnal tides in the MLT: multi-year MF radar observations from 2 to 70N, and the GSWM tidal model, J. Atmos. Sol. Terr. Phys., 61, 809-828, 1999

Manson, A.H., Meek, C.E., Chshyolkova, T., Aso, T., Drummond, J.R., Hall, C.M., Hocking, W.K., Jacobi, C., Tsutsumi, M., and Ward, W.E.: Arctic Tidal Characteristics at Eureka (80N, 86W) and Svalbard (78N, 16E) for 2006/7: Seasonal and longitudinal variations, migrating and non-migrating tides, Ann. Geophys., 27, 1-21, 2009

Mayr, H.G., and Mengel, J.G.: Interannual variations of the diurnal tide in the mesosphere generated by the quasi-biennial oscillation, J. Geophys. Res.-Atmos., VOL. 110, D10111, doi:10.1029/2004JD005055, 2005

McLandress, C., Shephard, G.G., Solheim, B.H.: Satellite observations of thermospheric tides: Results from the Wind Imaging Interferometer on UARS, J. Geophys. Res., 101, D2, 4093-4114, 1996

McLandress, C.: The seasonal variation of the propagating diurnal tide in the mesosphere and lower thermosphere: Part I The role of gravity waves and planetary waves, J. Atmos. Sci., 59, 893-906, 2002

McLandress, C.: The seasonal variation of the propagating diurnal tide in the mesosphere and lower thermosphere: Part II The role of tidal heating and zonal mean winds, J. Atmos. Sci., 59, 907-922, 2002

Mitchell, N.J., Pancheva, D., Middleton, H.R., and Hagan, M.E.: Mean winds and tides in the Arctic mesosphere and lower thermosphere, J. Geophys. Res.-Atmos, 107, A1, 1004, doi:10.1029/2001JA900127, 2002

Mitchell, N.J., and Beldon, C.L.: Gravity waves in the mesopause region observed by meteor radar: 1. A simple measurement technique, J. Atmos. Solar. Terr. Phys., 71, 866-874, 2009

Miyahara, S., Yoshida, Y., Miyoshi, Y.: Dynamic coupling between the lower and upper-atmosphere by tides and gravity waves, J. Atmos. Terr. Phys., 55, 7, 1039-1053, doi:10.1016/0021-9169(93)90096-H , 1993

Miyoshi, Y.: Numerical simulation of the 5-day and 16-day waves in the mesopause region, Earth Planets Space, 51, 7-8, 763-772, 1999

Miyoshi, Y. and Fujiwara, H.: Excitation mechanism of intraseasonal oscillation in the equatorial mesosphere and lower thermosphere, J. Geophys. Res.-Atmos., 111, D14108, 2006.

Murphy, D.J., and Vincent, R.A.: Estimates of momentum flux in the Mesosphere and Lower Thermosphere over Adelaide, Australia, from March 1985 to February 1986, J. Geophys. Res.-Atmos., 98, D10, 18617-18638, 1993

Murphy, D.J., and Vincent, R.A.: Mesospheric momentum fluxes over Adelaide during the 2-day wave: Results and interpretation, J. Geophys. Res.-Atmos., 103, D22, 28627-28636, 1998

Murphy, D.J., Tsutsumi, M., Riggin, D.M., Jones, G.O.L., Vincent, R.A., Hagan, M.E., and Avery, S.K.: Observations of a nonmigrating component of the semidiurnal tide over Antarctica, J. Geophys. Res.-Atmos., 108, D8, 4241

NicollsM.J., Fritts, D.C., Janches, D., and Heinselman, C.J.: Momentum flux determination using the multi-beam Poker Flat Incoherent Scatter Radar, Ann. Geophys., 30, 945-962, 2012

Norton, W. A. and Thuburn, J.: Sensitivity of mesospheric mean flow, planetary waves, and tides to strength of gravity wave drag, J. Geophys. Res.-Atmos., 104, 30897-30911, 1999.

Oberheide, J., Hagan, M.E., Roble, R.G., and Offermann, D.: Sources of nonmigrating tides in the tropical middle atmosphere, J. Geophys. Res.-Atmos., 107, D21, 4567, doi: 10.1029/2002JD002220, 2002

Oberheide, J., Wu, Q., Killeen, T.L., Hagan, M.E., and Roble, R.G.: Diurnal nonmigrating tides from TIMED Doppler Interferometer wind data: Monthly climatologies and seasonal variations, J. Geophys. Res.-Space, 111, A10, A10S03, doi: 10.1029/2005JA011491, 2006

Oberheide, J., Wu, Q., Killeen, T.L., Hagan, M.E., and Roble, R.G.: A climatology of nonmigrating semidiurnal tides from TIMED Doppler Interferometer (TIDI) wind data, J. Atmos. Sol. Terr. Phys., 69, 17-18, 2202-2218, doi: 10.1016/j.jastp.2007.05.010, 2007

Ortland, D. A., and Alexander, M. J.: Gravity wave influence on the global structure of the diurnal tide in the mesosphere and lower thermosphere, J. Geophys. Res., 22. Doi:10.1029/2005JA011467, 2006

Pancheva, D.V., Beard, A.G., and Mitchell, N.J.: Nonlinear interactions between planetary waves in the mesosphere/lower-thermosphere region, J. Geophys. Res., 105(A1), 157-170, 2000

Pancheva, D., Mitchell, N. J., and Younger, P. T.: Meteor radar observations of atmospheric waves in the equatorial mesosphere/lower thermosphere over Ascension Island, Ann. Geophys., 22, 387-404, 2004.

Pancheva, D., Mukhtarov, P., and Andonov, B.: Global structure, seasonal and interannual variability of the migrating semidiurnal tide seen in the SABER/TIMED temperatures (2002-2007), Ann. Geophys., 27, 687-703, 2009

Paulino, A.R., Batista, P.P., and Clemesha, R.: Lunar tides in the mesosphere and lower thermosphere over Cachoeira Paulista (22.7 degrees S; 45.0 degrees W), J. Atmos. Sol. Terr. Phys., 78-79, 31-36, doi: 10.1016/j.jastp.2011.04.018, 2012

Pedatella, N.M., Liu, H.L. and Hagan, M.E.: Day-to-day migrating and nonmigrating tidal variability due to the six-day planetary wave, J. Geophys. Res.-Space, 117, A06301, doi: 10.1029/2012JA017581

Placke, M., Stober,G., and Jacobi, C.: Gravity wave momentum fluxes in the MLTPart I: Seasonal variation at Collm (51.31N, 13.01E), J. Atmos. Solar. Terr. Phys., 73, 904-910, 2011

Placke, M., Hoffmann, P.,Becker, E., Jacobi, C., SingerW., and Rapp, M.: Gravity wave momentum fluxes in the MLTPart II: Meteor radar investigations at high and midlatitudes in comparison with modeling studies, J. Atmos. Solar. Terr. Phys., 73, 911-920, 2011

Portnyagin, Y.I., Forbes, J.M., Fraser, G.J., Vincent, R.A., Avery, S.K., Lysenko, I.A., and Makarov, N.A.: Dynamics of the Antarctic and Arctic mesosphere and lower thermosphere regions. 2. The Semidiurnal tide, J. Atmos. Terr. Phys., 55, 6, 843-855, doi: 10.1016/0021-9169(93)90025-T, 1993

Prata, A.J.: Observations of the 5-day wave in the stratosphere and mesosphere, J. Atmos. Sci., 46(15), 2473-2477, 1989

Rao, R. K., Gurubaran, S., Sathiskumar, S., Sridharan, S., Nakamura, T., Tsuda, T., Takahashi, H., Batista, P. P., Clemesha, B. R., Buriti, R. A., Pancheva, D. V., and Mitchell, N. J.: Longitudinal variability in intraseasonal oscillation in the tropical mesosphere and lower thermosphere region, J. Geophys. Res.-Atmos., 114, D19110, 2009.

Reid, I.M., and Vincent, R.A.: Measurements of mesospheric gravity wave momentum fluxes and mean flow accelerations at Adelaide, Australia, J. Atmos. Terr. Phys., 49, 443-460, 1987

Reid, I.M.: MF radar measurements of sub-scale mesospheric momentum flux, Geophys. Res. Lett., 31, 17, L17103, doi: 10.1029/2003GL019200, 2004

Riggin, D. M., Fritts, D. C., Tsuda, T., Nakamura, T., and Vincent, R. A.: Radar observations of a 3-day Kelvin wave in the equatorial mesosphere, J. Geophys. Res.-Atmos., 102, 26141-26157, 1997.

Riggin, D.M., Meyer, C.K., Fritts, D.C., Jarvis, M.J., Murayama, Y., Singer, W., Vincent, R.A., Murphy, D.J.: MF radar observations of seasonal variability of semidiurnal motions in the mesosphere at high northern and southern latitudes, J. Atmos. Sol. Terr. Phys., 65, 4, 483-493, doi: 10.1016/S1364-6826(02)00340-1, 2003

Rodgers, C. D.: Inverse Methods for Atmospheric Sounding: Theory and Practice, World Sci., Hackensack, N. J., 2000

Salby, M. L. and Garcia, R. R.: Transient-response to localized episodic heating in the tropics. 1. Excitation and short-time near-field behaviour, J. Atmos. Sci., 44, 458-498, 1987.

Salby, M. L., Hartmann, D. L., Bailey, P. L., and Gille, J. C.: Evidence for equatorial kelvin modes in NIMBUS-7 LIMS, J. Atmos. Sci., 41, 220-235, 1984.

Sandford, D., and Mitchell, N.J.: Lunar tides in the mesosphere over Ascensions Island (8^{o}S 14.4^{o}W), Ann. Geophys., 25, 9-12, 2007

Schoeberl, M.R., Douglass, A.R., Hilsenrath, E., Bhartia, P.K., Beer, R., Waters, J.W.,Gunson, M.R., Froidevaux, L., Gille, J.C., Barnett, J.J., Levelt, P.E., and DeCola, P.: Overview of the EOS Aura mission, IEEE Transactions on Geoscience and Remote Sensing, 44(5), 1066-1074, 2006

Schwartz, M. J., Lambert, A., Manney, G. L., Read, W. G., Livesey, N. J., Froidevaux, L., Ao, C. O., Bernath, P. F., Boone, C. D., Cofield, R. E., Daffer, W. H., Drouin, B. J., Fetzer, E. J., Fuller, R. A., Jarnot, R. F., Jiang, J. H., Jiang, Y. B., Knosp, B. W., Kruger, K., Li, J. L. F., Mlynkzac, M. G., Pawson, S., Russell, J. M., Santee, M. L., Snyder, W. V., Stek, P. C., Thurstans, R. P., Tompkins, A. M., Wagner, P. A., Walker, K. A., Waters, J. W., and Wu, D. L.: Validation of the aura microwave limb sounder temperature and geopotential height measurements, J. Geophys. Res.-Atmos., 113, D15S11, 2008.

Smith, A.K.: Global dynamics of the MLT, Surv. Geophys., 33, 1177-1230, doi:10.1007/s10712-012-9196-9, 2012

Sridharan, S., Gurubaran, S., and Rajaram, R.: Radar observations of the 3.5-day ultra-fast Kelvin wave in the low-latitude mesopause region, J. Atmos. Sol.-Terr. Phy., 64, 1241-1250, 2002.

Sridharan, S., Tsuda, T., and Gurubaran, S.: Long-term tendencies in the mesosphere/lower thermosphere mean winds and tides as observed by medium-frequency radar at Tirunelveli (8.7N, 77.8E), J. Geophys. Res.-Atmos., 115, doi:10.1029/2008JD011609, 2010

Swenson, G. R., Haque, R., Yang, W., and Gardner, C. S.: Momentum and energy fluxes of monochromatic gravity waves observed by an OH imager at Starfire Optical Range, New Mexico, J. Geophys. Res., 104, 6067-6080, 1999

Takahashi, M. and Boville, B. A.: A 3-dimensional simulation of the equatorial quasi-biennial oscillation, J. Atmos. Sci., 49, 1020-1035, 1992.

Takahashi, H., Wrasse, C. M., Fechine, J., Pancheva, D., Abdu, M. A., Batista, I. S., Lima, L. M., Batista, P. P., Clemensha, B. R., Schuch, N. J., Shiokawa, K., Gobbi, D., Mlynkzac, M. G., and Russell, J. M.: Signatures of ultra fast Kelvin waves in the equatorial middle atmosphere and ionosphere, Geophys. Res. Lett., 34, L11108, 2007.

Teitelbaum, H., Vial, F., Manson, A.H., Giraldez, R., and Massebeuf, M.: Non-linear interaction between the diurnal and semidiurnal tides - terdiurnal and diurnal secondary waves, J. Atmos. Terr. Phys., 51, 7-8, 627-634, doi: 10.1016/0021-9169(89)90061-5, 1989

Thomas, G.E.: Global change in the mesosphere-lower thermosphere region: Has it already arrived? J. Atmos. Sol. Terr. Phys., 58, 1629-1656, 1996

Tsuda, T., Ohnishi, K., Isoda, F., Nakamura, T., Vincent, R.A., Reid, I.M., Harijono, S.W.B., Sribimawati, T., Nuryanto, A., and Wiryosumarto, H.: Coordinated radar observations of atmospheric diurnal tides in equatorial regions, Earth Planets Space, 51, 579-592, 1999

Tunbridge, V.M., Sandford, D.J., and Mitchell, N.J.: Zonal wave numbers of the summertime 2 day planetary wave observed in the mesosphere by EOS Aura Microwave Limb Sounder, J. Geophys. Res.-Atmos, 116, D11103, doi:10.1029/2010JD014567, 2011

Vincent, R.A., and Reid, I.M.: HF Doppler Measurements of Mesospheric Gravity Wave Momentum Fluxes, J. Atmos. Sci., 40, 5, 1321-1333, doi: 10.1175/1520-0469(1983)040¡1321:HDMOMG¿2.0.CO;2, 1983

Vincent, R.A., Tsuda, T., and Kato, S.: A comparative study of mesospheric solar tides observed at Adelaide and Kyoto, J. Geophys. Res.-Atmos., 93, D1, 699-708, doi: 10.1029/JD093iD01p00699 , 1988

Vincent, R. A.: Long-period motions in the equatorial mesosphere, J. Atmos. Sol.-Terr. Phy., 55, 1067-1080, 1993.

Vincent, R.A., Kovalam, S., Fritts, D.C., and Isler, J.R.: Long-term MF radar observations of solar tides in the low-latitude mesosphere: Interannual variability and comparisons with the GSWM, J. Geophys. Res-Atmos., 103, D8, 8667-8683, 1998

Vincent, R.A., Kovalam, S., Reid, I.M., and Youngerm J.P.: Gravity wave flux retrievals using meteor radars, Geophys. Res. Lett., 37, L14802, doi:10.1029/2010GL044086, 2010

Wallace, J. M. and Kousky, V. E.: Observational evidence of Kelvin waves in tropical stratosphere, J. Atmos. Sci., 25, 900-907,1968.

Ward, W.E., Oberheide, J., Goncharenko, L.P., Nakamura, T., Hoffmann, P., Singer, W., Chang, L.C., Du, J., Wang, D.-Y, Batista, P., Clemesha, B., Manson, A.H., Riggin, D.M., She, C.-Y., Tsuda, T., and Yuan, T.: On the consistency of model, ground-based and satellite observations of tidal signatures: Initial results from the CAWSES tidal campaigns, J. Geophys. Res., 115, D07107, doi:10.1029/2009JD012593, 2010

Waters, J.W., Froidevaux, L., Jarnot, R.F., Read, W.G., Pickett, H.M., Harwood, R.S., Cofield, R.E., Filipiak, M.J., Flower, D.A., Livesey, N.J., Manney, G.L., Pumphrey, H.C., Santee, M.L., Siegel, P.H., and Wu, D.L: An overview of the EOS MLS experiment, Version 2.0 D-15745, Jet Propulsion Laboratory, 2004

Waters, J.W., Froidevaux, L., Harwood, R.S., Jarnot, R.F., Pickett, H.M., Read, W.G., Siegel, P.H., Cofield, R.E., Filipiak, M.J., Flower, DA., Holden, J.R., Lau, G.K.K., Livesey, N.J., Manney, G.L., Pumphrey, H.C., Santee, M.L., Wu, D.L., Cuddy, D.T., Lay, R.R., Loo, M.S., Perun, V.S., Schwartz, M.J., Stek, P.C., Thurstans, R.P., Boyles, M.A., Chandra, K.M., Chavez, M.C., Chen, G.S., Chudasama, B.V., Dodge, R., Fuller, R.A., Girard, M.A., Jiang, J.H., Jiang, Y.B., Knosp, B.W., LaBelle, R.C., Lam, J.C., Lee, K.A., Miller, D., Oswald, J.E., Patel, N.C., Pukala, D.M., Quintero, O., Scaff, D.M., Van Snyder, W., Tope, M.C., Wagner, P.A., and Walch, M.J.: The Earth Observing System Microwave Limb Sounder (EOS MLS) on the Aura satellite, IEEE Transactions on Geoscience and Remote Sensing, 44(5), 1075-1092, 2006

Williams, C.R., and Avery, S.K.: Diurnal nonmigrating tidal oscillations forced by deep convective clouds, J. Geophys. Res.-Atmos, 101, D2, 4079-4091, 1996

Wright, C.J., and Gille, J.C.: Detecting overlapping gravity waves using the S-Transform, Geophys. Res. Lett., 40, 9, 1850-1855, 2013

Wright, C.J., Osprey, S.M., and Gille, J.C., in preparation, 2014

Wu, D.L.,Hays, P.B., Skinner, W.R., Marshall, A.R., Burrage, M.D., Lieberman, R.S. and Ortland, D.A.: Observations of the Quasi-2-day wave from the High-Resolution Doppler Imager on UARS, Geophys. Res. Lett., 20, 24, 2853-2856, 1993

Wu, D.L., Hays, P. B., and Skinner,W. R.: Observations of the 5-day wave in the mesosphere and lower thermosphere, Geophys. Res. Lett., 21(24), 2733-2836, 1994

Wu, D. L., Hays, P. B., and Skinner, W. R.: A least-squares method for spectral analysis of space-time series, J. Atmos. Sci., 52, 3501-3511, 1995.

Wu, Q., Ortland, D.A., Solomon, S.C., Skinner, W.R., and Niciejewski, R.J.: Global distribution, seasonal, and inter-annual variations of mesospheric semidiurnal tide observed by TIMED TIDI, J. Atmos. Sol. Terr. Phys., 73, 2482-2502, 2011

Xu, J., Smith, A.K., Liu, H.-L., Yuan, W., Wu, Q., Jiang, G., Mlynczak, M.G., Russell III, J.M., Franke, S.J.: Seasonal and quasi-biennial variations in the migrating diurnal tide observed by Thermosphere, Ionosphere, Mesosphere, Energetics and Dynamics (TIMED), J. Geophys. Res., 114, doi:10.1029/2008JD011298, 2009a

Xu, J., Smith, A.K., Liu, H.-L., Yuan, W., Wu, Q., Jiang, G., Mlynczak, M.G., and Russell III, J.M.: Estimation of the equivalent Rayleigh friction in mesosphere/lower thermosphere region from the migrating diurnal tides observed by TIMED, J. Geophys. Res., 114, D23103, doi:10.1029/2009JD012209, 2009b

Yoshida, S., Tsuda, T., Shimizu, A., and Nakamura, T.: Seasonal variations of 3.0 similar to 3.8-day ultra-fast Kelvin waves observed with a meteor wind radar and radiosonde in Indonesia, Earth Planets Space, 51, 675-684, 1999.

Younger, P. T. and Mitchell, N. J.: Waves with period near 3 days in the equatorial mesosphere and lower thermosphere over Ascension Island, J. Atmos. Sol.-Terr. Phy., 68, 369-378, 2006.

Younger, P.T., Pancheva, D., Middleton, H.R., and Mitchell, N.J.: The 8-hour tide in the Arctic mesosphere and lower thermosphere, J. Geophys. Res.-Space, 107, A12, 1420, doi: 10.1029/2001JA005086, 2002

Younger, P.T., Astin, I., Sandford, D.J., and Mitchell, N.J.: The sporadic radiant and distribution of meteors in the atmosphere as observed by VHF radar at Arctic, Antarctic and equatorial latitudes, Ann. Geophys., 27, 7, 2831-2841, 2009

Zhang, X., Forbes, J.M., and Hagan, M.E.: Longitudinal variation of tides in the MLT region: 1. Tides driven by tropospheric net radiative heating, J. Geophys. Res.-Atmos., 115, A06316, doi: 10.1029/2009JA014897, 2010